Recycling and upcycling of cathode materials from lithium-ion batteries
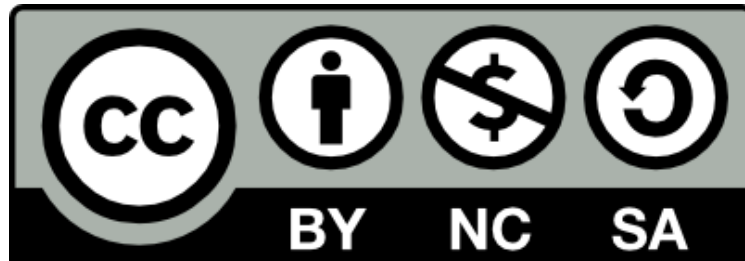
By

Rosie Madge

A thesis submitted to the University of Birmingham for the degree of Doctor of Philosophy

The School of Chemistry

College of Engineering and Physical Sciences

University of Birmingham

March 2024

University of Birmingham Research Archive

e-theses repository

Abstract

In the past decade there has been a significant increase in the number of electric vehicles (EVs) globally. In turn, this has led to increased amounts of end-of-life (EOL) lithium-ion batteries (LIBs). These EOL LIBs must be recycled to allow the materials from them to be reused. Ideally, closed-loop recycling methods should be used to allow recovered materials to be directly used in the manufacture of materials for new LIBs.

This work investigates recycling of cathode material from a Gen 1 Nissan Leaf which contains a mixture of spinel $LiMn_2O_4$ (LMO) and a Ni-rich layered oxide (LO). Both EOL and quality control (QC) rejected material was investigated in this thesis as they are representative of EOL batteries and manufacturing scrap that is likely to be present in the LIB recycling market.

This work develops a method which allows for separation of the LMO and LO phases. Citric acid was employed as a leaching agent to selectively leach the LMO component into solution while leaving the LO phase in the cathode. Citric acid also acts as a delamination agent to remove the remaining LO from the Al current collector. The optimal conditions for allowing facile separation with the best selectivity were 10 mL of 1 M acid at 50 °C with 0.3 g of cathode for 20 mins. The LMO and LO phases were recovered and then utilised in new LIBs. However, LMO is no longer used commercially and has a lower value than Ni/Co containing cathodes therefore this work investigated upcycling it into new cathode materials.

Firstly, LMO was upcycled into Ni-doped spinels. $LiMn_{1.5}Ni_{0.5}O_4$ (LMNO) is attracting commercial interest due its high operating voltage and high energy density. Both EOL

and QC LMO were upcycled into LMNO. This work investigates improving the electrochemical performance of upcycled LMNO by changing the composition, synthesis temperature, and synthesis atmosphere. EOL and QC LMNO were shown to have an improved capacity retention compared to pristine LMNO.

This work also investigates upcycling LMO into Mn-containing cation disordered rocksalt (DRS) materials. Firstly, work was done to prevent degradation and improve the electrochemical performance of $Li_4Mn_2O_5$ using coatings and alternative electrochemical testing procedures. F, Ni, Zn and Na doping were also investigated as ways to improve the capacity retention. Na doping was found to provide the best capacity retention of 78.9% after 20 cycles. Finally, EOL and QC LMO were upcycled into $Li_4Mn_2O_5$ and $Li_2MnO_{2.25}F$ which performed with a comparable electrochemical performance to DRS made using pristine starting materials.

This work details a method for the separation of mixed cathodes containing LMO and LO. It also demonstrates a method to upcycle lower value cathode materials, such as LMO, into current and next generation cathode materials, such as LMNO and DRS materials.

Acknowledgements

Firstly, I would like to thank my supervisor Professor Peter Slater for all his help and input throughout the years. I would also like to thank the Faraday Institution for funding my project and for creating such an amazing PhD training program.

I would like to give a huge thank you to the people who were there in the very beginning and taught me everything that I know about working in a lab: Dr Daniel Smith, Dr Mark Stockham, Dr Matthew James and Dr Abbey Jarvis. I would never have learnt to change a cylinder or XRD a sample without you! Dan, thank you for taking the time to show me how things worked at least 3 times and for thinking about my science as well as your own. Especially at the beginning, I don't know that you realise how much of a help this was. Mark, thank you for explaining anything and everything and for your unwavering commitment to trying to do science that matters. You inspire me to try harder. Matt, thank you for being honest about the PhD and making me feel like there was always someone that I could talk to. Abbey, thank you for the endless help and support and always being willing to put the time in. I appreciate it more than you will ever know! And more recently, thank you Jaime for your help with coatings/cells but also thanks for talking science with me. I also appreciate the endless conversations that had nothing to do with science as well! I would also like to thank Will for all his support with XANES.

Finally, thank you to the people in my personal life. Thank you, Mum. Thank you for always being there to discuss the thesis and thank you for always being there in life. Thank you for believing in me and making me feel like I could do it. Thank you to Musk.

Musk you always knew I'd be a scientist! I hope that you and Paddle are proud. Thank you, Dad. Dad, thank you for your 100% faith that I'd make it happen and for always being willing to talk about something else entirely! I can always rely on you to give me a different perspective to everybody else. Finally, thank you to Dan. Dan you have been here the whole time. Thank you for the scientific discussions, thank you for the advice, thank you for listening and most of all thank you for being there.

Contents

Abbreviations

BSE	Backscattered electrons
CCP	Cubic close-packed
DRS	Disordered rocksalt
EDX	Energy dispersive X-ray
EOL	End-of-life
EV	Electric vehicle
GOF	Goodness of fit
HOMO	Highest occupied molecular orbital
ICP-OES	Inductively coupled plasma optical emission spectroscopy
LCO	$LiCoO_2$
LFP	$LiFePO_4$
LIB	Lithium-ion battery
LMNO	$LiMn_{1.5}Ni_{0.5}O_4$
LMO	$LiMn_2O_4$
LO	Layered oxide
LUMO	Lowest unoccupied molecular orbital

NCA	$LiNi_{0.8}Co_{0.15}Al_{0.05}O_2$
NMC	$LiNi_xMn_yCo_{1-x-y}O_2$
NMC111	$LiNi_{1/3}Co_{1/3}Mn_{1/3}O_2$
NMC811	$LiNi_{0.8}Mn_{0.1}Co_{0.1}O_2$
PVDF	Polyvinylidene fluoride
QC	Quality control
R_{exp}	Experimental profile factor
R_p	Profile factor
R_{wp}	Weighted profile factor
S:L ratio	Solid to liquid ratio
SE	Secondary electrons
SEM	Scanning electron microscopy
TM	Transition metals
wt%	Weight percent
VT-XRD	Variable temperature X-ray diffraction
XANES	X-ray absorption near edge structure
XRD	X-ray diffraction

Chapter 1: Introduction

Fossil fuels cause detrimental environmental consequences and therefore there has been a shift towards the use of renewable energy sources, such as solar and wind power. Batteries are crucial in enabling this move towards the use of renewable energy as they counteract the intermittency of renewable energy sources by allowing energy to be stored and then released when it is required.

A rechargeable battery is an energy storage device that stores chemical energy, which can then be converted back to electrical energy for later use. One application where batteries are gaining prominence is in electric vehicles (EVs). EVs are commonly powered by electricity which is stored in lithium-ion batteries (LIBs) rather than a conventional internal combustion engine.

1.1. Lithium-ion batteries

A LIB is a rechargeable battery that works by shuttling both Li ions and electrons between electrodes (Figure 1-1). One electrode is generally a Li and transition metal (TM) oxide while the other electrode is graphite or a graphite-Si blend. During charging, the Li ions move from the Li TM oxide to the graphite while the electrons move in the same direction via an external circuit. During discharging, the Li ions and electrons move spontaneously in the opposite direction. The Li TM oxide is the cathode during the discharging process while the graphite is the anode. For the remainder of this thesis, the cathode will refer to the Li TM oxide and the anode will refer to the graphite. The electrodes are separated by a polymer separator, which allows Li ions to pass through but not electrons. The separator is soaked in an electrolyte, commonly $LiPF_6$

in organic solvents, which acts as a carrier for the Li ions. Current collectors allow the electrons to pass from the electrodes to the external circuit. Cu must be used on the graphite electrode as Al forms alloys with Li at low voltages.
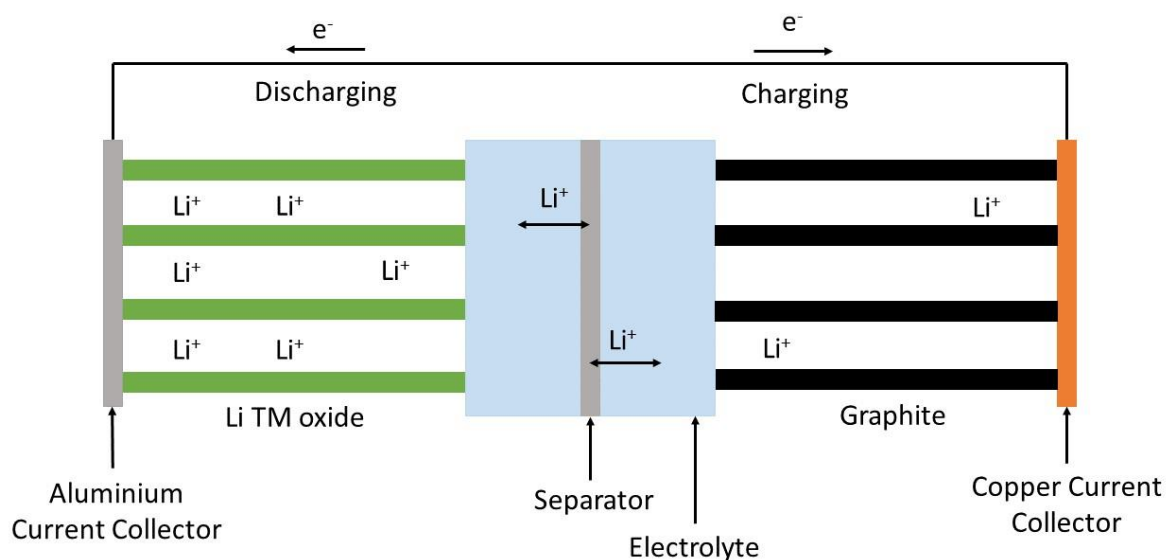
Figure 1-1: Diagram of a lithium-ion battery

The voltage of a LIB depends on the difference between the electrochemical potentials of the anode and the cathode (Figure 1-2).[1] The larger this difference, the larger the voltage (V_{oc}). However, the electrochemical potentials of the electrodes must fit within the gap between the highest occupied molecular orbital (HOMO) and lowest unoccupied molecular orbital (LUMO) of the electrolyte. If this is not the case, the electrons will cause oxidation/reduction of the electrolyte rather than traveling around the external circuit.[1] These oxidation/reduction reactions can cause the formation of a layer on the surface of the electrodes which is known as the solid electrolyte interface. The solid electrolyte interface is necessary on the graphite electrode as it acts as a passivating layer which allows Li^+ transport but blocks electrons and therefore prevents further electrolyte decomposition.[2]
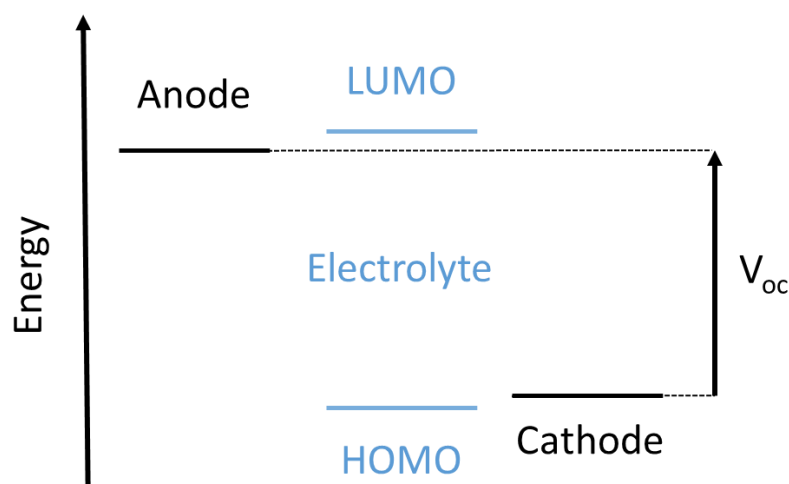
Figure 1-2: Diagram showing the relative energies of the electrodes and the HOMO and LUMO of the electrolyte

1.1.1. Conventional lithium-ion battery cathodes

Conventional LIB cathode materials commonly contain Li along with TMs (typically Co, Ni and Mn) which are redox active to facilitate the deintercalation/intercalation of Li from the structure. The gravimetric capacity of LIBs depends on the amount of Li that can be reversibly removed from the cathode and the molar mass of the cathode. The larger the amount of removable Li and the smaller the molar mass, the higher the capacity.[3] Ideally, LIBs will have as high a voltage and capacity as possible as this results in the highest energy density. As mentioned in section 1.1., the cathode material must also be stable with the electrolyte. Furthermore, the cathode material must have good electronic and ionic conductivity, to allow both the Li ions and electrons to easily pass through the material into/from the electrolyte and the current collector, respectively. The cathode material should also have a long cycle lifetime and low cost.[4] Ideally, the cathode materials will also consist of sustainable elements and be completely safe during use.

In the first generation of EVs utilising LIBs, $LiMn_2O_4$ (LMO) and $LiNi_xMn_yCo_{1-x-y}O_2$ (NMC) were used in the cathodes. Blended cathodes containing several cathode materials were also used to allow the positive properties of the different materials to be combined. For example, the First-Generation Nissan Leaf contains a blended NCA/LMO cathode.[5] There was then a move towards higher-Ni content cathodes such as $LiNi_{0.8}Mn_{0.1}Co_{0.1}O_2$ (NMC811) and $LiNi_{0.8}Co_{0.15}Al_{0.05}O_2$ (NCA) as these provide a higher capacity. Tesla originally used NCA and NMC chemistries in their early car models.[6] Recently, $LiFePO_4$ (LFP) has gained popularity as it is cheaper and safer. In October 2021, Tesla announced a move to LFP, with NCA only being used for its longer-range premium vehicles.[7]

1.1.1.1. $LiMn_2O_4$

LMO has a spinel structure and consists of a cubic close-packed (CCP) arrangement of O which contains Li in the tetrahedral holes and Mn in the octahedral holes (Figure 1-3). LMO contains 3D pathways that the Li ions can easily diffuse through to result in a high ionic conductivity. Furthermore, it is low cost, since it does not contain any Co or Ni. However, LMO has a limited capacity (~ 120 $mAhg^{-1}$) and experiences severe capacity fade during cycling. This capacity fade is primarily caused by the fact that Mn^{3+} can disproportionate into Mn^{2+} and Mn^{4+}.[8] Mn^{2+} can then dissolve into the electrolyte.[9] Furthermore, Mn^{3+} is Jahn-Teller active and causes a structural distortion from cubic to tetragonal symmetry, which has a detrimental impact upon electrochemical performance.[10] The LMO structure can incorporate extra Li into the empty octahedral holes to provide a higher capacity.[10] However, this causes the

proportion of Mn^{3+} to increase and therefore exacerbates the damage caused by Jahn-Teller distortions.

Li
Mn
O
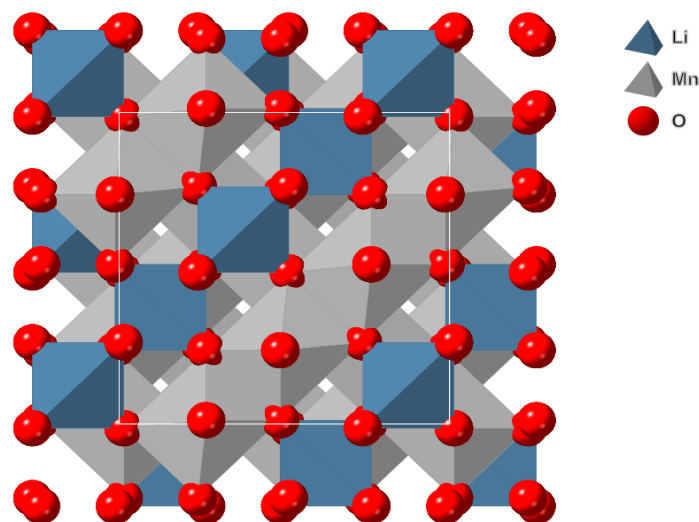
Figure 1-3: Crystal structure of LiMn$_2$O$_4$ with Li sites in blue, Mn sites in grey and O sites in red

1.1.1.2. LiNi$_x$Mn$_y$Co$_{1-x-y}$O$_2$

NMC materials have a CCP arrangement of O with alternating layers of Li and Ni/Mn/Co in the octahedral holes (Figure 1-4). The Co ions are crucial to prevent the migration of Ni into the Li layers. During cycling, Co and Ni change oxidation state to facilitate the removal of Li from the structure while Mn is redox inactive and instead acts to stabilise the structure.[11] NMC materials have a range of compositions with the ratio of different metals given. NMC111 corresponds to LiNi$_{1/3}$Co$_{1/3}$Mn$_{1/3}$O$_2$, while NMC811 corresponds to LiNi$_{0.8}$Co$_{0.1}$Mn$_{0.1}$O$_2$. Over time, there has been a move towards the use of NMC811 as it has a higher capacity ($\sim$ 200 mAhg^{-1}) than other NMC compositions, such as NMC111/532/622. As the Ni content increases, the capacity increases because Ni is the main redox active species. However, NMC811 suffers from problems such as Ni/Li disorder, surface sensitivity and micro-cracking which all have a detrimental impact upon the long-term cycling performance.[12–14] Nevertheless,

through the use of coatings and electrolyte additives to improve the stability[15–19], it has

become a favoured cathode, and indeed there is now a move to even higher Ni content

materials, such as $LiNi_{0.9}Co_{0.05}Mn_{0.05}O_2$ or suitably doped $LiNiO_2$.
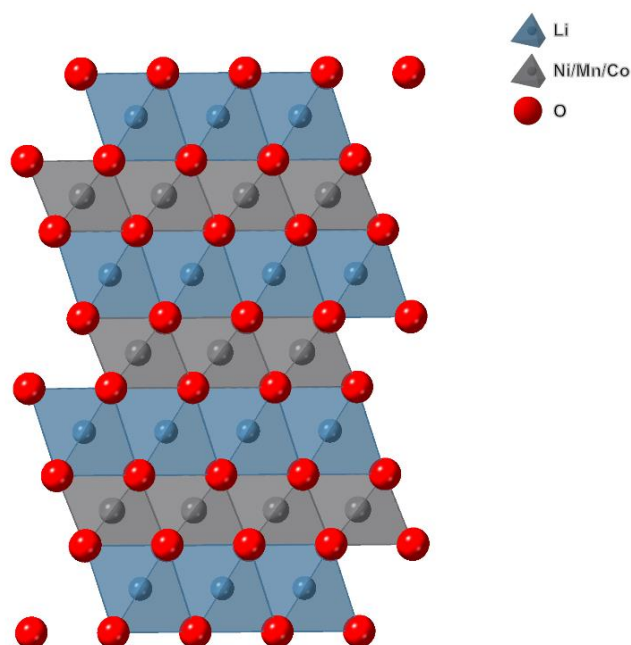
Figure 1-4: Crystal structure of $LiNi_xMn_yCo_{1-x-y}O_2$ with Li sites in blue, Ni/Mn/Co sites in grey and O sites in red

1.1.1.3. $LiNi_{0.8}Co_{0.15}Al_{0.05}O_2$

NCA is isostructural with NMC but contains Al instead of Mn. Al acts to provide

structural and thermal stability whilst also being low cost and low weight. During

cycling, Al is redox inactive akin to Mn in NMC. NCA provides a high capacity (180-

200 mAhg^{-1}) along with enabling the production of a battery with a high energy density

due to the high operating voltage. However, NCA degrades upon cycling due to

microcracking and irreversible phase transitions from the layered phase to a rocksalt

or spinel phase.[20,21]

1.1.1.4. LiFePO$_4$

LFP is a polyanionic material which has an olivine structure. It consists of a distorted hexagonal close-packed arrangement of O which contains Li and Fe in different octahedral sites (Figure 1-5). LFP can achieve capacities very close to its theoretical capacity of 170 mAhg^{-1}. LFP has the advantage of being low cost since it does not contain any Co or Ni. Furthermore, fully delithiated FePO$_4$ has the same framework as LFP which provides stability when undergoing continuous lithiation/delithiation processes.[22] LFP also has an excellent thermal stability which results in an improved safety compared to LIBs containing other cathode materials, such as NMCs.[23,24] However, LFP has a low electronic conductivity and poor Li diffusion. Methods such as carbon coatings, reducing particle sizes and doping have been utilised to counteract these issues.[25–27]
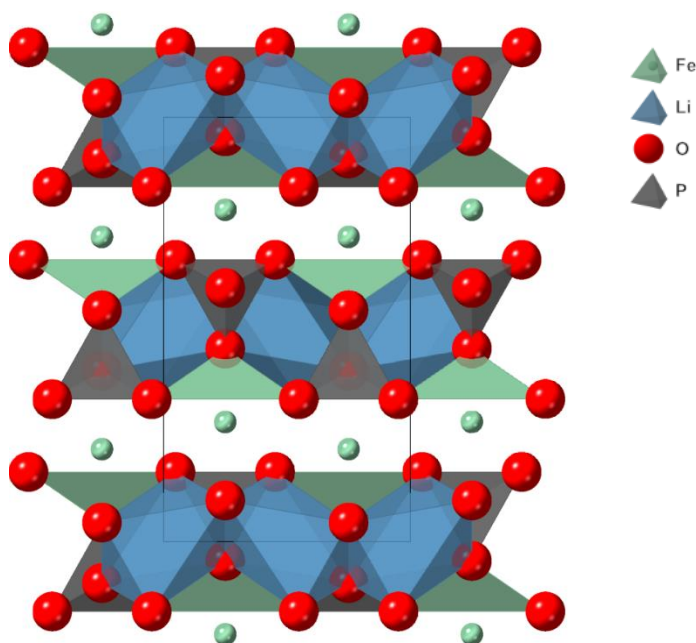
Figure 1-5: Crystal structure of LiFePO$_4$ with Li sites in blue, Fe sites in green, P sites in grey and O sites in red

1.2. Recycling lithium-ion battery cathodes

EVs are commonly powered by electricity stored by LIBs and these LIBs normally last for 5-20 years depending on their operating conditions.[28] The UK's transportation decarbonisation plan mandates that all new cars/vans must be fully zero emission from 2035.[29] In addition to this, the UK's Critical Minerals Strategy lists battery metals, such as Li and Co, as critical minerals for the UK, while Mn and Ni are on the watchlist.[30] This means that they are essential to national security and a healthy economy but also that they have unstable and unpredictable supply chains. The strategy suggests increasing recovery, reuse and recycling of these critical minerals through a circular economy as one way to mitigate these problems. The EU has created legislation that requires LIBs to contain a minimum level of recycled content (12% Co, 4% Li and 4% Ni) by 2030[31], while in the US, the Infrastructure Investment and Jobs Act provides $60 million for research into battery recycling.[32]

As the number of spent LIBs increases, it is essential that they are recycled, either to regain the valuable metals within them or to directly reform new battery materials. Recycling would also help to contribute to providing supply chain stability and lead to a reduction in the mining of specific elements, which could help prevent problems such as drought and vegetation decline linked to the mining of Li in Chile, and ethical issues associated with the use of child labour for the mining of Co in the Democratic Republic of Congo.[33,34] Furthermore, there is also the potential to develop recycling methods that have both an energy and economic saving when compared to the manufacture of LIB materials from virgin materials. Based on the recycling costs for ten hydrometallurgical recycling processes from the literature, it was found that recycling

based on shredded starting material offered cost savings of up to 20% for battery production compared to using virgin materials.[35] Alternatively, another way to extend the usefulness of LIB is to utilise the batteries in second life applications, such as stationary energy storage systems.[36]

However, recycling LIBs is difficult for a number of reasons. First of all, there is a huge variety of cell design, such as pouch, prismatic and cylindrical, and each of these different designs requires a different disassembly method. As mentioned in section 1.1., a LIB consists of numerous diverse components which will ideally be recycled individually via suitable methods. There is also variation in the materials used for the different components, especially in regards to the cathode where a number of different materials are employed commercially. Furthermore, cell manufacturers do not publish which materials are present in each of the different cells. This therefore makes recycling more difficult as the materials present in the cathode are often unknown. Recent EU regulation aims to help to combat this by introducing mandatory "battery passports" which will contain the necessary information relating to each battery.[37]

The cathode accounts for most of the cost of a LIB and therefore it is often the focus of recycling methods.[38] The recycling of LIB cathodes can be split into 2 main categories: reagent recovery and closed-loop recycling. Reagent recovery is where the individual starting reagents are recovered. Reagent recovery is a well-established technology however it can involve a large amount of energy consumption and multiple processing steps. Furthermore, it tends to focus only on the economically valuable products, such as Ni and Co. In comparison, closed-loop recycling is where the spent cathode material is directly used to form a new cathode material. Closed-loop recycling

involves fewer processing steps and is therefore quicker and cheaper than reagent recovery. It is also extremely important for recycling materials containing Fe or Mn, such as LFP and LMO, as these have a greater value as cathode materials than as starting reagents.[39,40]

1.2.1. Reagent recovery

Prior to the recovery, the battery must be discharged and then disassembled. The discharge step is commonly performed by submerging the LIBs into a salt-water solution.[41] Alternatively, thermal treatments or electrical discharge can also be used. This is then followed by breaking up the battery, which is achieved by either shredding or crushing the battery. More labour-intensive dismantling and physical separation is also possible, which leads to less cross-contamination of the battery components. The battery is then treated using one of the following methods.

1.2.1.1. Pyrometallurgical recovery

Pyrometallurgical recovery involves heating the LIBs to high temperatures (> 1000 °C) to recover an alloy of high value metals, with a waste slag containing Li and Mn. This is often followed by hydrometallurgical-type steps to separate the different metals from the alloy. Pyrometallurgical recovery is utilized due to the ease of the process and the fact that high value Ni and Co can be recovered. Furthermore, pyrometallurgical recovery can be performed without a prior discharging step and can be used on a range of different cell chemistries. However, the pyrometallurgical process is energy intensive and creates secondary pollution. Additionally, as there is a move towards

cathode materials with a lower Ni/Co content, such as LFP, the process becomes less economically viable.

1.2.1.2.   Hydrometallurgical recovery

Hydrometallurgical recovery uses aqueous solutions to leach specific elements from the cathode mixtures. The most common solution used is H_2SO_4 along with H_2O_2; which acts as a reducing agent. The concentration of the leaching acid, temperature of solution, solid-liquid ratio and the addition of a reducing agent have all been found to influence the leaching process.[42–49] After leaching, solvent extractions are performed for purification. Precipitation reactions are then used to extract individually different metals from the solution. Hydrometallurgical recovery can recover multiple metals in sequence, can be performed on a range of cathode materials, and has high metal recovery efficiencies. However, it does involve multiple steps and the use of hazardous acids, while the waste products can be pollutants.

1.2.1.3.   Bioleaching

Bioleaching uses bacteria or fungi to extract metals from spent cathode materials. *Acidithiobacillus ferrooxidans (Af)*[50–53]*, Acidithiobacillus thiooxidans (At)*[53–56] and *Aspergillus niger*[55,57] have all been investigated as bacteria candidates for the recycling process. Bioleaching can either be done as a one-step or two-step procedure; the former involves adding the cathode material and bacteria simultaneously to the culture medium while the latter involves adding the cathode material once the bacteria has already reached its maximum level of growth. Research has also studied the effect of pulp density, the number of leach stages and the initial pH upon the leaching

procedure. Bioleaching avoids the use of toxic chemicals and therefore avoids the generation of hazardous waste products. However, the bioleaching process is time consuming and has a lower efficiency than standard hydrometallurgical processes.

1.2.2. Closed-loop recycling

As for the above methods for reagent recovery, the battery must first be discharged and then disassembled to obtain the cathode only. Ideally the battery is carefully dismantled, and the particle morphology on the current collector maintained. If the LIBs are shredded, methods are then required to separate the cathode and anode material. Separation by froth flotation has been suggested however it does not have a very good recovery efficiency.[58–60] Furthermore, shredding causes issues with recovery of the current collector sheets and therefore prevents closed-loop recycling of the current collectors.

After disassembly, the cathode can be treated in 2 different ways. Direct regeneration involves separating the cathode from the current collector and binder before directly regenerating it. The separation is vital to ensuring that there is no Al or F contamination of the resultant cathode material. Alternatively hydrometallurgical-type methods can be used to regenerate the cathode material.

1.2.2.1. Direct regeneration

For direct regeneration, the cathode needs to be separated from the Al current collector. This separation can be done by sonication in a solvent, such as N-methyl-2-pyrrolidone[61], water[62] or trifluoroacetic acid[63]. The separation can also be done by

dissolution of the Al in alkaline solution[64] or by manually scraping the cathode material off the Al foil[65].

The subsequent step is to remove the PVDF binder from the cathode material. Within the literature, PVDF is commonly removed by thermal decomposition.[66–68] However, Slater has shown that PVDF is a powerful fluorinating reagent for oxides.[69] In support of this, Song et al has suggested that heat treatment can cause PVDF to decompose to HF, which then reacts with the cathode material and causes the formation of impurities.[70] More work is therefore required to investigate novel methods which can remove the PVDF without triggering any changes to the cathode material.

The recovered cathode material must then be returned to optimal operating conditions. For LFP, this is commonly done by reacting the recovered cathode material with appropriate amounts of $LiOH/Li_2CO_3$.[71,72] Literature surrounding this method often focusses on LFP because direct regeneration involves fewer processing steps than a hydrometallurgical-type route and therefore is an economically viable solution to recycle LFP. Methods for the relithiation of LMO[73,74] and NMCs[75,76] have also been investigated.

1.2.2.2. Hydrometallurgical-type routes

Closed-loop recycling can also be done via a hydrometallurgical-type route where the cathode materials are leached into solution and then a new cathode material is directly formed from this solution. In 2013, Zou et al proposed a closed-loop method to recycle mixed cathode materials including $LiCoO_2$ (LCO), LMO, NMC111 and LFP.[77] The cathode material was first leached using H_2SO_4 and H_2O_2, before then adding NaOH

solution to adjust the pH of the solution and cause $Fe(OH)_3$ to precipitate out, which was removed as a waste produce. The ratios of the different TMs in solution was adjusted to the required values via the addition of TM sulfates. The mixed TM hydroxide was precipitated out via adjustment of the pH. This hydroxide was ground and heated with recovered Li_2CO_3 to form regenerated NMC111, which displayed excellent electrochemical properties (initial discharge capacity 174 mAhg^{-1} at 0.07 C). Further research by this group has expanded upon this process to include the removal of the current collectors and investigation into the removal of impurity elements, such as Fe/Cu/Al, which was achieved using pH adjustments.[78,79] They also investigated the influence of Cu impurities on the regenerated material and found that the Cu impurity resulted in an improved capacity retention (70% compared to 58% without Cu) although at the expense of a decreased discharge capacity (140 compared to 160 mAhg^{-1}).[80] They have also regenerated different NMC compositions, such as NMC532 and NMC622 via a similar method.[81] Further work by this group has also reported that the unique microstructure of the recycled materials gives them a superior rate and cycle performance compared to those made from pristine materials.[82] The method has also been shown to work at a large scale and has successfully been used to recycle 30 kg of spent LiBs.[83]

Closed loop recycling utilising organic acids has also been achieved using malic[84] and lactic[85] acid to successfully regenerate cathode materials. Yao et al recovered and regenerated NCM111 from spent LIBs using malic acid along with H_2O_2 to act as a reducing agent.[84] They performed the leaching at 50 °C for 30 mins. The NMC111 generated using this method had an initial discharge capacity of 147.2 mAhg^{-1} at 0.2 C and a capacity retention of 95.06% after 100 cycles. Li et al followed a similar method

utilising lactic acid to leach and regenerate NMC111.[85] Their optimum conditions were 70 °C for 20 mins, also with the introduction of some H_2O_2 to act as a reducing agent. The NMC111 generated had similar performance with an initial discharge capacity of 138.2 mAhg^{-1} at 0.5 C and a capacity retention of 96% after 100 cycles. Closed-loop synthesis has also been used for the regeneration of $LiNi_xCo_yAl_zO_2$ (NCA) from NCA using multiple inorganic acids.[86]

1.2.2.3.   Upcycling

Closed-loop recycling can also be used to upcycle the cathode materials; either to form more relevant cathode materials or to form materials for use in other applications. Recovered LFP (and LMO) have been used to synthesise LFP/C (and $LiMnPO_4$/C) nanocomposites which have been reported to show an excellent cycling performance when used as cathode materials.[87,88] LFP has also been used as a precursor in the synthesis of advanced anode materials for Ni/Fe batteries[89,90], while recycled LMO has been utilised as a cathode material for sodium ion batteries.[65] Driscoll et al showed that recycled LMO can be upcycled into NMC532 by the addition of Co/Ni sulfates into the solution containing recycled LMO.[91] The upcycled NMC532 was found to have a comparable electrochemical performance to pristine NMC532 (158 and 161 mAhg^{-1} initial discharge capacities, respectively). Lin et al have shown a method for upcycling degraded LMO into disordered LMO which has an improved electrochemical performance.[92] Recently, there has also been an increase in work on upcycling low Ni-NMCs into high-Ni NMCs.[93–96]

1.2.3. Conclusions

In the future there must be a move towards closed-loop recycling and away from reagent recovery as the amounts of valuable metals, such as Co and Ni, within the cathode decreases. Closed-loop recycling will be key to creating recycling schemes which focus on low-cost cathode materials such as LMO/LFP. Furthermore, many of the closed-loop procedures can deal with multiple types of cathode materials and therefore can be used across the range of different LIB. Closed-loop methods also have the potential to be less energy intensive as they do not return the materials back to precursors and therefore reduce the number of processing steps required.

When considering closed-loop recycling, direct regeneration is superior as it involves fewer steps and avoids the need to use acids. However, it is only useful when considering cathodes that are still relevant such as LFP or high Ni-NMCs. For older cathodes, such as LMO or low Ni-NMCs, hydrometallurgical-type methods are more suitable as they can enable upcycling into more useful materials. Currently, most of the literature around close-loop recycling focuses on regeneration of the same cathode materials or upcycling low Ni-NMCs into high Ni-NMCs. Therefore, there is a need for work, such as in this thesis, to investigate upcycling into future generation cathode materials.

For recycling methods to progress, vast improvements must be made to both the battery design and the dismantling process. This can be achieved by designing a battery pack specifically for ease of recycling ("design for recycle") and by increased automation of battery disassembly. The development of new, easily removable binders will be critical in enabling quick and easy separation of the electrodes from the current

collectors. These new binders could also reduce some of the issues linked to the use of PVDF, such as the use of toxic NMP as a solvent (during manufacture of the LIB) and reaction of PVDF with the cathode during removal/cycling.

There is also a need for enhanced analysis to understand battery degradation/state of health. As spent EV batteries begin to be used in second life applications this will only become a more prominent issue. The second life batteries will have additional degradation and therefore may have to be recycled using different methods. Improved characterisation would ensure that the most suitable recycling technique can be employed for each battery.

1.3. Newer cathode materials

As the number of EVs increases, there is a growing demand for new and improved cathode materials. These new cathode materials will ideally have an increased energy density which will increase the range that EVs can travel on a single charge. Ideally these materials will also be low cost therefore enabling cost reduction in EVs. The materials will preferably contain elements that are not toxic, ethical to source and light weight. This will involve a move away from Co and potentially Ni containing cathodes. Furthermore, it would desirable if these materials could easily undergo recycling processes.

1.3.1. Ni-doped spinels

$LiMn_{1.5}Ni_{0.5}O_4$ (LMNO) is one of the cathode materials that is gaining interest for next generation LIBs due to its high operating voltage. LMNO is similar in structure to LMO however it has both a higher capacity ($\sim$ 135 mAhg^{-1}) and a higher operating voltage ($\sim$ 4.7 V) leading to a significant increase in energy density for a resulting battery. Its high operating voltage enables it to be used in conjunction with high voltage anodes, such as $Li_4Ti_5O_{12}$. However, this can introduce problems when using standard electrolytes as they are not typically stable at these higher voltages.[97]

LMNO can form either an ordered ($P4_332$) or disordered ($Fd\bar{3}m$) structure depending on the degree of cation ordering between Ni^{2+} and Mn^{4+} in the structure (Figure 1-6).[98] An ordered structure is obtained when the Ni^{2+} and Mn^{4+} ions are located in the 4b and 12d Wyckoff sites, respectively, to give a structure with distinct Mn and Ni sites.[99] In contrast, it is also possible to obtain a disordered structure where the Ni^{2+} and Mn^{4+}

are randomly distributed among the 16d octahedral sites. The XRD patterns of the two structures both contain the characteristic spinel peaks while the ordered structure also contains weak superstructure reflections due to its decreased crystal symmetry.[100]
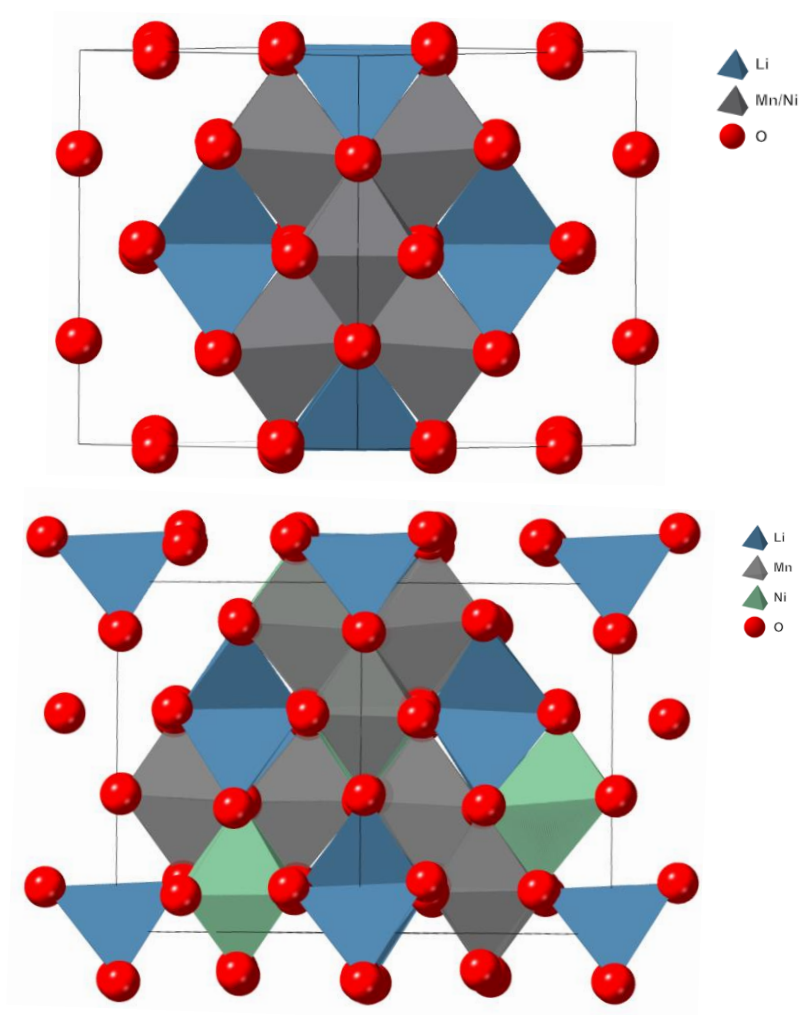
Figure 1-6: Crystal structure of LiMn$_{1.5}$Ni$_{0.5}$ with disordered (Fd$\bar{3}$m, above) and ordered (P4$_3$32, below) structures. Li sites in blue, Mn(/Ni for disordered structure) sites in grey, Ni sites in green and O sites in red

The two structures have different voltage profiles (Figure 1-7). The flat plateau at ~ 4.7 V is due to the Ni$^{2+/3+/4+}$ redox couples while the smaller plateau at ~ 4.0 V is due to the Mn$^{3+/4+}$ redox couple.[101] The ordered phase shows no plateau at ~ 4.0 V indicating that there is no Mn^{3+} present in the lattice and that all the capacity is due to Ni redox, whereas the disordered phase has a significant plateau at ~ 4.0 V indicating the

presence of Mn^{3+} in the structure. Furthermore, for the disordered phase there is also a distinction between the $Ni^{2+/3+}$ plateau at ~ 4.6 V and the $Ni^{3+/4+}$ plateau at ~ 4.8 V.
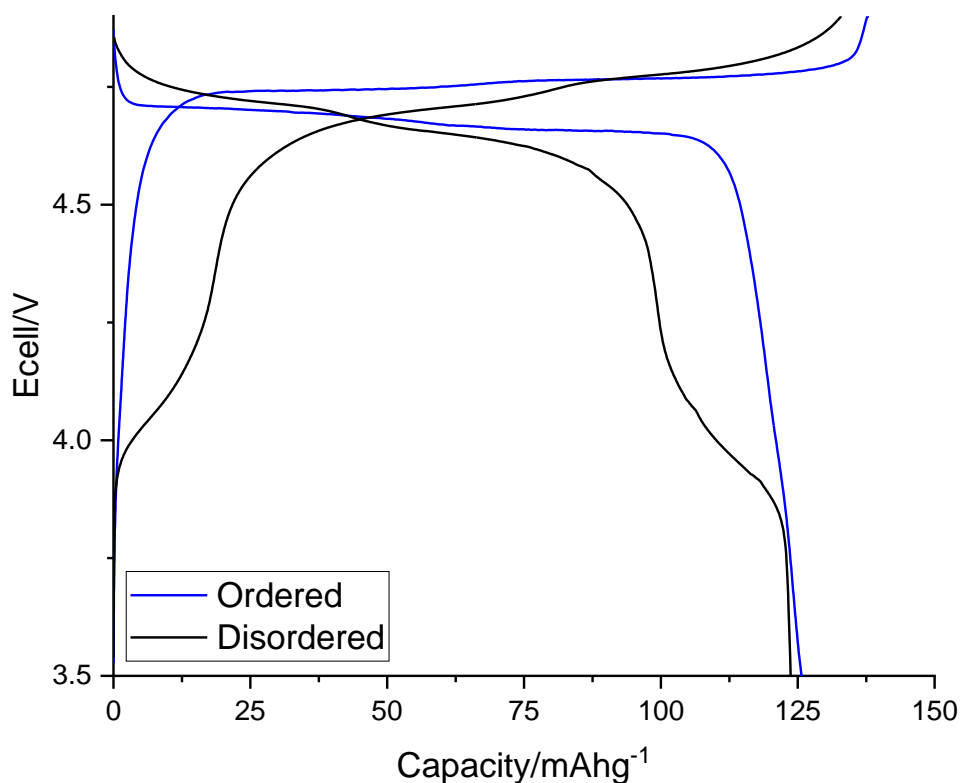
Figure 1-7: Typical galvanostatic charge-discharge profiles for the ordered and disordered LiMn$_{1.5}$Ni$_{0.5}$O$_4$ structures

The degree of cation ordering is influenced by the synthesis conditions, specifically the synthesis temperature. The disordered structure is commonly synthesised by heating to high temperatures (~ 900 °C) with rapid cooling rates whereas the ordered structure is typically synthesised by annealing a disordered sample at a lower temperature (~ 700 °C).[100,102,103] In practise, a fully ordered or fully disordered structure is hard to obtain, and most samples contain a mixture that lies somewhere in the middle.[100] The higher synthesis temperatures that favour formation of the disordered structure also lead to the reduction of Mn^{4+} to Mn^{3+}. Mn^{3+} then causes the lower voltage plateau in

the cycling profile of disordered samples. This reduction at higher temperatures is attributed to either O deficiencies or decreased Ni solubility in the spinel phase, the latter leading to the formation of a rocksalt impurity phase, $Li_xNi_{1-x}O$.[104–106]

Although ordered LMNO provides a higher voltage and higher power, disordered LMNO gives a more stable long-term performance and high-rate capability.[107] Disordered LMNO has improved Li diffusion and electronic conductivity compared to ordered LMNO, however it does form rocksalt impurity phases more readily and has a less favourable voltage profile due to the voltage plateau at 4.0 V.[108] Furthermore, disordered LMNO contains Mn^{3+} which is not desired as Mn loss and degradation can occur due to disproportionation of Mn^{3+} to Mn^{2+} and Mn^{4+}.[109] However, it has been suggested that the presence of Mn^{3+} is responsible for the improved cycling performance of disordered LMNO as it results in increased electronic conductivity.[110]

The widespread adoption of LMNO is hindered by its capacity fade during cycling and more significantly the instability of conventional LIB electrolytes at the required high voltages. Several approaches have been taken to solve the performance issues of LNMO and they fall under: particle morphology, elemental doping, surface engineering and electrolyte modification. Doping LMNO with a range of elements, such as Ti[111], Cr[112] and Fe[113], results in improvements to the capacity retention. Luo et al showed that by co-doping LMNO with Cr and Ti, a capacity retention of 88.5% after 300 cycles was obtained, compared to 40% without doping.[114] Nguyen et al showed that the addition of (3-aminopropyl)triethoxysilane, an electrolyte additive, stabilised the interface between the LMNO electrode and the electrolyte which significantly improved the long-term cycling stability.[115] Addition of the additive resulted in an excellent

capacity retention of 92% after 350 cycles, compared to 60% without the additive present.

Ultimately, the main use of LMNO is likely to be in high power batteries where it is used with high voltage anodes. Echion has utilised LMNO along with a Nb oxide based anode to produce a 3 V LIB.[116] Meanwhile, in November 2023, Toshiba announced a 5 V LIB which utilises LMNO with a Nb Ti oxide anode.[117]

1.3.2. Cation disordered rocksalt materials

Materials with a disordered rocksalt (DRS) structure are a type of cathode material that can provide high gravimetric capacities for LIBs. The DRS structure consists of a CCP arrangement of O with a disordered arrangement of TM/Li in the octahedral sites (Figure 1-8). DRS materials are typically stabilised by the inclusion of d^0 TMs. These d^0 ions can occupy distorted octahedral sites with a limited energy cost therefore leaving the less distorted sites free to accommodate variable oxidation state TMs.[118] Apart from the disordered nature of Li and TMs, a key requirement for these DRS cathodes is a Li:TM ratio >1. Lee et al showed that when these materials contain 10% excess Li they have excellent 3D Li percolation networks.[119] As the amount of Li is increased, there is more Li present in octahedral sites and this allows the formation of a pathway with a low energy barrier to Li^+ diffusion to be formed. It has also been shown that a greater (26%) excess Li is required to allow 1 Li per f.u. to be removed from the structure.[119]
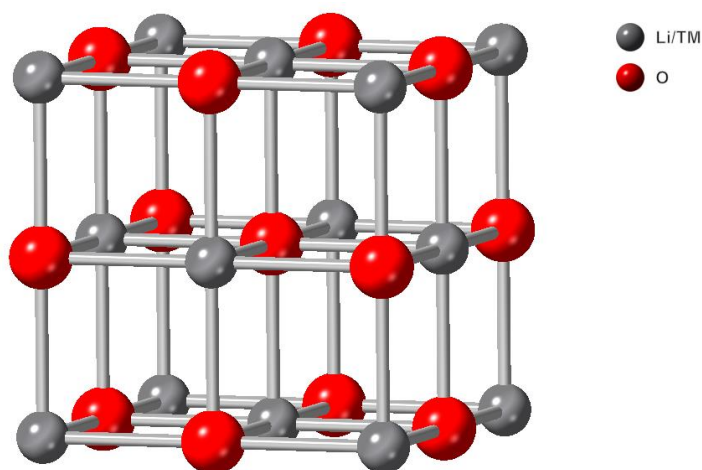
Figure 1-8: Crystal structure of a disordered rocksalt phase with Li/TM sites in grey and O sites in red

DRS materials can provide higher gravimetric capacities, > 250 mAhg^{-1}, than conventional cathodes. It has been shown that these high capacities are due to the materials undergoing O redox alongside TM redox.[120,121] However, the high levels of O redox displayed by these DRS materials can trigger O_2 loss, which can then have a detrimental impact upon the long term cycling performance.[122–125] Another problem with these DRS materials is that they have a steeper voltage profile than layered materials, due to the fact that they contain several different Li environments. A flatter voltage profile is desirable as it results in a more constant energy output. Computer modelling has been used to show that the introduction of short range order can help to mitigate this issue, as an increase in the local order of the system results in a decrease in the number of different Li sites.[126] However, further work is needed to achieve this goal experimentally.

DRS materials containing several different TM have been successfully synthesised and shown to have good electrochemical performance. However, in this thesis, the focus has been on Mn-based DRS as they are of interest when recycling Mn-containing

cathodes, such as LMO. Mn-based DRS materials are commonly synthesised via either solid state or mechanochemical synthesis. Alternative synthesis methods, such as microwave[127] and sol-gel[128] synthesis, have also been developed. Regardless of the synthesis route used, an extensive milling step is always required to achieve a good electrochemical performance.

Freire et al have reported $Li_4Mn_2O_5$ which was prepared by mechanochemical ball-milling of $LiMnO_2$ and Li_2O at room temperature. $Li_4Mn_2O_5$ can reach discharge capacities of 355 mAhg^{-1}, although, the discharge capacity drops to 250 mAhg^{-1} after 8 cycles.[120] Further research by this group has suggested that the composition of the material is actually $0.93Li_{3.6}Mn_{2.4}O_{5.4}$–$0.07Li_2O$ and that Li_2O is crucial for reaching higher capacities; 30% higher than when Li_2O is not present.[129] Work by Yao et al predicted that doping the structure with V or Cr (to form $Li_4[Mn,M]_2O_5$ where M = V, Cr) will further improve the electrochemical properties of the material.[130]

Groups have also reported the solid state synthesis of $Li_{1.3}Nb_{0.3}Mn_{0.4}O_2$[131] and $Li_{1.25}Nb_{0.25}Mn_{0.5}O_2$[121] with a DRS structure. After subsequent milling, these materials were found to have high capacities (~ 300 mAhg^{-1}) with both the Mn^{3+}/Mn^{4+} and O^{2-}/O^{-} redox couples contributing to the redox activity. In-situ XRD analysis showed that the rocksalt structure was maintained during cycling. Further work by Chen et al showed that when $Li_{1.3}Nb_{0.3}Mn_{0.4}O_2$ is cycled to a voltage limit of 4.2 V, O redox is not activated and a constant capacity (~ 112 mAhg^{-1}) is obtained upon subsequent cycling. However, when cycled above 4.2 V, O redox is activated and subsequent cycling results in capacity fade, voltage decay and voltage hysteresis.[132] Mn-based DRS have also been doped with Ti and Zn. Work has shown that Ti doping is superior, which is

attributed to it having a more favourable effect upon the short-range ordering which in turn resulted in improved Li$^+$ percolation.[133] Chen et al have shown that Ti doping is also superior to Nb doping as O redox was more reversible in the Ti doped sample and led to an improved cycling stability.[134]

One proposed solution to reduce the levels of O redox in these materials is to partially substitute some O for F to form oxyfluoride materials.[135,136] This substitution lowers the average anion valence meaning that oxyfluoride materials contain a higher content of redox-active TM and therefore rely less upon O redox processes. Although, it is worth noting that the introduction of F may increase the complexity of recycling these materials. House et al have reported $Li_{1.9}Mn_{0.95}O_{2.05}F_{0.95}$ (prepared by ball milling) which has a high capacity of 280 mAhg^{-1} and undergoes negligible O loss during cycling.[137] Lee et al have reported $Li_2Mn_{2/3}Nb_{1/3}O_2F$ and $Li_2Mn_{0.5}Ti_{0.5}O_2F$ (similarly prepared by ball milling) which utilize the Mn^{2+}/Mn^{4+} redox couple, to reach capacities of 317 and 321 mAhg^{-1} respectively, and avoid excessive reliance upon O redox.[138] However, these oxyfluoride materials still exhibit capacity fade after repeated cycling. The incorporation of F also causes changes to the Li percolation network, as F preferentially bonds to Li rather than TM.[139] At low F concentrations, this causes isolated Li-rich domains to form, while at higher F concentrations, these Li-rich clusters become connected and improve the Li percolation network.[140,141]

1.3.3. Conclusions

LMNO is currently of commercial interest as a cathode material due to its high operating voltage which results in a high energy density. Furthermore, it does not contain any high value/ethically compromised Co. This therefore makes it a material of

interest when considering upcycling of current end-of-life (EOL) cathode materials, such as LMO, especially for potential applications in > 3 V high power batteries. However, further work on stable high voltage electrolytes and additives to pair with LMNO, alongside improvements to their capacity retention, is needed if they are undergo widespread adoption.

DRS materials appear very promising due to their high-capacities and the fact that some of these materials contain only Li, Mn and O. They therefore have great potential to lower the cost of LIB, as they are much cheaper than Co/Ni containing cathode materials. Furthermore, they are believed to be more stable to low levels of material impurities and so may facilitate simpler recycling procedures. However, considerable research is required to improve their long-term cycling performance, to look at ways to mitigate O loss during cycling and to investigate methods to adjust their voltage profiles. For DRS materials, F doping overcomes some of the problems related to O loss. However, these oxyfluoride materials still display relatively poor capacity retention and therefore require further research.

1.4. Thesis aims

The aim of this thesis is to develop a method to allow the separation of mixed cathode materials containing a layered oxide and LMO, and to then upcycle the LMO component into current and next generation cathode materials. Present literature focuses on recycling of single component cathode streams consisting of pristine materials. This work therefore investigates the separation of mixed cathode materials and has focused on both EOL and quality control (QC) rejected material from Gen 1 Nissan Leaf EVs. This is representative of material that will be present in near future recycling pools and contains additional components that are not present in pristine materials. Although extensive literature exists concerning closed-loop recycling, this primarily focuses on remanufacture of the original cathode material and therefore is in danger of becoming obsolete with the fast pace of battery development. This work therefore investigates upcycling as it allows closed-loop methods to be utilised with a focus on cathodes of current commercial interest, such as LMNO, or next generation cathodes, such as DRS materials.

1.5. References

1   J. B. Goodenough and K. S. Park, *J. Am. Chem. Soc.*, 2013, **135**, 1167–1176.

2   E. Peled, D. Golodnitsky and G. Ardel, *J. Electrochem. Soc.*, 1997, **144**, L208–L210.

3   C. Liu, Z. G. Neale and G. Cao, *Mater. Today*, 2016, **19**, 109–123.

4   B. Xu, D. Qian, Z. Wang and Y. S. Meng, *Mater. Sci. Eng. R Reports*, 2012, **73**, 51–65.

5   J. Marshall, D. Gastol, R. Sommerville, B. Middleton, V. Goodship and E. Kendrick, *Metals (Basel).*, 2020, **10**, 1–22.

6   Tesla   blog,   https://www.tesla.com/en_gb/blog/panasonic-enters-supply-agreement-tesla-motors-supply-automotivegrade-battery-c,   (accessed   12 Febuary 2024).

7   Tesla, *Q3 2021 Update*, 2021.

8   J. C. Hunter, *J. Solid State Chem.*, 1981, **39**, 142–147.

9   D. Aurbach, M. D. Levi, K. Gamulski, B. Markovsky, G. Salitra, E. Levi, U. Heider, L. Heider and R. Oesten, *J. Power Sources*, 1999, **81**–**82**, 472–479.

10   M. M. Thackeray, W. I. F. David, P. G. Bruce and J. B. Goodenough, *Mater. Res. Bull.*, 1983, **18**, 461–472.

11   M. H. Kim, H. S. Shin, D. Shin and Y. K. Sun, *J. Power Sources*, 2006, **159**,

1328–1333.

12   D. L. Vu and J. won Lee, *Korean J. Chem. Eng.*, 2016, **33**, 514–526.

13   H. R. Kim, S. G. Woo, J. H. Kim, W. Cho and Y. J. Kim, *J. Electroanal. Chem.*, 2016, **782**, 168–173.

14   Y. K. Ahn, Y. N. Jo, W. Cho, J. S. Yu and K. J. Kim, *Energies*, 2019, **12**, 1–10.

15   H. Liang, Z. Wang, H. Guo, J. Wang and J. Leng, *Appl. Surf. Sci.*, 2017, **423**, 1045–1053.

16   S. Dai, M. Yuan, L. Wang, L. Luo, Q. Chen, T. Xie, Y. Li and Y. Yang, *Ceram. Int.*, 2019, **45**, 674–680.

17   S. Dai, G. Yan, L. Wang, L. Luo, Y. Li, Y. Yang, H. Liu, Y. Liu and M. Yuan, *J. Electroanal. Chem.*, 2019, **847**, 113197.

18   J. V. Laveda, J. E. Low, F. Pagani, E. Stilp, S. Dilger, V. Baran, M. Heere and C. Battaglia, *ACS Appl. Energy Mater.*, 2019, **2**, 7036–7044.

19   Q. Dong, F. Guo, Z. Cheng, Y. Mao, R. Huang, F. Li, H. Dong, Q. Zhang, W. Li, H. Chen, Z. Luo, Y. Shen, X. Wu and L. Chen, *ACS Appl. Energy Mater.*, 2020, **3**, 695–704.

20   K. J. Park, J. Y. Hwang, H. H. Ryu, F. Maglia, S. J. Kim, P. Lamp, C. S. Yoon and Y. K. Sun, *ACS Energy Lett.*, 2019, **4**, 1394–1400.

21   C. Lv, Z. Li, X. Ren, K. Li, J. Ma and X. Duan, *J. Mater. Chem. A*, 2021, **9**, 3995–4006.

22   A. K. Padhi, K. S. Nanjundaswamy and J. B. Goodenough, *J. Electrochem. Soc.*, 1997, **144**, 1188–1194.

23   A. S. Andersson, J. O. Thomas, B. Kalska and L. Häggström, *Electrochem. Solid-State Lett.*, 2000, **3**, 66–69.

24   J. Schöberl, M. Ank, M. Schreiber, N. Wassiliadis and M. Lienkamp, *eTransportation*, 2023, **19**, 100305.

25   D. Choi and P. N. Kumta, *J. Power Sources*, 2007, **163**, 1064–1069.

26   H. T. Chung, S. K. Jang, H. W. Ryu and K. B. Shim, *Solid State Commun.*, 2004, **131**, 549–554.

27   W. Lin, P. Yang, K. Zhou, L. Wang and C. Shen, *Solid State Ionics*, 2023, **403**, 116322.

28   American Chemical Society, Understanding the life of lithium ion batteries in electric vehicles, https://www.acs.org/content/acs/en/pressroom/newsreleases/2013/april/understanding-the-life-of-lithium-ion-batteries-in-electric-vehicles.html, (accessed 18 February 2020).

29   Department for Transport, *Decarbonising transport: A better, greener Britain*, 2021.

30   HM Government, *Resilience for the Future: The United Kingdom's Critical Minerals Strategy*, 2022.

31   European Commission, *Regulation (EU) 2023/1542 of the European Parliament and of the Council concerning batteries and waste batteries*, 2023.

32   H.R.3684, *Infrastructure Investment and Jobs Act*, 117th Congress, 2021.

33   B. K. Sovacool, *Extr. Ind. Soc.*, 2019, **6**, 915–939.

34   W. Liu, D. B. Agusdinata and S. W. Myint, *Int. J. Appl. Earth Obs. Geoinf.*, 2019, **80**, 145–156.

35   D. Thompson, C. Hyde, J. M. Hartley, A. P. Abbott, P. A. Anderson and G. D. J. Harper, *Resour. Conserv. Recycl.*, 2021, **175**, 105741.

36   L. Ahmadi, S. B. Young, M. Fowler, R. A. Fraser and M. A. Achachlouei, *Int. J. Life Cycle Assess.*, 2017, **22**, 111–124.

37   European Commission, *Regulation of the European Parliament and of the Council concerning batteries and waste batteries, repealing. Directive 2006/66/EC and amending Regulation (EU) No 2019/1020*, 2020.

38   M. Wentker, M. Greenwood and J. Leker, *Energies*, 2019, **12**, 1–18.

39   EPA, *Modeling the Cost and Performance of Lithium-Ion Batteries for Electric-Drive Vehicles*, 2012.

40   L. Gaines, *Sustain. Mater. Technol.*, 2014, **1**, 2–7.

41   J. Shaw-Stewart, A. Alvarez-Reguera, A. Greszta, J. Marco, M. Masood, R. Sommerville and E. Kendrick, *Sustain. Mater. Technol.*, 2019, **22**, e00110.

42   H. Wang and B. Friedrich, *J. Sustain. Metall.*, 2015, **1**, 168–178.

43   F. Wang, R. Sun, J. Xu, Z. Chen and M. Kang, *RSC Adv.*, 2016, **6**, 85303–85311.

44   L. P. He, S. Y. Sun, X. F. Song and J. G. Yu, *Waste Manag.*, 2017, **64**, 171–181.

45   W. S. Chen and H. J. Ho, *Metals (Basel).*, 2018, **8**, 321.

46   Z. Zheng, M. Chen, Q. Wang, Y. Zhang, X. Ma, C. Shen, D. Xu, J. Liu, Y. Liu, P. Gionet, I. O'Connor, L. Pinnell, J. Wang, E. Gratz, R. Arsenault and Y. Wang, *ACS Sustain. Chem. Eng.*, 2018, **6**, 13977–13982.

47   R. Sattar, S. Ilyas, H. N. Bhatti and A. Ghaffar, *Sep. Purif. Technol.*, 2019, **209**, 725–733.

48   F. Peng, D. Mu, R. Li, Y. Liu, Y. Ji, C. Dai and F. Ding, *RSC Adv.*, 2019, **9**, 21922–21930.

49   C. H. Jo and S. T. Myung, *J. Power Sources*, 2019, **426**, 259–265.

50   D. Mishra, D. J. Kim, D. E. Ralph, J. G. Ahn and Y. H. Rhee, *Waste Manag.*, 2008, **28**, 333–338.

51   G. Zeng, X. Deng, S. Luo, X. Luo and J. Zou, *J. Hazard. Mater.*, 2012, **199–200**, 164–169.

52   L. Li, G. sheng Zeng, S. lian Luo, X. rong Deng and Q. ji Xie, *J. Korean Soc. Appl. Biol. Chem.*, 2013, **56**, 187–192.

53   N. J. Boxall, K. Y. Cheng, W. Bruckard and A. H. Kaksonen, *J. Hazard. Mater.*,

2018, **360**, 504–511.

54   Y. Xin, X. Guo, S. Chen, J. Wang, F. Wu and B. Xin, *J. Clean. Prod.*, 2016, **116**, 249–258.

55   B. K. Biswal, U. U. Jadhav, M. Madhaiyan, L. Ji, E. H. Yang and B. Cao, *ACS Sustain. Chem. Eng.*, 2018, **6**, 12343–12352.

56   T. Naseri, N. Bahaloo-Horeh and S. M. Mousavi, *J. Environ. Manage.*, 2019, **235**, 357–367.

57   N. Bahaloo-Horeh and S. M. Mousavi, *Waste Manag.*, 2017, **60**, 666–679.

58   R. Zhan, Z. Oldenburg and L. Pan, *Sustain. Mater. Technol.*, 2018, **17**, e00062.

59   J. Yu, Y. He, Z. Ge, H. Li, W. Xie and S. Wang, *Sep. Purif. Technol.*, 2018, **190**, 45–52.

60   G. Zhang, Y. He, H. Wang, Y. Feng, W. Xie and X. Zhu, *J. Clean. Prod.*, 2019, **231**, 1418–1427.

61   Y. Shi, G. Chen and Z. Chen, *Green Chem.*, 2018, **20**, 851.

62   T. Sieber, J. Ducke, A. Rietig, T. Langner and J. Acker, *Nanomaterials*, 2019, **9**, 246.

63   X. Zhang, Y. Xie, H. Cao, F. Nawaz and Y. Zhang, *Waste Manag.*, 2014, **34**, 1715–1724.

64   J. Chen, Q. Li, J. Song, D. Song, L. Zhang and X. Shi, *Green Chem.*, 2016, **18**,

2500–2506.

65   X. J. Nie, X. T. Xi, Y. Yang, Q. L. Ning, J. Z. Guo, M. Y. Wang, Z. Y. Gu and X. L. Wu, *Electrochim. Acta*, 2019, **320**, 134626.

66   C. Hanisch, T. Loellhoeffel, J. Diekmann, K. J. Markley, W. Haselrieder and A. Kwade, *J. Clean. Prod.*, 2015, **108**, 301–311.

67   X. Li, J. Zhang, D. Song, J. Song and L. Zhang, *J. Power Sources*, 2017, **345**, 78–84.

68   J. Li, Y. Wang, L. Wang, B. Liu and H. Zhou, *J. Mater. Sci. Mater. Electron.*, 2019, **30**, 14580–14588.

69   P. R. Slater, *J. Fluor. Chem.*, 2002, **117**, 43–45.

70   D. Song, X. Wang, E. Zhou, P. Hou, F. Guo and L. Zhang, *J. Power Sources*, 2013, **232**, 348–352.

71   L. Li, J. Lu, L. Zhai, X. Zhang, L. Curtiss, Y. Jin, F. Wu, R. Chen and K. Amine, *CSEE J. Power Energy Syst.*, 2018, **4**, 219–225.

72   X. Song, T. Hu, C. Liang, H. L. Long, L. Zhou, W. Song, L. You, Z. S. Wu and J. W. Liu, *RSC Adv.*, 2017, **7**, 4783–4790.

73   C. Wu, M. Xu, C. Zhang, L. Ye, K. Zhang, H. Cong, L. Zhuang, X. Ai, H. Yang and J. Qian, *Energy Storage Mater.*, 2023, **55**, 154–165.

74   H. Gao, Q. Yan, P. Xu, H. Liu, M. Li, P. Liu, J. Luo and Z. Chen, *ACS Appl. Mater. Interfaces*, 2020, **12**, 51546–51554.

75   Y. Shi, M. Zhang, Y. S. Meng and Z. Chen, *Adv. Energy Mater.*, 2019, **9**, 1–9.

76   X. Yu, S. Yu, Z. Yang, H. Gao, P. Xu, G. Cai, S. Rose, C. Brooks, P. Liu and Z. Chen, *Energy Storage Mater.*, 2022, **51**, 54–62.

77   H. Zou, E. Gratz, D. Apelian and Y. Wang, *Green Chem.*, 2013, **15**, 1183–1191.

78   E. Gratz, Q. Sa, D. Apelian and Y. Wang, *J. Power Sources*, 2014, **262**, 255–262.

79   Q. Sa, E. Gratz, M. He, W. Lu, D. Apelian and Y. Wang, *J. Power Sources*, 2015, **282**, 140–145.

80   Q. Sa, J. A. Heelan, Y. Lu, D. Apelian and Y. Wang, *ACS Appl. Mater. Interfaces*, 2015, **7**, 20585–20590.

81   Q. Sa, E. Gratz, J. A. Heelan, S. Ma, D. Apelian and Y. Wang, *J. Sustain. Metall.*, 2016, **2**, 248–256.

82   X. Ma, M. Chen, Z. Zheng, D. Bullen, J. Wang, C. Harrison, E. Gratz, Y. Lin, Z. Yang, Y. Zhang, F. Wang, D. Robertson, S. B. Son, I. Bloom, J. Wen, M. Ge, X. Xiao, W. K. Lee, M. Tang, Q. Wang, J. Fu, Y. Zhang, B. C. Sousa, R. Arsenault, P. Karlson, N. Simon and Y. Wang, *Joule*, 2021, **5**, 2955–2970.

83   M. Chen, Z. Zheng, Q. Wang, Y. Zhang, X. Ma, C. Shen, D. Xu, J. Liu, Y. Liu, P. Gionet, I. O'Connor, L. Pinnell, J. Wang, E. Gratz, R. Arsenault and Y. Wang, *Sci. Rep.*, 2019, **9**, 1–9.

84   L. Yao, H. Yao, G. Xi and Y. Feng, *RSC Adv.*, 2016, **6**, 17947–17954.

85   L. Li, E. Fan, Y. Guan, X. Zhang, Q. Xue, L. Wei, F. Wu and R. Chen, *ACS Sustain. Chem. Eng.*, 2017, **5**, 5224–5233.

86   S. U. Muzayanha, C. S. Yudha, A. Nur, H. Widiyandari, H. Haerudin, H. Nilasary, F. Fathoni and A. Purwanto, *Metals (Basel).*, 2019, **9**, 615.

87   D. Bian, Y. Sun, S. Li, Y. Tian, Z. Yang, X. Fan and W. Zhang, *Electrochim. Acta*, 2016, **190**, 134–140.

88   Q. Meng, J. Duan, Y. Zhang and P. Dong, *J. Ind. Eng. Chem.*, 2019, **80**, 633–639.

89   E. Shangguan, S. Fu, S. Wu, Q. Wang, C. Wu, J. Li, X. Cai, Z. Chang, Z. Wang, Q. Li and K. Jiang, *J. Power Sources*, 2018, **403**, 38–48.

90   E. Shangguan, Q. Wang, C. Wu, S. Wu, M. Ji, J. Li, Z. Chang and Q. Li, *ACS Sustain. Chem. Eng.*, 2018, **6**, 13312–13323.

91   L. L. Driscoll, A. Jarvis, R. Madge, J. Price, R. Sommerville, F. S. Totini, M. Bahri, B. L. Mehdi, E. Kendrick, N. D. Browning, P. K. Allan, P. A. Anderson and P. R. Slater, Phase-selective recovery and regeneration of end-of-life electric vehicle blended cathodes via selective leaching and direct recycling, *ChemRxiv*, 2023, DOI:10.26434/chemrxiv-2023-56rkk. This content is a preprint and has not been peer-reviewed.

92   J. Lin, E. Fan, X. Zhang, Z. Li, Y. Dai, R. Chen, F. Wu and L. Li, *Adv. Energy Mater.*, 2022, **12**, 1–12.

93   K. S. Kim, M. K. Jeon, S. H. Song, S. Hong, H. S. Kim, S. W. Kim, J. Kim, P. Oh,

J. Hwang, J. Song, J. Ma, J. J. Woo, S. H. Yu and H. Kim, *J. Mater. Chem. A*, 2023, **11**, 21222–21230.

94   G. Qian, Z. Li, Y. Wang, X. Xie, Y. He, J. Li, Y. Zhu, S. Xie, Z. Cheng, H. Che, Y. Shen, L. Chen, X. Huang, P. Pianetta, Z. F. Ma, Y. Liu and L. Li, *Cell Reports Phys. Sci.*, 2022, **3**, 100741.

95   H. Gao, Q. Yan, D. Tran, X. Yu, H. Liu, M. Li, W. Li, J. Wu, W. Tang, V. Gupta, J. Luo and Z. Chen, *ACS Energy Lett.*, 2023, **8**, 4136–4144.

96   T. Wang, H. Luo, J. Fan, B. P. Thapaliya, Y. Bai, I. Belharouak and S. Dai, *iScience*, 2022, **25**, 103801.

97   L. Yang, B. Ravdel and B. L. Lucht, *Electrochem. Solid-State Lett.*, 2010, **13**, 6–9.

98   Y. Idemoto, H. Narai and N. Koura, *J. Power Sources*, 2003, **119**–**121**, 125–129.

99   G. Liang, V. K. Peterson, K. W. See, Z. Guo and W. K. Pang, *J. Mater. Chem. A*, 2020, **8**, 15373–15398.

100   J. Kim, A. Huq, M. Chi, N. P. W. Pieczonka, E. Lee, C. A. Bridges, M. M. Tessema, A. Manthiram, K. A. Persson and B. R. Powell, *Chem. Mater.*, 2014, **26**, 4377–4386.

101   Y. Terada, K. Yasaka, F. Nishikawa, T. Konishi, M. Yoshio and I. Nakai, *J. Solid State Chem.*, 2001, **156**, 286–291.

102   M. Kunduraci and G. G. Amatucci, *J. Electrochem. Soc.*, 2006, **153**, A1345.

103   N. Emery, A. Bhatia, Y. Ghaleb, A. O. Mitrushchenkov, C. Léonard, J. P. Pereira-Ramos, R. Baddour-Hadjean and R. I. Smith, *Chem. Mater.*, 2022, **34**, 3152–3167.

104   D. Pasero, N. Reeves, V. Pralong and A. R. West, *J. Electrochem. Soc.*, 2008, **155**, A282.

105   J. Song, D. W. Shin, Y. Lu, C. D. Amos, A. Manthiram and J. B. Goodenough, *Chem. Mater.*, 2012, **24**, 3101–3109.

106   J. Cabana, F. O. Omenya, N. A. Chernova, D. Zeng, M. S. Whittingham and C. P. Grey, *Chem. Mater.*, 2012, **24**, 2952–2964.

107   A. Manthiram, K. Chemelewski and E. S. Lee, *Energy Environ. Sci.*, 2014, **7**, 1339–1350.

108   J. Yoon, D. Kim, J. H. Um, M. Jeong, W. Oh and W. S. Yoon, *J. Alloys Compd.*, 2016, **686**, 593–600.

109   J. H. Kim, N. P. W. Pieczonka, Z. Li, Y. Wu, S. Harris and B. R. Powell, *Electrochim. Acta*, 2013, **90**, 556–562.

110   M. Kunduraci, J. F. Al-Sharab and G. G. Amatucci, *Chem. Mater.*, 2006, **18**, 3585–3592.

111   S. Niketic, C. H. Yim, J. Zhou, J. Wang and Y. Abu-Lebdeh, *Inorganics*, 2022, **10**, 10.

112   T. A. Arunkumar and A. Manthiram, *Electrochim. Acta*, 2005, **50**, 5568–5572.

113   Y. Gao, H. Yu, P. Sandineni, X. He, A. Choudhury, J. Park and X. Liang, *J. Phys. Chem. C*, 2021, **125**, 7560–7567.

114   Y. Luo, Z. Cui, C. Wu, B. Sa, C. Wen, H. Li, J. Huang, C. Xu and Z. Xu, *ACS Omega*, 2023, **8**, 22721–22731.

115   M. T. Nguyen, H. Q. Pham, J. A. Berrocal, I. Gunkel and U. Steiner, *J. Mater. Chem. A*, 2023, **11**, 7670–7678.

116   H. Geary, C. F. Elkjær, L. El Ouatani, J. Pezin, B. Ting, F. Flemming, J. W. Hedegaard and J. Højberg, *Developing a high-performance, cobalt-free, 3 V battery cell*, 2021.

117   Toshiba, https://www.global.toshiba/ww/technology/corporate/rdc/rd/topics/23/2311-02.html, (accessed 12 February 2024).

118   A. Urban, A. Abdellahi, S. Dacek, N. Artrith and G. Ceder, *Phys. Rev. Lett.*, 2017, **119**, 176402.

119   J. Lee, A. Urban, X. Li, D. Su, G. Hautier and G. Ceder, *Science (80-.).*, 2014, **343**, 519–522.

120   M. Freire, N. V. Kosova, C. Jordy, D. Chateigner, O. I. Lebedev, A. Maignan and V. Pralong, *Nat. Mater.*, 2016, **15**, 173–177.

121   R. Wang, X. Li, L. Liu, J. Lee, D. H. Seo, S. H. Bo, A. Urban and G. Ceder, *Electrochem. commun.*, 2015, **60**, 70–73.

122   J. Lee, D. H. Seo, M. Balasubramanian, N. Twu, X. Li and G. Ceder, *Energy Environ. Sci.*, 2015, **8**, 3255–3265.

123   S. L. Glazier, J. Li, J. Zhou, T. Bond and J. R. Dahn, *Chem. Mater.*, 2015, **27**, 7751–7756.

124   I. Källquist, A. J. Naylor, C. Baur, J. Chable, J. Kullgren, M. Fichtner, K. Edström, D. Brandell and M. Hahlin, *Chem. Mater.*, 2019, **31**, 6084–6096.

125   E. Zhao, L. He, B. Wang, X. Li, J. Zhang, Y. Wu, J. Chen, S. Zhang, T. Liang, Y. Chen, X. Yu, H. Li, L. Chen, X. Huang, H. Chen and F. Wang, *Energy Storage Mater.*, 2019, **16**, 354–363.

126   A. Abdellahi, A. Urban, S. Dacek and G. Ceder, *Chem. Mater.*, 2016, **28**, 5373–5383.

127   V. C. Wu, H. A. Evans, R. Giovine, M. B. Preefer, J. Ong, E. Yoshida, P. E. Cabelguen and R. J. Clément, *Adv. Energy Mater.*, 2023, **13**, 2203860.

128   S. Patil, D. Darbar, E. Self, T. Malkowski, V. Wu, R. Giovine, N. Szymanski, R. McAuliffe, B. Jiang, J. Keum, K. Koirala, B. Ouyang, K. Page, C. Wang, G. Ceder, R. Clement and J. Nanda, *Adv. Energy Mater.*, 2023, **13**, 2203207.

129   M. Freire, M. Diaz-Lopez, P. Bordet, C. V. Colin, O. I. Lebedev, N. V. Kosova, C. Jordy, D. Chateigner, A. L. Chuvilin, A. Maignan and V. Pralong, *J. Mater. Chem. A*, 2018, **6**, 5156–5165.

130   Z. Yao, S. Kim, J. He, V. I. Hedge and C. Wolverton, *Sci. Adv.*, 2018, **4**, eeao6754.

131 N. Yabuuchi, M. Takeuchi, M. Nakayama, H. Shiiba, M. Ogawa, K. Nakayama, T. Ohta, D. Endo, T. Ozaki, T. Inamasu, K. Sato and S. Komaba, *Proc. Natl. Acad. Sci. U. S. A.*, 2015, **112**, 7650–7655.

132 D. Chen, W. H. Kan and G. Chen, *Adv. Energy Mater.*, 2019, **9**, 1–15.

133 H. Ji, A. Urban, D. A. Kitchaev, D. H. Kwon, N. Artrith, C. Ophus, W. Huang, Z. Cai, T. Shi, J. C. Kim, H. Kim and G. Ceder, *Nat. Commun.*, 2019, **10**, 1–9.

134 D. Chen, J. Wu, J. K. Papp, B. D. McCloskey, W. Yang and G. Chen, *Small*, 2020, **16**, 1–12.

135 R. Chen, S. Ren, M. Knapp, D. Wang, R. Witter, M. Fichtner and H. Hahn, *Adv. Energy Mater.*, 2015, **5**, 1–7.

136 J. Lee, J. K. Papp, R. J. Clément, S. Sallis, D. H. Kwon, T. Shi, W. Yang, B. D. McCloskey and G. Ceder, *Nat. Commun.*, 2017, **8**, 981.

137 R. A. House, L. Jin, U. Maitra, K. Tsuruta, J. W. Somerville, D. P. Förstermann, F. Massel, L. Duda, M. R. Roberts and P. G. Bruce, *Energy Environ. Sci.*, 2018, **11**, 926–932.

138 J. Lee, D. A. Kitchaev, D. H. Kwon, C. W. Lee, J. K. Papp, Y. S. Liu, Z. Lun, R. J. Clément, T. Shi, B. D. McCloskey, J. Guo, M. Balasubramanian and G. Ceder, *Nature*, 2018, **556**, 185–190.

139 W. D. Richards, S. T. Dacek, D. A. Kitchaev and G. Ceder, *Adv. Energy Mater.*, 2018, **8**, 1–7.

140   Z. Lun, B. Ouyang, Z. Cai, R. J. Clément, D. H. Kwon, J. Huang, J. K. Papp, M. Balasubramanian, Y. Tian, B. D. McCloskey, H. Ji, H. Kim, D. A. Kitchaev and G. Ceder, *Chem*, 2020, **6**, 153–168.

141   B. Ouyang, N. Artrith, Z. Lun, Z. Jadidi, D. A. Kitchaev, H. Ji, A. Urban and G. Ceder, *Adv. Energy Mater.*, 2020, **1903240**, 1–11.

Chapter 2: Experimental

2.1. Synthetic routes

2.1.1. Solid state synthesis

Solid state synthesis involves grinding together stoichiometric amounts of starting reagents to form a homogeneous mixture.[1] This mixture is then heated to high temperatures (500 – 1100 °C) in a furnace. For Li-containing materials, excess Li is commonly added to account for its volatility at high temperatures. The heating is commonly done under air but it can also be done under N_2 or Ar for air sensitive materials or if the oxygen content needs to be controlled. Reactions between solids take place at the interface between the reagent particles. Grinding increases the surface area of the reagent particles and therefore increases the surface contact between them. This enables more facile diffusion of ions across the surface when heat is applied. In some instances, an intermediate regrind before reheating is necessary to create fresh interfaces between the reagents and to allow the reaction to reach completion.

Overall, solid state synthesis is an easy method to perform, however it can involve very high temperatures and long reaction times. Furthermore, it normally produces the most thermodynamically stable phase and therefore other methods may be required to obtain metastable phases.

2.1.2. Hydrothermal synthesis

Hydrothermal synthesis involves heating starting reagents with a liquid under pressure.[1] The solid reagent is put into a teflon liner along with a liquid to give a pressure creating medium. This liner is then placed into a steel autoclave, which is then heated to moderate temperatures (typically < 300 °C) in an oven. This creates pressure within the liner which allows the reagents to react without the high temperatures normally required for solid state synthesis.

Hydrothermal synthesis can allow reaction at lower temperatures than solid state synthesis however requires the use of autoclaves to generate the high pressures, which can be expensive. Furthermore, the reaction scale is limited by the size of the autoclave.

2.1.3. Mechanochemical synthesis

Mechanochemical synthesis induces a chemical reaction by the direct absorption of mechanical energy.[1] It is commonly performed using a planetary ball mill, which consists of a container filled with mixing balls and appropriate stoichiometric amounts of starting reagents. The container is rotated at high speeds (200 – 800 rpm) which causes the balls to crush the reagents together and allows them to react. High local temperatures are generated inside the container as mechanical energy is transformed into heat and this can help to initiate the reaction.

Mechanochemical synthesis does not require a separate heating step and enables metastable phases to be formed. It also produces particles with a small particle size,

which is often desirable for cathode materials. However, the synthesis by this route can take a long time and is not commercially scalable at present.

2.2. Techniques

2.2.1. X-ray diffraction

X-ray diffraction (XRD) is a widely used technique that can be used for the identification of different phases and for determining the structure of crystalline materials. It can provide a wide range of information about a material, such as lattice parameters, atomic positions, lattice strain and crystallite size.

2.2.1.1. Crystal structures

Crystalline materials have a regular arrangement of atoms that extends in 3 dimensions. A unit cell is the smallest repeating unit that represents the full symmetry of the crystal structure. The unit cell is described by 3 lattice parameters, a, b and c, which provide information about the length of the sides, and 3 internal angles, α, β and γ, which provide information about the angle between these sides (Figure 2-1).
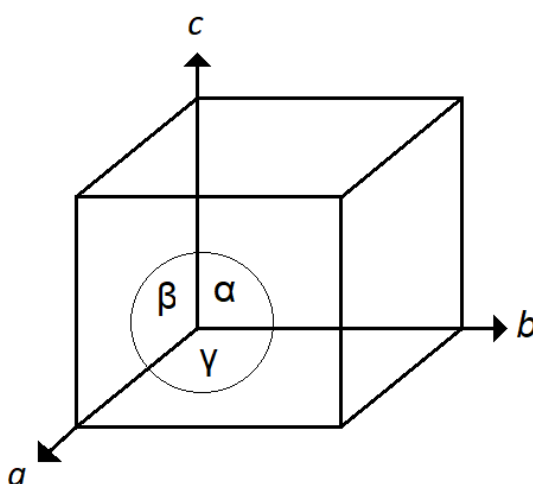

Figure 2-1: A diagram of a unit cell

The unit cell can have 7 different crystal systems (Table 2-1). Each crystal system has unique unit cell dimensions and symmetry elements.

Table 2-1: The seven different crystal systems. Note the symbol ≠ means not necessarily equal to.

Crystal System	Unit Cell Dimensions	Essential Symmetry
Cubic	$a = b = c$, $\alpha = \beta = \gamma = 90°$	Four 3-fold axes
Hexagonal	$a = b \neq c$, $\alpha = \beta = 90°$, $\gamma = 120°$	One 6-fold axes
Trigonal/Rhombohedral	$a = b = c$, $\alpha = \beta = \gamma \neq 90°$	One 3-fold axes
Tetragonal	$a = b \neq c$, $\alpha = \beta = \gamma = 90°$	One 4-fold axes
Orthorhombic	$a \neq b \neq c$, $\alpha = \beta = \gamma = 90°$	Three 2-fold axes
Monoclinic	$a \neq b \neq c$, $\alpha = \gamma = 90°$, $\beta \neq 90°$	One 2-fold axes
Triclinic	$a \neq b \neq c$, $\alpha \neq \beta \neq \gamma \neq 90°$	None

There are also 4 lattice centrings that define the positions of the lattice points within the unit cell (Table 2-2 and Figure 2-2).

63

Table 2-2: The four different lattice centrings. Note there is also a centring in the rhombohedral crystal system that is like body centred but slightly different

| Lattice Centrings	Description
Primitive (P)	Has a lattice point at each corner
Body Centred (I)	Has a lattice point at each corner and in the centre of the cell
Face Centred (F)	Has a lattice point at each corner and the centre of each face
Base Centred (A, B, C)	Has a lattice point at each corner and one pair of points at the centre of one pair of faces (eg. an A-centred lattice would possess a pair of lattice points on the *bc* face)
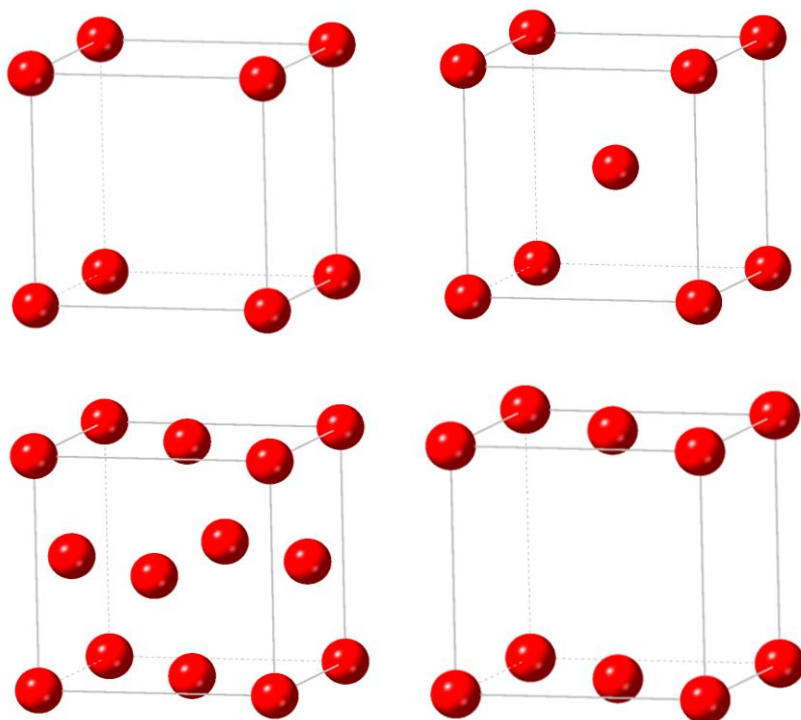
Figure 2-2: The four different lattice centrings (From top left to bottom right: Primitive, Body, Face and Base)

The 7 crystal systems and 4 lattice centrings can be combined to give 14 different Bravais lattices (i.e. there are 14 different types of unit cell). These Bravais lattices can be combined with the available point groups to give 230 space groups. These space groups describe the full symmetry of a crystal structure.

The concept of lattice planes was introduced by W. L. Bragg and W. H. Bragg as a method to aid with the analysis of XRD data.[2] They proposed that lattice planes could act as diffraction grating that X-rays could interact with. Lattice planes are identical sets of planes which are parallel to each other and equally spaced apart. One member of each set must pass through the origin of the unit cell. Each plane can be described by the Miller indices h, k and l. The values of h, k and l are the reciprocal values of the points of intersections of the plane on the a, b and c axes of the unit cell. A plane that

is adjacent to the plane that passes through the origin is used when calculating the Miller indices. If the plane does not cross a particular axis then the corresponding Miller index will be 0.

The distance between lattice planes is known as the interplanar spacing or d-spacing (d_{hkl}). For a given (hkl), the d-spacing can be calculated if the lattice parameters are known (equation 1, equation for an orthorhombic system). For higher symmetry systems the equation is simpler while for lower symmetry systems it is more complex, as in these latter cases the unit cell angles must be accounted for.

$$\text{Equation 1:} \quad \frac{1}{d_{hkl}^2} = \frac{h^2}{a^2} + \frac{k^2}{b^2} + \frac{l^2}{c^2}$$

where d_{hkl} is the d-spacing, h/k/l are the miller indices for the plane and a/b/c are the lattice parameters.

2.2.1.2. X-ray diffractometers

X-rays are electromagnetic radiation with wavelengths ~ 1 Å (10^{-10} m). X-rays are produced when a beam of electrons strikes a metal target, such as Cu, Co or Mo. The incident electrons ionise some of the 1s electrons and result in a vacancy in the 1s orbital. This orbital is then filled by electrons in outer orbitals (such as 2p or 3p) dropping down. This also results in a release of energy in the form of X-ray radiation. The electron transition energies have fixed values and therefore a characteristic spectrum of X-rays is produced.

For Cu, both the 2p → 1s transition, called Kα, and 3p → 1s transition, called Kβ, can occur to give X-rays at wavelengths of 1.5418 Å and 1.3922 Å respectively. The Kα

transition occurs more frequently and so the radiation produced is more intense and therefore Kα radiation is used in XRD experiments. Although, Kα produces a doublet with 2 different wavelengths due to the 2 possible spin states of the 2p electron. Therefore, particularly at higher angles, this can cause 2 peaks to be seen in diffraction patterns. However, this problem can be overcome by removing the weaker Kα wavelength using a monochromator.

For X-ray diffraction experiments, a monochromatic beam of X-rays is desired. For Cu, this can be partially achieved by the use of a Ni foil, which acts a filter to remove undesirable wavelengths, such as Kβ, and leave just the Kα wavelengths (technically, Ni foil does not produce monochromatic X-rays as both of the Kα wavelengths remain). A single-crystal of Si or Ge can also be used as a monochromator to select a single wavelength, such as $K\alpha_1$.

X-rays can interact with matter by either scattering or being absorbed. If there is no energy loss during scattering, then the X-rays are coherent. If there is an energy loss, they are incoherent. The coherent X-rays are used in XRD experiments while the incoherent X-rays contribute to the background of X-ray diffraction patterns. Alternatively, X-rays can be absorbed and cause ionisation of electrons or electron promotion to higher energy levels. When these promoted electrons return to the ground state they emit radiation, this is known as fluorescence. This fluorescence also contributes to the background. Cathode materials commonly contain Mn/Ni and therefore it can be beneficial to use a Co X-ray source, as Mn and Ni produce significant fluorescence when a Cu X-ray source is used.

The Bragg approach considers crystals to be made up of lattice planes. These planes are considered to reflect incoming X-rays. Bragg's Law considers X-rays interacting with 2 planes of the same set (Figure 2-3). Using trigonometry, equation 2 can then be established:
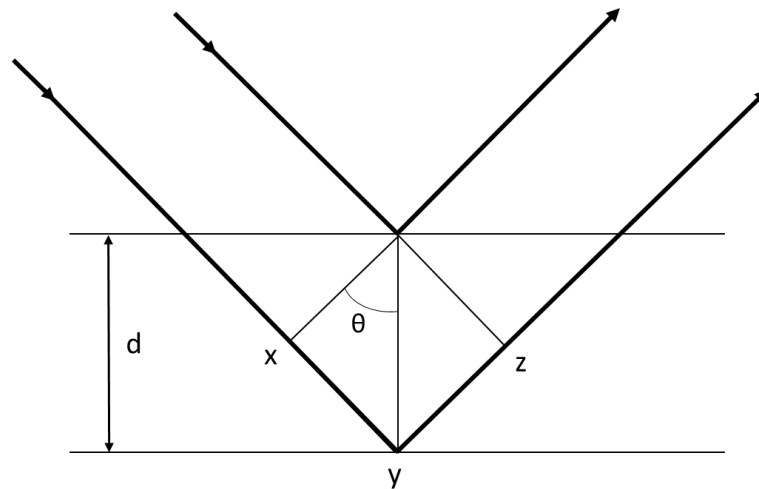
$$\text{Equation 2:} \quad xy = yz = d_{hkl}sin\theta$$

Figure 2-3: Derivation of Bragg's Law

The first X-ray strikes the top layer and is scattered, with a reflection angle that matches the incidence angle. The second X-ray passes through the top layer and is instead scattered by the next layer. This second X-ray must travel an extra distance of xy + yz to remain in phase with the first X-ray. For constructive interference to occur, the X-rays must be in phase and therefore xy + yz must be equal to an integer of the wavelength (i.e. xy + yz = nλ). From this, Bragg's Law can then be derived (equation 3). When Bragg's Law is obeyed there is constructive interference, and a peak in intensity is seen in the resulting XRD pattern. However, when X-rays are not in phase, they cause destructive interference and therefore no intensity is seen.

$$\text{Equation 3:} \quad n\lambda = 2d_{hkl}sin\theta$$

In this thesis, 2 different diffractometers were used: a Bruker D8 diffractometer with a Cu Kα radiation source and a Bruker D2 phaser with a Co Kα radiation source. Samples were prepared by grinding the powder in a pestle and mortar before being placed into a sample holder for measurements to be taken. Normal, low background and airtight sample holders (for air sensitive samples) were used. Measurements were conducted in the range of 10 – 90° with a step size of ∼ 0.02°.

Variable temperature XRD (VT-XRD) was conducted using a Bruker D8 diffractometer fitted with an Anton Paar variable temperature sample stage. For the VT-XRD measurements, the sample was placed upon a heated stage within an insulated casing. The sample was then heated and measurements were taken at regular temperature intervals.

2.2.1.3. Powder X-ray diffraction

Powder XRD involves a monochromatic beam of X-rays hitting a finely powdered sample that ideally has randomly orientated crystals. This random orientation means every type of orientation that is possible is present. This then means that there is a high probability that for each set of planes, some crystals will be orientated at the correct Bragg angle to the incident X-ray radiation and therefore cause diffraction. By obtaining data over a range of 2θ angles, a distinctive XRD pattern is produced. By looking at the position, intensity and shape of peaks in the XRD pattern information can be gained about the sample.

The position of the peaks is dictated by Bragg's Law and therefore peak positions can be used to determine d-spacings. From d-spacings, lattice parameters can then be deduced (using Equation 1, for an orthorhombic system). In principle, each set of lattice planes should give rise to a diffracted beam and a peak in intensity. However, in practise, the intensity of the beams at certain angles is 0. These are known as systematic absences and are caused by destructive interference due to the symmetry of the structure. Each lattice type has distinctive systematic absences (Table 2-3) that can be used to help identify them. Other symmetry elements containing a translational component, such as a glide plane or screw axes, also give rise to systematic absences. Additional factors, such as zero-point error and sample height error, also have an influence on the peak positions and should be corrected for.

Table 2-3: Systematic absences for different lattice centrings

Lattice Centrings	Rule for reflections to be observed
Primitive (P)	All values of hkl are observed
Body Centred (I)	The sum of h + k + l must be even
Face Centred (F)	Values of h, k, and l are either all odd or all even
Base Centred (A, B, C)	The sum of k + l must be even

Peak intensity depends on several factors. It partly depends on the scattering power of different atoms. X-rays are scattered by electrons and therefore as the atomic number increases, the number of electrons increases and so this contributes to the

intensity of the scattered X-rays increasing. As a result of this, light elements, such as Li, are extremely difficult to locate in XRD. Multiplicity is the number of lines that overlap because of crystal symmetry, and this also influences individual peak intensities. Peak intensity is also influenced by atomic positions, thermal vibrations, phase fractions and preferred orientation. The absolute intensity of the XRD pattern depends on experimental factors, such as the duration of the scan, and instrumental factors, such as the intensity of the applied radiation and the detector efficiency.

Peak shape is influenced by both sample and instrumental factors. The particle size, structural defects and local disorder all contribute to peak broadening. Instrumental factors, such as alignment and the radiation source can also influence the peak shape.

2.2.2. Rietveld refinements

A Rietveld refinement is a whole pattern refinement that compares an experimental XRD profile to that of a calculated profile for a model structure. The calculated profile is constructed from a starting model of the crystal structure in combination with experimental factors, which help to describe the background and peak shape. The crystal model must contain information such as lattice parameters, atomic positions, fractional occupancies, and atomic displacement parameters. A least squares method is then used to reduce the differences between the calculated and experimental XRD patterns by varying these parameters.

The progress of the refinement can be monitored visually by inspecting the difference between the 2 patterns. The experimental and calculated patterns can be plotted along with a difference plot (Figure 2-4, an example refinement plot). The difference plot is a

quick visual tool that shows how the refinement is progressing. If a perfect fit is achieved, then the difference plot will be a straight line.
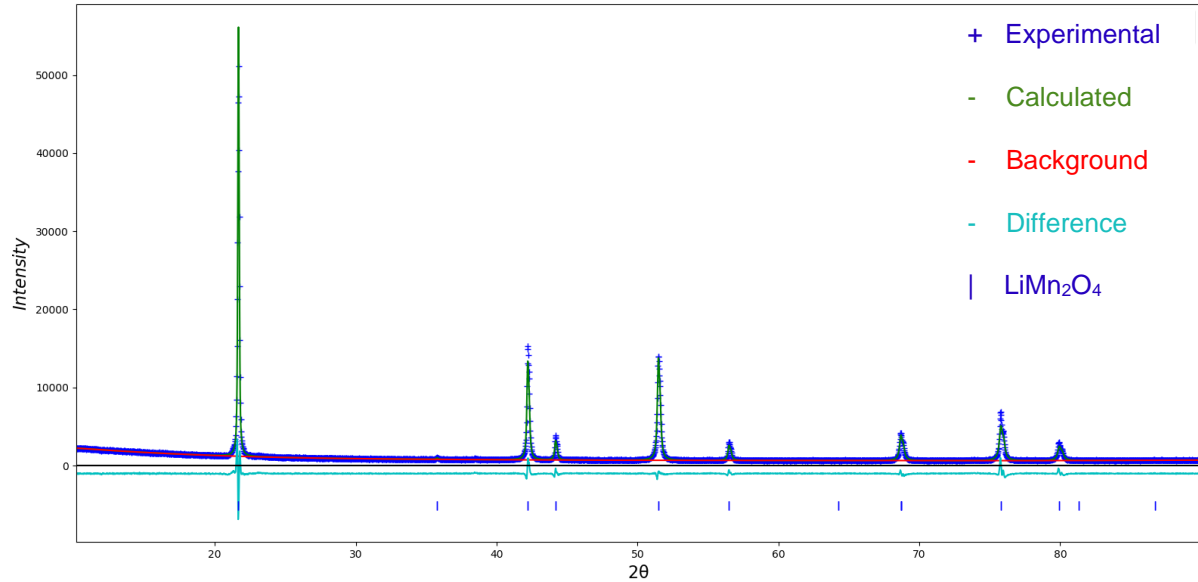

Figure 2-4: Rietveld refinement plot of LiMn₂O₄ generated by GSAS

The R-factors are also important when considering the progress of the refinement. They are statistical factors which should ideally decrease as the refinement progresses. The 3 most important R-factors are the profile factor (R_p), the weighted profile factor (R_{wp}) and the experimental profile factor (R_{exp}) [equations 4 – 6].

$$\text{Equation 4:} \quad R_p = \frac{\sum|y_i(obs) - y_i(calc)|}{\sum y_i(obs)}$$

$$\text{Equation 5:} \quad R_{wp} = \sqrt{\frac{\sum w_i[y_i(obs) - y_i(calc)]^2}{\sum w_i[y_i(obs)]^2}}$$

$$\text{Equation 6:} \quad R_{exp} = \sqrt{\frac{(N - P - C)}{\sum w_i[y_i(obs)]^2}}$$

where y_i(obvs) is the observed intensity at the ith point, y_i(calc) is the calculated intensity at the ith point, w_i is the weighting factor, N is the number of observations, P is the number of refined parameters and C is the number of constraints used.

R_{wp} is the most relevant statistical value as its numerator is the value that is minimized during the refinement. However, the background has a substantial effect on R_{wp} and therefore this R-factor should be used with caution for XRD patterns with a high background. R_{exp} is the lowest obtainable value that R_{wp} can potentially achieve. The goodness of fit (GOF, χ^2) is another parameter that can be considered (equation 7). When χ^2 is equal to 1, the calculated and experimental patterns match exactly.

$$\text{Equation 7:} \quad \chi^2 \;=\; \left(\frac{R_{wp}}{R_{exp}}\right)^2$$

The final thing that must be considered is whether the observed structure makes chemical sense. The refinement is a mathematical process rather than a chemical one and therefore does not account for whether a sensible structure has been proposed. Consequently, the final structure model should be considered carefully.

In this work, all Rietveld refinements were performed using the GSAS-II program.[3] A GSAS-II refinement requires three files; an XRD data file (the experimental file), a parameter file that contains information about the diffractometer used and a crystallographic information file which contains information about the crystal structure. The GSAS-II program then refines the structural parameters until an acceptable level of agreement is reached with the experimental data.

2.2.3. Pawley refinements

An alternative analysis technique to Rietveld refinement for XRD data is Pawley refinement. It is a similar method to Rietveld refinement, but detailed structural information is not required and instead only the space group and unit cell parameters are needed. Peak intensities are used to provide information on lattice parameters, size and microstrain.

In this work, all Pawley refinements were performed using TOPAS version 6.[4,5]

2.2.4. Raman spectroscopy

Raman spectroscopy is a vibrational spectroscopy that provides information about the bonding in materials.[6] For a material to be Raman active it must have a change in polarisation when it vibrates. Raman spectroscopy is a non-destructive technique which involves exposing a sample to laser irradiation in the visible region of the spectrum. This laser irradiation causes the sample to move to a virtual excited state. Relaxation then occurs via either elastic or inelastic scattering. Raman spectroscopy detects only the inelastic scattering.

Elastic scattering (otherwise known as Rayleigh scattering) is when the emitted photons have equal energy to the incident photons (Figure 2-5). Inelastic scattering is when the emitted photons have different energy than the incident photons. There are two types of inelastic scattering: Stokes and Anti-Stokes. Stokes scattering occurs when the energy of the incident photon is greater than that of the emitted photon. Anti-Stokes scattering occurs when the energy of the incident photon is lower than that of the emitted photon.
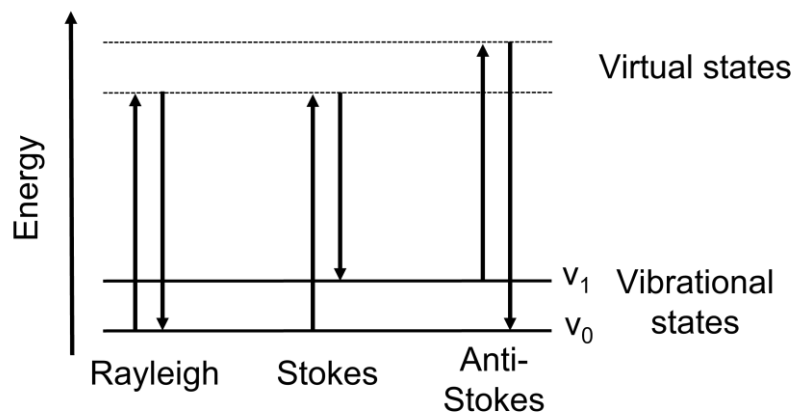
Figure 2-5: Rayleigh, stokes and anti-Stokes scattering processes

In this work, a Renishaw Invia reflex microscope was used. Samples were irradiated using a 633 nm laser which was focused using a 20x objective lens. A beam power of 10% was used and 10 accumulations were taken.

2.2.5. Electrochemical testing

In this work, both coin and Swagelok cells were used to test the electrochemical performance of the cathode materials. Coin cells were used for all the electrochemical testing in this thesis unless it is stated otherwise. All the electrochemical testing was performed using a Biologic BCS-805 battery cycler.

2.2.5.1. Coin cell preparation

Using a method previously optimised by other members of this group, electrodes were prepared by mixing 80 wt% cathode material with 10 wt% carbon black and 10 wt% PVDF. Carbon black was added to improve the electronic conductivity while PVDF was added to act as a binder. These materials were dissolved in NMP and mixed at 1300 rpm for 10 minutes (followed by a degassing step at 1800 rpm for 3 minutes) in a

THINKY ARE-250 planetary mixer to form a slurry. The slurry was then coated onto Al foil. Individual circular electrodes were then cut out of the electrode coatings.

Before use, the electrodes and coin cell parts were dried in a vacuum oven overnight to remove any trace moisture. They were then transferred into a glove box with Ar atmosphere. 2032-type coin cells were manufactured by assembling a bottom cap, an electrode, a separator soaked in electrolyte (1M $LiPF_6$ in a solution of 50:50 ethylene carbonate:dimethyl carbonate), a metallic Li counter electrode, a spacer, a spring and a top cap with a gasket (Figure 2-6). These coin cells were then crimped closed using a crimper machine. Cells were left to sit for 12 hours before any electrochemical testing was performed to allow the electrolyte to sufficiently soak through the electrode.

Top cap with gasket

Spring

Spacer

Metallic lithium electrode

Separator soaked in $LiPF_6$

Electrode (cathode or anode)

Bottom cap
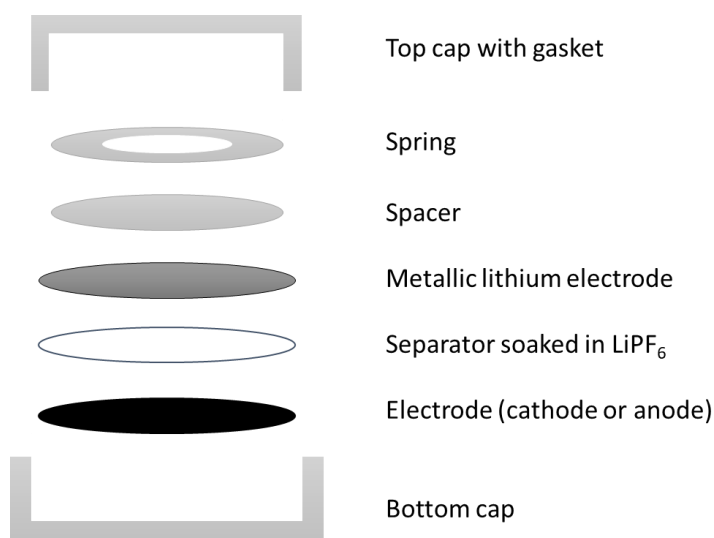
Figure 2-6: Diagram showing coin cell assembly

2.2.5.2. Swagelok cell preparation

For air sensitive materials, Swagelok cells were used to avoid exposing the material to air. Rather than making wet electrodes, either cathode powders or pellets were used

instead. For the cathode powders, 70 wt% cathode material was ball milled with 30 wt% carbon black under Ar atmosphere using a Pulverisette 7 planetary ball-mill at 450 rpm for 2 hrs. <10 mg of the subsequent powder was used as the electrode. For the pellets, 70 wt% cathode material was ball milled with 20 wt% carbon black and 10 wt% PVDF under Ar atmosphere using a Pulverisette 7 planetary ball-mill at 450 rpm for 2 hrs. 10-20 mg of this mixture was then pressed into a pellet.

Swagelok cells were then assembled in the glovebox using a metallic Li counter electrode, a separator soaked in electrolyte (1M LiPF6 in a solution of 50:50 ethylene carbonate:dimethyl carbonate) and powder/pellet electrode. These cells were also left to sit for 12 hours before testing.

2.2.5.3.   Electrochemical performance testing

The electrochemical performance of the cell can be tested to gain information about the voltage profile, specific charge/discharge capacities and capacity retention of the cell (Figure 2-7).[7] In this thesis, electrochemical testing was performed using constant current-constant voltage cycling.[8] This is a two-step charging method in which a constant current is applied until an upper voltage limit is reached. There is then a switch to a constant voltage mode, where the voltage is maintained at the upper voltage limit until the current has decayed by a set amount. The discharging is then performed with a constant current. In this thesis, charging/discharging was performed at a rate of 10 mAg[-1] unless stated otherwise. For some of the cathode materials, a range of voltage windows and different charge rates were also investigated.
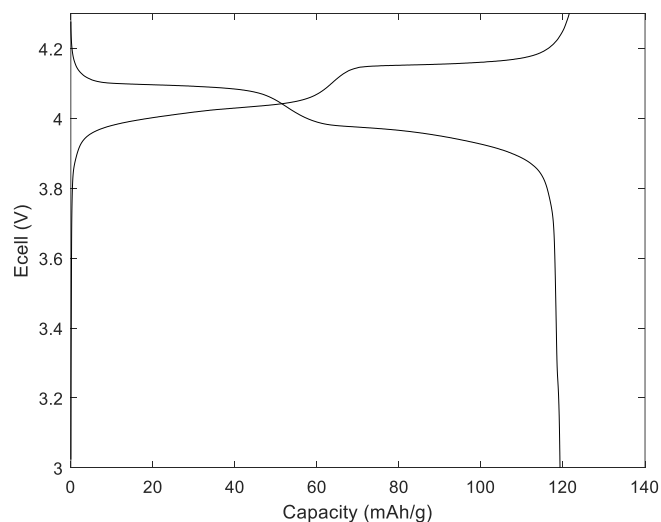
Figure 2-7: Galvanostatic charge-discharge profile of LiMn$_2$O$_4$ cycled at 10 mAg^{-1} between 3-4.3 V

Differential capacity analysis can be used to help visualise small changes in the voltage during cycling.[9] dQ/dV plots can distinguish different redox peaks, demonstrate the level of polarisation within the cell and indicate degradation if there are changes to the plot with subsequent cycling (Figure 2-8).
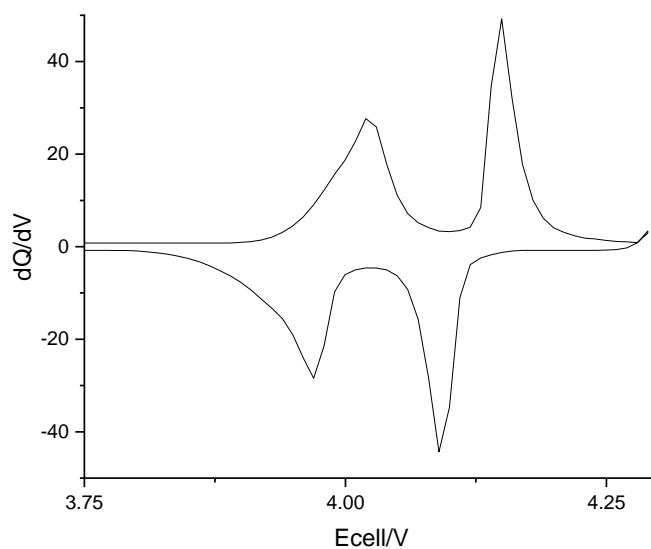

Figure 2-8: dQ/dV plot of LiMn$_2$O$_4$ cycled at 10 mAg^{-1} between 3-4.3 V

2.2.6. Scanning electron microscopy

Scanning electron microscopy (SEM) is a technique that is used to visualise materials on a micrometre scale.[10,11] A beam of high energy electrons is scanned across a sample to allow an image of the sample to be built up. The electrons hit the surface of the sample and undergo a range of interactions (Figure 2-9). Secondary electrons (SE) are loosely bound outer shell electrons that are emitted from the sample due to collisions with incident electrons. SE originate from close to the surface of the sample as only surface electrons have enough energy to escape the sample surface. SE provide topographical information about the sample. In comparison, backscattered electrons (BSE) are incident electrons that are scattered by the nucleus of an atom in the sample. BSE provide information about the composition of a sample; with higher atomic number elements appearing brighter in the resulting image. BSE have higher energy than SE and therefore provide information about deeper regions within the sample.
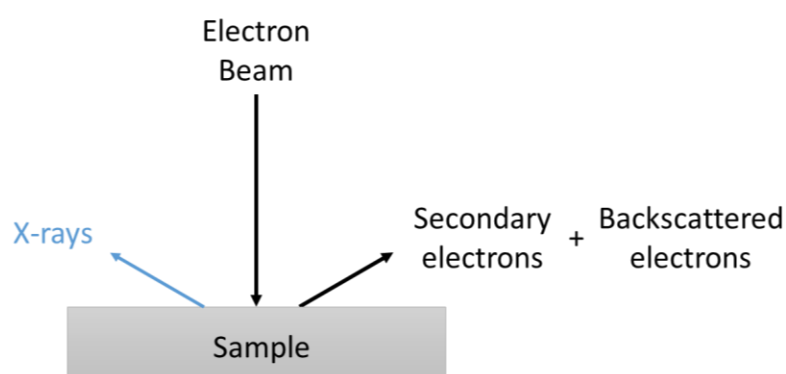
Figure 2-9: Diagram depicting the relevant interactions of high energy electrons with a solid sample

SEM requires thin and conductive samples. The samples must be conductive to prevent a build-up of electric charge on the surface. This is commonly achieved by

coating the surface of the samples with a thin layer of gold or carbon. SEM images must be analysed with caution as they only show one part of the sample and therefore are not representative of the entire sample unlike powder XRD. Consequently, multiple regions should be examined. In this work, a HITACHI TM4000plus SEM was used.

2.2.6.1. Energy dispersive X-ray analysis

Energy dispersive X-ray (EDX) analysis is used to examine the elemental composition of a sample. As shown in Figure 9, some of the incident electrons are absorbed by the sample and in turn this can cause X-rays to be emitted.[12] The resulting X-ray emission spectra can then be used to identify individual elements within the sample. However, this technique cannot be used to identify lighter elements, such as Li. In this work, an EDS Oxford Instruments MICSF + X-stream-2 attachment was used with an interaction size of up to 500 nm at 15 keV.

2.2.7. Inductively coupled plasma optical emission spectroscopy

Inductively coupled plasma optical emission spectroscopy (ICP-OES) is used to quantify the amounts of different elements within a sample.[13] ICP-OES is extremely sensitive and can detect elements that are present in the sample in parts per billion. During a measurement, samples are introduced into a plasma as an aerosol using a nebulizer. The plasma consists of a high temperature source of ionised Ar gas and gives energy to the sample. This causes the sample atoms to become excited. When the excited atoms return to their low energy state, they emit characteristic radiation. This radiation can be used to identify the elements present and to determine the amount of each element within the sample. The wavelengths analysed must be

considered carefully as other elements present in the sample can provide interference (for example, Ni 228.708 nm interferes with Co 228.615 nm).[14]

ICP-OES instruments can be configured to take measurements in either an axial or radial mode. Radial measurements are taken when the plasma is viewed from the side while axial measurements are taken when the plasma is viewed end on.[15] Radial measurements tend to be more precise however axial measurements allow for lower detection limits. In this work, radial measurements were used as the concentration of metals in solution were relatively high and radial measurements are also better for alkali metals, such as Li.

Calibration standards containing the elements of interest are prepared with a range of concentrations. These allow a calibration curve to be plotted and the sample concentrations are then deduced from this. Samples may require dilution to move them into an appropriate concentration range. Solid samples need to be digested before analysing. This is achieved by digesting the sample in a strong acid, such as aqua regia or conc. HNO_3. In some instances, a microwave may also be required to aid the digestion.

In this work, a Milestone Ethos UP AM182 microwave and an Agilent 5110 ICP-OES instrument were used. Solid samples were digested in aqua regia (0.1 g in 10 mL acid) using microwave digestion at 170 °C using 1800 MW for 45 mins. Liquid samples were directly used. Samples were then passed through a 0.22 μm filter and acidified with 2% ultrapure HNO_3 to prevent any solid particulates from blocking the nebulizer. Samples were diluted with 2% ultrapure HNO_3 to within a 0-100 ppm range. Standards were prepared from a multielement standard to concentrations of 1, 5, 10, 50 and 100

ppm. The most intense wavelength with the least interference was chosen for each element; Li 670.783 nm, Mn 294.921 nm, Ni 216.555 nm, Co 230.786 nm, Al 396.152 nm and Cu 324.754 nm.

2.3. References

1   A. R. West, *Solid State Chemistry and its Applications*, Wiley, 2014.

2   W. H. Bragg and W. L. Bragg, *Proc. R. Soc. Lond. A.*, 1913, **88**, 428–38.

3   B. H. Toby and R. B. Von Dreele, *J. Appl. Crystallogr.*, 2013, **46**, 544–549.

4   A. Coelho, *J. Appl. Crystallogr.*, 2018, **51**, 210–218.

5   J. S. O. Evans, *Mater. Sci. Forum*, 2010, **651**, 1–9.

6   D. J. Gardiner, *Practical Raman Spectroscopy*, Springer, 1989.

7   S. Petrovic, *Battery Technology Crash Course*, Springer, 2021.

8   S. S. Zhang, *J. Power Sources*, 2006, **161**, 1385–1391.

9   BioLogic, https://www.biologic.net/documents/dcs-dca-battery-application-note-40/ (acessed 2nd May 2024).

10   D. McMullan, *Scanning*, 2006, **17**, 175–185.

11   A. Ul-Hamid, *A Beginners' Guide to Scanning Electron Microscopy*, Springer, 2018.

12   J. C. Russ, *Fundamentals of Energy Dispersive X-Ray Analysis*, BMM, 1984.

13   J. Noite, *ICP Emission Spectroscopy: A Practical Guide*, Wiley-VCH, 2020.

14   N. Daskalova and I. Boevski, *Spectrochim. Acta Part B*, 1999, **54**, 1099–1122.

15   Agilent Technologies, *Dedicated axial or radial plasma view for superior speed and performance*, 2012.

Chapter 3: Hydrometallurgical recycling of mixed cathode materials

3.1. Introduction

As mentioned in section 1.2.1.2. hydrometallurgical methods are widely used to leach different elements from cathode materials. The method involves using an acidic solution to extract the metal ions from the cathode material into the solution. The leaching process can be reductive whereby metal ions are reduced from a high valence solid phase to a low valence aqueous one. Reductive leaching is often encouraged via the addition of a reducing agent, such as H_2O_2. For NMC, reducing agents help to reduce Co^{3+} and Mn^{4+} to more soluble Co^{2+} and Mn^{2+}. Meanwhile, they also help with the dissolution of Li and Ni as these are bound along with Co/Mn within the same oxide structure. Chelating agents in solution can then stabilise these lower valence aqueous ions by complexation.

The rate and efficiency of the leaching process are affected by the type of acid, the acid concentration, solution temperature, reducing agent concentration and amount of solid in the leaching solution (solid to liquid ratio). Increasing the acid concentration is found to increase the leaching rate up to a point, after which further increases in acid concentration have no effect or potentially an adverse effect upon the leaching rate. This can be due to the rate limiting step changing as the acid concentration is increased.[1] The same trend in leaching rate is also seen when the solution temperature is increased. Increasing the solution temperature has also been shown to increase the leaching efficiency, as metal leaching is usually an endothermic process.[2,3] An

increase in the reducing agent concentration also increases the leaching rate, as the metal ions are reduced and this promotes their dissolution into the solution. Increasing the solid to liquid ratio (S:L ratio) is shown to decrease the leaching rate and efficiency, as there is less acid present to aid in the metal dissolution.[3]

The metal ion selectivity of the leaching solution is related to the acid used and the metals that are present in the cathode materials. The reducing ability of the acid and the oxidation potential of the metals will also determine which metals are leached into solution. The chelating ability of the acid can also determine whether the metal ions are stable once in solution. Furthermore, the pKa of the acid determines the pH of the solution which in turn determines which metal species are soluble and controls whether any precipitates are formed.

The focus of this thesis is on the recovery of materials from Gen 1 Nissan leaf cells. These cells contain a mix of a layered oxide (LO) and $LiMn_2O_4$ (LMO). The focus of this chapter was to investigate a leaching method that could selectively leach the LMO into solution while leaving the LO intact. The separated LMO and LO were then recovered and recycled into new cathode materials.

3.2. Experimental

3.2.1. Initial LiMn$_2$O$_4$ leaching experiments

To check which acids were able to leach LMO, 0.15 g of LMO was added to 20 mL of 1.25 M acid. Table 3-1 shows the acids that were investigated. These acids were selected to provide a range of different properties and pKa values. The solution was then stirred. Visual inspection was used as an initial indication for whether any leaching had occurred. If there was no solid LMO visibly left in the solution then it was assumed that the acid could leach LMO. Meanwhile if there was solid LMO left in the solution then it was assumed that the acid could not leach LMO or that only partial leaching had occurred.

For the more detailed LMO leaching investigations, a specific amount of LMO was added to an acidic solution of known concentration, temperature, and volume. The solution was then stirred for a set duration of time. The leaching time was taken as the point at which no remaining LMO powder was visible in the solution. The pH of this solution was also taken using pH test strips. The solution was then dried on a hotplate until ~10 mL of solution was remaining before being put into an oven at 200 °C overnight. Once dry, the remaining residue was ground by hand in a pestle and mortar and placed into an alumina crucible covered by a lid. This crucible was then put into a furnace and heated at 700 °C for 12 hours to reform the LMO.

3.2.2. Translation of methodology to EV batteries

From the above experiments, citric acid was shown to be the most promising acid for selectively leaching the LMO phase into solution, therefore it was employed for EV

batteries. Cathode material from two different large-format Li-ion pouch cells (dimensions 290 × 216 × 7 mm) were investigated. One cell was from the battery pack of an end-of-life (EOL) Gen 1 Nissan Leaf (2011 model, 40,000 miles). The other cell was a quality control (QC) rejected cell obtained from Nissan. The cells were safely removed from the module before being discharged to 2.7 V (EOL) and <1 V (QC). The cells were then manually disassembled using the method reported by Marshall et al to obtain the cathode sheets.[4] The cathode sheets were then washed in diethyl carbonate to remove any residual electrolyte before being dried in a fume hood. The disassembled cells were provided by the University of Newcastle and the washed cathode sheets were provided by the Kendrick group at the University of Birmingham.

For the cathode leaching procedure, the cathode sheets (200 by 220 mm) were cut into small pieces (approximately 1 by 1 cm). 0.3-0.4 g of the cathode pieces were added to 10 mL of citric acid at a known concentration and temperature. At the end of the stated leaching time the solution was filtered to separate the remaining cathode from the citric acid solution. A small sample of the solution was used for ICP-OES analysis. The remaining cathode solid was put into an oven at 80 °C to dry.

3.2.3. Recycling cathode materials

The recycled LMO was recovered by first drying the leaching solution in an oven at 200 °C for 4 hours. The remaining residue was ground by hand in a pestle and mortar and placed into an alumina crucible covered by a lid. This crucible was then put into a furnace and heated at 700 °C for 6-12 hours. An additional grinding step was assessed by regrinding some samples before reheating.

The recycled LO was recovered by thermal and hydrothermal treatments. For the thermal treatments, the dried cathode was ground by hand in a pestle and mortar and placed into an alumina crucible (Sigma-Aldrich). This crucible was then put into a furnace and heated at 450-900 °C for 2-12 hours. For the hydrothermal treatments, 0.2 g of dried cathode was added to a 23 mL teflon container in a Parr hydrothermal vessel containing 10 mL 0.5-4 M NaOH. The hydrothermal vessel was heated overnight at 150-170°C for 8-16 hours to decompose the PVDF binder. The resulting powder was filtered using 11 μm filter paper, washed and dried. The recovered powder was then mixed with 10 wt% Li_2CO_3 (powder, Sigma-Aldrich, 99.99% purity) and heated to 800 °C for 12 hours to resynthesise the LO.

3.2.4. Rietveld refinements

Rietveld refinements were carried out using the XRD data. For the QC and EOL cathodes, the primary phase (LO) was fitted with the $R\overline{3}m$ space group, the secondary phase (LMO) was fitted with the $Fd\overline{3}m$ space group and the tertiary phase (graphite) was fitted with the $P6_3/mmc$ space group. Once the LMO had been leached from the cathode it was no longer fitted as a phase in the refinement. Some of the leached cathode samples contained an additional LO phase that was also fitted to the $R\overline{3}m$ space group. Lattice parameters, sample displacement and strain were refined for all samples. When the samples contained multiple phases, the weight fractions were also refined. Constraints were added to make the strain equivalent for all the phases and to make the sum of the weight fractions equal to 1. For samples containing the LO phase, a March-Dollase preferred orientation term was added along the (003) axis. Occupancies, atomic positions and thermal parameters were fixed to sensible values.

An example Rietveld refinement plot for the QC cathode is shown in Figure 3-1. The Rietveld refinement plots for this chapter are shown in Appendix A.
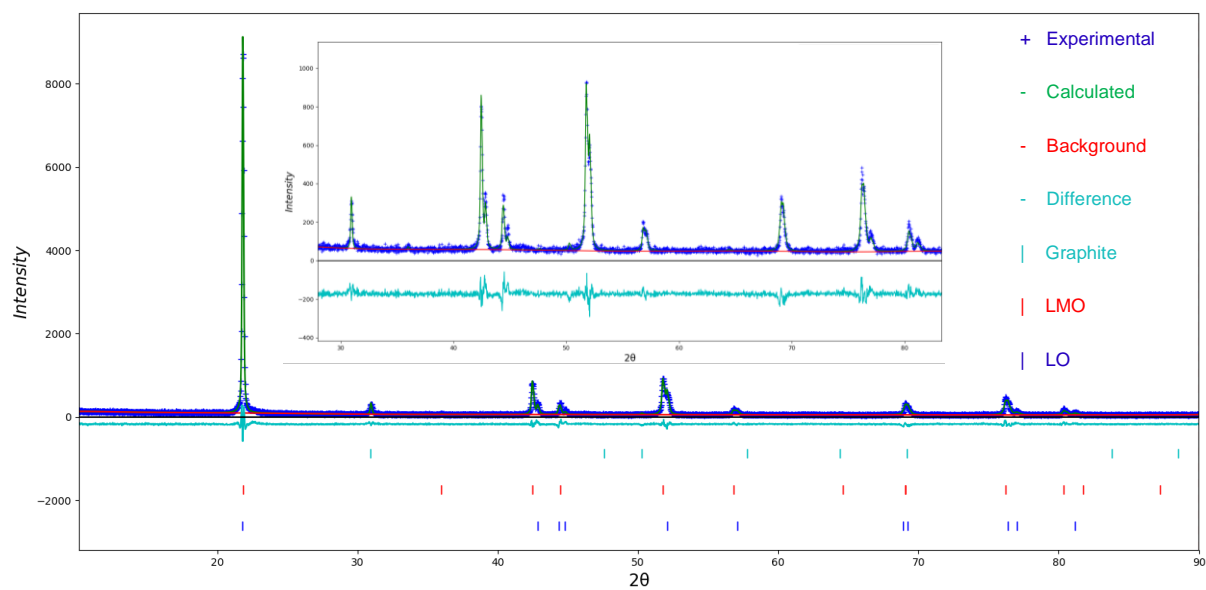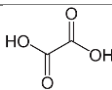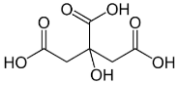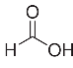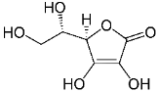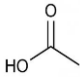
Figure 3-1: Rietveld refinement plot for the QC cathode (λ = 1.79 Å). R_{wp} = 12.86% and GOF = 1.30.

3.3. Investigation into different organic acids as leaching agents for LiMn$_2$O$_4$

Table 3-1 shows the different organic acids that were investigated as leaching agents for LMO. Oxalic, citric, formic and ascorbic acid were selected as they are all reducing agents with a range of different pKa values. Acetic acid was selected for comparison as it is not a reducing agent.

Table 3-1: Organic acids investigated as leaching agents for LMO

Acid	Structure	pKa
Oxalic		1.23, 4.29[5]
Citric		3.13, 4.76, 6.40[6]
Formic		3.75[7]
Ascorbic		4.12[8]
Acetic		4.12, 11.51[7]

Oxalic, citric, and ascorbic acid leached the LMO while formic and acetic acid did not. This can be explained by the fact that acetic acid is not reducing, this means that the Mn within the LMO will not be reduced to Mn^{2+}. This therefore may have inhibited any leaching from occurring. Oxalic, citric, ascorbic, and formic acid are all reducing however only oxalic, citric, and ascorbic acid leached the LMO. Formic acid has a

similar pKa to both citric and ascorbic acid which suggests that the ability of an acid to leach is not related to pKa or reducing ability alone. In this respect, oxalic, citric, and ascorbic acid are all chelating agents while formic acid is not. This could mean that formic acid is unable to stabilise the aqueous ions in solution and therefore they do not leach effectively.

Ascorbic acid has already been investigated as a selective leaching agent for LMO by other members of this research group.[9] Therefore, oxalic and citric acid were explored here as alternative selective leaching agents.

Although a study looking at the exact mechanism of leaching has not been undertaken as part of this thesis, a mechanism can be proposed based upon the chemistry involved. It is likely that the oxidising ability of oxalic and citric acid is causing the $Mn^{3+/4+}$ ions to be reduced to Mn^{2+} ions. These Mn^{2+} ions are then likely to chelate to the oxalate and citrate ions to form metal complexes. Additional studies would be required to investigate exactly which complexes are being formed.

3.3.1. Oxalic acid leaching of $LiMn_2O_4$

Oxalic acid is an organic acid that can release up to 2 H^+ ions per molecule. Oxalic acid ($H_2C_2O_4$) can dissociate to form either $HC_2O_4^-$ or $C_2O_4^{2-}$ depending on the solution pH. Oxalic acid is the predominant species below pH 1.23 while $C_2O_4^{2-}$ is the dominant species above pH 4.19.[5] These species can then form oxalate complexes with aqueous metal ions. When LMO was added to a solution of oxalic acid, a precipitate was formed. Figure 3-2 shows that this precipitate matches to Mn oxalate [$MnC_2O_4(H_2O)_2$]. Mn oxalate is insoluble and therefore precipitates out of solution.

Another solid was obtained by evaporating the water from the remaining solution, however, the pattern of the dried solution could not be matched. It did not match to any of the expected products, such as lithium oxalate or oxalic acid. It could therefore be a mix of different oxalate complexes.
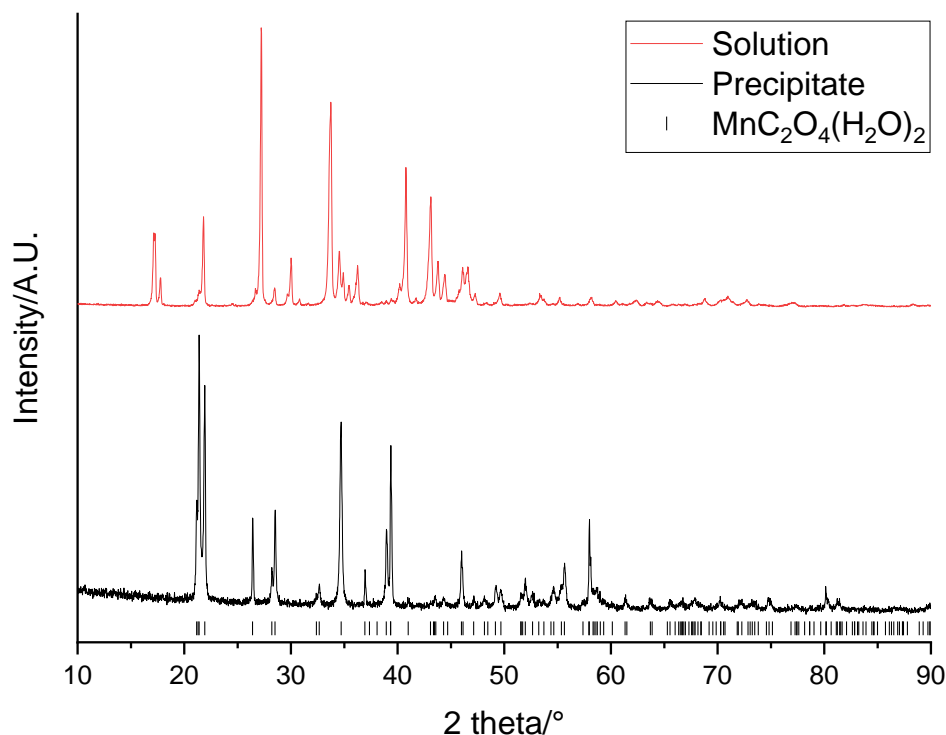
Figure 3-2: XRD patterns of 1.25 M oxalic acid leaching precipitate (black) and solution (red) (λ = 1.79 Å). Tick marks correspond to $MnC_2O_4(H_2O)_2$ (black).

Both the Mn oxalate precipitate and the dried solution were placed into a furnace. Figure 3-3 shows that the Mn oxalate formed Mn_2O_3 upon heating while the solution formed Li_2MnO_3. These results suggest that not all of the Mn is precipitating out from the solution and that some is remaining in solution to allow the formation of Li_2MnO_3. It also suggests that Li is not precipitating out of the solution, hence the formation of a Li rich phase from the solution. Li oxalate ($Li_2C_2O_4$) is soluble so it seems likely that the Li is complexing to the oxalate ions and remaining in the solution.
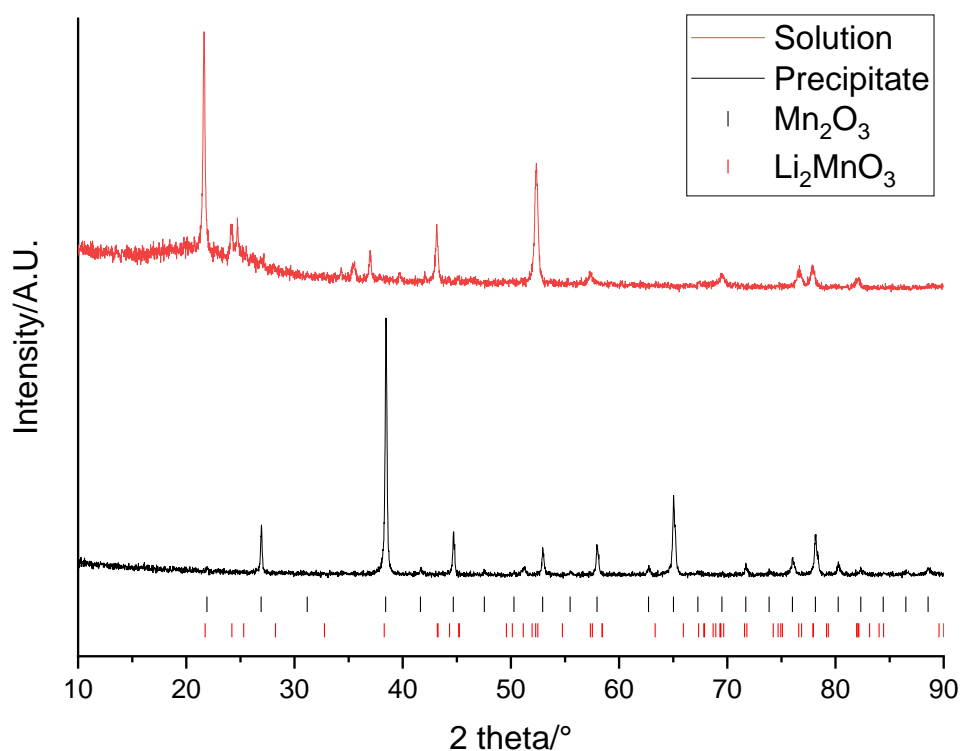
Figure 3-3: XRD patterns of 1.25 M oxalic acid leaching precipitate (black) and solution (red) after heating to 700 °C for 12 hrs (λ = 1.79 Å). Tick marks correspond to Mn_2O_3 (black) and Li_2MnO_3 (red).

This leaching procedure was then repeated with 0.5 and 2 M oxalic acid solution. Figure 3-4 shows that the XRD patterns look the same as those obtained for 1.25 M. This suggests that at higher and lower acid concentrations, some of the Mn is precipitated while the Li remains in solution.
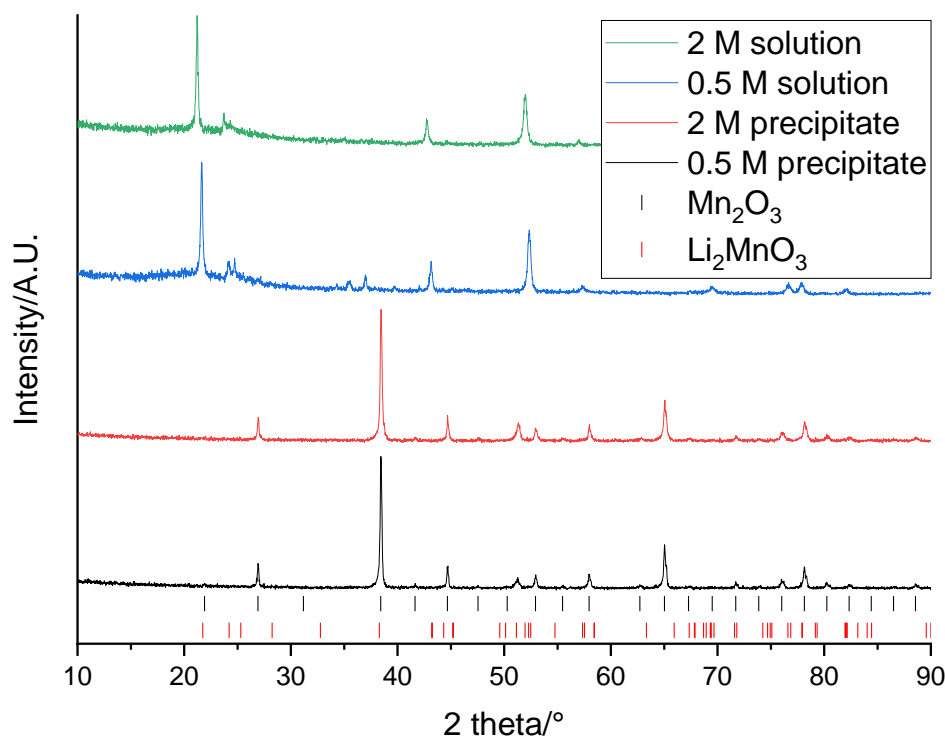
Figure 3-4: XRD patterns of 0.5 M oxalic acid leaching precipitate (black) and solution (blue) and 2 M oxalic acid leaching precipitate (red) and solution (green) after heating to 700 °C for 12 hrs (λ = 1.79 Å). Tick marks correspond to Mn_2O_3 (black) and Li_2MnO_3 (red).

Although, oxalic acid can leach Li and Mn into solution it also causes some of the Mn to be precipitated out of solution as Mn oxalate. This would cause problems when attempting to selectively leach LMO from mixed cathode materials as the precipitate would then have to be separated from any remaining cathode material in a subsequent step. However, oxalic acid could be a useful acid for separating Mn and Li in other cathode materials, such as novel cathode materials which contain only Li-Mn-O, via precipitation of Mn out of solution.

3.3.2. Citric acid leaching of $LiMn_2O_4$

Citric acid is a weak organic acid that can release up to 3 H^+ ions per molecule. Citric acid can dissociate to form $H_7C_6O_7^-$, $H_6C_6O_7^{2-}$ or $H_5C_6O_7^{3-}$. Similarly to oxalic acid, the species present in solution is dependent on the pH of the solution.[6] These species can form citrate complexes with aqueous metal ions, such as $Li_3H_5C_6O_7$, $MnH_{14}C_{12}O_{14}$, $MnH_6C_6O_7$ and $Mn_3H_{10}C_{12}O_{14}$.

Citric acid was investigated as a leaching agent. The LMO powder leached into the solution, and this was accompanied by the solution changing colour from colourless to pale yellow. Figure 3-5 shows that the XRD pattern of the solid residue from evaporating the solution matches to $Mn(C_6H_6O_7)(H_2O)$.[10] Furthermore, Liu et al have reported an identical XRD pattern which they attribute to Mn citrate complexes.[11] Appendix A (Figure A1) shows the corresponding refinement plot. The resulting dried solution was then placed into a furnace where upon heating it formed LMO (Figure 3-5, red XRD pattern). This indicates that citric acid can be used to leach LMO into solution and that, upon heating, the LMO can be recovered back out of solution.
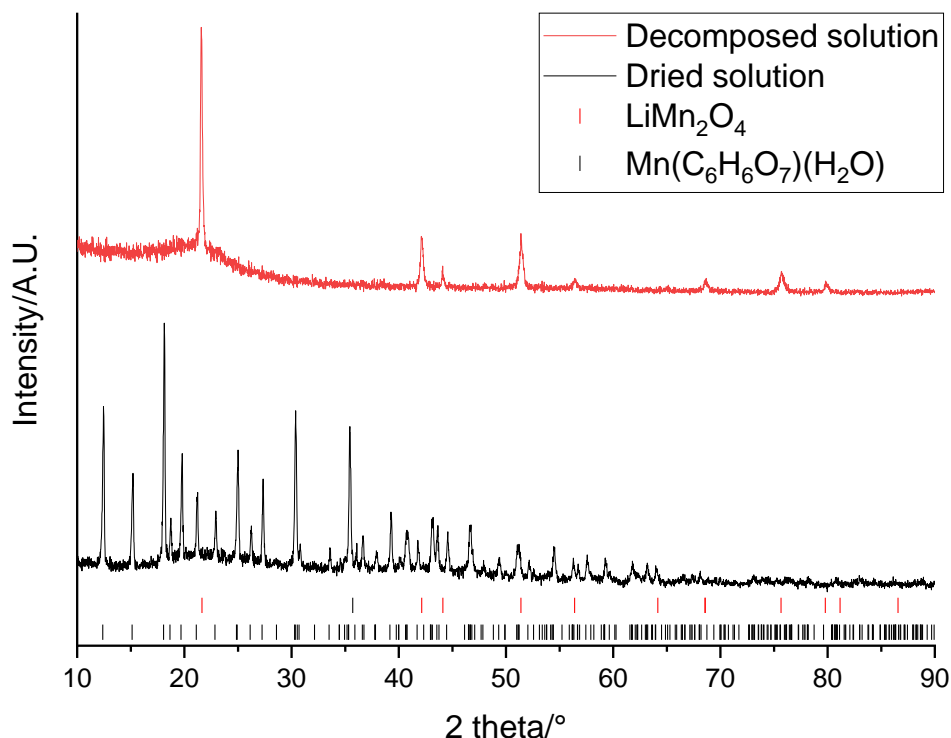
Figure 3-5: XRD patterns of 1.25 M citric acid leaching solution when dry (black) and after heating to 700 °C for 12 hrs (red) ($\lambda = 1.79$ Å). Tick marks correspond to $LiMn_2O_4$ (red) and $Mn(C_6H_6O_7)(H_2O)$ (black).

Further experiments were then performed to investigate this leaching process in more detail. 0.1, 0.2, 0.3 and 0.4 g of LMO were placed into 10 mL of 1 M citric acid (corresponding to 10, 20, 30 and 40 g/L) at 30, 40, 50, 60 and 70 °C to investigate the influence of both S:L ratio and solution temperature upon the leaching time. Table 3-2 shows the time taken to leach LMO under these different conditions. For the lower S:L ratios (10, 20 and 30 g/L), as the leaching temperature increases, the leaching time decreases. This is due to the increased temperature causing the reaction rate to increase. Furthermore, as the S:L ratio increases, the leaching time increases. This is due to the increased solid amount causing the leaching processes to take longer to reach completion.

Table 3-2: Time taken to completely leach 0.1, 0.2, 0.3 and 0.4 g LMO from 10 mL of 1 M citric acid solution at 30, 40, 50, 60 and 70 °C (solutions were stirred at 100 rpm). Ppt indicates that the Mn citrate precipitate was formed.

	Time taken to leach LMO at different S:L ratios/mins			
Temperature/°C	**10 g/L**	**20 g/L**	**30 g/L**	**40 g/L**
30	>60	>60	>60	ppt
40	14	16	17	ppt
50	4.10	4.30	5.00	ppt
60	2.40	3.00	3.50	ppt
70	1.20	1.40	ppt	ppt

For 40 g/L the leaching behaviour is different, and a precipitate is formed at every temperature. Figure 3-6 shows that the XRD pattern of this precipitate matches to Mn citrate compounds. This shows that at higher S:L ratios, the Mn citrate is precipitated out of solution. It is possible that the 30 g/L 70 °C sample may have precipitated due to the higher temperature causing an increased amount of water evaporation from the solution which would have consequently led to the S:L ratio being altered. In future studies, the beaker was covered with a lid to reduce evaporation from the solution.
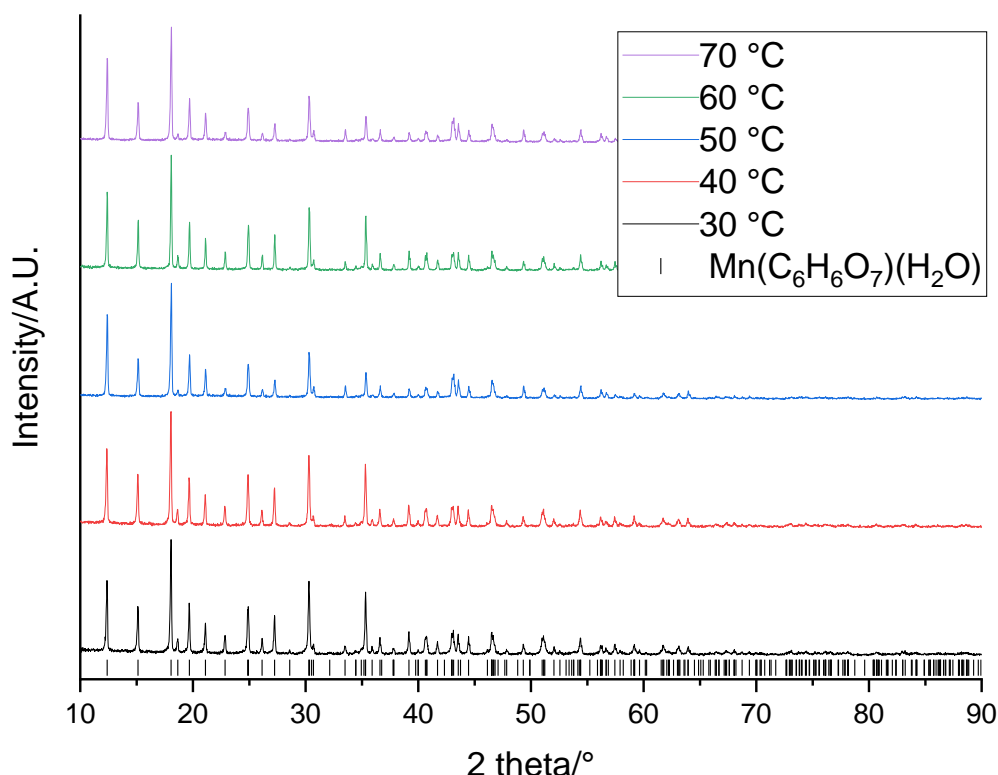
Figure 3-6: XRD patterns of precipitate formed when 40 g/L LMO was added to 1 M citric acid at 30 (black), 40 (red), 50 (blue), 60 (green) and 70 °C (purple) (λ = 1.79 Å). Tick marks correspond to $Mn(C_6H_6O_7)(H_2O)$ (black).

A pH study was performed to identify whether pH was an important factor in accounting for the precipitation at higher S:L ratios. Table 3-3 shows the pH study performed on a range of S:L ratios in 10 mL of 1 M citric acid solution at 60 °C. The 40 g/L sample formed a precipitate (as seen in experiments above) and the leaching solution had a pH of 3. The lower S:L ratios did not precipitate out and the solutions all had pH values below 3. A sodium hydroxide solution was added dropwise to these solutions to see if the precipitate would form. For both 20 and 30 g/L, once the pH was adjusted to 3 the precipitate formed. This suggests that the presence of the precipitate is linked to the pH of the solution, with the Mn citrate precipitate only being formed above pH 3. The first dissociation reaction of citric acid occurs at pH 3.13 therefore it seems likely that

at around pH 3 $MnH_{14}C_{12}O_{14}$ is formed and this then precipitates out of the solution.[6]

The 10 g/L solution did not precipitate even once the pH had reached beyond 5, which could be due to there being insufficient Mn present for the precipitate to form.

Table 3-3: pH study performed on 0.1, 0.2, 0.3 and 0.4 g LMO in a 10 mL of 1 M citric acid solution at 60 °C

S:L ratio in g/L	Precipitation?	pH when completely leached	pH when precipitated
10	No	1	-
20	No	2	3
30	No	2/3	3
40	Yes	-	3

The leaching experiments were then repeated at a lower acid concentration (0.5 M) at 60 and 70 °C, as these temperatures provided the fastest leaching times at 1 M. Table 3-4 shows that the same trends in leaching time were seen for 10 and 20 g/L (faster leaching times with higher temperature and smaller S:L ratio). However, for 30 g/L, the leaching was not complete and there was visible powder remaining in the solution. This suggests that for higher S:L ratios, a higher acid concentration must be used to ensure that all the solid is leached into solution.

Table 3-4: Time taken to completely leach 0.1, 0.2 and 0.3 g LMO from 10 mL of 0.5 M citric acid solution at 60 and 70 °C. Incomplete leaching indicates that there was some powder visibly left in the solution.

	Time taken to leach at different S:L ratios/mins		
Temperature/°C	**10 g/L**	**20 g/L**	**30 g/L**
60	3.48	5.01	Incomplete leaching
70	1.49	3.00	Incomplete leaching

Going forward, this leaching study has shown that the optimum conditions for leaching LMO using a citric acid solution are 30 g/L with 1 M acid at 60 °C. This is to achieve the fastest leaching time with the maximum amount of solid sample. These conditions also facilitate leaching without the formation of the Mn citrate precipitate. The Mn citrate precipitate would create extra complexity for the separation of mixed cathodes as it would require further separation steps to separate the precipitate from the remaining cathode material.

3.4. Characterisation of QC and EOL cathode material

Cathodes from two different sources were investigated in this thesis. One cathode was from a quality control (QC) rejected cell obtained from Gen 1 Nissan Leaf. The reason why the cell failed the quality control check was not given. This is representative of manufacturing scrap, which is already a major feedstock for commercial recyclers.[12] The other cathode was from an end-of-life (EOL) Nissan Leaf (Gen 1, 2011 model, 40,000 miles). This is representative of end-of-life material that is going to become widely available as the number of EVs rapidly increases. Characterisation of these cathodes was performed using XRD, SEM-EDX and ICP-OES.

Pristine Gen 1 Nissan Leaf cells are rated at 32.5 Ah and contain 17 double-sided cathode layers and 18 double-sided anode layers. Testing by the University of Newcastle has shown that the EOL cells have a reduced capacity of around 28.1 Ah (there is variation in the capacity depending on the orientation of the cell in the module).[13] The QC rejected cells were not tested but it can be assumed that they will have a similar capacity to the pristine cells.

Figure 3-7 shows the XRD patterns of the cathodes which both contain a mixture of LMO ($Fd\bar{3}m$ space group) and a layered oxide (LO; $R\bar{3}m$ space group). The LO is likely to be $LiNi_vMn_xCo_yAl_zO_2$ (where v + x + y + z = 1) but the exact composition cannot be identified using XRD alone. Previous work has reported the LO phase in these cells as NCA.[4] The cathodes also contain a graphitic phase, which could either be due to migration from the anode or due to conductive carbon additives. The EOL cathode produces peaks that are much less intense than the QC cathode, which could be due to a decrease in crystallinity of the active material due to degradation. Rietveld

refinement analysis shows that the cathodes contain around 60 wt% LMO and 20-30 wt% LO (Appendix A, Table 3-5). Both the LMO and LO phases have lattice parameters similar to those reported in the literature.[14–16] The EOL cathode contains more graphite which again could be due to a decrease in the cathode crystallinity (the weight percent is only applicable to crystalline phases and does not include the amorphous carbon/binder added during coating).
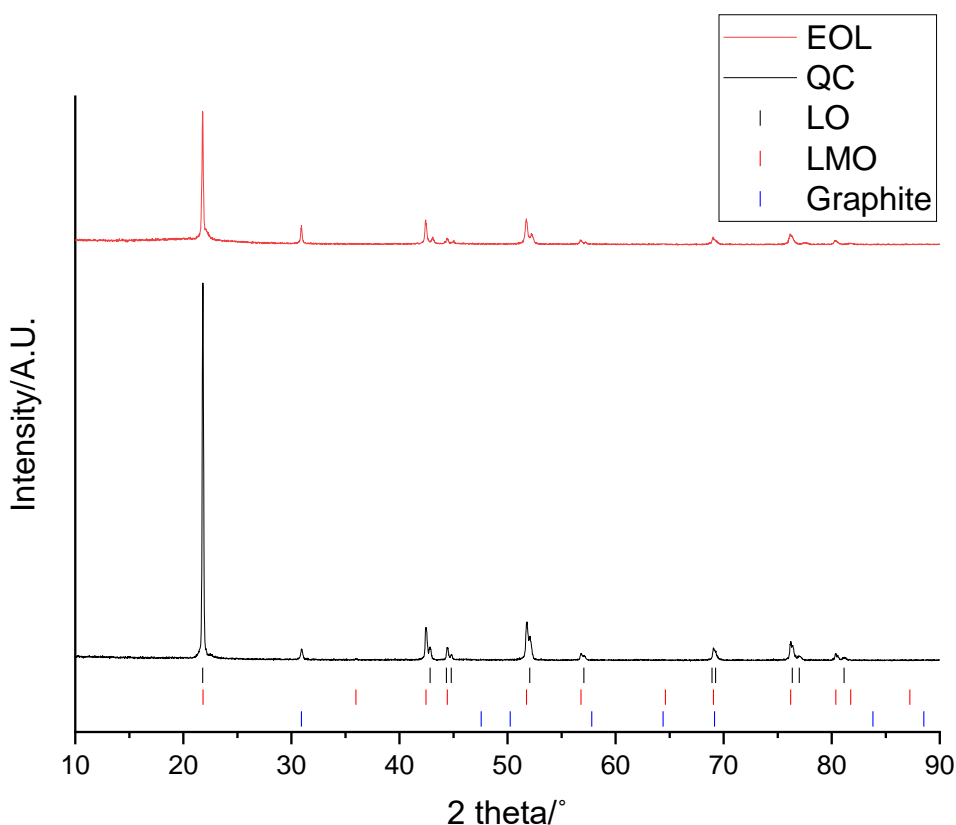
Figure 3-7: XRD patterns of QC (black) and EOL (red) cathodes (λ = 1.79 Å). Tick marks correspond to LO (black), LMO (red) and graphite (blue).

Table 3-5: Lattice parameters and weight percentages of phases in QC and EOL cathodes.
R_{wp} = 12.86, 12.82% and GOF = 1.30, 1.23, respectively.

		Cathodes	
Phase		**QC**	**EOL**
LMO	a/Å	8.2043(3)	8.2083(4)
LO	a/Å	2.8750(3)	2.8594(5)
LO	c/Å	14.236(1)	14.263(1)
LMO	wt%	57.0(1)	61.9(1)
LO	wt%	30.2(7)	18.3(5)
Graphite	wt%	12.8(1)	19.8(1)

SEM images of the cathodes show that the surfaces consist of particles of active material (Figure 3-8). The particles on the EOL cathode appear to consist of agglomerations of smaller particles, which may be due to the particles cracking during cycling. There are no visible mechanical failures on the surface of either cathode. For both cathodes, the EDX images show that high levels of Mn are present over the majority of surface apart from some regions where there is lower Mn and higher Ni levels. The regions of high Mn content correspond to areas that are rich in the LMO phase while regions of high Ni content correspond to areas that are rich in the LO phase.
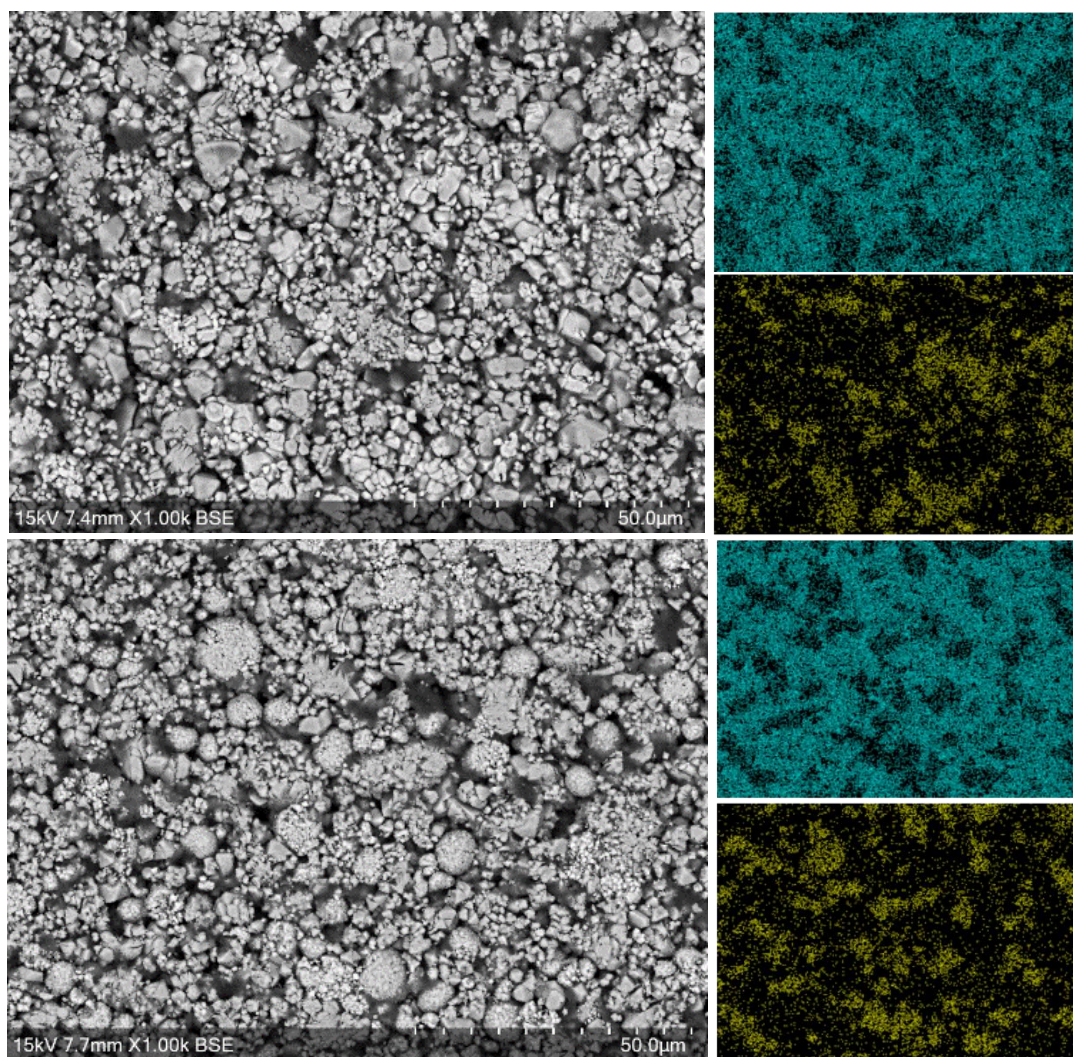
Figure 3-8: SEM (left) and EDX (right) images of the QC (top) and EOL (bottom) cathodes. EDX images show Mn (teal, top) and Ni (yellow, bottom).

ICP-OES analysis of the digested cathodes shows that both cathodes contain Li, Ni, Mn, Co and Al. The QC cathode also contains a trace amount of Cu. The QC cell was discharged to a lower voltage (<1 V) which results in Cu dissolution from the anode current collector, and then re-precipitation throughout the cell. Table 3-6 shows that the EOL cathode has a higher ratio of TM to Li and therefore it is Li deficient compared to the QC cathode. This is probably due to degradation resulting in Li loss from the EOL cathode material. The QC cell was discharged to <1 V and therefore can be assumed to be fully discharged (e.g. the cathode will be fully lithiated) whereas the

EOL cell was discharged to 3.73 V and therefore will not be fully discharged (e.g. the cathode will not be fully lithiated). However, this accounts for <10% of the Li being in the anode.[17,18] Taking this into account, the EOL cathode still has a serious Li deficiency compared to the QC cathode. Both cathodes contain similar ratios of metals, although the EOL cathode does contain around double as much Co as the QC cathode. This could be due to the cathode formulation changing in the time between manufacture of the two cells. Note, before ICP-OES analysis, the samples were put in NaOH to remove the Al current collector before being digested and therefore there could be trace amounts of Al present due to incomplete removal of the current collector.

Table 3-6: ICP-OES analysis of QC and EOL cathodes (units are mol:mol)

Cathode	Li:TM	Ni:Mn:Co:Al(:Cu)
QC	1:1.597	0.183:0.761:0.023:0.031(:0.001)
EOL	1:1.913	0.189:0.739:0.048:0.025

It is not possible to work out the stoichiometry of the LMO or LO phases from the ICP-OES results alone, as ICP-OES does not distinguish which metals are present in which phase. However, if you assume that all the Mn is present in the LMO phase, an approximate stoichiometry of the LO phase can be calculated using the ICP-OES results. The QC cathode has a molar ratio of 0.77:0.10:0.13 and the EOL cathode has a molar ratio of 0.72:0.18:0.09 (Ni:Co:Al). This again shows that the EOL cathode contains around double as much Co as the QC cathode.

Overall, this characterisation shows that the QC and EOL Nissan Leaf cathodes both contain of a mixture of LMO and a LO. The cathodes contain 60 wt% LMO and 20-30 wt% LO along with a graphitic phase. SEM-EDX images show that the Mn and Ni

occupy distinct regions in the cathode, corresponding to discrete areas of LMO and LO respectively. The QC and EOL cathodes appear to have similar ratios of metals, although the EOL cathode is significantly more Li deficient which is probably due to degradation.

3.5. Citric acid leaching of $LiMn_2O_4$ from mixed cathode materials

Citric acid was investigated as a leaching agent to leach LMO from the QC and EOL cathodes. Initial tests were performed using 0.3 g of cathode material in 10 mL of citric acid solution at 50 °C. Figure 3-9 shows XRD patterns of the QC cathode taken at intervals throughout the leaching process. They show that the LMO phase is completely leached from the cathode after 20 minutes of leaching. This is indicated by the peaks at 42.4˚, 51.8˚ and 56.8˚ no longer being present. As the leaching time is increased, the peaks corresponding to LMO decrease in intensity showing that there is increased LMO leaching with time. The peaks corresponding to the LO phase remain throughout showing that the LO is not leached into solution.
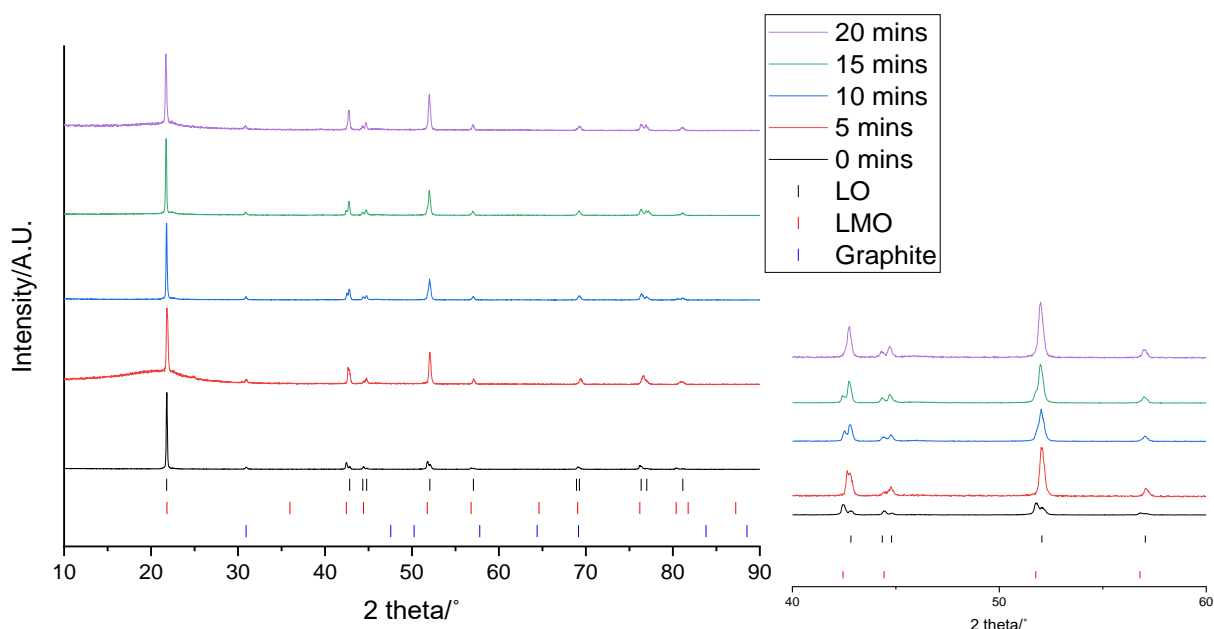
Figure 3-9: XRD patterns of 0.3 g QC cathode after leaching in 10 mL of 1 M citric acid for 0 (black), 5 (red), 10 (blue), 15 (green) and 20 minutes (purple) (λ = 1.79 Å). Tick marks correspond to LO (black), LMO (red) and graphite (blue).

The leaching of the EOL cathode was investigated in the same way. The EOL cathode shows similar leaching behaviour with the LMO phase being completely leached by 20 minutes (Figure 3-10). This indicates that even after extensive cycling, LMO can be leached from the cathode material. However, in comparison to the QC cathode, the XRD patterns show an additional shoulder on the peak at 21°. Extensive cycling of LO can lead to a transformation from a layered structure to a rocksalt structure, however this extra peak does not match to a rocksalt phase.[19] Instead this shoulder can be attributed to the presence of an additional LO phase being present. This additional LO phase has a = 2.8829(1) Å and c = 13.986(3) Å. The c value is significantly lower than the original LO phase suggesting that it may be a Li-deficient LO.[20] This suggests that cell degradation due to extensive cycling has resulted in formation of a Li-deficient LO phase. Alternatively, this phase may rise from loss of Li during formation of the anode SEI.
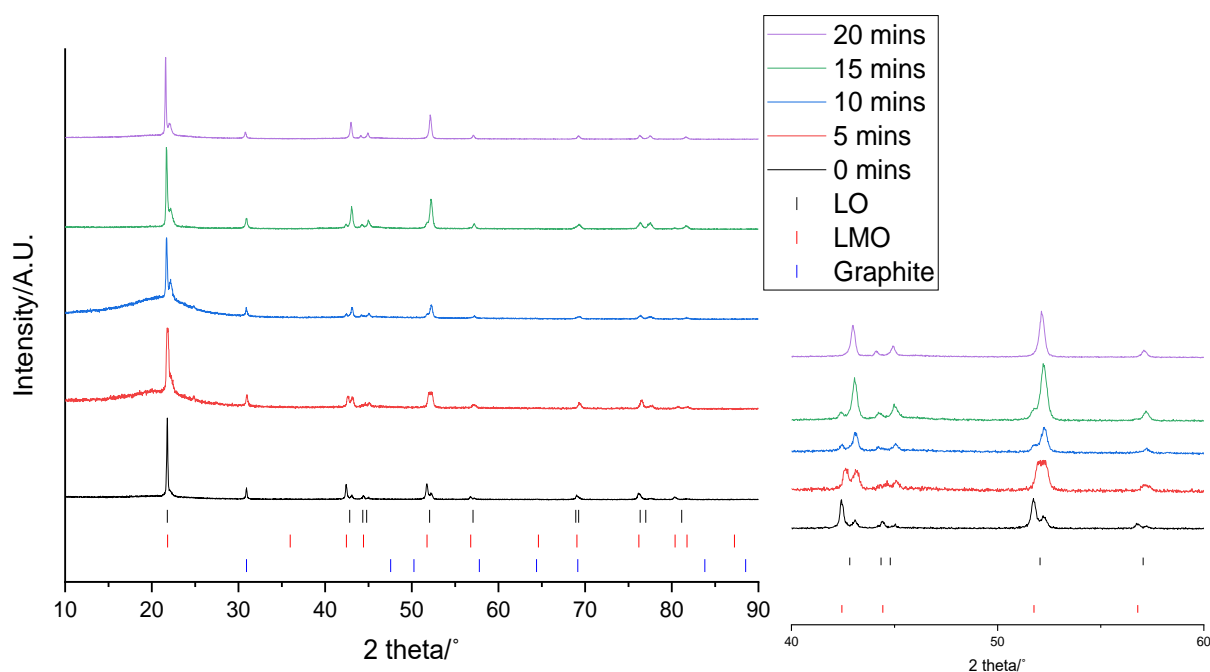
Figure 3-10: XRD patterns of 0.3 g EOL cathode after leaching in 10 mL of 1 M citric acid for 0 (black), 5 (red), 10 (blue), 15 (green) and 20 minutes (purple) (λ = 1.79 Å). Tick marks correspond to LO (black), LMO (red) and graphite (blue).

In summary, the XRD patterns suggests that citric acid has the capability to selectively leach LMO from the cathode material. Meanwhile, the LO phase remains in the cathode material as a solid.

3.5.1. Optimisation of the leaching process

Next the acid concentration, acid temperature and S:L ratio were varied to investigate the impact that these conditions have on the leaching process. As mentioned in the introduction (section 3.1.), these factors normally affect the leaching rate and efficiency. An optimised set of conditions will then be taken forward for further analysis.

In these studies, XRD and ICP-OES were used to probe the leaching behaviour. XRD analysis was performed on the cathodes and ICP-OES analysis on the leaching

solution at set intervals. Weight percentages obtained from structure refinements using the XRD data were then used to calculate the percentage of LO present in the active material, where active material corresponds to the LO and LMO phases. As the LMO phase is leached into solution there is a lower amount present in the cathode and therefore the percentage of LO present increases. The percentage of active material was used as the graphite phase is also present in the cathode material, although its amount should remain constant. The XRD patterns are included in Appendix B. All the ICP-OES results are included in the text apart from the results for the Cu concentration which are in Appendix C. Additional results showing the percentage of LMO present in the active material are contained in Appendix D.

3.5.1.1.   Investigating acid concentration

Citric acid concentrations of 0.5 M, 0.75 M and 1 M were used with the same temperature and S:L ratio (50 °C and 30 g/L).

Figure 3-11 shows the percentage of LO in the active material at set intervals. Both cathodes show increased LMO leaching with time, which is indicated by the percentage of the LO increasing. A LO percentage of 100% indicates that all the LMO has been leached from the cathode. There are a couple of outlier points where the LO percentage seems to decrease (QC 0.75 M 15 minutes and EOL 0.5 M 20 minutes). These results are unusual as it suggests that the LMO is going back into the cathode material, and so these anomalous points suggest that there could be issues with analysing the leaching progress using XRD. The cathode was cut into small pieces before leaching, and XRD was performed on some of these pieces, therefore these pieces maybe not be representative of the whole sample being leached. ICP-OES

analysis was performed on the entire leaching solution and therefore is a more representative technique.
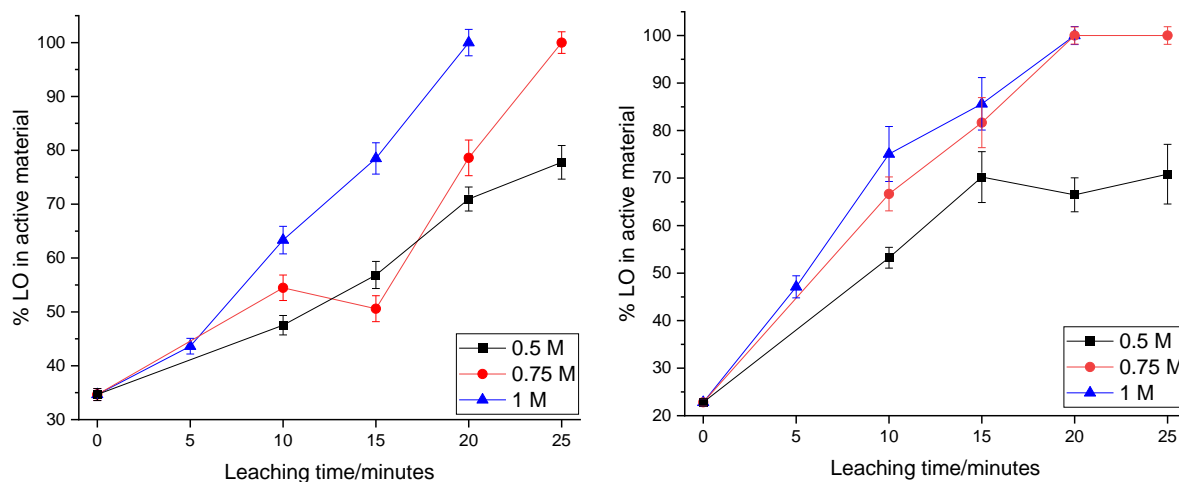
Figure 3-11: Percentage of LO in the active material in the QC (left) and EOL (right) cathodes at different leaching times when using 0.5 M (square), 0.75 M (circle) and 1 M (triangle) acid concentration at 50 °C and 30 g/L S:L ratio. Error bars were calculated by combining the uncertainty from refinement results.

In Figure 3-11 (left), the results for the QC cathode show that as the acid concentration increases, the lines (% LO left vs time) become steeper indicating that the leaching rate increases. This is expected as an increased acid concentration means that a larger number of citrate ions are present in solution to chelate to the Li and Mn and therefore leach the LMO into solution. For the 1 M solution, the LMO is completely leached into solution in 20 minutes, as shown by the LO percentage being 100%. At 0.75 M it takes 25 minutes and for 0.5 M there is still LMO present in the cathode even after 25 minutes of leaching.

The results for the EOL cathode do not show a clear trend between acid concentration and leaching rate (Figure 3-11 right). Once the errors are considered, the leaching rates for the 1 and 0.75 M acid concentrations appear very similar and, in both cases,

the LMO is completely leached into solution by 20 minutes. The 0.5 M citric acid does appear to be slower at leaching and has LMO present in the cathode after 25 minutes. For 1 and 0.5 M the times for complete leaching of the LMO phase are the same as for the QC cathode. At 0.75 M, the LMO is leached faster from the EOL than the QC cathode. Overall, the acid concentrations have less effect on the leaching rate for the EOL cathode which could be due to degradation of the cathode influencing the leaching behaviour.

Figure 3-12 shows the concentration of Mn and Li present in solution at various times. It shows that there is increased concentrations of Mn and Li present in solution as time increases. This shows that more LMO is present in solution, matching to the results from the XRD data. This trend is the same for all the acid concentrations. The ICP-OES results show the same trend for all the points indicating that the outlier points in Figure 3-11 are anomalous. The Mn concentration reaches a plateau at longer times showing that a point is reached where all the Mn has been leached into solution and this corresponds to a point where all the LMO is in solution. The Mn concentration reaches a maximum of 11,400 ppm while the Li concentration reaches a maximum of 880 ppm. This gives a Mn:Li molar ratio of 1:0.61. The likely Mn:Li ratio in LMO is 1:0.5 to enable charge balancing, and this therefore suggests that any additional Li being leached is likely to be removed from the LO phase. The maximum Mn/Li concentrations are around what would be expected assuming that 0.3 g of the cathode contains 60 wt% LMO (Table 3-5). The final concentration of Mn and Li in solution is similar for all the acid concentrations suggesting that they have a similar leaching efficiency. Further analysis will be done in section 3.5.2. to investigate the efficiency of the leaching process.
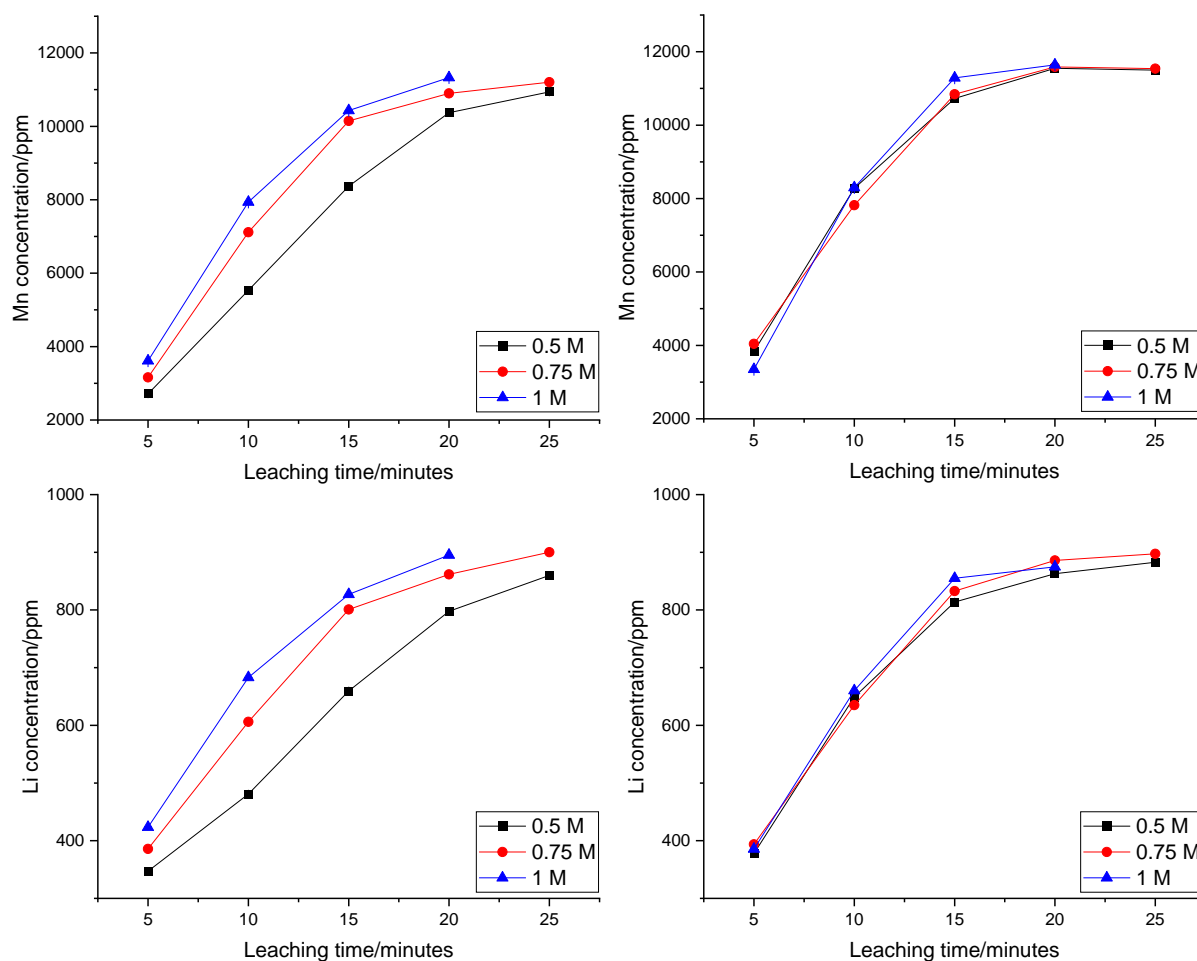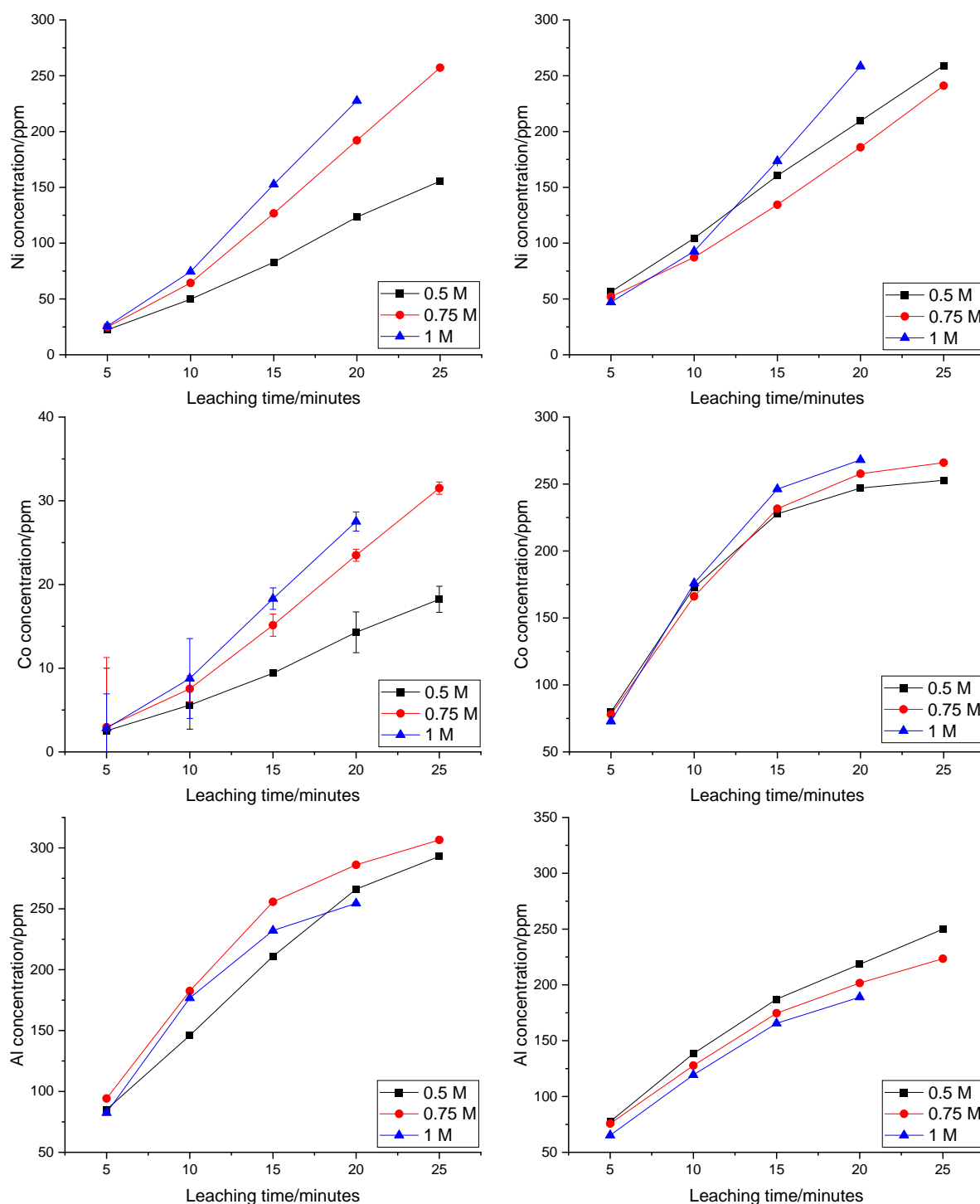
Figure 3-12: ICP-OES results showing the concentration of Mn (top) and Li (bottom) in solution at different leaching times for the QC (left) and EOL (right) cathodes with 0.5 M (square), 0.75 M (circle) and 1 M (triangle) acid concentration. Error bars show the relative standard deviation across 3 repeats and are on the order of the point size so cannot be seen.

For the QC cathode, higher acid concentrations result in steeper lines for both the Mn and Li concentrations, indicating faster leaching rates (Figure 3-12 left). This matches to the trends shown with the XRD analysis. The Mn concentration reaches a maximum at the same times shown in Figure 3-11 (20 minutes for 1 M and 25 minutes for 0.75 M), although, additional ICP points could be examined to confirm that there are no further increases in concentration. While the Mn concentration reaches a plateau, the

Li concentration has an upwards trajectory which could indicate that Li is leached from the LO phase at longer leaching times.

In contrast, Figure 3-12 (right) shows that the EOL cathode has similar concentrations of Mn and Li in solution for all the acid concentrations at each of the times. This suggests that there are similar leaching rates for the different acid concentrations. This differs from the XRD results which showed that 0.5 M had a slower leaching rate. This again suggests that XRD is not the best method for analysis as it is not capturing the entire picture. While 1 M citric acid appears to have a maximum Mn concentration at 20 minutes, so do 0.5 and 0.75 M which differs from the XRD results. It suggests that the EOL cathode degradation could be altering the leaching process. The degradation could cause the LMO particles to have weaker binding to the cathode and therefore enables them to have facile leaching regardless of acid concentration. Alternatively, it could be that there are inconsistencies between the different cathode samples used for the different acid concentrations or there could be differences between the two cathodes to begin with.

Initial ICP-OES analysis of the cathodes showed that there was also Ni, Co, Al and Cu present (section 3.4.). Figure 3-13 shows the concentration of these additional elements in solution (note Cu results are in Appendix C as the amount present is so small). It shows that Ni, Co and Al is leached from the LO phase along with the Li and Mn from the LMO phase. It is worth noting that an assumption is made that the LO contains the Ni, Co and Al. However, it is possible that the LO contains a small amount of Mn or that there is Ni present in the LMO phase.[21,22] Furthermore, it is also possible that the Al is leached from the current collector rather than the LO phase. This shows

114

that while the citric acid is more selective for LMO, it does leach small amounts of metals from the LO phase. Potential reasons for the selectivity will be explored in section 3.5.3.. Figure 3-13 also shows that there are increasing concentrations of Ni, Co and Al present in solution with increased leaching time. The Ni, Co and Al concentrations all have an upwards trajectory suggesting that they would continue to leach if the cathode was left in the acid for longer times.

Figure 3-13: ICP-OES results showing the concentration of Ni (top), Co (middle) and Al (bottom) in solution at different leaching times for the QC (left) and EOL (right) cathodes with 0.5 M (square), 0.75 M (circle) and 1 M (triangle) acid concentration. Error bars show the relative standard deviation across 3 repeats and are on the order of the point size so cannot be seen in all cases.

The QC cathode shows that higher acid concentrations result in steeper lines for both Ni and Co, indicating faster leaching rates (Figure 3-13 left). The Al lines are less distinct suggesting that Al leaching is less affected by acid concentration. The Ni concentrations reach a maximum of 250 ppm, the Co concentrations reach a maximum of 30 ppm and the Al concentrations reach a maximum of 300 ppm. While these are significant amounts in solution, the concentrations are much lower than the Mn and Li concentrations showing that the majority of leaching is from the LMO phase. 1 M acid results in the highest concentration of Ni and Co in solution at 20 minutes. However, 0.75 M acid at 25 minutes, which is necessary to leach all the LMO, has higher Ni and Co concentrations than 1 M at 20 minutes. Overall, the results suggest that leaching in 1 M acid is the optimum to achieve complete LMO leaching with minimum leaching from the LO phase.

Figure 3-13 (right) shows that the EOL cathode does not show a clear trend in increased Ni/Co/Al leaching with increased acid concentration. Potential reasons for this are mentioned above in relation to the Mn and Li concentration. Interestingly, although the concentration of Ni and Al in solution is similar to the QC cathode (250 ppm in both cases), the concentration of Co in solution is significantly higher (275 ppm vs 30 ppm). Further work is required to identify the reasons for the increased Co leaching.

In conclusion, to achieve leaching with the fastest rate the results suggest that an acid concentration of 1 M should be used. This results in complete leaching of the LMO phase by 20 minutes. The different acid concentrations all leach similar amounts of Mn and Li. There are also low levels of leaching of Ni, Co and Al from the LO phase. The QC cathode shows the least Ni, Co and Al leaching at 0.5 M acid concentration

however, 0.5 M does not fully leach the LMO into solution. When comparing 1 and 0.75 M acid concentrations, 1 M results in less Ni, Co and Al leaching at 20 minutes than 0.75 M at 25 minutes. Therefore, a 1 M acid concentration is preferable for both rate and selectivity reasons. The EOL cathode shows no pattern in the Ni, Co and Al leaching for the different acid concentrations. Therefore, in the interest of adopting a recycling process that is viable for multiple different input streams, a 1 M acid concentration is the optimum to ensure fast, efficient, and selective leaching of both the QC and EOL cathodes.

3.5.1.2. Investigating acid temperature

Next, temperatures of 50 °C, 60 °C and 70 °C were used with the same acid concentration and S:L ratio (1 M and 30 g/L).

Figure 3-14 shows the percentage of LO in the active material at set intervals. For the acid temperature studies, the QC and EOL cathodes show similar behaviour. Both cathodes show increased LMO leaching with time. Both cathodes also show that as the acid temperature increases, the lines become steeper and therefore the leaching rate increases. The dissociation process of citric acid is endothermic, therefore as the temperature increases this dissociation is favoured.[2] This means at higher temperatures, there are more citrate ions present to leach the Mn and Li into solution. At 50 °C the LMO is completely leached into solution by 20 minutes, at 60 °C it takes 15 minutes and at 70 °C it takes 10 minutes. Interestingly, acid temperature has an influence upon the leaching rate for the EOL cathode whereas acid concentration did not.
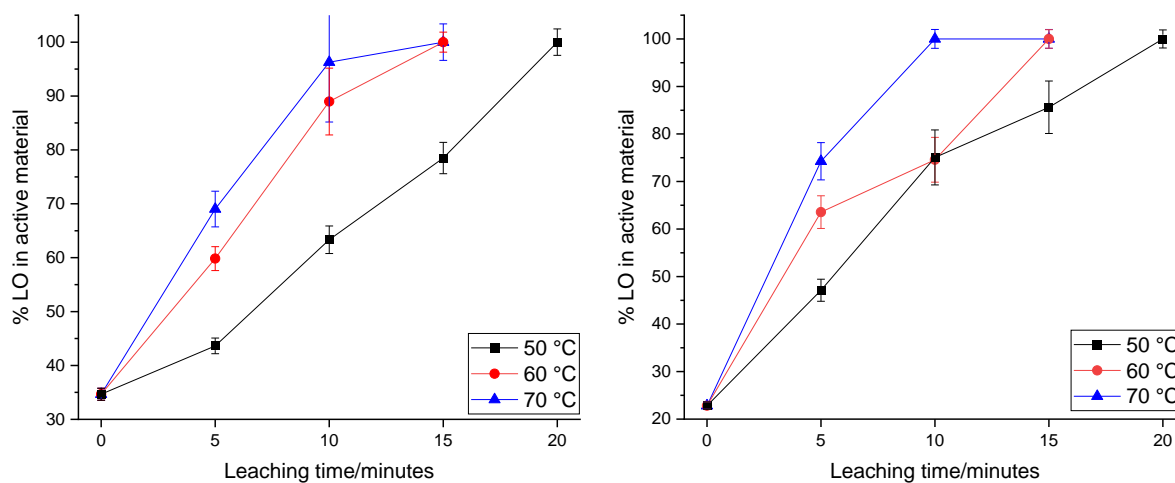
Figure 3-14: Percentage of LO in the active material in the QC (left) and EOL (right) cathodes at different leaching times when using 50 °C (square), 60 °C (circle) and 70 °C (triangle) 1 M citric acid and 30 g/L S:L ratio. Error bars were calculated by combining the uncertainty from refinement results.

However, after 15 minutes at 70 °C, there was a precipitate present in the solution. Figure 3-15 shows the XRD patterns of the cathodes which has the precipitate present on the surface. The precipitate matches to the Mn citrate mentioned previously in section 3.3.2.. The precipitate is therefore due to Mn precipitating out of solution. This poses an issue as all the Mn is no longer in solution for subsequent steps. Furthermore, additional steps are then required to separate the precipitate from the solid LO phase. This shows that the leaching should be performed with temperatures below 70 °C to avoid this issue, as the precipitate was not present at lower temperatures.
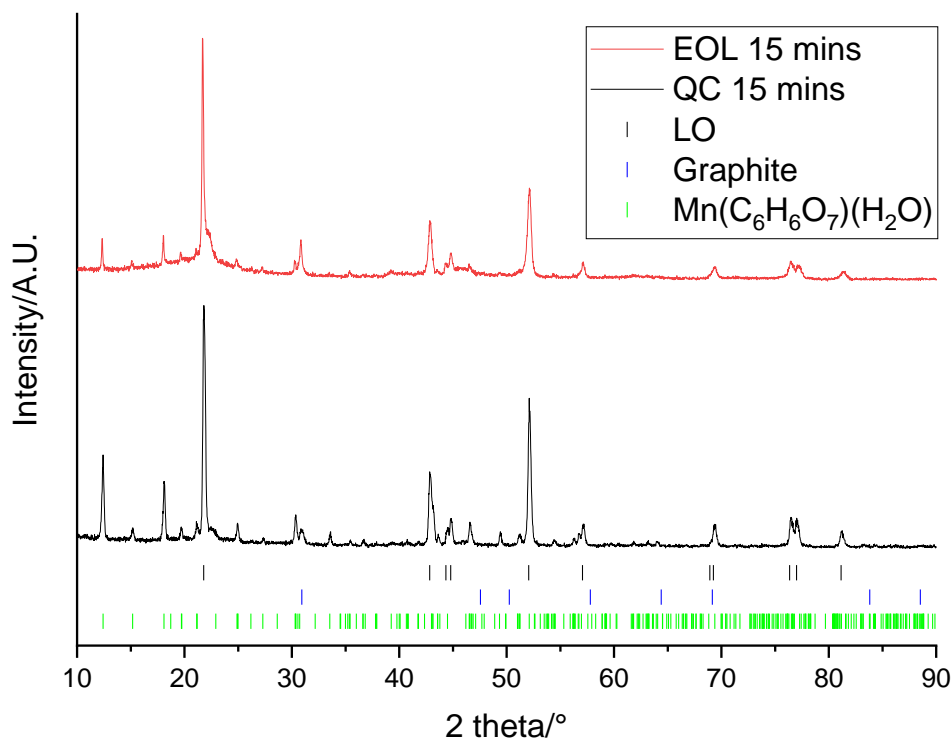
Figure 3-15: XRD patterns of QC (black) and EOL (red) cathodes after leaching for 15 minutes at 70 °C (λ = 1.79 Å). Tick marks correspond to LO (black), graphite (blue) and Mn(C₆H₆O₇)(H₂O) (green).

Figure 3-16 shows the concentration of Mn and Li present in solution at various times. It shows that there is an increased concentration of Mn and Li present in solution as time increases showing that more LMO is present in solution. However, the Mn concentration drops after 20 minutes at 70 °C. This can be attributed to precipitation of Mn citrate from solution which causes the Mn concentration in solution to decrease. The precipitation is visible at 15 minutes in the XRD patterns therefore there is a delay between when the precipitation is visible via the two techniques. ICP-OES samples are taken at the exact time whereas XRD samples must be filtered and therefore will have an associated delay between when the samples are taken and when the sample is separated from solution. 60 °C also shows a decrease in the Mn concentration at 20

minutes suggesting that precipitation may also be an issue at this temperature (this precipitation may not have been seen by XRD as samples were not taken at 20 minutes for this temperature).
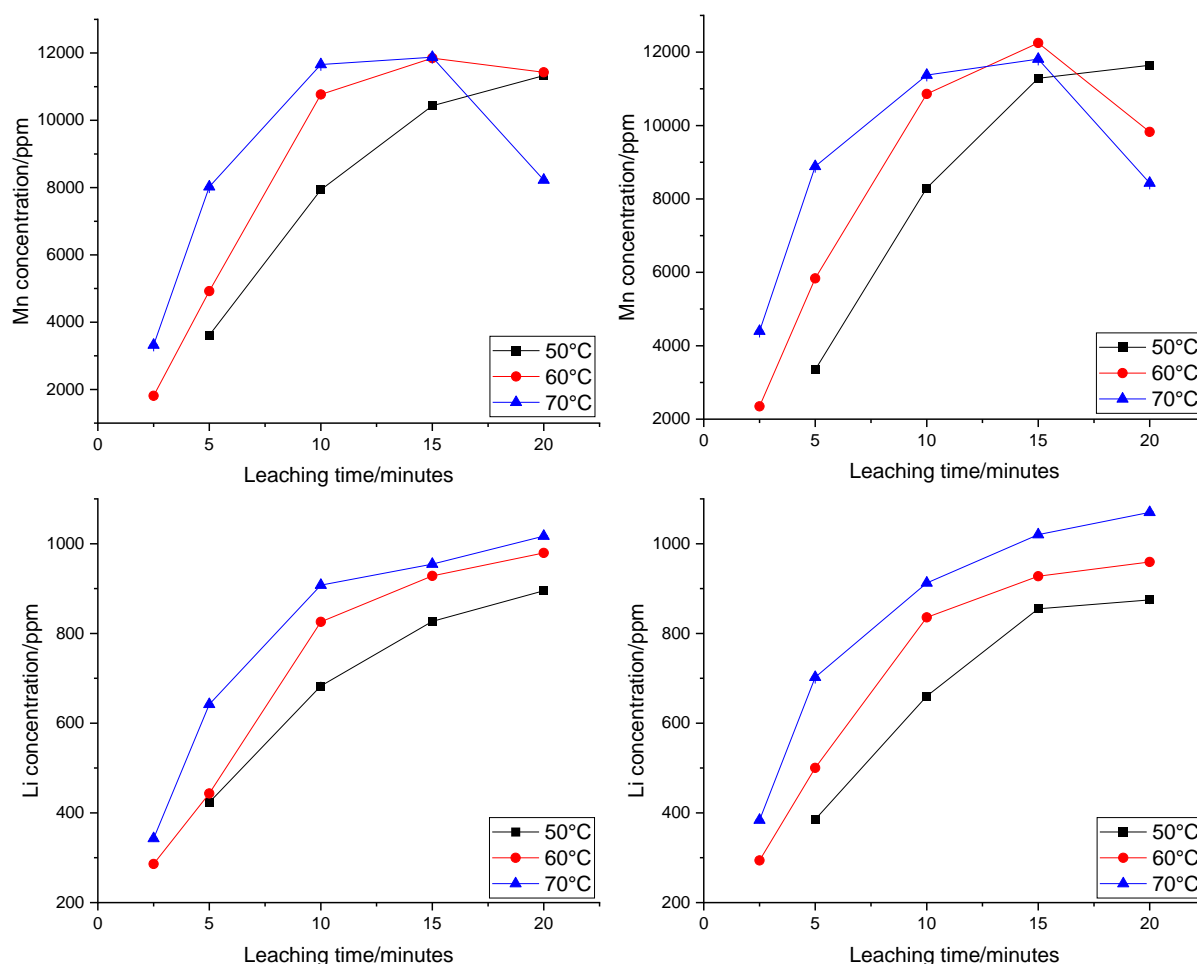
Figure 3-16: ICP-OES results showing the concentration of Mn (top) and Li (bottom) in solution at different leaching times for the QC (left) and EOL (right) cathodes with 50 °C (square), 60 °C (circle) and 70 °C (triangle) acid temperature. Error bars show the relative standard deviation across 3 repeats and are on the order of the point size so cannot be seen.

As with the XRD data, Figure 3-16 shows that the QC and EOL cathodes both have the same trend with increased acid temperature resulting in increased leaching rate. The Mn concentration reaches a maximum at the same times shown in Figure 3-14 (10 minutes for 70 °C, 15 minutes for 60 °C and 20 minutes for 50 °C). However, the

maximum Mn concentrations for the higher temperatures are slightly higher than the maximum concentrations for 50 °C. This could be due to leaching of some Mn from the LO phase or due to small differences in the samples used for each temperature or simply increased solubility at higher temperatures. The concentration of Li in solution is higher at higher temperatures. It reaches 1050 ppm for 70 °C and 960 ppm for 60 °C compared to only 880 ppm for 50 °C. This indicates that more Li is being leached from the LO phase at higher temperatures.

Figure 3-17 shows the concentration of the additional elements in solution. As before, there are increased concentrations of Ni, Co and Al present in solution with increased leaching time, with increasing the acid temperature resulting in faster leaching rates, although the differences between acid temperatures appears much more significant than the changes seen between different acid concentrations (Figure 3-13). This therefore indicates that the leaching process is significantly less selective towards LMO over the LO at higher temperatures. While the QC and EOL cathodes show the same trends, the maximum concentrations of Ni, Co and Al present in solution differs. At 70 °C, the EOL cathode has higher maximum concentrations than the QC cathode, which agrees with the proposal that degradation allows for more facile leaching. The Ni, Co and Al concentrations all have an upwards trajectory suggesting that they would continue to leach in significant amounts from the LO phase if the cathode was left in the acid for longer times. This suggests that 50 °C is the optimum temperature to minimise leaching from the LO phase and retain the selectivity for the LMO component.
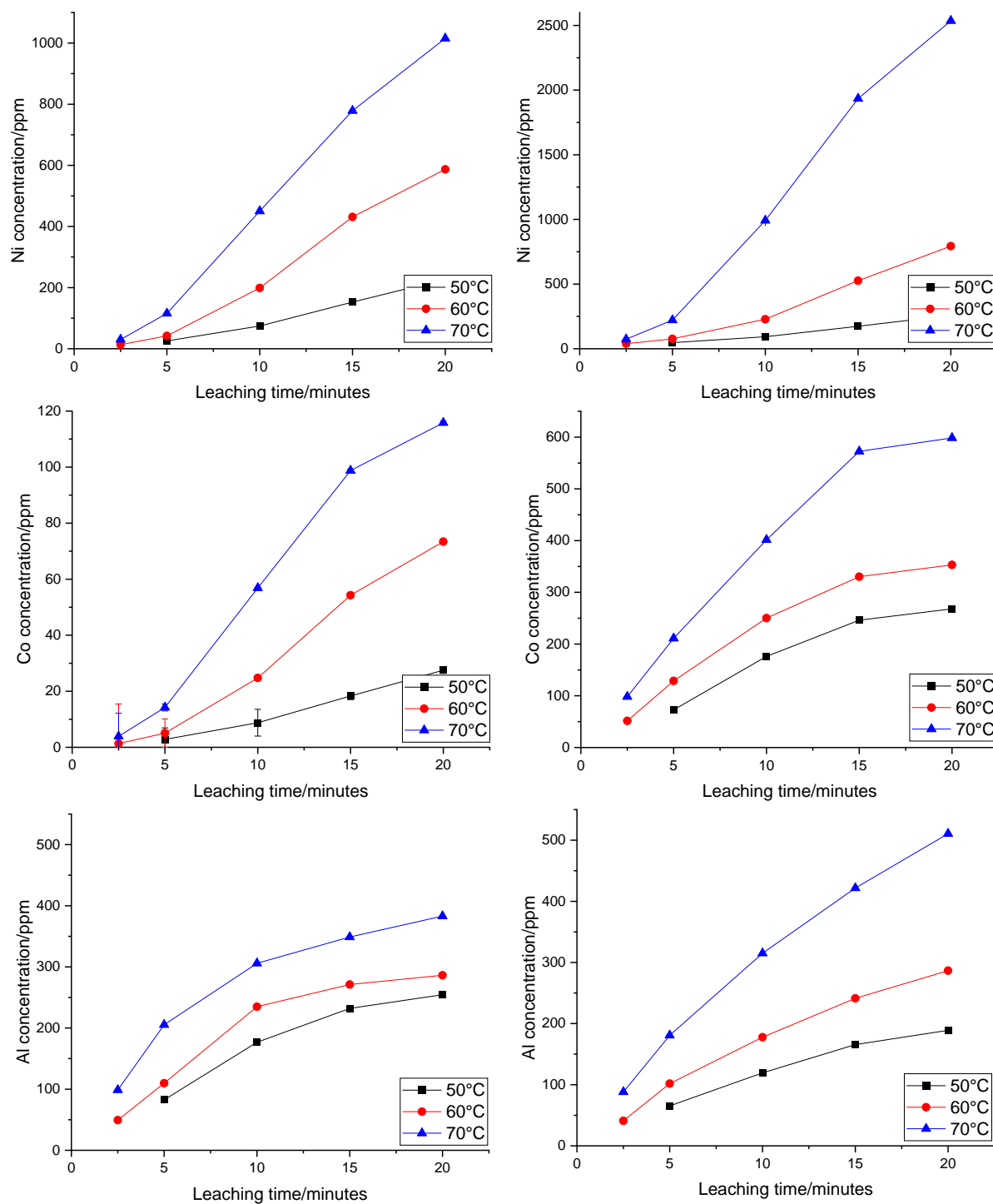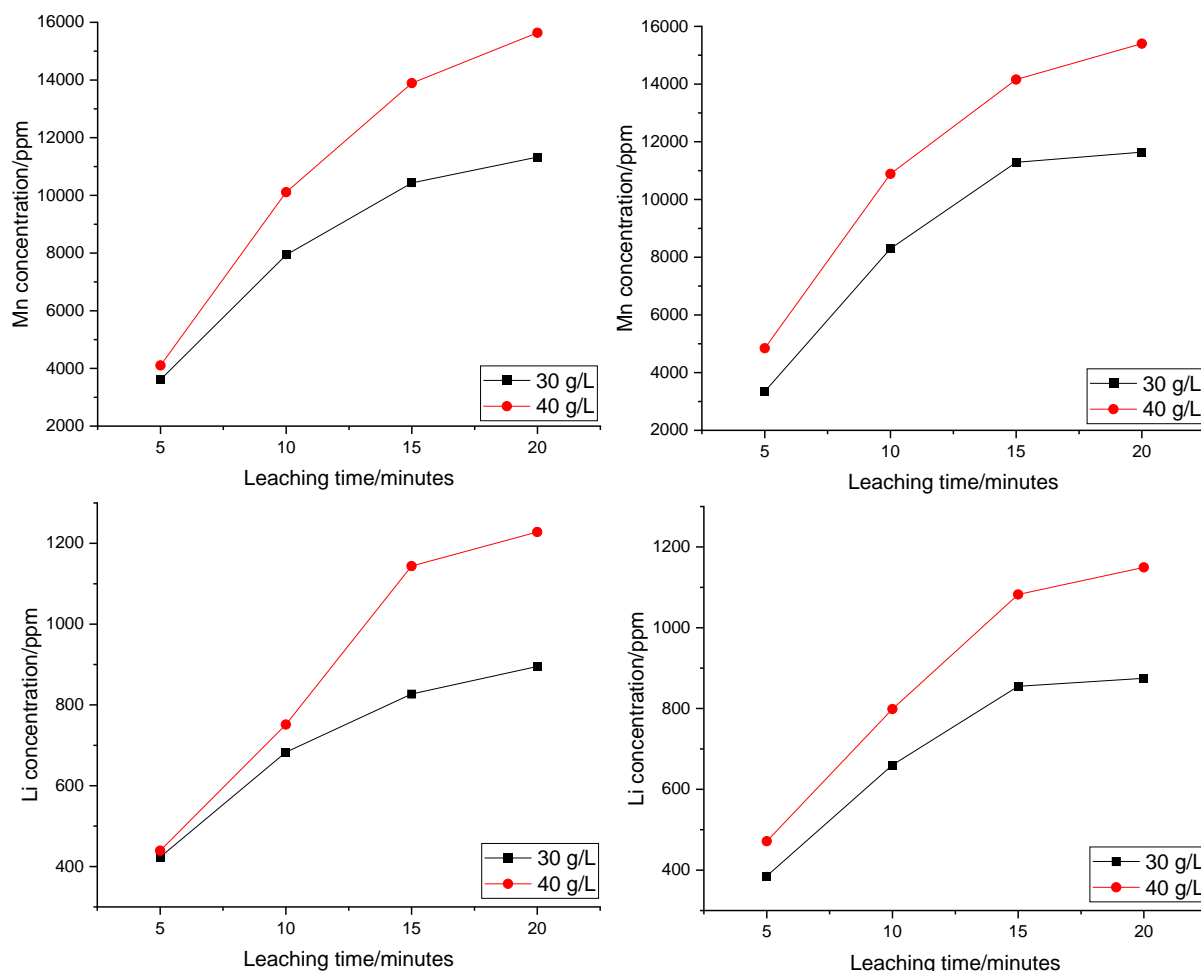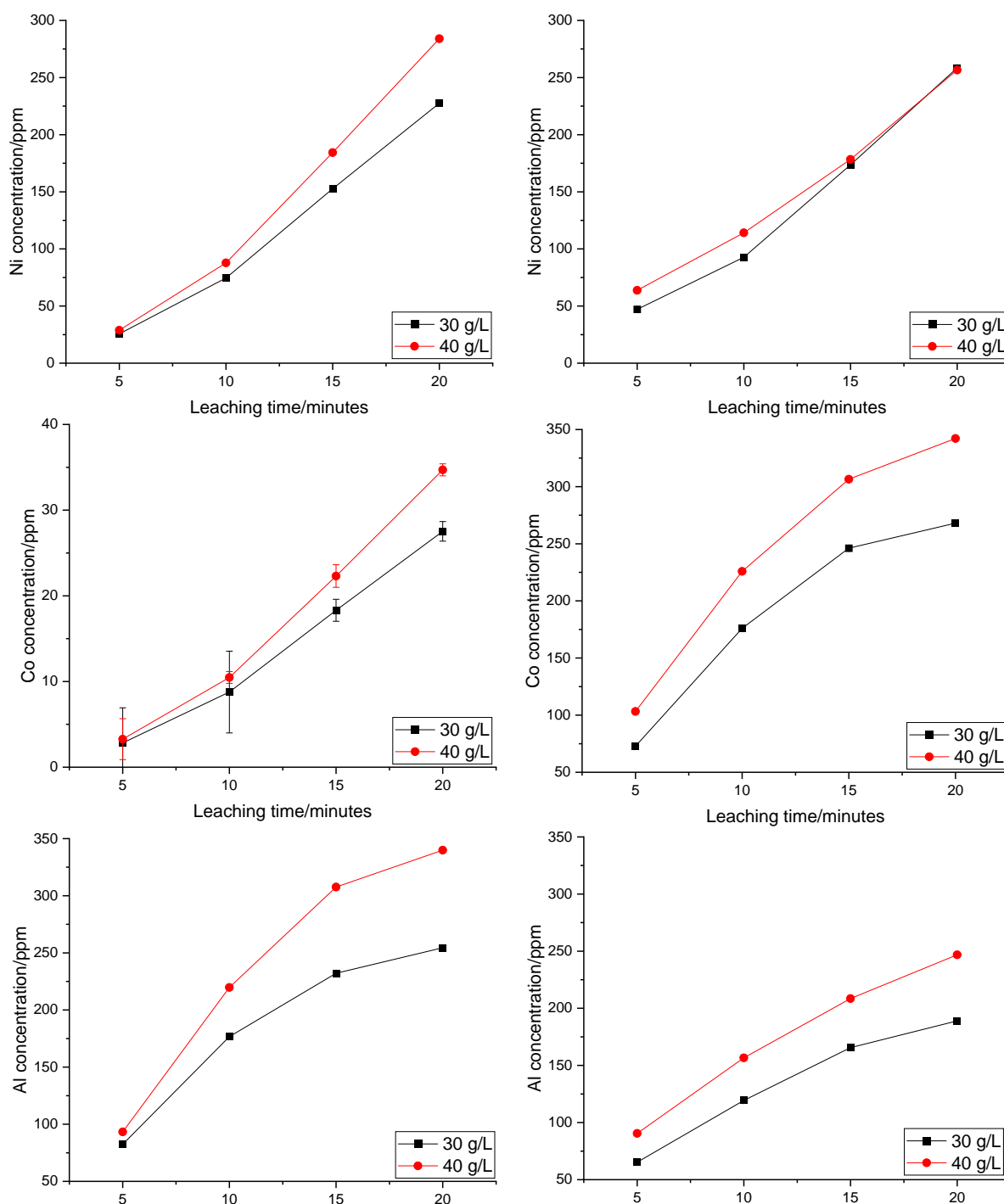
Figure 3-17: ICP-OES results showing the concentration of Ni (top), Co (middle) and Al (bottom) in solution at different leaching times for the QC (left) and EOL (right) cathodes with 50 °C (square), 60 °C (circle) and 70 °C (triangle) acid temperature. Error bars show the relative standard deviation across 3 repeats and are on the order of the point size so cannot be seen in all cases.

In conclusion, the optimum acid temperature appears to be 50 °C. Although higher temperatures have quicker rates for leaching LMO, they have problems with Mn citrate precipitation at longer times. This then removes Mn from solution and will cause problems for subsequent steps in the recycling process. Furthermore, higher temperatures also result in significantly increased leaching from the LO phase. This then reduces the selectivity of the leaching process.

3.5.1.3. Investigating solid:liquid ratio

Different S:L ratios of 0.3 and 0.4 g in 10 mL (equivalent to 30 and 40 g/L) were also tested with the same acid concentration and temperature (1 M and 50 °C).

Figure 3-18 shows the percentage of LO in the active material at set intervals. As before, both cathodes show increased LMO leaching with time. The XRD analysis is inconclusive with no trend displayed for either cathode. It was expected that a higher S:L ratio (40 g/L) would result in a lower leaching rate and efficiency as there is an increased amount of solid present to be leached. 40 g/L of the QC cathode has incomplete leaching of LMO at 20 minutes which is expected however it appears to leach faster than 30 g/L at shorter times. Meanwhile, 40 g/L of the EOL cathode appears to leach faster than 30 g/L and the LMO is completely leached by 15 minutes. This does not fit with the expected results and further ICP-OES analysis is therefore needed to probe what is happening.
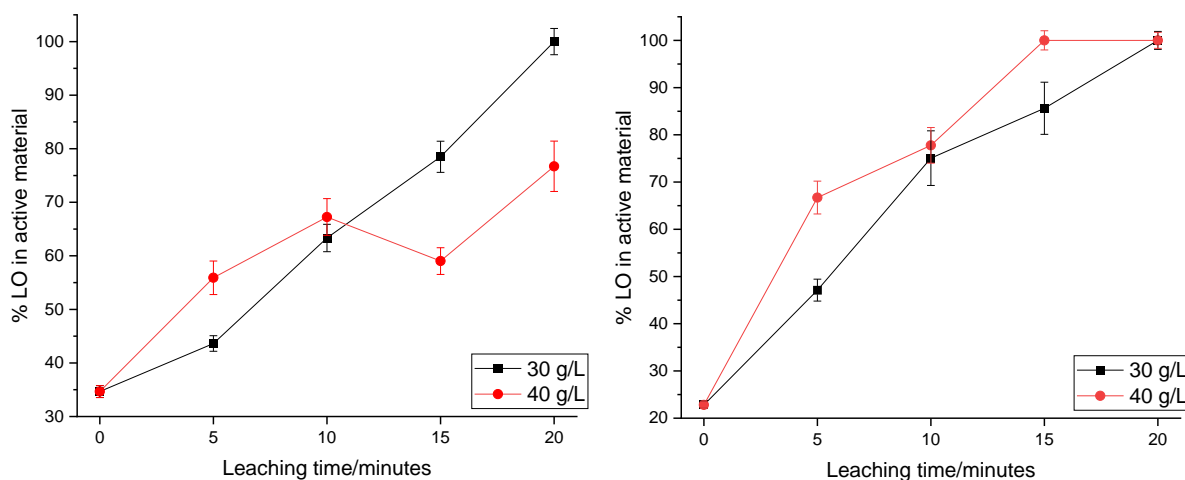
Figure 3-18: Percentage of LO in the active material in the QC (left) and EOL (right) cathodes at different leaching times when using 30 (square) and 40 g/L (circle) cathode material in 1 M citric acid at 50 °C. Error bars were calculated by combining the uncertainty from refinement results.

For the 40 g/L samples it was noticed that there was a precipitate present after 20 minutes of leaching. XRD shows that the precipitate is Mn citrate (Figure 3-19). As there is more Mn present in the larger amount of cathode, it is likely that the solubility limit is reached, and this therefore causes Mn citrate to precipitate. This suggests that 40 g/L is too high a S:L ratio as it is likely to cause Mn precipitation which can cause issues at subsequent stages in the recycling process. The shoulder present on the peak at 21° for the EOL cathode is due to an additional LO phase, as discussed at the beginning of section 3.5..
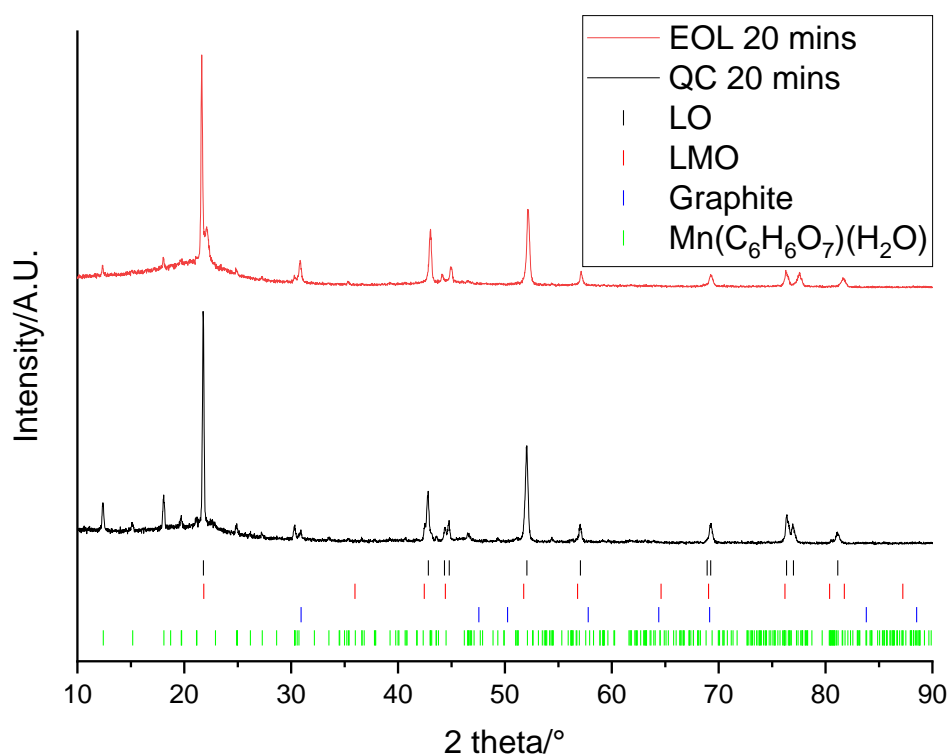
Figure 3-19: XRD patterns of 40 g/L of QC (black) and EOL (red) cathodes after leaching in 1 M for 20 minutes at 50 °C (λ = 1.79 Å). Tick marks correspond to LO (black), LMO (red), graphite (blue) and $Mn(C_6H_6O_7)(H_2O)$ (green).

Figure 3-20 shows the concentration of Mn and Li present in solution at different times. Similarly to before, there is an increased concentration of Mn and Li present in solution as time increases, showing that more LMO is present in solution. There is a clear trend shown by these results, unlike in Figure 3-18, suggesting again that XRD is not the best technique to analyse the leaching process. The concentrations of Mn and Li in solution are all higher for the 40 g/L sample, because there is more Mn and Li present in the larger amount of cathode. Similar amounts of Mn and Li are leached from 0.4 g of both cathodes. At the end of the process, the Mn concentration reaches 15500 ppm and Li concentration reaches 1200 ppm. This matches to the amounts expected for 40 g/L of cathode material (1.3 times more than 30 g/L). In section 3.5.1.2. it was shown

that precipitation is seen in the XRD results before the ICP-OES results. Therefore, a drop in the Mn concentration due to the Mn citrate precipitate would probably be seen in the ICP-OES results if a 25 minute samples was taken.

Figure 3-20: ICP-OES results showing the concentration of Mn (top) and Li (bottom) in solution at different leaching times for the QC (left) and EOL (right) cathodes with 30 (square) and 40 g/L (circle) cathode in 10 mL acid solution. Error bars show the relative standard deviation across 3 repeats and are on the order of the point size so cannot be seen.

Figure 3-21 shows the concentration of the additional elements in solution. The concentrations of Ni, Co and Al in solution increases with time. The QC and EOL cathodes show the same trends, with an increased S:L ratio resulting in increased Ni, Co and Al in solution most cases. The only exception is Ni for the EOL cathode which

appears to leach in similar amounts from 30 and 40 g/L size samples. The increased

concentration in solution is expected, as there will be more of these elements present

in a larger amount of cathode material. The Ni, Co and Al concentrations for 40 g/L are

all lower than or matching to 1.3 times the amount present for 30 g/L. This shows that

the percentage of Ni, Co and Al leached is the same at different S:L ratios and shows

that changing the S:L ratio does not impact the selectivity of the leaching process.

Figure 3-21: ICP-OES results showing the concentration of Ni (top), Co (middle) and Al (bottom) in solution at different leaching times for the QC (left) and EOL (right) cathodes with 30 (square) and 40 g/L (circle) cathode in 10 mL acid solution. Error bars show the relative standard deviation across 3 repeats and are on the order of the point size so cannot be seen in all cases.

In conclusion, from the detailed analysis of the leaching process, 0.3 g is the optimum mass to use with 10 mL of liquid (30 g/L). Although, a higher S:L ratio may be preferable industrially as it enables more cathode to be leached at a time, the results indicate that there are issues when moving to a higher ratio. The higher mass of 0.4 g (in 10 mL) results in Mn citrate precipitation at longer leaching times. However, unlike acid concentration and acid temperature, selectivity was maintained with similar proportions of Ni, Co and Al being leached at both S:L ratios.

3.5.1.4.   Conclusion

Overall, this study has shown the optimum conditions for leaching to be 0.3 g of cathode material in 10 mL of 1 M citric acid at 50 °C. This enables fast leaching of the LMO by 20 minutes. The leaching is most selective with these conditions and results in low amounts leaching from the LO phase. It also gives comparable results for both the QC and EOL cathodes.

Both acid concentration and acid temperature were found to influence the LMO leaching rate, with acid temperature causing the greatest rate increases. However, higher temperatures and concentrations were both found to reduce the selectivity of the process and result in increased leaching from the LO phase. In contrast, changing the S:L ratios did not affect the selectivity of the process. However, high acid temperatures and high S:L ratios were also found to cause Mn citrate precipitation from solution which could create a problem in future steps. There were noticeable differences between the leaching behaviour of the QC and EOL cathodes, such as increased Co leaching from the EOL cathode. The observed small differences in the

leaching of the QC and EOL cathodes are potentially linked to degradation of the EOL cathode, which results in more facile leaching.

3.5.2. In depth analysis of leaching

As mentioned in the previous section 3.5.1., initial work identified an optimum set of conditions for the leaching process (0.3 g of cathode material in 10 mL of 1 M citric acid at 50 °C). In this section, additional techniques and further analysis will be used to analyse the leaching process using these conditions.

The XRD patterns for these conditions were shown initially in Figures 3-9 and 3-10. They showed complete leaching of the LMO phase after 20 mins. Rietveld refinements were performed using these XRD data (Rietveld refinement fits shown in Appendix A). The refinement parameters are displayed in Table 3-7 and 3-8. It shows that over time there is a decrease in the wt% of the LMO phase which is accompanied by an increase in the wt% of the LO phase. Both the QC and EOL cathodes show the same pattern although the EOL cathode appears to leach quicker with the LMO wt% decreasing faster. As mentioned previously, this is attributed to degradation of the EOL cathode allowing for more facile leaching. The leaching process does not appear to have any significant impact upon the lattice parameters of either phase for either the QC or EOL cathodes.

Table 3-7: Lattice parameters and weight percent of phases in QC cathode at different leaching times. R_{wp} = 12.86, 14.05, 14.21, 14.32, 15.90% and GOF = 1.30, 1.43, 1.41, 1.60, 1.43, respectively for 0, 5, 10, 15 and 20 mins.

Phase		0	5	10	15	20
		Leaching time/mins				
LMO	a/Å	8.2043(3)	8.162(4)	8.186(4)	8.191(6)	/
LO	a/Å	2.8750(3)	2.875(2)	2.875(2)	2.875(2)	2.876(2)
LO	c/Å	14.236(1)	14.217(7)	14.223(8)	14.226(8)	14.217(1)
LMO	wt%	57.0(1)	51.4(1)	32.5(1)	19.5(1)	0
LO	wt%	30.2(7)	39.8(9)	56.1(1)	71.3(1)	90.7(2)
Graphite	wt%	12.8(1)	8.7(1)	11.5(2)	9.2(2)	9.3(4)

Table 3-8: Lattice parameters and weight percent of phases in EOL cathode at different leaching times. R_{wp} = 12.82, 14.67, 15.66, 19.22, 18.17% and GOF = 1.23, 1.52, 2.13, 2.22, 2.41, respectively for 0, 5, 10, 15 and 20 mins.

		Leaching time/mins				
Phase		**0**	**5**	**10**	**15**	**20**
LMO	a/Å	8.2083(4)	8.177(1)	8.201(2)	8.204(2)	/
LO	a/Å	2.8594(5)	2.857(6)	2.856(7)	2.859(4)	2.857(3)
LO	c/Å	14.263(1)	14.267(2)	14.273(4)	14.286(2)	14.272(2)
LMO	wt%	61.9(1)	41.8(2)	19.6(1)	11.1(6)	0
LO	wt%	18.3(5)	37.3(1)	58.9(2)	66.1(1)	79.6(2)
Graphite	wt%	19.8(1)	20.9(2)	21.5(4)	22.8(3)	20.4(3)

SEM and EDX images were taken of the QC and EOL cathodes after leaching for 20 minutes (Figure 3-22). Before leaching, the cathode surfaces were fully covered in particles and EDX images showed that there was an even distribution of Mn across the surface with areas of lower Mn content corresponding to areas of high Ni content (Figure 3-8). After leaching, the SEM images shows voids across the surface of the cathodes. These voids are areas where the LMO particles have been leached from the cathode. The grey fluffy regions are due to remaining binder and amorphous carbon (EDX also detected F on the surface). The EDX images show that there is a lower Mn

content across the entire surface. In contrast, there is a higher Ni content across the surface with areas of higher Ni content corresponding to areas where large particle agglomerations remain in the SEM image. The morphology of these larger particles appears to have been retained. This provides further evidence to support the conclusion that the LO remains during the leaching process.
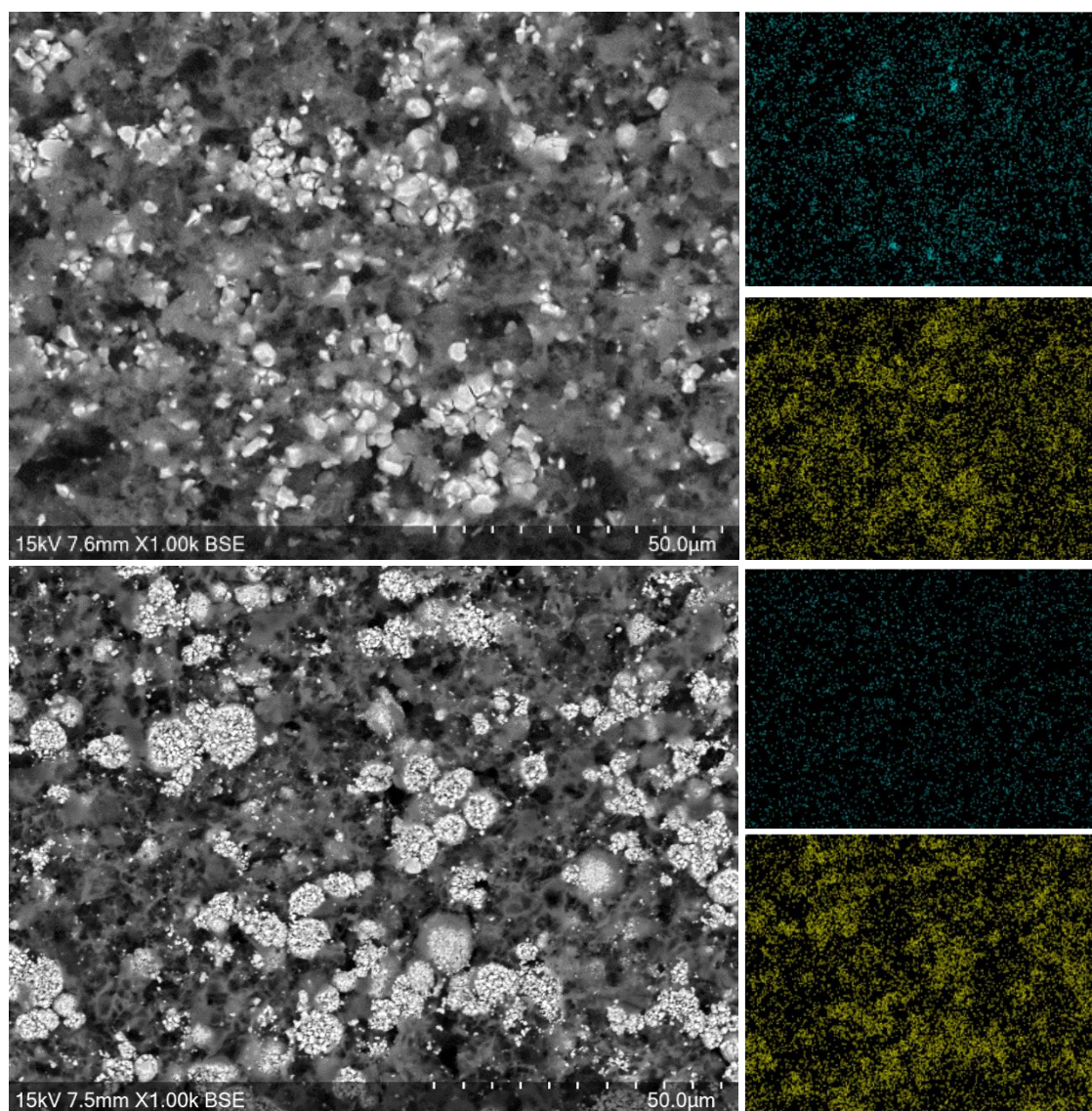
Figure 3-22: SEM (left) and EDX (right) images of the QC (top) and EOL (bottom) cathodes after 20 minutes of leaching. EDX images show Mn (teal, top) and Ni (yellow, bottom).

In addition to the ICP-OES analysis that was performed on the leaching solutions in section 3.5., ICP-OES was also performed on the cathode material at the same

intervals. The data were then used to calculate the atom percentage of each element that is present in solution compared to the total that is present in both the solution and cathode. This enables the efficiency of the leaching process to be analysed in more detail. Table 3-9 shows that after 20 minutes, 96.4% of the Mn has been leached into solution along with 72.1% of the Li. Assuming that all the Mn is in the LMO phase, this gives a 96% leaching efficiency for Mn. The Li leaching efficiency appears lower however, the active material in the cathode consists of 65% LMO therefore this suggests that all the Li is leached from the LMO phase with a small amount being leached from the LO phase as well (matching to the results seen in section 3.5.1.1.). In contrast, < 8% of the Ni, Al and Co is leached into solution. While this may appear to be a significant amount of Ni, Al and Co leaching, the concentration values (Figure 3-13) show that the amounts of these metals in solution are considerably smaller compared to the amount of Mn present. It is hard to determine whether the Al is being leached from the LO phase or the Al current collector, although it is assumed that the Al is leached from the LO as the amounts of Al in solution are comparable to Ni/Co leaching and larger amounts of Al would be expected if it was also being leached from the current collector. Most of the Cu is leached however, it is present in such low amounts (<50 ppm) in the initial cathode that the amount is negligible. These results show that the Mn and Li are leached into solution with high efficiencies while the other elements are leached in much smaller amounts, supporting the selectivity for the LMO over the LO phase.

Table 3-9: ICP-OES results showing the percentage of each element in solution compared to the total amount of the element present in both the cathode and the solution for the QC cathode

Leaching time/minutes	Atom percentage of element in solution					
	Li	Mn	Ni	Co	Al	Cu
5	33.16	31.78	0.90	0.97	2.26	90.65
10	62.63	74.98	3.13	3.08	8.62	95.44
15	66.08	88.20	4.29	4.20	4.87	96.29
20	72.14	96.35	7.09	6.93	6.15	97.68

Table 3-10 shows the same results for the EOL cathode. It shows that slightly more Mn and Li (99.9 and 80.9%) are leached into solution compared to the QC cathode. This shows a higher Mn leaching efficiency which again fits the conclusion that the EOL cathode has more facile leaching due to degradation. For the EOL cathode, the LMO phase makes up 77% of the active material therefore indicating that a small amount of Li is being leached from the LO phase. Similarly to the QC cathode, < 8% of Ni and Al are leached. In contrast, the Co leaching is significantly higher at 30%. Although, the concentration values (Figure 3-13) show that the amount of Co in solution is similar to the amount of Al and Ni that is present. Therefore, although it appears that more Co is being leached, the amount in solution is consistent with the Al and Ni.

Table 3-10: ICP-OES results showing the percentage of each element in solution compared to the total amount of the element present in both the cathode and the solution for the EOL cathode

Leaching time/minutes	Atom percentage of element in solution				
	Li	Mn	Ni	Co	Al
5	42.09	43.60	1.90	12.22	2.33
10	63.51	76.73	2.73	21.24	3.47
15	76.04	98.67	3.72	24.47	4.13
20	80.85	99.94	7.91	30.83	5.89

The ICP-OES results were also used to calculate the molar ratio of metals in the two leaching solutions at 20 minutes (Table 3-11). The QC cathode has a M:Li molar ratio of 1:0.55 while the EOL cathode has a ratio of 1:0.52 (where M = Mn, Ni, Co, Al, Cu). Pristine LMO has a ratio of 1:0.50 therefore the leaching solutions contain a M:Li ratio that is similar to LMO. While previous results showed that Li was being leached from the LO phase (section 3.5.1.1.), when considering the Li molar ratio compared to all the metals present in solution, not just the Mn, the ratio is comparable to what would be expected. This therefore allows the synthesis of LMO with a small number of additional metal elements but the correct amount of Li (the small excess of Li will help to account for Li loss at high temperatures). The metals have molar ratios of 0.94:0.02:0:0.04 and 0.93:0.02:0.02:0.03 (Mn:Ni:Co:Al for QC and EOL respectively). This indicates that LMO can be reformed from the solution with only a small amount of Ni/Co/Al contamination.

Table 3-11: ICP-OES analysis of QC and EOL cathode leaching solution after 20 minutes of leaching. M = Mn, Ni, Co, Al, Cu (units are mol:mol)

Cathode	M:Li	Mn:Ni:Co:Al(:Cu)
QC	1:0.546	0.942:0.015:0.002:0.039(:0.003)
EOL	1:0.521	0.928:0.020:0.019:0.033

Table 3-12 shows the molar ratio of metals in the two cathodes after 20 minutes of leaching. The remaining layered oxides can be calculated to have metals in the following molar stoichiometries: $Ni_{0.83}Mn_{0.05}Co_{0.10}Al_{0.02}$ for the QC cathode and $Ni_{0.78}Mn_{0.03}Co_{0.14}Al_{0.04}$ for the EOL cathode. This ratio matches well to that of NCA other than the presence of a small amount of Mn. This could be due to incomplete leaching of the LMO phase, Mn-doping into the NCA structure or reaction during manufacture of the blended cathode. The results suggest that the remaining LO is Li-deficient as in both cases the M:Li molar ratio is not 1:1 as would be expected for a LO. The EOL cathode is extremely Li deficient and this is consistent with the presence of a delithiated LO phase which is seen in the XRD patterns for the leached EOL cathode (Figure 3-10). At least some of the Li deficiency originates from the use in operation, as initial ICP-OES analysis showed that the EOL cathode contained less Li than the QC cathode prior to leaching (Table 3-6) and that this deficiency could not solely be accounted for by different discharge voltages (Section 3.4.).

Table 3-12: ICP-OES analysis of QC and EOL cathodes after 20 minutes of leaching. M = Mn, Ni, Co, Al, Cu (units are mol:mol)

Cathode	M:Li	Ni:Mn:Co:Al
QC	1:0.782	0.827:0.050:0.101:0.022
EOL	1:0.397	0.784:0.031:0.142:0.043

Overall, these results show that the leaching process has no effect upon the lattice parameters of the LMO and LO phases. Furthermore, there is a high efficiency for the Li and Mn from the LMO phase while the LO phase has much lower leaching efficiencies, leading to a selective leaching process. The recovered LMO has small amounts of Ni, Co and Al impurities while the remaining LO is shown to be Li deficient.

3.5.3. Investigation into the selectivity of citric acid

A range of different techniques were then used to investigate why citric acid is selective for the LMO phase.

Figure 3-23 shows the pH and temperature of the leaching solution. Before adding the cathode (prior to 0 minutes), the solution temperature was 50 °C and the pH was 1.5. After adding the cathode there was an increase in the solution temperature to 53 °C. Meanwhile, the pH gradually increased to a maximum of 2.35.
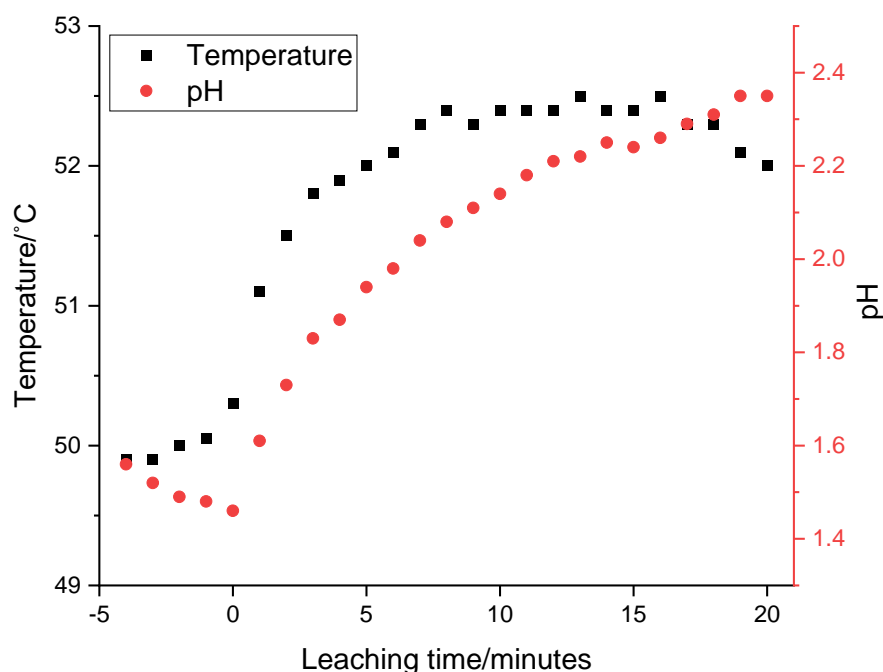
Figure 3-23: Temperature and pH of leaching solution when 0.3 g QC cathode is leached in 10 mL of 1 M citric acid at 50 °C. Cathode was added to the solution at 0 minutes.

The selectivity could therefore be related to the pH of the solution, as the pH determines which citrate complexes are formed. During leaching, the pH remains at 1.4-2.4 therefore the citric acid will mainly be present as H_2Cit^-.[6] Both Mn and Ni have different stability constants with the different citrate species. With H_2Cit^-, Mn has a much higher stability constant than Ni (Table 3-13) and therefore Mn citrate complexes will be more likely to form. This could therefore explain the selectivity of citric acid for LMO over the LO phase. Although, if the solution was at higher pH, which would favour formation of Cit^{3-}, the Ni has a higher stability constant and therefore leaching of the LO phase may be favoured.

Table 3-13: Stability constants for Mn and Ni citrate complexes

Citrate complex	Stability constant/log K [mol^{-1}]	
	Mn^{2+}[23]	Ni^{2+}[24]
H$_2$Cit$^-$	11.4-11.6	2.24
HCit^{2-}	7.8-9.3	4.18
Cit^{3-}	3.7-4.2	6.86

In conclusion, it seems likely the selectivity of citric acid for the LMO phase is related to the pH of the solution. When the citric acid species is H$_2$Cit$^-$, Mn has a much higher stability constant than Ni and therefore it will preferentially bind to the citrate ions. In turn this leads to LMO leaching being favoured and a selective leaching process.

3.6. Recovery of LiMn$_2$O$_4$

Once the LMO component has been leached into solution it can then be separated from the solid LO phase via filtration. The LMO can then be recovered from the solution using thermal treatments. The remanufactured LMO was then tested to investigate its electrochemical performance. Recovery of the LO phase will be explored in section 3.7..

3.6.1. Pristine LiMn$_2$O$_4$

Firstly, LMO was synthesised from pristine reagents. The electrochemical properties were then tested to give a baseline for comparison to the recycled LMO.

The pristine LMO was made using solid state synthesis. Figure 3-24 shows the formation of the desired spinel phase without the presence of any impurity phases, as all the diffraction peaks in the pattern can be indexed based on the spinel structure ($Fd\bar{3}m$ space group). The LMO has a lattice parameter of 8.2367(2) Å, which is similar to values obtained in the literature for LMO.[14]
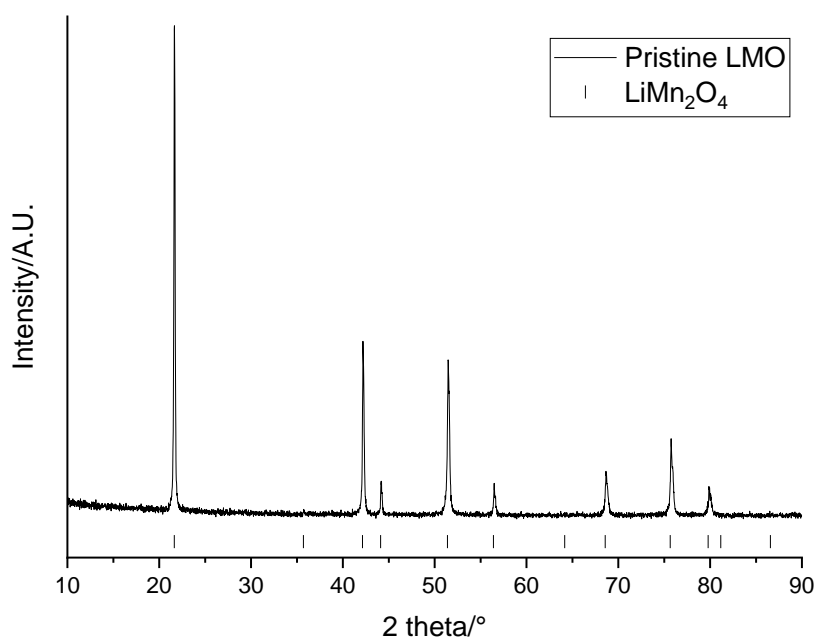
Figure 3-24: XRD pattern of LMO made using pristine reagents (λ = 1.79 Å). Tick marks correspond to LiMn$_2$O$_4$.

Figure 3-25 shows SEM and EDX images of pristine LMO. The SEM image shows that the powder consists of small particles while the EDX image shows that Mn is evenly distributed over the surface of the powder.
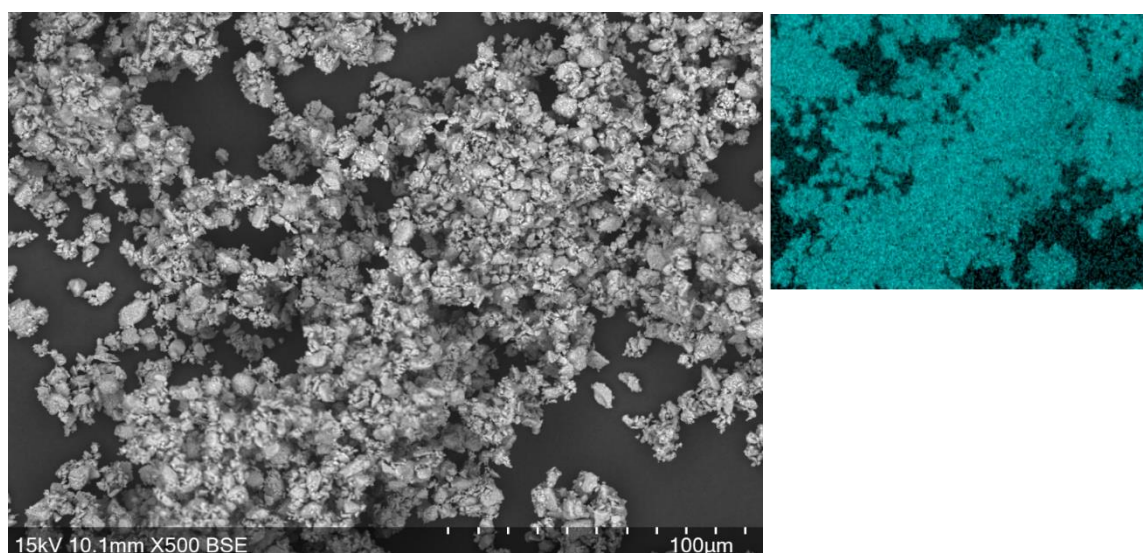
Figure 3-25: SEM (left) and EDX (right) images of pristine LMO. EDX image shows Mn (teal).

Figure 3-26 shows the Raman spectrum for pristine LMO. LMO is predicted to have 5 Raman active modes: one of A_{1g} symmetry, one of E_g symmetry and three of T_{2g} symmetry. This results in peaks being observed at 365, 432, 480, 590 and 625 cm^{-1}.[25] Figure 3-26 shows that the pristine LMO has the characteristic intense peak at 620 and shoulder at 586 cm^{-1}. These are due to Mn-O bonding. The other Raman active modes are less intense and therefore are not distinguishable in this Raman spectrum.
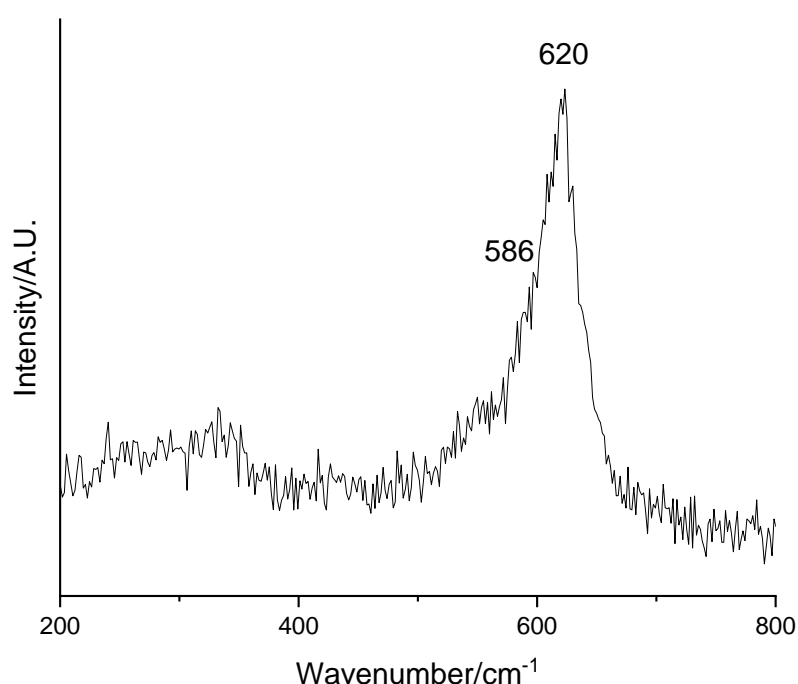
Figure 3-26: Raman spectrum of pristine LMO

Figure 3-27 shows the electrochemical data for pristine LMO. The voltage profile looks as expected with a plateau at ~ 4V due to the Mn$^{3+/4+}$ redox couple. The plateau has a voltage step in the middle. This is due to the delithiation of LMO occurring via a biphasic reaction to a $Li_{0.5}Mn_2O_4$ intermediate. $Li_{0.5}Mn_2O_4$ has a different Li ordering to LMO and therefore the remaining Li is harder to remove and requires a higher voltage.[26] This is shown more clearly in the dQ/dV plot which shows two peaks at 4 and 4.15 V on

charging. The LMO gives an initial specific discharge capacity of 116.2 mAhg^{-1} which decreases to 101.6 mAhg^{-1} after 50 cycles. This corresponds to a capacity retention of 87.4%. Capacity fade is common for LMO and is attributed to Mn^{2+} dissolution into the electrolyte or due to structural distortions arising from Jahn-Teller activity of Mn^{3+} (see section 1.1.1.1.).
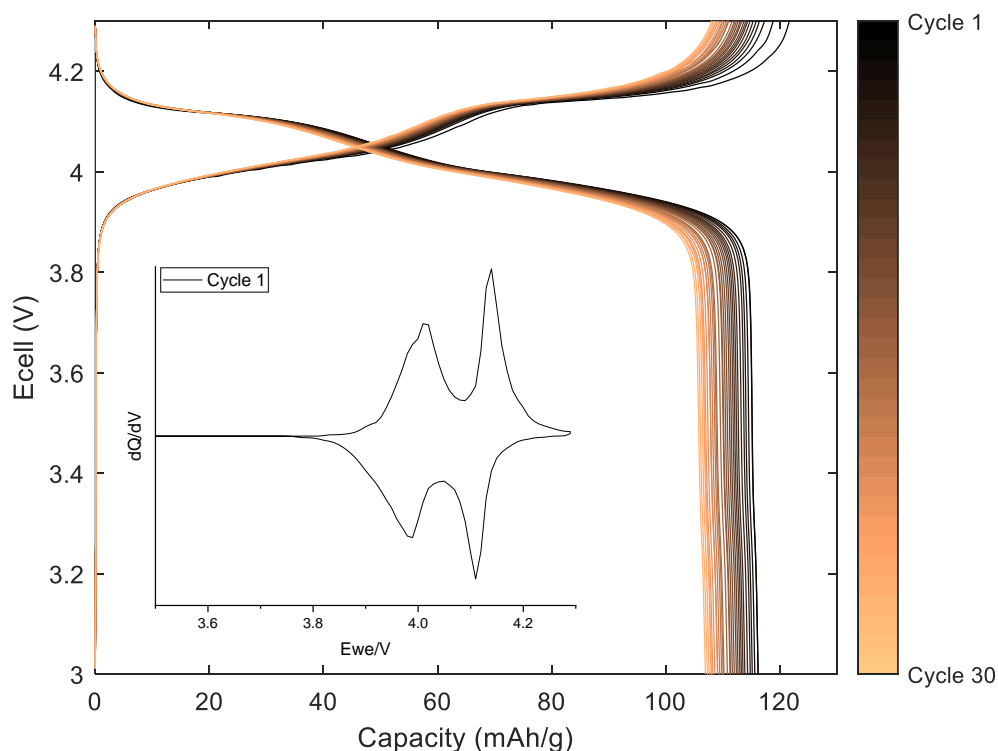
Figure 3-27: Galvanostatic charge-discharge profile and dQ/dV (inset) for pristine LMO when cycled at 10 mAg^{-1} between 3-4.3 V

3.6.2. Recycled LiMn$_2$O$_4$

Next, recycled LMO was made using the leaching solution as a source of Li and Mn. The leaching solution was put into an oven to burn off the organic material before being put into a furnace to reform the LMO. A range of different synthesis conditions were investigated. Molar ratios determined from the ICP-OES analysis of the leaching solution (Table 3-11) showed that the recycled LMO is likely to have a composition of

$Li_{1.04}Mn_{1.86}Ni_{0.04}Co_{0.04}Al_{0.07}O_4$ for the EOL cathode and $Li_{1.09}Mn_{1.88}Ni_{0.03}Al_{0.08}O_4$ for the QC cathode. Therefore, the recycled LMO is likely to contain a small amount of Ni, Co and Al doping. There is 5-10% more Li present that required in the LMO stoichiometry and this additional Li should help to account for Li that is lost during the heating procedure. The results for the EOL cathode will be discussed here while the QC cathode results are shown in Appendix E.

The synthesis was performed at 700 °C with each sample being heated for a different time (6 hours or 12 hours). Another sample was also prepared by heating at 700 °C for 12 hrs with an intermediate grinding step before heating at 700 °C for a further 12 hrs. Figure 3-28 shows the XRD patterns of the product formed when the leaching solution is heated. For all the synthesis conditions, LMO is formed from the leaching solution. All the diffraction peaks in the patterns can be indexed based on the spinel structure and there are no impurity phases present.
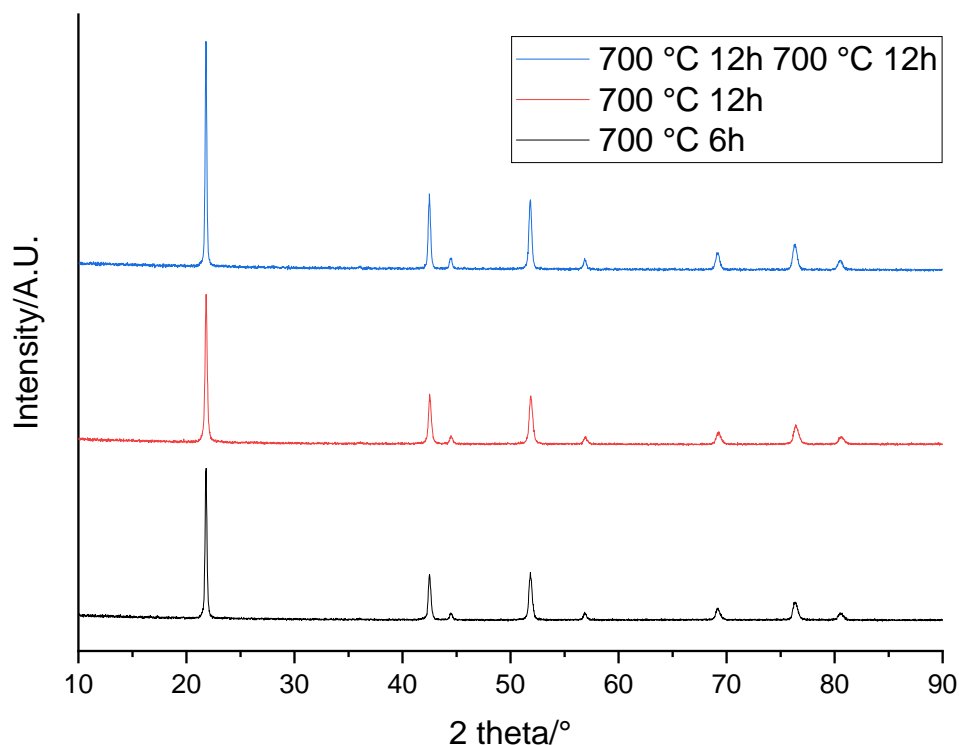
Figure 3-28: XRD pattern of recycled LMO made from the EOL cathode (λ = 1.79 Å). The synthesis was performed at 700 °C for 6h (black), 700 °C for 12h (red) and 700 °C for 12h twice (blue).

The lattice parameters for the recycled LMO are shown in Table 3-14. The samples heated for 12 hrs have very similar lattice parameters while the sample heated for 6 hrs has a smaller lattice parameter. All the lattice parameters are slightly smaller than pristine LMO (8.2367 Å). In the literature, LMO experiences a lattice parameter decrease from 8.20 Å to 8.05 Å when delithiated.[15] The recycled LMO has smaller lattice parameters than pristine LMO which suggests that it may have some Li deficiency, although, the difference is small suggesting that any Li deficiency is likely to be very low, < 10% Li deficiency. However, in the literature, Ni, Co and Al doping into the LMO structure have all been found to cause a decrease in the lattice

parameter.[27–29] Therefore, the presence of these additional elements could be causing the smaller lattice parameter.

Table 3-14: Lattice parameters of recycled LMO made from the EOL cathode

Synthesis procedure	*a*/Å
700 °C 6h	8.1801(3)
700 °C 12h	8.2014(4)
700 °C 12h 700 °C 12h	8.2021(3)

Figure 3-29 shows the electrochemical data for the 6h-recycled LMO. The voltage profile for the recycled LMO looks considerably different to the voltage profile of pristine LMO (Figure 3-27). Rather than two plateaus, the 6h-recycled LMO has a sloping voltage profile with the dQ/dV plot showing two very broad peaks which overlap. This suggests that the delithiation is a solid-solution-type reaction as continual changes to the voltage are required to remove Li. The Li ordering must therefore be different in the 6h-recycled LMO compared to the pristine LMO. It suggests that the Li is in different sites to the pristine LMO and therefore different voltage are required to remove it during delithiation.
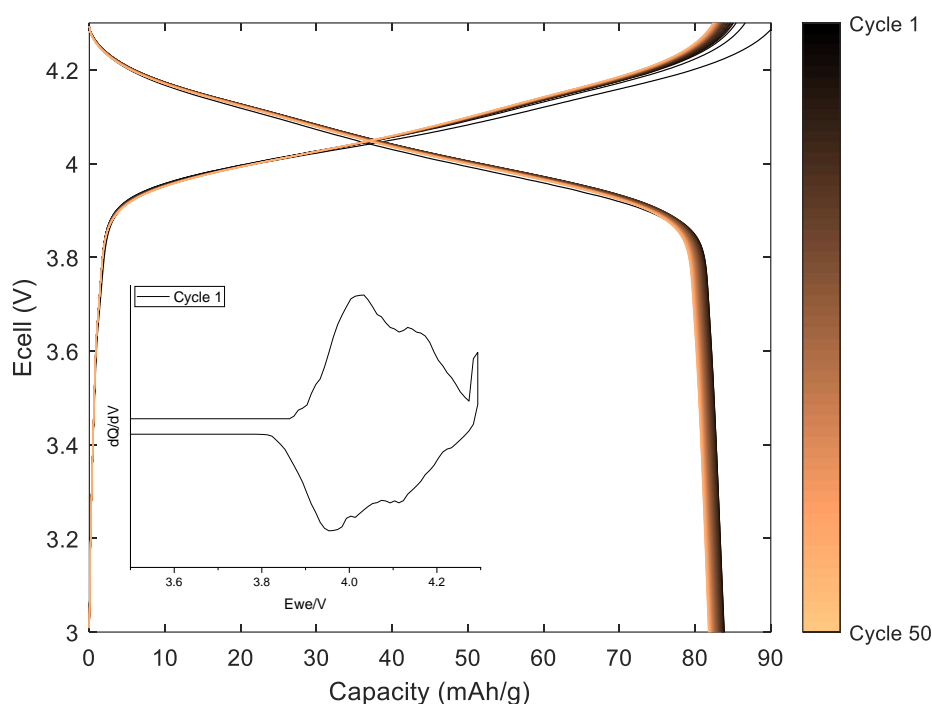
Figure 3-29: Galvanostatic charge-discharge profile of recycled LMO synthesised at 700 °C for 6 hrs (from the EOL cathode) when cycled at 10 mAg^{-1} between 3-4.3 V

The 6h-recycled LMO shows an initial specific discharge capacity of 83.7 mAhg^{-1} which decreases to 81.7 mAhg^{-1} after 50 cycles. This corresponds to a capacity retention of 97.6%. Therefore, the 6h-recycled LMO has a much lower capacity than pristine LMO but a far superior capacity retention. The lower capacity suggests that some of the Li in the structure is not removed/inserted during charging/discharging. The proposed different Li ordering in the 6h-recycled LMO may lead to trapped Li which cannot be removed/inserted during charge/discharge. The superior capacity retention could be due to small amounts of impurity elements which could be helping with the capacity retention.

Figure 3-30 shows the electrochemical data for the 12h-recycled LMO. The voltage profile matches more closely to pristine LMO. This suggests that 6 hrs of heating is not sufficient for the structure to fully form however, 12 hrs is and therefore the 12h-recycled LMO displays the expected electrochemical behaviour. The 12h-recycled LMO displays a specific discharge capacity of 88.8 mAhg^{-1}. While the discharge capacity is higher than the 6h sample, it is still lower than pristine LMO. This low capacity could be due to insufficient Li content in the structure. Alternatively, the lower capacity could be related to the impurity elements, which could be affecting the performance.
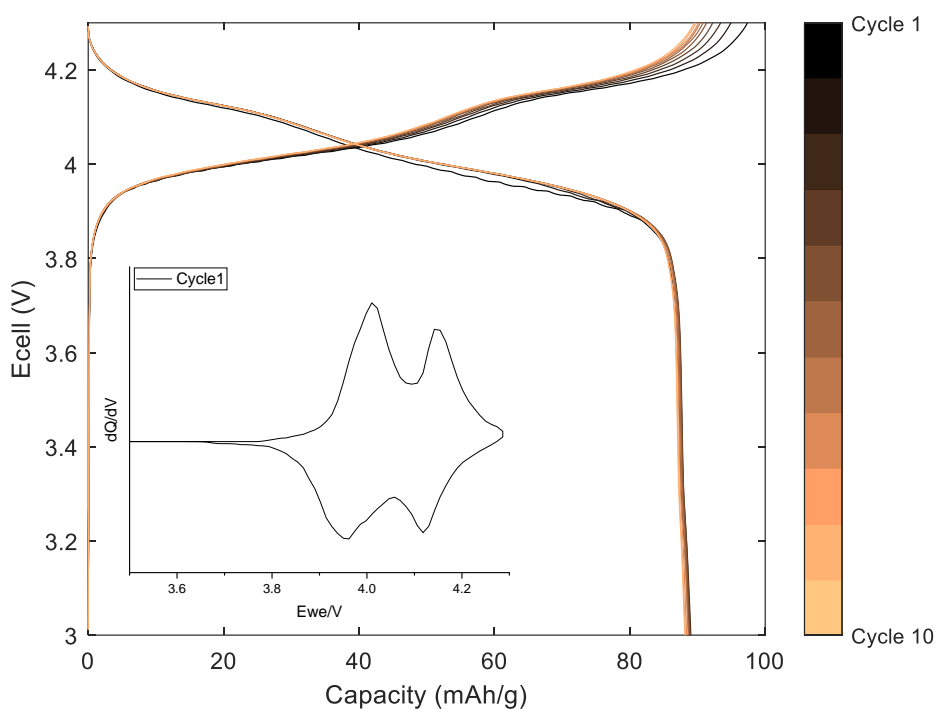
Figure 3-30: Galvanostatic charge-discharge profile of recycled LMO synthesised at 700 °C for 12 hrs (from the EOL cathode) when cycled at 10 mAg^{-1} between 3-4.3 V

Figure 3-31 shows the electrochemical data for the reheated 12h-recycled LMO. The voltage profile looks similar to pristine LMO. However, the discharge capacity is even

lower in this case (81.7 mAhg^{-1}). This could be because additional Li is lost when the recycled LMO is heated for a second time.
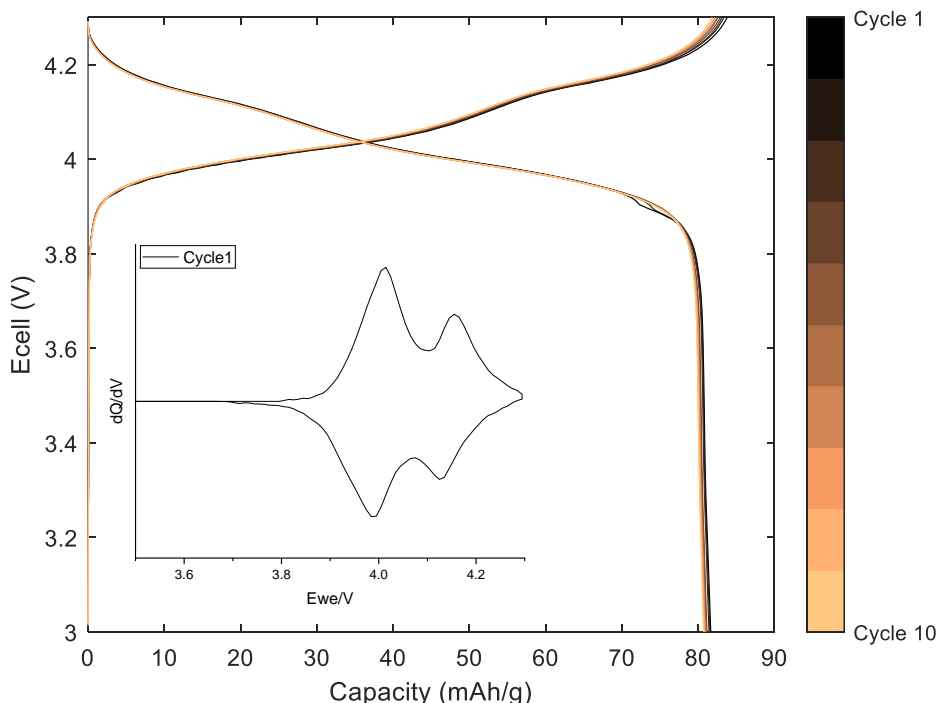
Figure 3-31: Galvanostatic charge-discharge profile of recycled LMO synthesised at 700 °C for 12 hrs and then reheated to 700 °C for 12 hrs (from the EOL cathode) when cycled at 10 mAg^{-1} between 3-4.3 V

Overall, these results show that recycled LMO can be made from the leaching solution, however, the recycled LMO has a different electrochemical performance depending on the synthesis time used. The results suggest that heating at 700 °C for 12 hrs produces the optimum electrochemical results although the discharge capacity is still lower than pristine LMO. When the recycled LMO is heated for 6 hrs the electrochemical behaviour is significantly different while heating the recycled LMO for longer time periods results in a lower discharge capacity.

3.6.2.1. In depth analysis of recycled LiMn$_2$O$_4$

In this section, additional techniques and further analysis will be used to compare the 12h-recycled LMO to pristine LMO to identify possible causes for the lower capacity of recycled LMO.

ICP-OES analysis showed that pristine LMO had a M:Li ratio of 1:0.54 while the recycled LMO had a M:Li ratio of 1:0.63. This indicates that the recycled LMO still contains excess Li as predicted by ICP-OES of the leaching solution (Table 3-11). This therefore indicates that the recycled LMO should contain enough Li to provide the expected capacity. Although, ICP-OES does not analyse where the Li is within the structure and therefore it is possible that some of the Li is present in other compounds on the surface of the material.

Table 3-15 shows the crystallite size of the pristine and recycled LMO. The crystallite size was calculated using the Scherrer equation.[30] The full width at half maximum was identified for each peak in the pattern and then the crystallite size was averaged across all the peaks. It shows that the recycled LMO has a significantly smaller crystallite size than pristine LMO. This suggests that differences in the electrochemical performance may be related to differences in the crystallite size.

Table 3-15: Crystallite size of pristine and recycled LMO

LMO	Crystallite size/Å
Pristine	800
EOL	400
QC	400

Figure 3-32 shows the SEM and EDX images for 12h-recycled LMO. The SEM image shows that the particle size is larger and less uniform for the EOL LMO (10-80 μm) compared to the pristine LMO (Figure 3-25, <10 μm). These particle sizes are significantly larger than the crystallite sizes shown in Table 3-15 (800 Å = 0.08 μm) which suggests that the particles consist of several small crystals. The EDX images show that Mn, Al, Ni and Co are present on the surface of the LMO. EDX analysis of molar ratios gives the ratio of metals as $Mn_{0.90}Ni_{0.06}Co_{0.02}Al_{0.01}$, which is similar to the ratio found from ICP-OES analysis of the leaching solution (Table 3-11). EDX did not detect any F present on the surface. The Mn and F emissions overlap and therefore it can be hard to identify low levels of F using EDX. Therefore, F could be present at levels too low to be detected by EDX analysis. Other techniques would be required to confirm the presence of F.
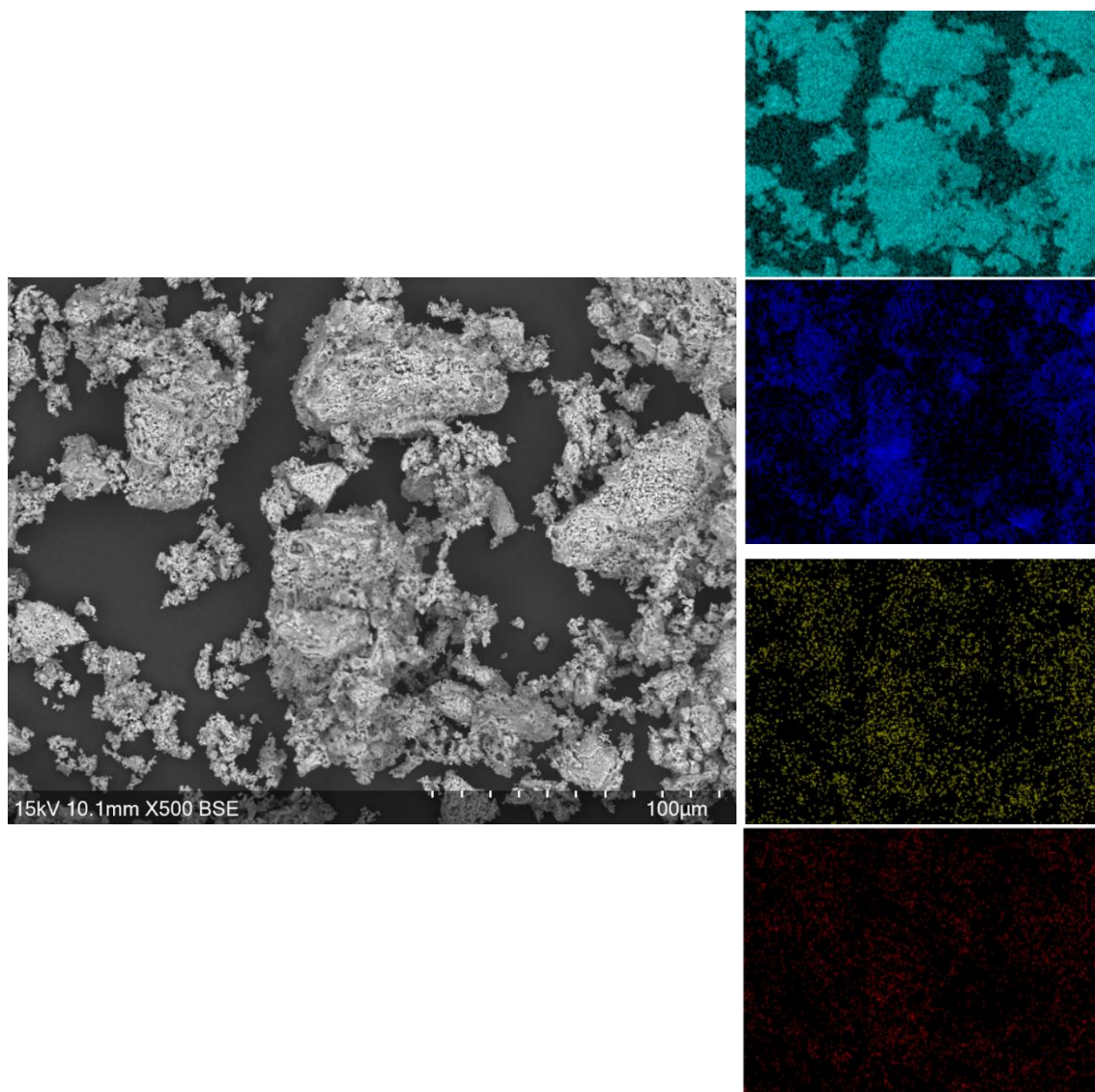
Figure 3-32: SEM (left) and EDX (right) images of recycled LMO synthesised at 700 °C for 12 hrs from the EOL cathode. EDX images from top to bottom show Mn (teal), Al (blue), Ni (yellow) and Co (red).

Figure 3-33 shows the Raman spectrum for 12h-recycled LMO. It has additional intense bands that are not present for pristine LMO (Figure 3-25). The peaks at 623 and 580 cm^{-1} are expected for LMO and are due to Mn-O bonding. Although, the shoulder at 580 cm^{-1} is more prominent than for pristine LMO. A higher intensity peak at this position is attributed to LMO with a Li deficiency and may therefore indicate that there is some level of Li deficiency within the structure.[31,32] However, this is often

accompanied by the presence of a peak at 680-690 cm^{-1}. This peak is not present and therefore it is not possible to conclusively say that the structure is Li deficient. It is also worth noting that Raman is a surface sensitive technique and therefore does not probe the bulk of the sample. The additional intense peak at 480 cm^{-1} and weaker peak at 390 cm^{-1} match to peaks seen in the Raman spectrum of $LiMn_{1.5}Ni_{0.5}O_4$ due to Ni-O bonding.[33] This confirms that Ni impurities are present in the recycled LMO. There are no peaks present above 700 cm^{-1} (Figure 3-33 inset). This indicates that there are no Li-containing phases present on the surface, such as Li_2CO_3 or LiOH, as these would cause peaks to be present at 1090 and 840 cm^{-1} respectively.[34,35] This therefore suggests that all the Li is present within the LMO structure and that the low capacities are due to blocked Li pathways as opposed to a Li deficiency.
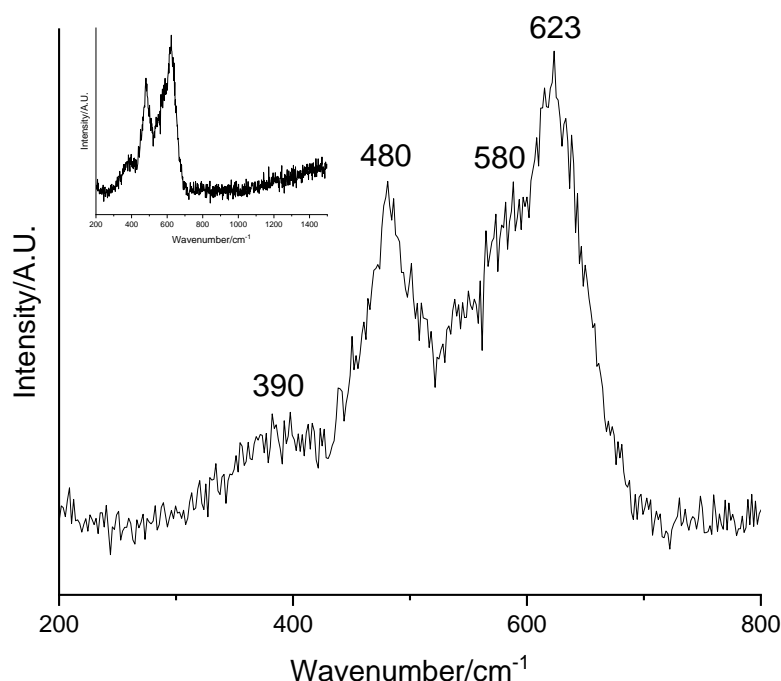
Figure 3-33: Raman spectrum of recycled LMO synthesised at 700 °C for 12 hrs (from the EOL cathode)

Another potential reason for the lower capacity could be that there is amorphous content present in the recycled LMO which negatively affects the capacity. This would not be detected by traditional XRD analysis as it is not crystalline material. To check for possible amorphous phases XRD analysis was performed on the recycled LMO along with a crystalline standard and this showed that there was no amorphous content present in the recycled LMO (Appendix A, Figure A12).

To examine whether the lower capacity was related to the impurity elements, a replica sample of recycled LMO with the same amounts of impurity elements was made using pristine LMO to see how this performed. XRD patterns showed that the LMO phase was formed with a lattice parameter of 8.2144(6) Å. As for the recycled material, the lattice parameter is smaller than pristine LMO suggesting that the cause of the cell parameter reduction is the presence of Ni, Co and Al impurity elements.[21,36] The replica recycled LMO had a crystallite size of 593 Å which is closer to pristine LMO. This is probably because a solid state preparation method was used to synthesise the replica recycled LMO.

Figure 3-34 shows the electrochemical data for the replica recycled LMO. The voltage profile looks as expected with the dQ/dV plot showing two distinct peaks on charge and discharge. The replica recycled LMO shows a specific discharge capacity of 99.3 mAhg^{-1}. This is around 10 mAhg^{-1} higher than the 12h-recycled LMO but 15 mAhg^{-1} lower than pristine LMO. This indicates that unless the impurity elements can be removed, recycled LMO will always have a lower capacity than pristine LMO. Although, there is the potential to increase the capacity of recycled LMO by a further 10 mAhg^{-1}.
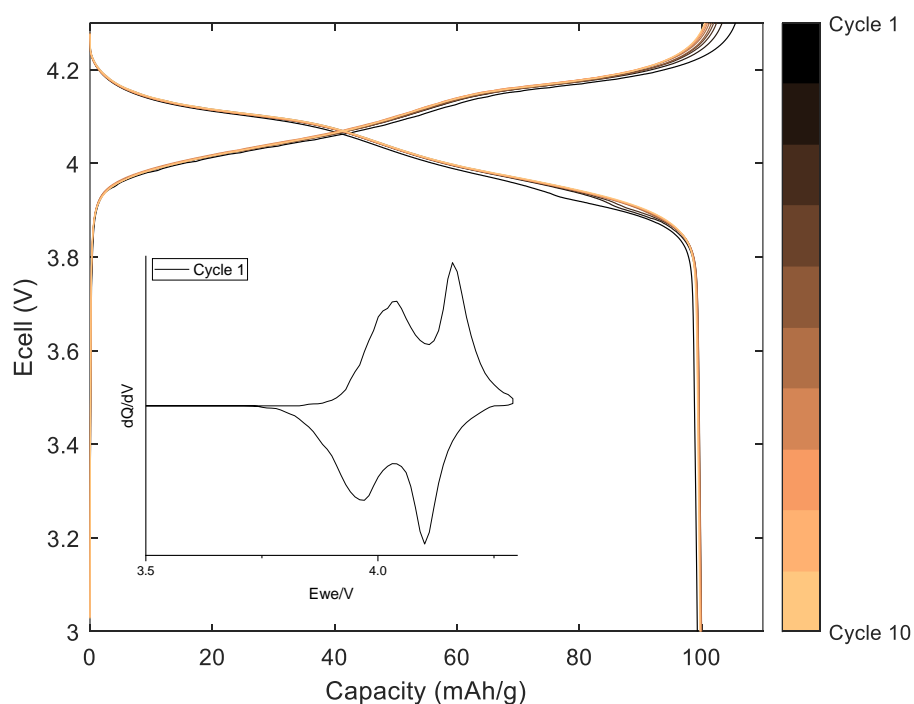
Figure 3-34: Galvanostatic charge-discharge profile of replica recycled LMO when cycled at 10 mAg^{-1} between 3-4.3 V

Figure 3-35 shows the Raman spectrum for the replica recycled LMO. It has similar additional bands (402 and 493 cm^{-1}) to the recycled LMO sample (Figure 3-33) proving that these additional peaks are due to small amounts of Ni impurities.
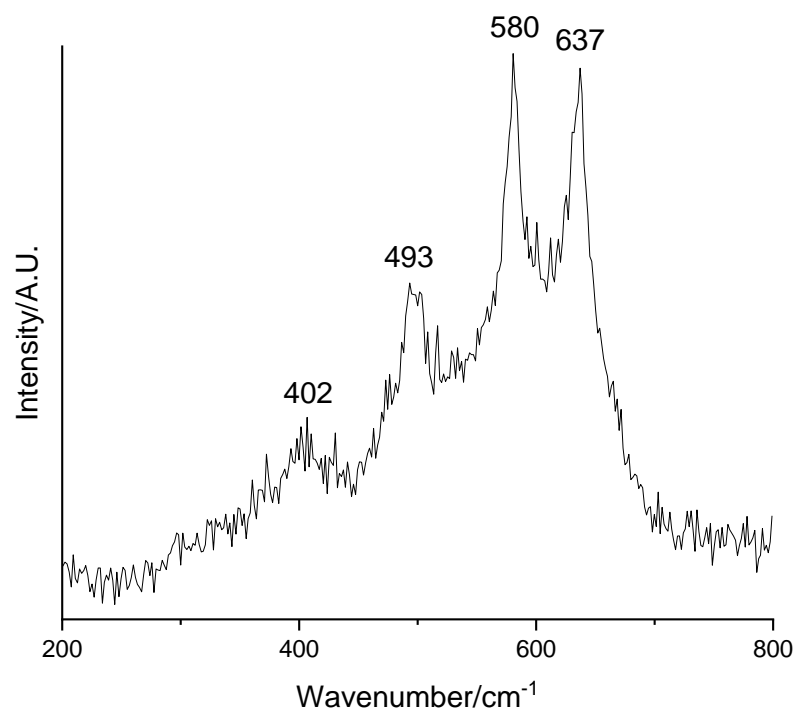
Figure 3-35: Raman spectrum of replica recycled LMO

In conclusion, it has been shown that it is possible to recycle LMO from the leaching solution. However, the recycled LMO has a lower capacity than pristine LMO. Potential reasons for this are Li loss during the heating procedure, impurity elements affecting the electrochemical performance or crystallite size issues. Further analysis is required to identify the definitive cause.

3.7. Recovery of the layered oxide

Once the LMO and LO have been separated using the leaching process, the solid LO can then be separated from the leaching solution using filtration. The remaining LO is solid and therefore it could hypothetically be placed directly back into a new cell. However, SEM images show that there is PVDF/amorphous carbon present in the cathode along with the remaining LO (Figure 3-22). If these are not removed, it will cause the LO to have a lower capacity as these inactive materials will contribute to the mass of the material without providing any electrochemical capability. Furthermore, as shown in section 3.5.2., the calculated composition of the remaining LO in the EOL cathode is $Li_{0.40}Ni_{0.78}Mn_{0.03}Co_{0.14}Al_{0.04}$ while the composition of the LO in the QC cathode is $Li_{0.78}Ni_{0.83}Mn_{0.05}Co_{0.10}Al_{0.02}$ (Table 3-12). This indicates that the remaining LO is Li deficient and therefore a method must be employed which introduces Li back into the structure. It is worth mentioning that the remaining LO is much more Li deficient for the EOL cathode than the QC cathode. For the EOL cathode, there is also potential for the LO structure to have degraded due to extensive cycling.

A recycling method is therefore required that will remove the remaining PVDF/amorphous carbon and relithiate the LO structure. In the literature, several methods have been shown to remove PVDF from cathode materials. Thermal decomposition has been shown to remove PVDF.[37,38] However, thermal treatments have also been shown to result in fluorination of the structure or formation of rocksalt impurity phases.[39,40] Alternatively, the cathode can be treated hydrothermally, as PVDF is known to decompose under alkaline hydrothermal conditions.[41] These different methods were investigated as ways to recycle the LO. Recycling the EOL LO

will be investigated in section 3.7.1. while recycling the QC LO will be studied in section 3.7.2..

3.7.1. EOL recycled layered oxide

Firstly, the EOL LO was thermally treated to remove the PVDF. Two different heating methods were employed: heating at 900 °C with no extra Li and heating at 450 °C before regrinding and heating at 850 °C with 10% excess Li. These treatments were based upon work done by other members of the group on thermal treatments to achieve PVDF removal. Figure 3-36 shows that in both cases a rocksalt phase was formed. While the formation of rocksalt phases has been reported in the literature, normally rocksalt phases are present as an impurity along with the layered structure.[39] In this case, the entire sample has converted to a rocksalt structure. This complete conversion to a rocksalt structure could be due to the extreme Li deficiency within the sample.
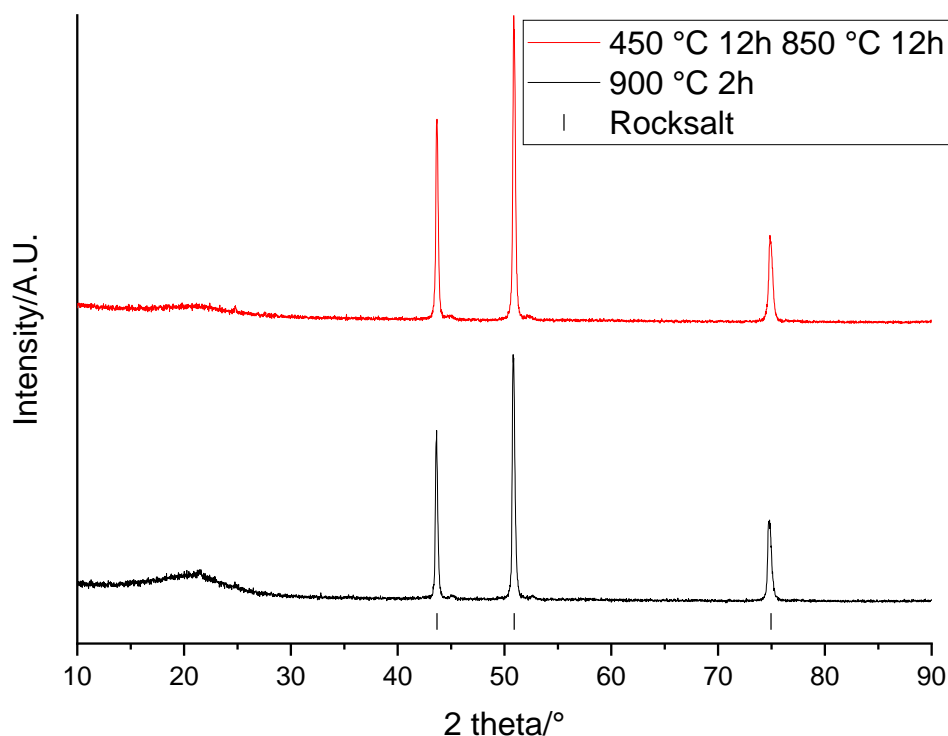
Figure 3-36: XRD patterns of recovered LO from the EOL cathode when heated to 900 °C for 2h (black) and 450 °C for 12h followed by 850 °C for 12h (red) (λ = 1.79 Å). Tick marks correspond to rocksalt (black).

As the heat treatment proved to be unsuccessful, a hydrothermal method was employed instead, using NaOH to remove any remaining PVDF. Different concentrations of NaOH were used along with a constant sample amount and temperature. Figure 3-37 shows the XRD patterns of the product formed after hydrothermal treatment of the LO. When 4 and 2 M NaOH are used, a hydroxide phase is formed, suggesting that the Li is removed from the structure. Meanwhile, when lower NaOH concentrations are used (1 and 0.5 M), the hydroxide and LO phases are both present. The peak at 21.6° corresponding to the LO phase decreases in intensity as the NaOH concentration increases showing that there is less of the LO phase present with increasing NaOH concentrations. The conversion to a pure hydroxide scenario

occurs at 2 M which, assuming the reaction is stoichiometric, is the point at which the moles of NaOH are equal to the moles of LO. Work by other members of the group has shown that the remaining solution after hydrothermal treatment contains NaF proving that the PVDF is decomposed during the treatment.[9] The XRD patterns also show a small peak at 30.8˚ which suggests that there is some graphite remaining after the hydrothermal treatment. This is further supported by STEM images from similar work.[9]
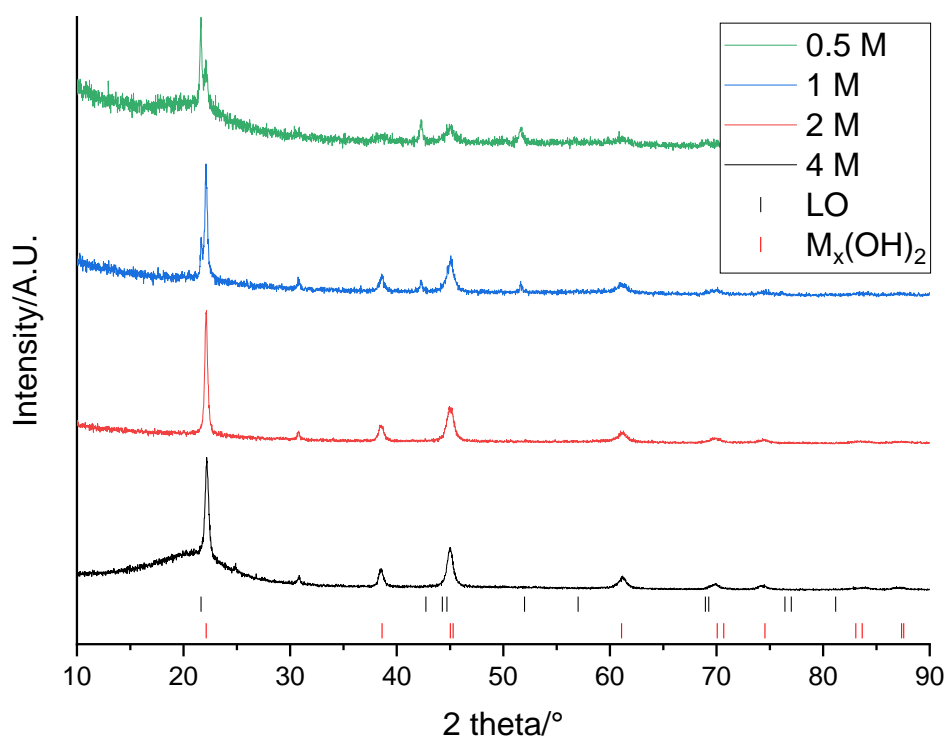
Figure 3-37: XRD of remaining LO from EOL cathode after hydrothermal treatment with 4 M (black), 2 M (red), 1 M (blue) and 0.5 M (green) NaOH (λ = 1.79 Å). Tick marks correspond to LO (black) and $M_x(OH)_2$ (red).

The next step taken was to mix the hydroxide (or the LO/hydroxide mixture) with Li_2CO_3 to reform the LO. The amount of Li_2CO_3 added was calculated using EDX analysis of each sample after hydrothermal treatment. A 10% excess of Li_2CO_3 was added to

account for Li loss at high temperatures. The samples were then heated at 800 °C for 12 hrs. Figure 3-38 shows that after heating all the samples reformed the LO phase. The small peak at 30.8˚ is no longer present showing that the graphite contamination was removed by the heating step. After leaching, the LO had a shoulder on the peak at 21°, this was attributed to a Li-deficient LO phase (Figure 3-9). This shoulder is no longer present after the hydrothermal treatment, indicating that the LO has been successfully regenerated. This is further supported by STEM images from similar work.[9]
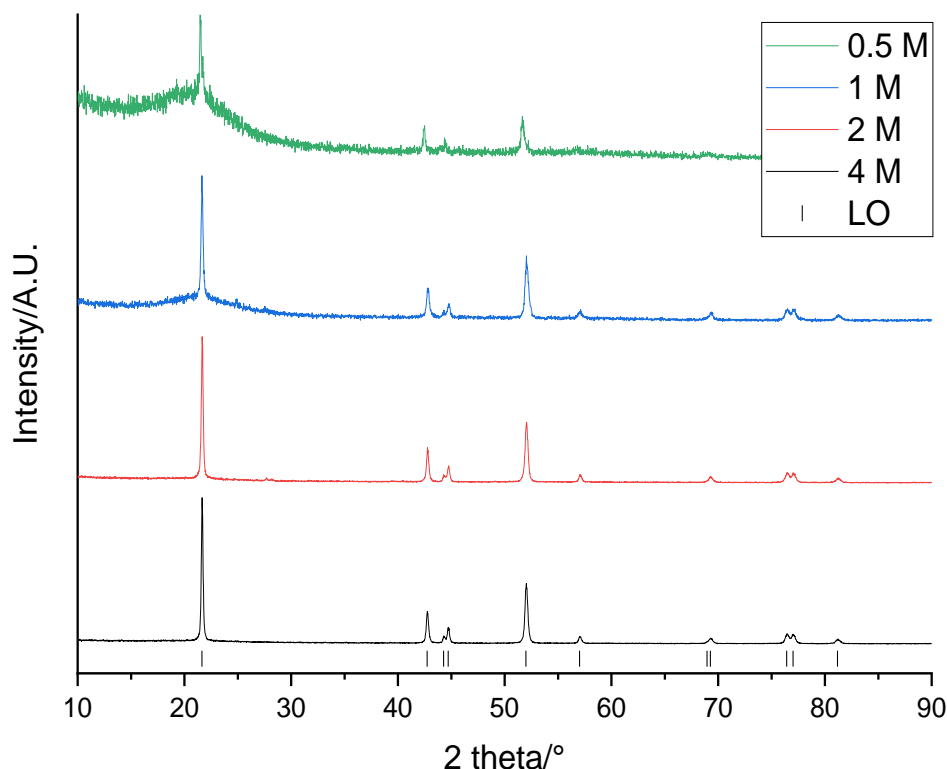
Figure 3-38: XRD patterns of recycled LO recovered from the EOL cathode. The initial hydrothermal step was performed with 4 M (black), 2 M (red), 1 M (blue) and 0.5 M (green) NaOH (λ = 1.79 Å). The samples were then heated to 800 ℃ for 12h. Tick marks correspond to LO (black).

2 M was the lowest NaOH concentration that resulted in complete formation of the hydroxide phase after hydrothermal treatment. It was therefore taken forward for further optimisation. It is ideal for the whole sample to convert to hydroxide as it is then simpler to work out how much Li to add in the subsequent step. Next, different oven temperatures and durations were investigated for the hydrothermal step. For all the temperatures and times studied, the LO was completely converted to the hydroxide phase. Then the samples were heated at 800 °C with Li_2CO_3. Figure 3-39 shows the XRD patterns of the samples after heating. In all cases, the samples reformed the desired LO. The lowest hydrothermal treatment temperature and shortest time (150 °C for 8h) will be taken forward for further optimisation.
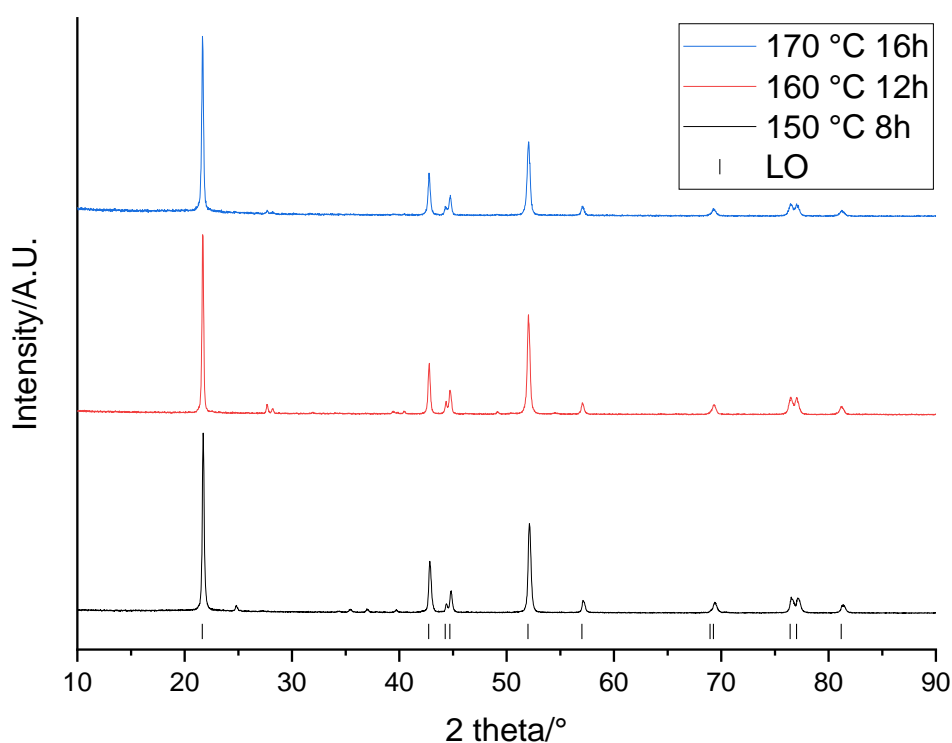
Figure 3-39: XRD patterns of recycled LO recovered from the EOL cathode. The initial hydrothermal step was performed with 2 M NaOH and heating to 150 °C for 8h (black), 160 °C for 12 h (red) and 170 °C for 16h (blue) (λ = 1.79 Å). The samples were then heated to 800 °C for 12h. Tick marks correspond to LO (black).

The recycled LO was then heated under an O_2 atmosphere in a tube furnace (with a flow rate of 1 bubble per second). It has been shown that when NCA is heated in air, Li_2CO_3 can form on the surface due to reaction with CO_2 and have a detrimental impact upon the electrochemical performance of the NCA.[42] Figure 3-40 shows the XRD patterns of the LO heated under both air and O_2 atmospheres. It shows that in both cases the desired LO phase is formed. Furthermore, in both cases, the (006)/(102) and (108)/(110) peaks are well split which suggests that there is a well-defined layered structure in the lattice.[43] The XRD data show that the air sample displays small peaks that correspond to Li_2CO_3, while these peaks are not present for the O_2 sample. This suggests that synthesis under O_2 is one way to prevent formation of Li_2CO_3 on the surface of the LO. As the O_2 sample did not contain any Li_2CO_3 impurities it was taken forward for further analysis.
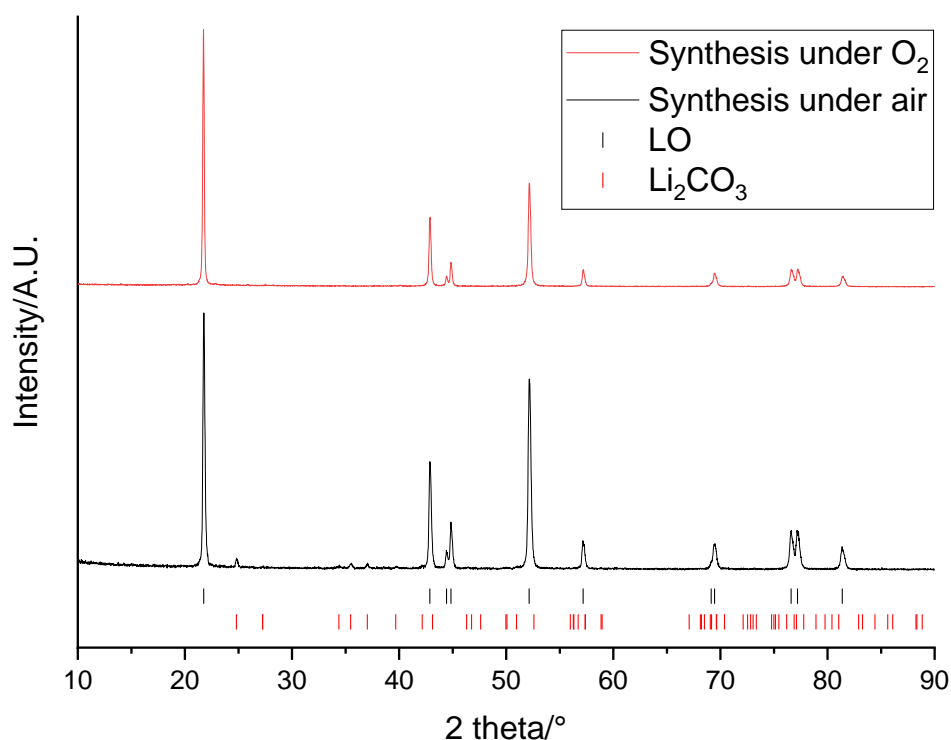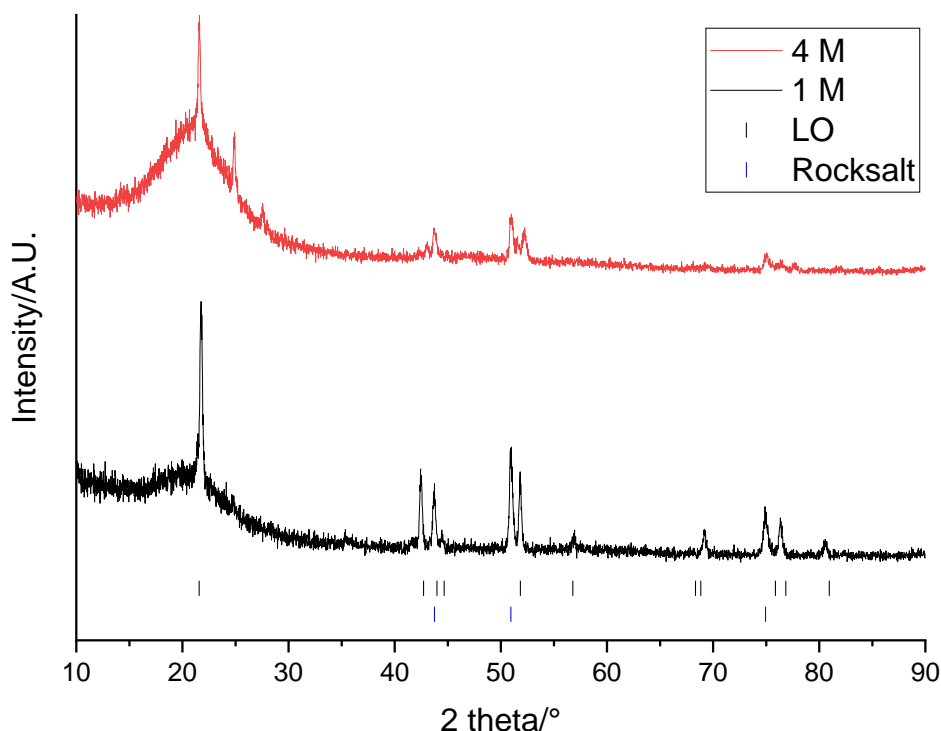
Figure 3-40: XRD pattern of recycled LO recovered from the EOL cathode. The initial hydrothermal step was performed with 2 M NaOH and heating at 150 °C (λ = 1.79 Å). The samples were then heated to 800 °C for 12h under an air (black) and O₂ (red) atmosphere. Tick marks correspond to LO (black) and Li₂CO₃ (red).

3.7.1.1. In depth analysis of recycled layered oxide

Additional techniques, such as SEM/EDX and electrochemical testing, were then performed on the recycled LO synthesised under an O_2 atmosphere.

Table 3-16 shows the lattice parameters for the recycled LO. The lattice parameters are as expected for NCA. The recycled LO has an I(003)/I(104) value > 1.2 which indicates that the cation mixing is negligible.[44] This shows that the recycled LO has formed the NCA structure with minimal cation mixing.

Table 3-16: Lattice parameters and intensity comparison for the recycled LO

	a/Å	c/Å	I(003)/I(104)
Recycled LO	2.8636(2)	14.164(8)	2.47

Figure 3-41 shows SEM/EDX images of the recycled LO. The SEM images show that the LO has a relatively small particle size (<30 μm). The EDX images show that Ni and Co are uniformly distributed across the surface while the Al is concentrated in certain regions. This could be due to Al being transferred from the current collector to the cathode in certain areas. EDX analysis of molar ratios gives the ratio of metals as $Ni_{0.83}Co_{0.14}Al_{0.03}$ which is consistent with NCA.
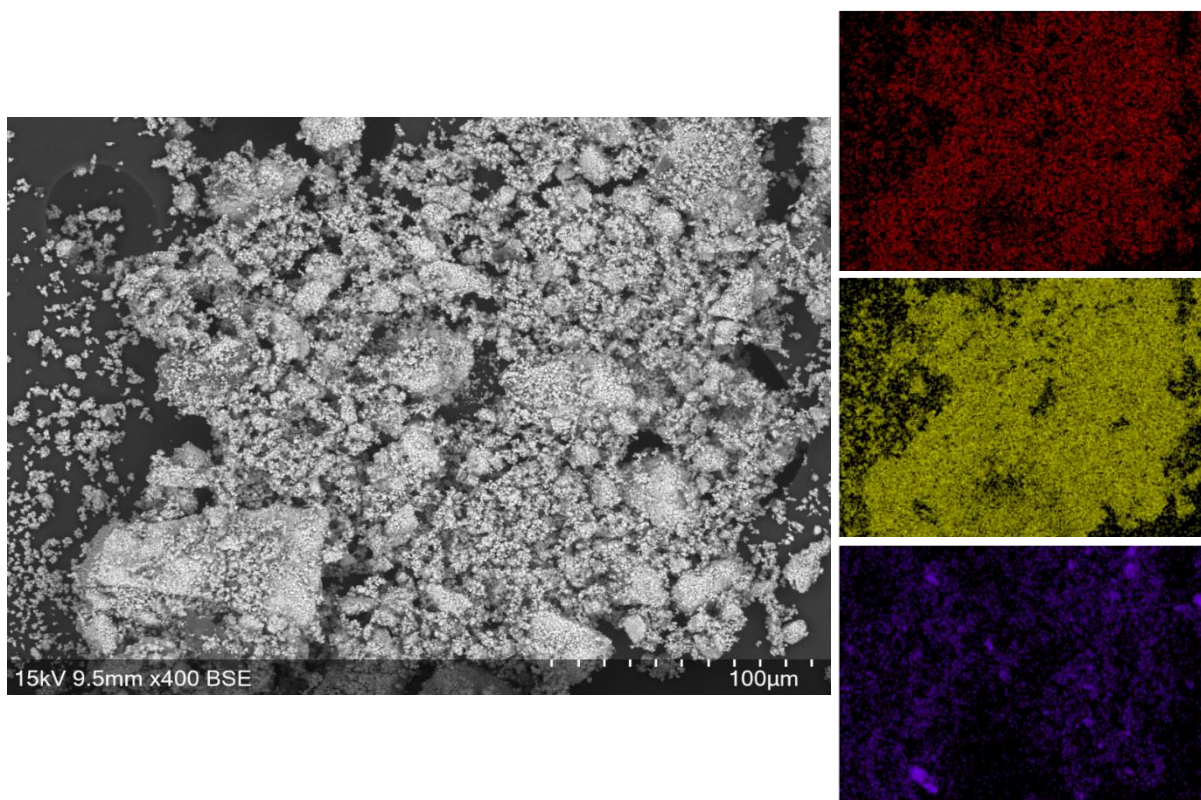
Figure 3-41: SEM (left) and EDX (right) images of recycled LO. EDX images shows Co (red, top), Ni (yellow, middle) and Al (purple, bottom).

Figure 3-42 shows the Raman spectrum for the recycled LO which displays a broad band at 520 cm^{-1}. The Raman spectrum for NCA normally has peaks at 475 and 554 cm^{-1}, which are due to O-Ni-O bending and Ni-O stretching modes respectively.[45] However, these peaks are often very broad and overlap, as shown here.[46] Unlike the recycled LMO (Figure 3-33), there are no additional bands due to the presence of other species.
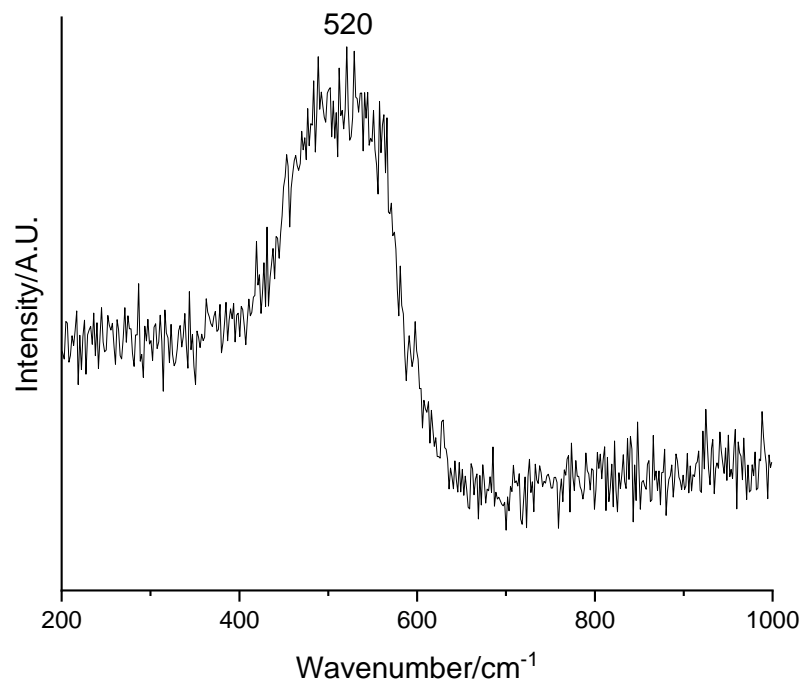
Figure 3-42: Raman spectrum of recycled LO recovered from the EOL cathode

Figure 3-43 shows the electrochemical data for the recycled LO. The voltage profile looks as expected for a NCA cathode. The recycled LO gives an initial specific discharge capacity of 141.1 mAhg^{-1} which decreases to 108.6 mAhg^{-1} after 10 cycles. This corresponds to a capacity retention of 77.0%. The capacity is considerably lower than pristine NCA (180-200 mAhg^{-1}). The low capacity could be due to Li deficiency or due to the testing method used. The electrochemical performance was tested using powder Swageloks cells due to the air sensitive nature of NCA. In Chapter 5, powder Swagelok cells are used extensively and problems relating to them will be explored in further detail. Further work is required to optimise both the synthesis conditions and electrochemical testing method for the recycled LO.
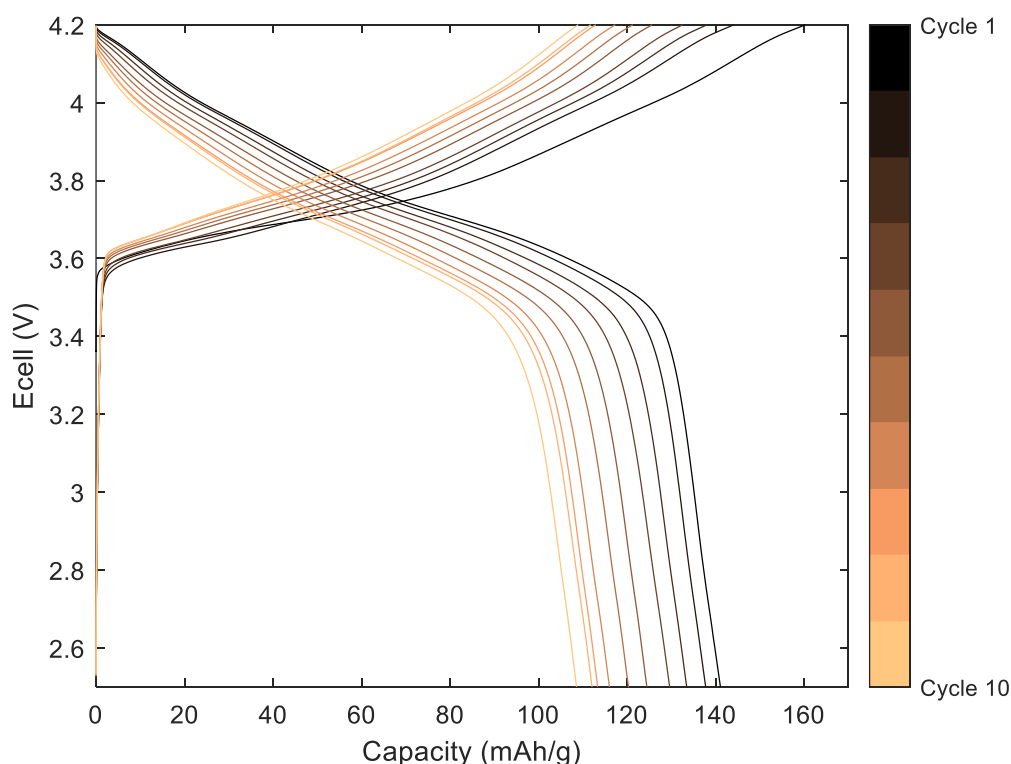
Figure 3-43: Galvanostatic charge-discharge profile of recycled LO recovered from the EOL cathode when cycled at 10 mAg⁻¹ between 2.5-4.2 V

In conclusion, it has been shown that it is possible to recycle the LO from the EOL cathode. However, the recycled LO has a lower capacity than pristine NCA. It is suspected that this lower capacity could be related to the electrochemical testing method and therefore the capacity could be increased by optimising the method used.

3.7.2. QC recycled layered oxide

Firstly, the QC LO was thermally treated to remove the PVDF. Two different heating methods were employed: heating at 900 °C with no extra Li and heating at 450 °C before regrinding and heating at 850 °C with 10% excess Li. Figure 3-44 shows the XRD patterns of the products after heating. In both cases the LO is present along with extra peaks at 43.8, 51.0 and 75.2° which are due to the presence of a rocksalt phase.

The rocksalt peaks are more intense in the double heat treatment sample suggesting that more of the rocksalt is formed when the sample is heated for longer. Unlike the thermally treated EOL samples (Figure 3-36), there is still some LO present. This suggests that the formation of the rocksalt is related to Li deficiencies within the LO. The EOL LO is more Li deficient and therefore more of the rocksalt phase is formed.
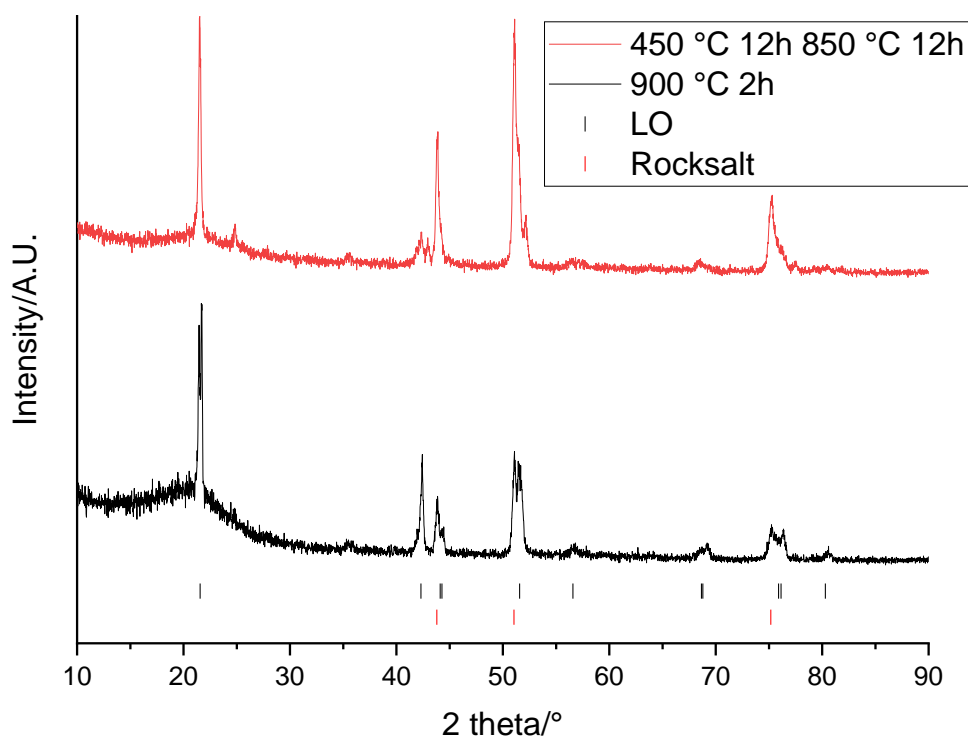
Figure 3-44: XRD patterns of recovered LO from the QC cathode when heated to 900 °C for 2h (black) and 450 °C for 12h followed by 850 °C for 12h (red) (λ = 1.79 Å). Tick marks correspond to rocksalt (black).

Subsequently, given the issues above with rock salt phase formation, the LO was treated using the hydrothermal method. 1 and 4 M NaOH concentrations were used. Figure 3-45 shows XRD patterns of the samples after hydrothermal treatment. In both cases, the hydroxide is present along with the LO. This shows that the LO does not fully convert to the hydroxide phase even at high NaOH concentrations. There is also

a peak at 51.0° in the 1 M sample which suggests that a rocksalt phase is also present alongside the other phases.
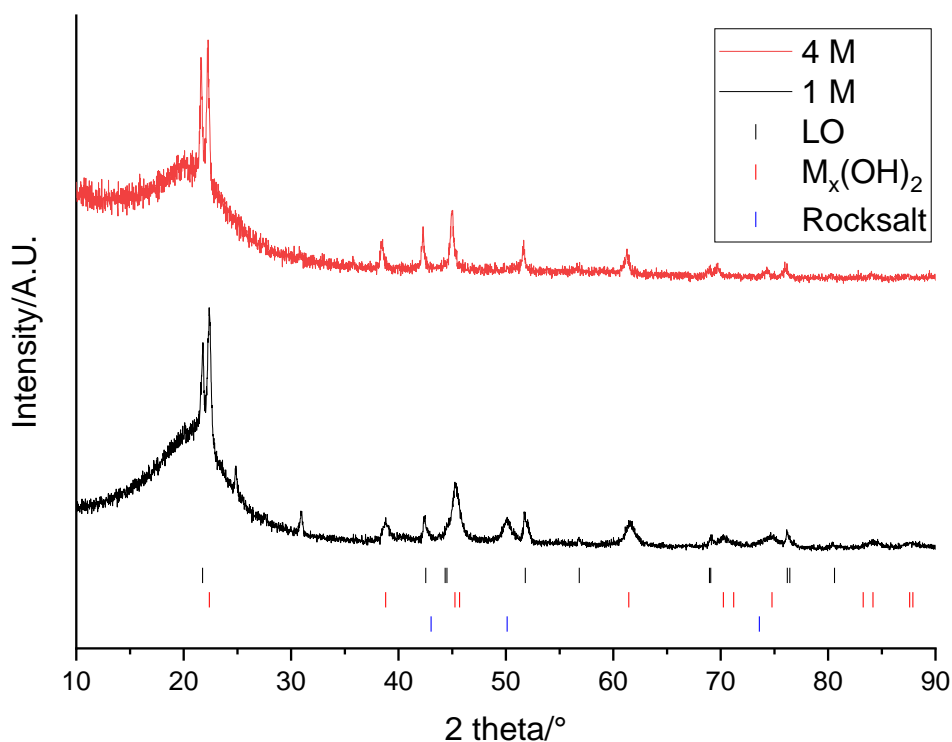
Figure 3-45: XRD of remaining LO from QC cathode after hydrothermal treatment with 1 M (black) and 4 M (red) NaOH (λ = 1.79 Å). Tick marks correspond to LO (black), $M_x(OH)_2$ (red) and rocksalt (blue).

The next step taken was to mix the hydrothermal samples with Li_2CO_3 followed by a heat treatment to try and reform the LO. Figure 3-46 shows that after heating both samples contained a LO and a rocksalt phase. These samples were not tested electrochemically as the presence of rocksalt phases has been shown to impact detrimentally upon the electrochemical performance of LO cathodes.[47,48]

Figure 3-46: XRD patterns of recycled LO recovered from the QC cathode. The initial hydrothermal step was performed with 1 M (black) and 4 M (red) NaOH (λ = 1.79 Å). The samples were then heated to 800 °C for 12h. Tick marks correspond to LO (black) and rocksalt (blue).

In conclusion, the QC LO appears to form rocksalt phases regardless of the method used to remove the PVDF binder. This could be due to several reasons: there may be a coating that is present on the QC cathode that prevents the thermal and hydrothermal treatments from working. Alternatively, the QC cathode is likely to have undergone minimal degradation and therefore it may be harder to remove the PVDF binder and therefore a rocksalt phase is forming because the PVDF is still present. Further work is required to see whether a method can be found to successfully reform the LO from the QC cathode.

3.8. Conclusions

Citric acid has been shown to work as an effective leaching agent for LMO powder. 1 M citric acid, 30 g/L (corresponding to 0.3g of LMO powder in 10 mL solution) and a 60 °C solution was found to fully leach LMO powder into solution within 4 minutes. A higher S:L ratio of 40g/L, was found to increase the pH of the solution and cause $Mn(C_6H_6O_7)(H_2O)$ to be precipitated.

Characterisation was performed on the Gen 1 Nissan Leaf cathodes and showed that the QC and EOL cathodes both contained of a mixture of LMO and a LO. The cathodes appear similar other than the presence of a degree of Li deficiency within the EOL cathode. Citric acid has also been shown to work as a selective leaching agent to remove LMO from these mixed cathode materials. The LMO is leached into solution while the LO is left solid in the remaining cathode along with the binder and amorphous carbon.

The optimum leaching conditions were found to be 0.3 g of cathode material in 10 mL of 1 M citric acid at 50 °C. This enables fast leaching of the LMO by 20 minutes. The LO is largely left inact within the solid cathode although some Ni, Co and Al is leached into solution. The leaching is most selective with these conditions as it results in the lowest levels of leaching from the LO phase. It also gives comparable results for both the QC and EOL cathodes, although there is increased Co leaching from the EOL cathode. Higher leaching temperatures and higher S:L ratios were found to result in precipitation of Mn citrates, which removes Mn from the solution.

It seems likely the selectivity of citric acid for the LMO phase is related to the pH of the solution, with the pH of the solution determining which citric acid species is present. With the conditions used, Mn has a much higher stability constant than Ni and therefore it will preferentially bind to the citrate ions. In turn this leads to LMO leaching being favoured and a selective leaching process.

LMO can then be recovered and recycled from the leaching solution. The recycled LMO displays a different electrochemical performance depending on the synthesis time used. The results show that heating at 700 °C for 12 hrs produces the optimum electrochemical results although the discharge capacity (88.8 mAhg^{-1} for the EOL recycled LMO) is still lower than pristine LMO. The lower capacity could be due to Li loss during the heating procedure, impurity elements affecting the electrochemical performance or crystallite size issues. Further analysis is required to identify the definitive cause.

It is also possible to recycle the LO after the leaching process. Thermal and hydrothermal treatments were investigated as possible ways to remove the PVDF binder remaining in the cathode after leaching. The hydrothermal treatment of the EOL LO resulted in a recycled LO with a discharge capacity (141.1 mAhg^{-1}) that was considerably lower than pristine NCA. In comparison, the LO from the QC cathode could not be successfully recycled as a rocksalt phase was formed after every method used. Further work is required to explain this and to determine whether a method can be found to successfully reform the LO from the QC cathode.

3.9. References

1   L. Li, J. Ge, R. Chen, F. Wu, S. Chen and X. Zhang, *Waste Manag.*, 2010, **30**, 2615–2621.

2   L. Li, J. Ge, F. Wu, R. Chen, S. Chen and B. Wu, *J. Hazard. Mater.*, 2010, **176**, 288–293.

3   S. Sakultung, K. Pruksathorn and M. Hunsom, *Asia-Pacific J. Chem. Eng.*, 2008, **3**, 374–379.

4   J. Marshall, D. Gastol, R. Sommerville, B. Middleton, V. Goodship and E. Kendrick, *Metals (Basel).*, 2020, **10**, 1–22.

5   A. Verma, R. Kore, D. R. Corbin and M. B. Shiflett, *Ind. Eng. Chem. Res.*, 2019, **58**, 15381–15393.

6   I. A. Mudunkotuwa and V. H. Grassian, *J. Am. Chem. Soc.*, 2010, **132**, 14986–14994.

7   A. L. Bacarella, E. Grunwald, H. P. Marshall and E. L. Purlee, *J. Org. Chem.*, 1955, **20**, 747–762.

8   W. D. Kumler and T. C. Daniels, *J. Am. Chem. Soc.*, 1935, **57**, 1929–1930.

9   L. L. Driscoll, A. Jarvis, R. Madge, J. Price, R. Sommerville, F. S. Totini, M. Bahri, B. L. Mehdi, E. Kendrick, N. D. Browning, P. K. Allan, P. A. Anderson and P. R. Slater, Phase-selective recovery and regeneration of end-of-life electric vehicle blended cathodes via selective leaching and direct recycling, *ChemRxiv*, 2023,

DOI:10.26434/chemrxiv-2023-56rkk. This content is a preprint and has not been peer-reviewed.

10   Y. F. Deng, Z. H. Zhou, H. L. Wan and S. W. Ng, *Acta Crystallogr., Sect. E Struct. Rep. Online*, 2003, **59**, m310.

11   J. Liu, D. Hu, T. Huang and A. Yu, *J. Alloys Compd.*, 2012, **518**, 58–62.

12   L. Gaines, Q. Dai, J. T. Vaughey and S. Gillard, *Recycling*, 2021, **6**, 1–18.

13   Z. Milojevic, P. S. Attidekou, M. Muhammad, M. Ahmeid, S. Lambert and P. K. Das, *J. Power Sources*, 2021, **506**, 230242.

14   K. Kanamura, H. Naito, T. Yao and Z. I. Takehara, *J. Mater. Chem.*, 1996, **6**, 33–36.

15   K. W. Nam, W. S. Yoon, H. Shin, K. Y. Chung, S. Choi and X. Q. Yang, *J. Power Sources*, 2009, **192**, 652–659.

16   H. Kondo, Y. Takeuchi, T. Sasaki, S. Kawauchi, Y. Itou, O. Hiruta, C. Okuda, M. Yonemura, T. Kamiyama and Y. Ukyo, *J. Power Sources*, 2007, **174**, 1131–1136.

17   M. Ahmeid, M. Muhammad, S. Lambert, P. S. Attidekou and Z. Milojevic, *J. Energy Storage*, 2022, **50**, 104562.

18   Y. Kobayashi, T. Kobayashi, K. Shono, Y. Ohno, Y. Mita and H. Miyashiro, *J. Electrochem. Soc.*, 2013, **160**, A1181–A1186.

19   I. Belharouak, W. Lu, D. Vissers and K. Amine, *Electrochem. commun.*, 2006, **8**,

329–335.

20   R. Robert, C. Bunzli, E. J. Berg and P. Novák, *Chem. Mater.*, 2015, **27**, 526–536.

21   M. Kunduraci and G. G. Amatucci, *J. Electrochem. Soc.*, 2006, **153**, A1345.

22   G. T. Park, S. Bin Kim, J. I. Yoon, N. Y. Park, M. C. Kim, S. M. Han, D. H. Kim, M. S. Kim and Y. K. Sun, *Adv. Energy Mater.*, 2024, **2400130**, 1–12.

23   P. Amico, P. G. Daniele, V. Cucinotta, E. Rizzarelli and S. Sammartano, *Inorganica Chim. Acta*, 1979, **36**, 1–7.

24   O. Y. Zelenin, *Russ. J. Coord. Chem. Khimiya*, 2007, **33**, 346–350.

25   B. Ammundsen, G. R. Burns, M. S. Islam, H. Kanoh and J. Rozière, *J. Phys. Chem. B*, 1999, **103**, 5175–5180.

26   M. Bianchini, F. Fauth, E. Suard, J. B. Leriche, C. Masquelier and L. Croguennec, *Acta Crystallogr. Sect. B Struct. Sci. Cryst. Eng. Mater.*, 2015, **71**, 688–701.

27   Y. J. Wei, L. Y. Yan, C. Z. Wang, X. G. Xu, F. Wu and G. Chen, *J. Phys. Chem. B*, 2004, **108**, 18547–18551.

28   W. Xu, Y. Zheng, Y. Cheng, R. Qi, H. Peng, H. Lin and R. Huang, *ACS Appl. Mater. Interfaces*, 2021, **13**, 45446–45454.

29   C. H. Shen, R. S. Liu, R. Gundakaram, J. M. Chen, S. M. Huang, J. S. Chen and C. M. Wang, *J. Power Sources*, 2001, **102**, 21–28.

30   A. Patterson, *Phys. Rev.*, 1939, **56**, 978–982.

31   B. Slautin, D. Alikin, D. Rosato, D. Pelegov, V. Shur and A. Kholkin, *Batteries*, 2018, **4**, 21.

32   C. M. Julien and A. Mauger, *AIMS Mater. Sci.*, 2018, **5**, 650–698.

33   S. Niketic, M. Couillard, D. Macneil and Y. Abu-Lebdeh, *J. Power Sources*, 2014, **271**, 285–290.

34   P. Pasierb, S. Komornicki, M. Rokita and M. Rękas, *J. Mol. Struct.*, 2001, **596**, 151–156.

35   G. Li, H. Li, Y. Mo, L. Chen and X. Huang, *J. Power Sources*, 2002, **104**, 190–194.

36   J. L. Wang, Z. H. Li, J. Yang, J. J. Tang, J. J. Yu, W. B. Nie, G. T. Lei and Q. Z. Xiao, *Electrochim. Acta*, 2012, **75**, 115–122.

37   X. Li, J. Zhang, D. Song, J. Song and L. Zhang, *J. Power Sources*, 2017, **345**, 78–84.

38   J. Li, Y. Wang, L. Wang, B. Liu and H. Zhou, *J. Mater. Sci. Mater. Electron.*, 2019, **30**, 14580–14588.

39   E. C. Giles, P. R. Slater, P. A. Chater, P. K. Allan and P. A. Anderson, Pvdf-Induced Degradation of Nmc-Based Cathode Materials During Direct Recycling, *SSRN,* 2022, DOI:10.2139/ssrn.4264094. This content is a preprint and has not been peer-reviewed.

40   P. R. Slater, *J. Fluor. Chem.*, 2002, **117**, 43–45.

41   M. F. Rabuni, N. M. Nik Sulaiman, M. K. Aroua and N. A. Hashim, *Ind. Eng. Chem. Res.*, 2013, **52**, 15874–15882.

42   G. V. Zhuang, G. Chen, J. Shim, X. Song, P. N. Ross and T. J. Richardson, *J. Power Sources*, 2004, **134**, 293–297.

43   W. He, J. Qian, Y. Cao, X. Ai and H. Yang, *RSC Adv.*, 2012, **2**, 3423–3429.

44   H. He, J. Dong, D. Zhang and C. Chang, *Ceram. Int.*, 2020, **46**, 24564–24574.

45   G. Peng, X. Yao, H. Wan, B. Huang, J. Yin, F. Ding and X. Xu, *J. Power Sources*, 2016, **307**, 724–730.

46   J. Lei, F. McLarnon and R. Kostecki, *J. Phys. Chem. B*, 2005, **109**, 952–957.

47   S. K. Jung, H. Gwon, J. Hong, K. Y. Park, D. H. Seo, H. Kim, J. Hyun, W. Yang and K. Kang, *Adv. Energy Mater.*, 2014, **4**, 1–7.

48   F. Lin, I. M. Markus, D. Nordlund, T. C. Weng, M. D. Asta, H. L. Xin and M. M. Doeff, *Nat. Commun.*, 2014, **5**, 3529.

Chapter 4: Upcycling $LiMn_2O_4$ into $LiMn_{1.5}Ni_{0.5}O_4$

4.1. Introduction

Chapter 3 showed that $LiMn_2O_4$ (LMO) can be recycled from mixed LMO-LO cathodes. However, the recycled LMO has a poor electrochemical performance and LMO is no longer widely used as a commercial cathode material. Therefore, there is little value in recycling it and instead, there is more value in upcycling the LMO to form new higher value cathode materials, such as $LiMn_{1.5}Ni_{0.5}O_4$ (LMNO). As mentioned in section 1.3.1., LMNO is gaining interest as a cathode material due to its high operating voltage (~ 4.7 V) which gives it a higher energy density and enables it to be used in high power, high voltage applications. Ni acts to increase the operating voltage, however, it also increases the price of the cathode as Ni has a higher price than Mn.[1] The presence of Ni also changes the cation ordering within the structure and enables LMNO to form either an ordered or a disordered structure.

In the literature, LMNO has been synthesised by a variety of methods such as solid state, sol-gel, co-precipitation, and hydrothermal.[2] The different synthesis methods and reaction conditions have an impact upon the structure, physical properties, and electrochemical performance of LMNO. The disordered structure is normally synthesised by heating to high temperatures (~ 900 °C) while the ordered structure is typically synthesised by annealing a disordered sample at lower temperatures (~ 700 °C).[3,4] Ordered LMNO has a flat voltage profile with a voltage plateau at ~ 4.7 V due to Ni redox activity. In contrast, disordered LMNO contains Mn^{3+} and this results in an additional voltage plateau at 4 V due to Mn^{3+} redox. LMNO often contains $Li_xNi_{1-x}O$

impurities, and these are more common when heating at the higher temperatures required to form the disordered phase. It has been suggested that impurity formation is due to decreased Ni solubility in the LMNO phase at high temperatures or due to O loss within the structure.[5,6]

The focus of this chapter was to use the Li/Mn leaching solution as a precursor to synthesise LMNO. Different synthesis conditions were used to control the ordering and consequent electrochemical performance of the final product. The differences between LMNO made from the quality-control rejected (QC) and end-of-life (EOL) cathodes was also investigated.

4.2. Experimental

4.2.1. Synthesis of pristine $LiMn_{1.5}Ni_{0.5}O_4$

The pristine LMNO was synthesised by adding stoichiometric amounts of LMO, $Li(NO_3)$ and $Ni(NO_3).6H_2O$ to 10 mL of 1 M citric acid. The solution was stirred and heated to 60 °C for 30 minutes. The solution was then dried on a hotplate before being put into an oven at 350 °C for 8 hours. The remaining residue was then ground by hand in a pestle and mortar and placed into an alumina crucible. This crucible was then put into a furnace at 700-900 °C for 12 hours under an air/O_2 atmosphere as per the literature.[4]

4.2.2. Synthesis of $LiMn_{1.5}Ni_{0.5}O_4$ from QC and EOL cathode materials

The upcycled LMNO was synthesised using a similar method to the pristine synthesis. The cathode materials and leaching procedure from Chapter 3 (section 3.2.) were used to obtain the leaching solution containing LMO. This was then filtered to separate it from the remaining LO. The required stoichiometric amounts of $Li(NO_3)$ and $Ni(NO_3).6H_2O$ were added to the solution. The amounts added were calculated by weighing the starting cathode and the remaining LO after leaching; these values could then be used to calculate the mass of LMO in solution. The solution was stirred and heated to 60 °C for 30 minutes. The solution was then dried on a hotplate before being put into an oven at 350 °C for 8 hours. The remaining residue was then ground by hand in a pestle and mortar and placed into an alumina crucible. This crucible was then put into a furnace at 650-900 °C for 12 hours under an air/O_2 atmosphere with a 50/300 °C hr^{-1} ramping rate.

4.2.3. Rietveld refinements

Rietveld refinements were carried out using the XRD data. The primary phase (LMNO) was fitted with the $Fd\bar{3}m$ space group. Some of the samples contained an additional $Li_xNi_{1-x}O$ phase and this was fitted to the $Fm\bar{3}m$ space group. Lattice parameters, sample displacement, strain and crystallite size were refined for all samples. When the samples contained multiple phases, the weight fractions were also refined. Constraints were added to make the strain equivalent for all the phases and to make the sum of the weight fractions equal to 1. The similarities in scattering factor of Mn and Ni preclude the possibility of refining fractional occupancies. Therefore, Mn and Ni were set to their intended ratios and not refined further. Atomic positions and thermal parameters were fixed to sensible values. An example Rietveld refinement plot for pristine LMNO is shown in Figure 4-1.
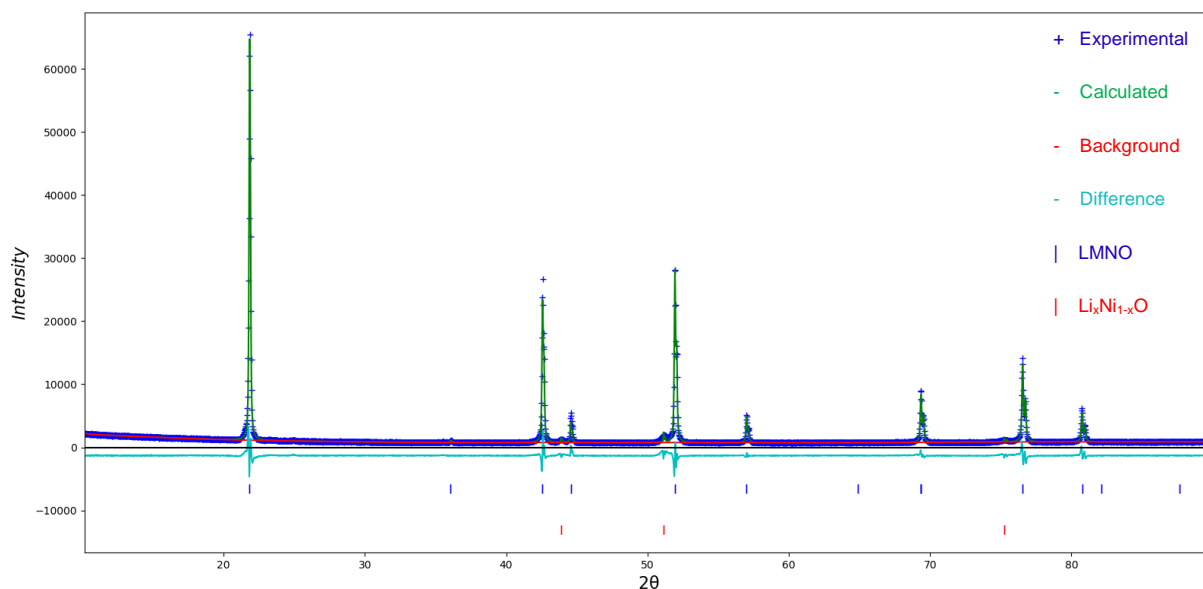
Figure 4-1: Rietveld refinement plot for pristine LMNO synthesised at 900 °C (λ = 1.79 Å). R_{wp} = 9.22% and GOF = 3.34.

4.3. Pristine $LiMn_{1.5}Ni_{0.5}O_4$

Firstly, LMNO was synthesised using pristine reagents and different synthesis conditions. Different synthesis conditions were used to investigate how this altered the LMNO structure and electrochemical properties.

Pristine LMNO was made using a solution-based method. This method was chosen as it can easily be used as a subsequent step following the LMO recycling process investigated in Chapter 3. Samples were made by heating at 700 °C for 12 hours; one sample was heated under air and one sample was heated under O_2. Figure 4-2 shows that in both instances LMNO was formed with the desired spinel structure ($Fd\bar{3}m$ space group). For the sample heated in air, there are also peaks at 43.7, 50.9 and 74.9° which are due to $Li_xNi_{1-x}O$ (3.2 wt%). $Li_xNi_{1-x}O$ is a common impurity for LMNO and is usually formed when the synthesis is performed at higher temperatures, as this results in a decrease in the Ni solubility within the spinel structure.[5] Previous work in the literature, has also shown that heat treatments in O_2 help to ensure a single phase product.[7] The LMNO has a lattice parameter of 8.1716(3) Å and 8.1735(6) Å for the air and O_2 samples respectively. This shows that both heat treatments give a product with a very similar lattice parameter which is also similar to values obtained in the literature. This initial work showed the importance of O_2 heat treatments to produce a pure LMNO product. All further synthesises will be performed under O_2 unless stated otherwise.
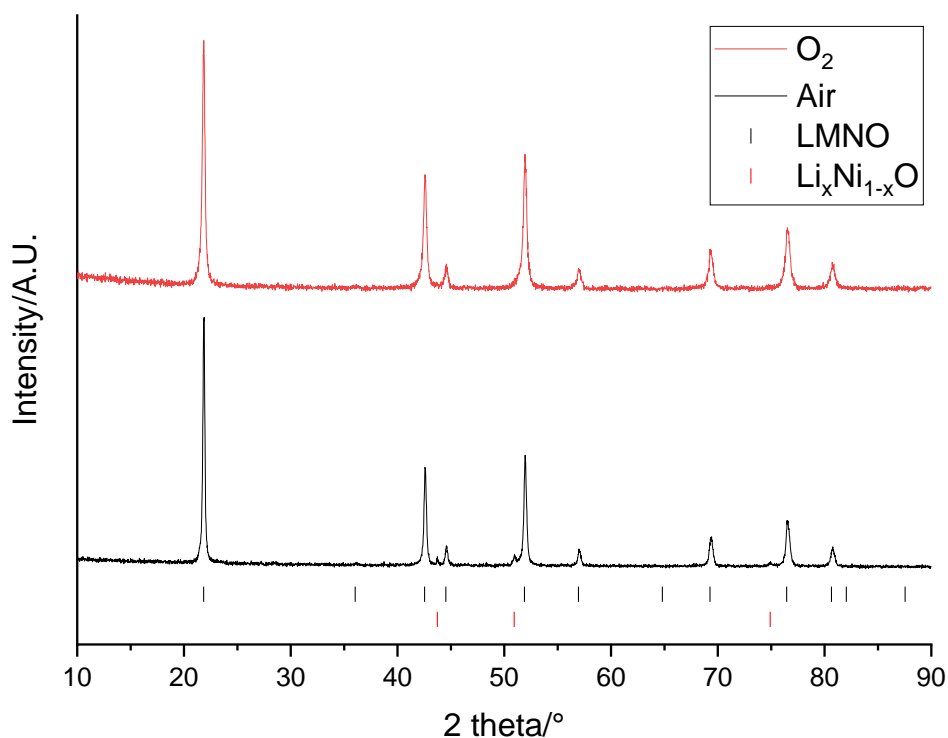
Figure 4-2: XRD pattern of LMNO made using pristine reagents and heating under air (black) and O_2 (red) at 700 °C (λ = 1.79 Å). Tick marks correspond to LMNO (black) and $Li_xNi_{1-x}O$ (red).

Figure 4-3 shows the Raman spectrum for pristine LMNO synthesised at 700 °C under O_2. There are peaks at 140, 195, 345, 380, 470, 502, 569, 586 and 614 cm^{-1}. The Raman spectrum matches closely to spectra shown in the literature for ordered LMNO.[8,9] The peaks at 380, 470, 502, 586 and 614 cm^{-1} are due to Ni-O bonding while the peak at 569 cm^{-1} is due to Mn-O bonding and the peak at 345 cm^{-1} is due to Li-O bonding. The peaks at 140 and 195 cm^{-1} are due to lattice translation modes.
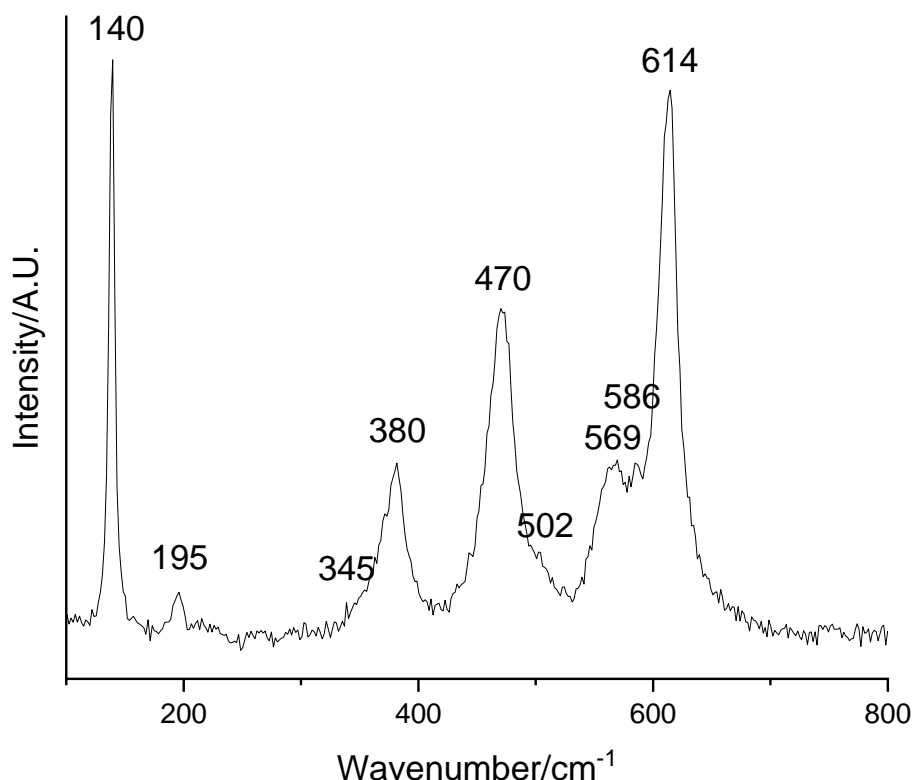
Figure 4-3: Raman spectrum of pristine LMNO synthesised at 700 °C under O_2

Figure 4-4 shows the electrochemical data for pristine LMNO synthesised at 700 °C under O_2. The LMNO was cycled to a high voltage limit (4.9 V) to enable the Ni redox couples to activate. The voltage profile looks as expected for ordered LMNO with a voltage plateau at ~ 4.7 V due to the $Ni^{2+/3+}$ and $Ni^{3+/4+}$ redox couples.[4] The voltage plateau has a voltage step in the middle and there is a distinction between the regions corresponding to the $Ni^{2+/3+}$ and $Ni^{3+/4+}$ redox couples. Normally the ordered phase produces a completely flat voltage plateau, and this suggests that there is a small amount of disorder within the structure. The dQ/dV plot has two peaks on both charge and discharge and these peaks are separated by 25 mV. This separation is close to the 20 mV separation obtained for ordered LMNO in the literature.[10]
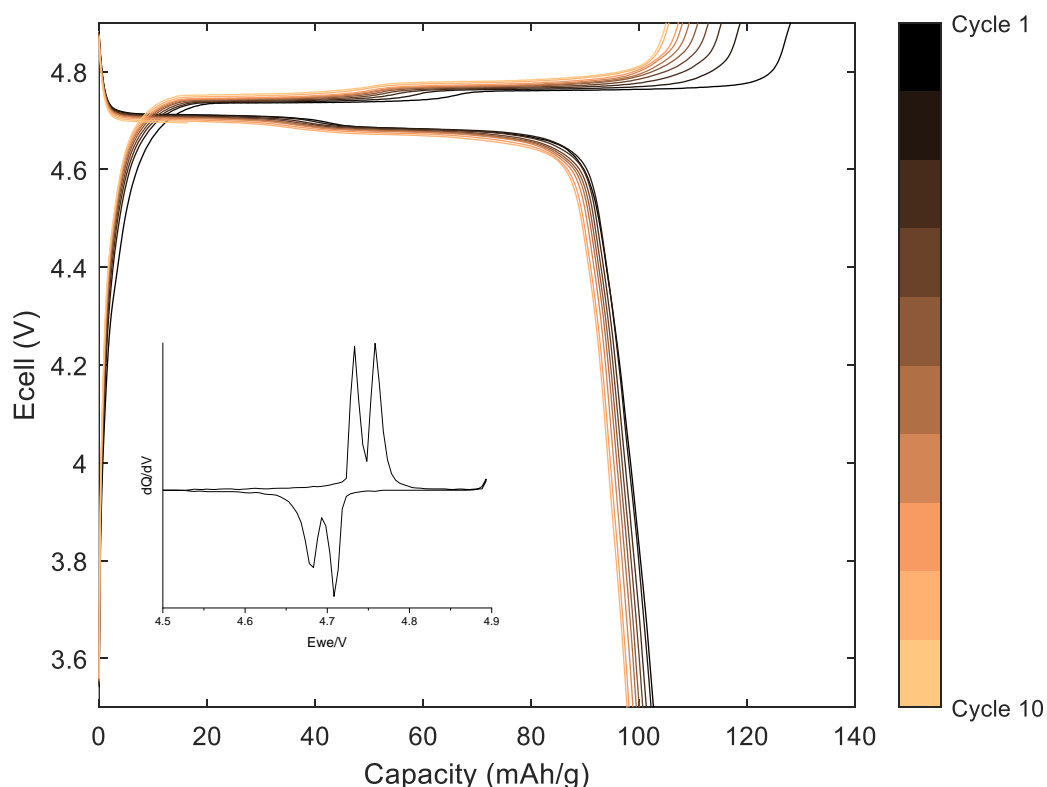
Figure 4-4: Galvanostatic charge-discharge profile of pristine LMNO synthesised at 700 °C under O_2 cycled at 10 mAg^{-1} between 3.5-4.9 V

Figure 4-4 shows that the specific discharge capacity is low, starting at 102.6 $mAhg^{-1}$ and falling to 97.7 $mAhg^{-1}$ by 10 cycles. This is considerably lower than the discharge capacities obtained in the literature for LMNO (135 $mAhg^{-1}$).[11] Furthermore, the specific charge capacity also decreases during cycling, starting at 128.0 $mAhg^{-1}$ but falling to 118.7 $mAhg^{-1}$ by the second cycle. The charge capacity is much higher than the discharge capacity showing that some of the Li is not being inserted back into the cathode during discharge. This also shows that Li is being lost after each cycle as the charge capacity is decreasing. The sample was not kept in a glovebox for the duration between material synthesis and making cells. Therefore, the sample was remade and kept in a glovebox to see if this improved the electrochemical performance.

Figure 4-5 shows the electrochemical data for pristine LMNO synthesised at 700 °C (same as Figure 4-4) when stored in glovebox. The overall voltage profile is similar to figure 4-4 although the plateau at ~ 4.7 V looks flatter. This suggests that the sample is more ordered and that some level of disorder is introduced when the sample is left in air for an appreciable amount of time. The LMNO gives an initial specific discharge capacity of 118.7 mAhg^{-1} which decreases to 112.3 mAhg^{-1} after 10 cycles. The discharge capacity is much higher than Figure 3 showing that keeping the sample in a glovebox also helps to achieve a higher capacity. This suggests that long-term air exposure causes sample degradation.
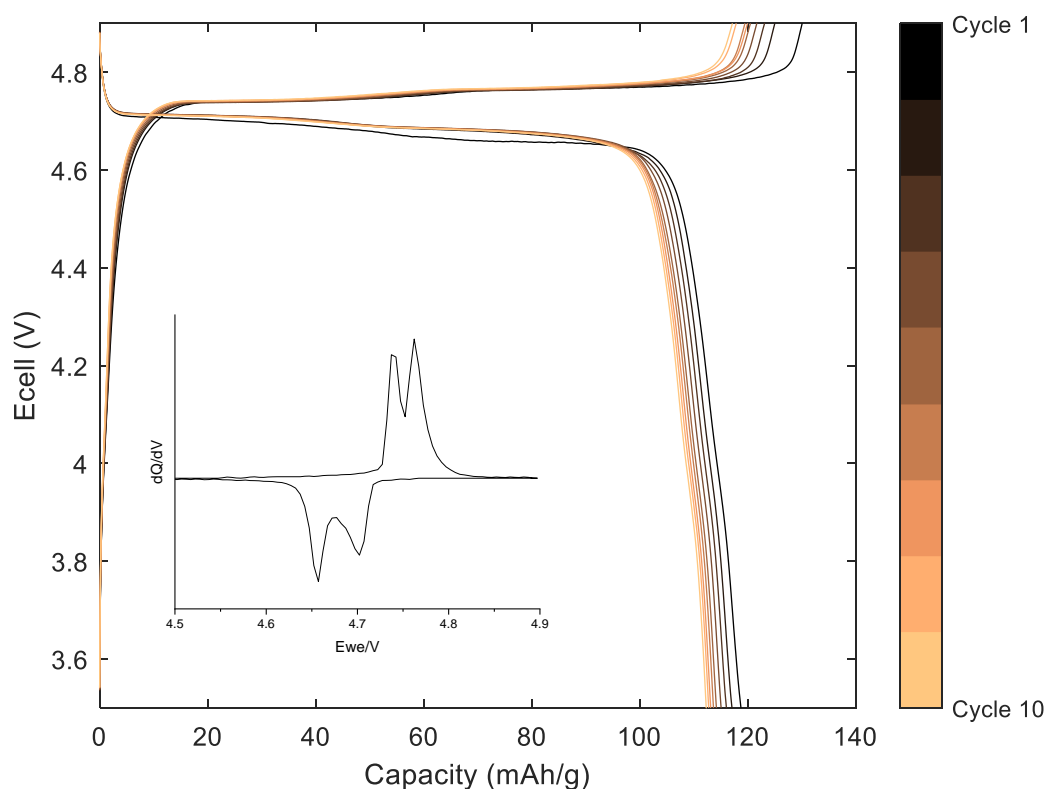
Figure 4-5: Galvanostatic charge-discharge profile and dQ/dV (inset) of pristine LMNO synthesised at 700 °C under O$_2$ (stored in glovebox) cycled at 10 mAg^{-1} between 3.5-4.9 V

Figure 4-6 shows the discharge capacity against cycle number for pristine LMNO synthesised at 700 °C and stored in a glovebox. The specific discharge capacity

decreases to 100.1 mAhg^{-1} after 50 cycles which corresponds to a capacity retention of 84.3%. The capacity fade is probably due to the electrolyte as the electrolyte has not been optimised in this work. LMNO can be cycled to high voltages, however, at these high voltages the electrolyte degrades and therefore over time this causes issues such as capacity fade.[12] Alternative electrolytes or additives can be used to improve the stability of the electrolyte at these high voltages and therefore improve the capacity fade.
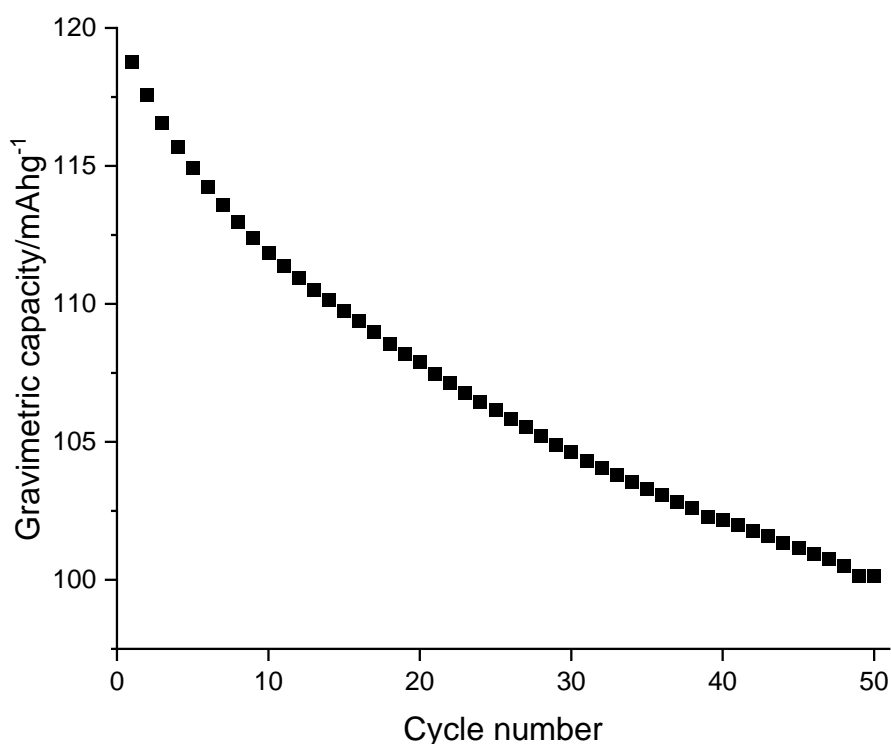
Figure 4-6: Discharge capacity of pristine LMNO synthesised at 700 °C under O$_2$

In the literature, synthesis at higher temperatures results in formation of the disordered phase. At lower temperatures, the ordering of Ni^{2+} and Mn^{4+} ions results in a reduction in the symmetry and therefore a move from the *Fd$\bar{3}$m* to the *P*4$_3$32 space group.[3] The synthesis was repeated with heating at higher temperature (900 °C) to try and form the disordered structure. Figure 4-7 shows the XRD patterns of pristine LMNO made at

both temperatures (700 and 900 °C). These XRD patterns were taken over a longer time (6 hrs) to allow the $P4_332$ peaks to be detected if present. In both cases, the patterns match to the $Fd\bar{3}m$ space group. Figures 4-4 and 4-5 showed that LMNO synthesised at 700 °C had a voltage profile matching to ordered LMNO. However, the XRD pattern shown here does not have the extra reflections matching to the $P4_332$ space group. This suggests that the sample is not fully ordered. The LMNO has a lattice parameter of 8.1635(4) Å and 8.1671(1) Å for 700 and 900 °C respectively. The ordered phase normally has a slightly smaller lattice parameter than the disordered phase due to all the Mn being Mn^{4+}, which has a smaller ionic radius than Mn^{3+}.[13] The 700 °C sample has a smaller lattice parameter fitting to the proposition that it is the more ordered sample. Electrochemical and Raman data for the 900 °C LMNO will confirm whether it is disordered LMNO.
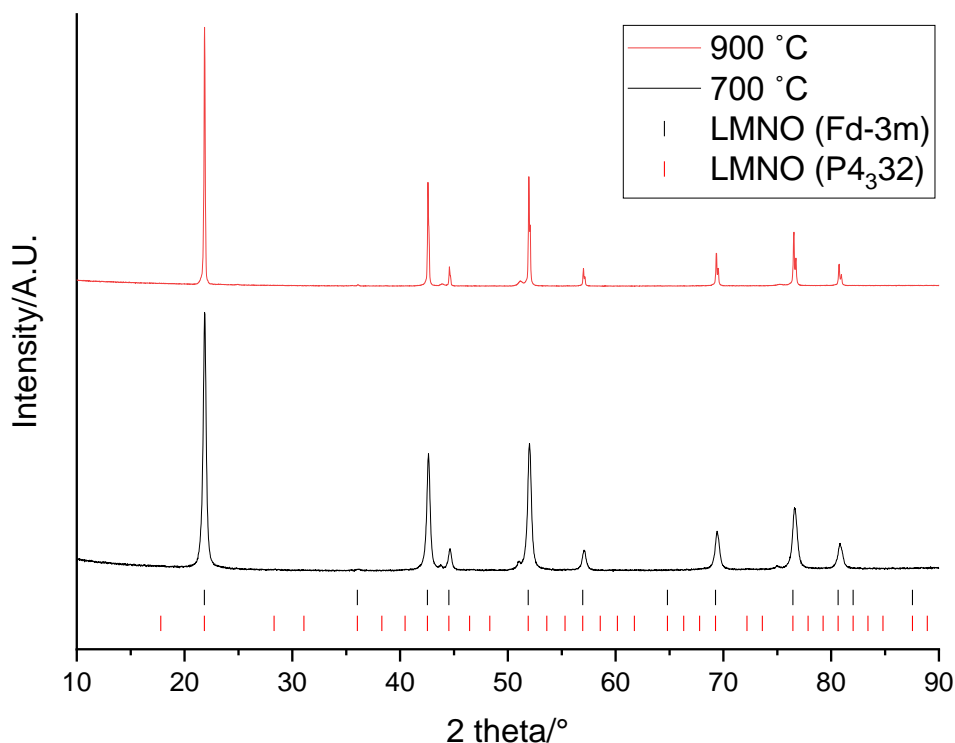
Figure 4-7: XRD pattern of LMNO made using pristine reagents and heating to 700 °C (black) and 900 °C (red) (λ = 1.79 Å). Tick marks correspond to LMNO with Fd-3m (black) and P4₃32 (red) space group.

Figure 4-8 shows the Raman spectrum for pristine LMNO synthesised at 900 °C. There are peaks at 160, 210, 400, 493, 596 and 632 cm^{-1}. This is characteristic of Raman spectra shown in the literature for disordered LMNO.[9,14] Compared to ordered LMNO (Figure 4-3), the Raman modes are broadened and exhibit lower intensities, especially the peak at 160 cm^{-1} which is considerably less intense. The Raman bands become broader due to the Ni and Mn ordering becoming less significant.
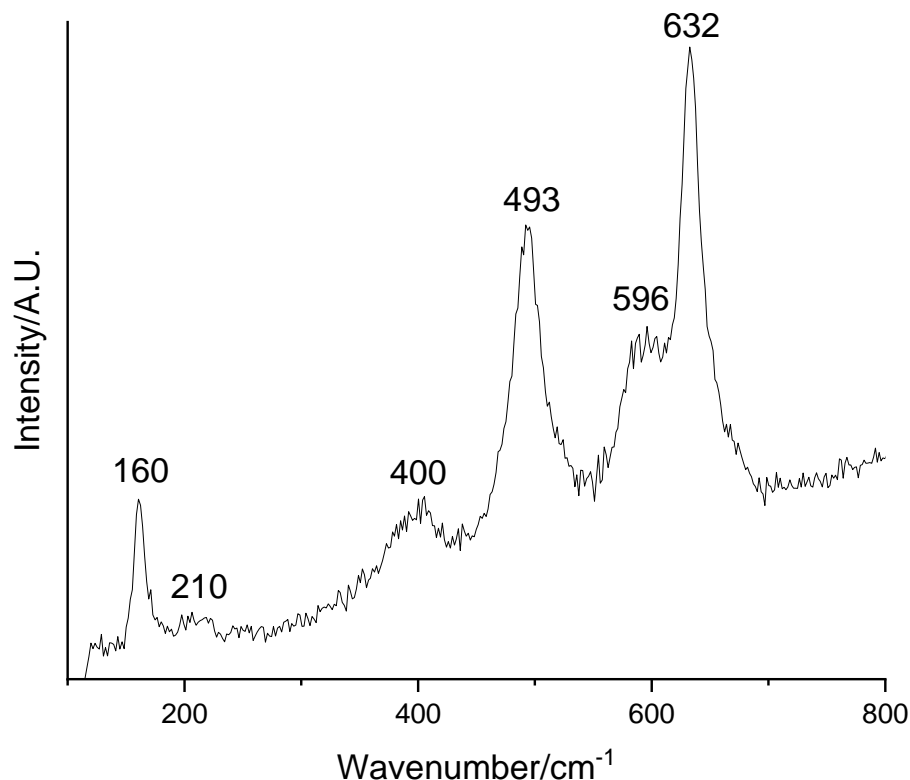
Figure 4-8: Raman spectrum of pristine LMNO synthesised at 900 °C

Figure 4-9 (above) shows the electrochemical data for pristine LMNO synthesised at 900 °C. The voltage profile looks as expected for disordered LMNO with voltage plateaus at ~ 4.7 and ~ 4 V.[4] The voltage plateau at ~ 4.7 V is clearly separated into two distinct regions corresponding to the two different Ni redox couples while the voltage plateau at 4 V is due to the $Mn^{3+/4+}$ redox couple. Mn^{3+} is commonly present in disordered LMNO and this is attributed to reduction of Mn^{4+} to Mn^{3+} at higher temperatures. It is interesting that this has occurred even though the synthesis was performed under an O_2 atmosphere. The dQ/dV plot shows the two peaks at 4.7 V due to Ni redox but also a small broad peak at 4 V due to the Mn redox. The peaks at 4.7 V are separated by 55 mV which matches to the value of 60 mV obtained for disordered LMNO in the literature.[10] Figure 4-9 (below) shows that the disordered LMNO (900 °C)

has an initial specific discharge capacity of 118.3 $mAhg^{-1}$ that falls to 108.5 $mAhg^{-1}$ after 50 cycles. This corresponds to a capacity retention of 91.7%. The initial discharge capacity is the same as ordered LMNO (700 °C). In contrast, the disordered LMNO has a significantly improved capacity retention compared to ordered LMNO (84.3% capacity retention after 50 cycles). In the literature, the improved capacity retention of disordered LMNO has been linked to the presence of Mn^{3+}.[15]
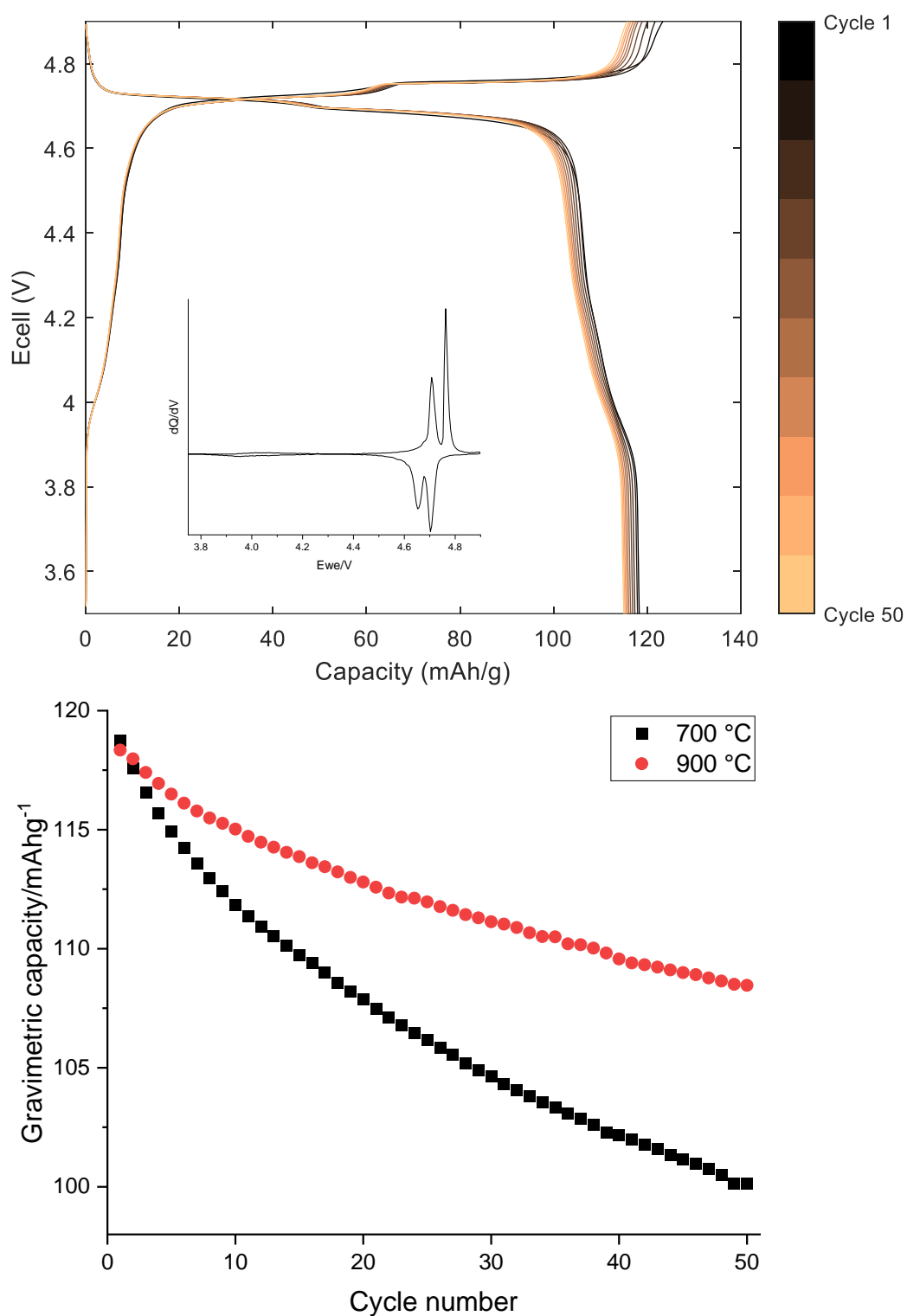
Figure 4-9: Galvanostatic charge-discharge profile and dQ/dV (inset) of pristine LMNO synthesised at 900 °C cycled at 10 mAg⁻¹ between 3.5-4.9 V (above) and discharge capacity of pristine LMNO synthesised at 700 (black) and 900 (red) °C (below)

Figure 4-10 shows the VT-XRD patterns for pristine LMNO when heated. It is worth mentioning that the VT-XRD was performed under air rather than O_2 due to equipment capability. As the sample is heated it becomes more crystalline and the individual peaks become separated and more distinct. The peaks match to the LMNO phase throughout showing that the sample loosely has the LMNO structure prior to the furnace step. The $Li_xNi_{1-x}O$ impurity is present, and the peaks corresponding to this become stronger as the sample is heated and becomes more crystalline. The $Li_xNi_{1-x}O$ impurity does not appear to be present in the pattern at 900 °C which suggests that high temperatures are required to incorporate this impurity phase into the LMNO structure. This does not agree with behaviour seen in the literature where impurity formation occurs at higher temperatures and therefore could be due to the slower ramping rates utilised when performing a VT-XRD.[16]
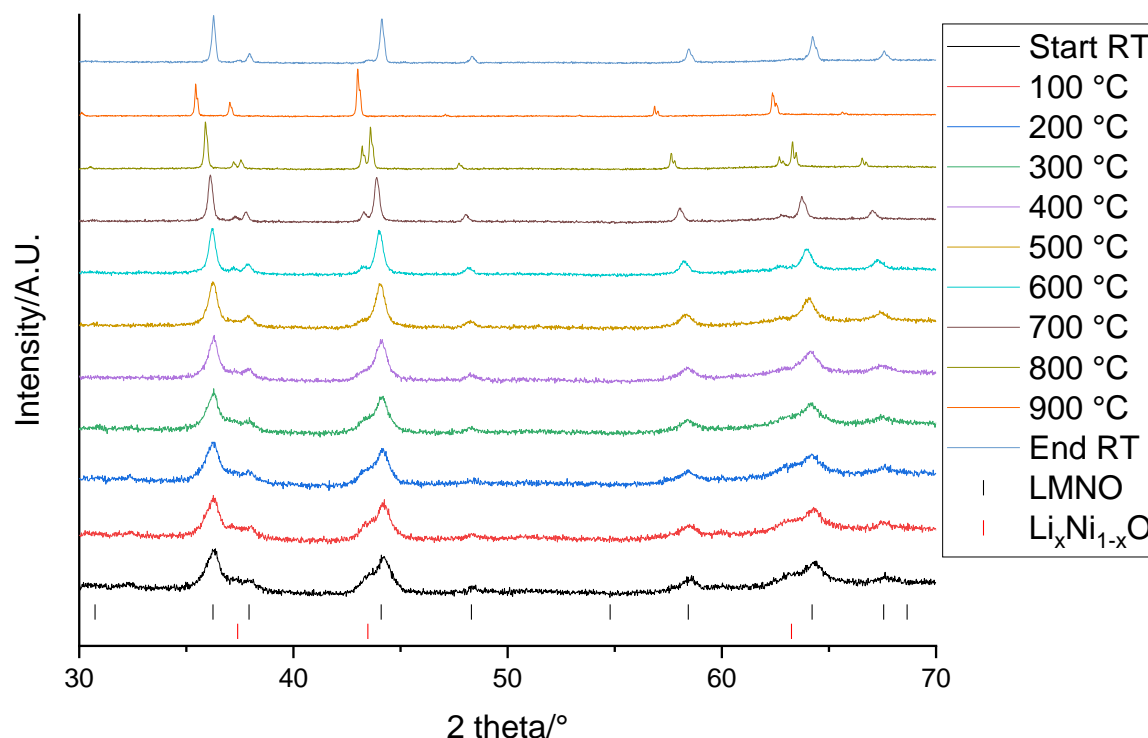
*Figure 4-10: VT-XRD patterns of pristine LMNO heated from 100 to 900 °C at 100 °C intervals
(λ = 1.54 Å). Tick marks correspond to LMNO (black) and $Li_xNi_{1-x}O$ (red).*

In conclusion, the ordering of LMNO can be tuned by altering the synthesis temperature used. At low temperature (700 °C) the ordered phase is formed while at higher temperatures (900 °C) the disordered phase is formed. The ordered phase has been formed without an initial high temperature heating step often used in the literature. While XRD analysis shows no differences between the ordering of the two phases, they have different Raman spectra. The spectrum for the disordered phase has considerably more broad and less intense peaks when compared to the spectrum for the ordered phase. The electrochemical performance of the two phases also differs; they have a similar discharge capacity however they have different voltage profiles and capacity retention behaviour (Figure 4-5 and 4-9).

4.4. Synthesis of upcycled $LiMn_{1.5}Ni_{0.5}O_4$ from EOL material

In this section, LMNO was synthesised using materials recovered from the EOL cathode. The EOL cathode was leached using the process explored in Chapter 3 and the leaching solution was then used as a source of Mn and Li for the synthesis of LMNO.

4.4.1. Initial synthesis

Initially the synthesis method from section 4.3. was utilised. 700 °C was used as a starting point to attempt to form the ordered structure. The amount of LMO in solution was calculated using ICP-OES analysis of the leaching solution. Stoichiometric amounts of Ni and Li nitrates were added into the solution to provide the desired LMNO composition.

Figure 4-11 shows the XRD pattern of the upcycled LMNO synthesised using material recycled from the EOL cathode (EOL LMNO). The product has the desired spinel structure but there are also peaks matching to a $Li_xNi_{1-x}O$ impurity phase (6.1 wt%, calculated from Rietveld refinement). This was not present when LMNO was made using pristine reagents under these conditions. The EOL LMNO has a lattice parameter of 8.1611(3) Å. The lattice parameter is smaller than the lattice parameter for pristine LMNO (8.1635 Å) suggesting that all the Mn is Mn^{4+}, as the presence of Mn^{3+} would result in a larger lattice parameter. Alternatively, the presence of a small amount of Co or Al remaining from the leaching procedure could be causing the smaller lattice parameter.[17,18] XRD data confirm that the LMNO structure has been formed, however,

Raman and electrochemical data are needed to confirm whether the structure is ordered or disordered.
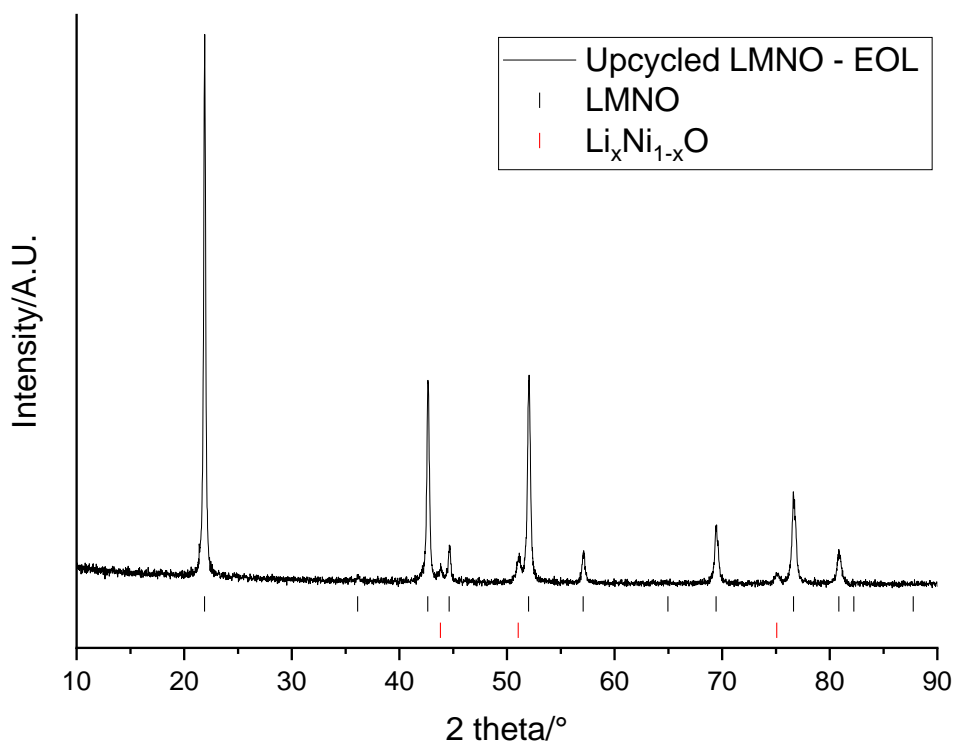
Figure 4-11: XRD pattern of EOL LMNO (λ = 1.79 Å). Tick marks correspond to LMNO (black) and $Li_xNi_{1-x}O$ (red).

Figure 4-12 shows the Raman spectrum of EOL LMNO. The Raman spectrum matches more closely to the disordered phase (Figure 4-8) as it contains broad peaks with low intensity, especially the peak at 160 cm^{-1} which has much lower intensity than seen for the ordered phase (Figure 4-3). Electrochemical data should confirm whether the disordered phase has been formed.
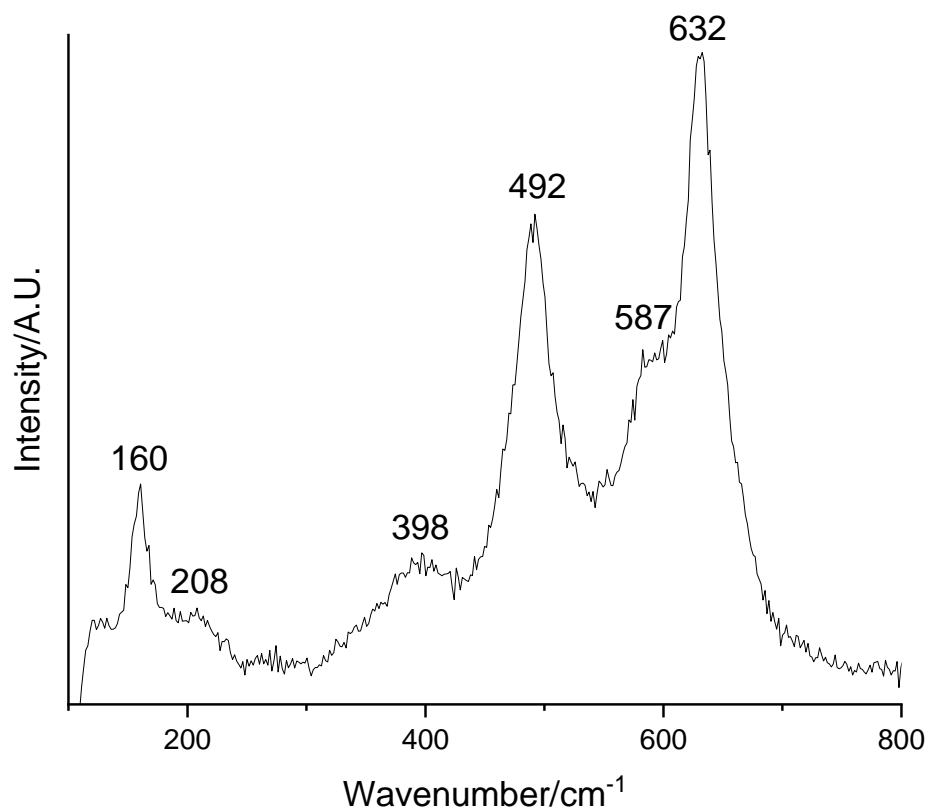
Figure 4-12: Raman spectrum of EOL LMNO

Figure 4-13 shows the electrochemical data for EOL LMNO. The voltage profile matches disordered LMNO with voltage plateaus at ~ 4.7 and ~ 4 V (matching to Figure 4-9). The dQ/dV plot shows two peaks at 4.7 V due to Ni redox but also a small broad peak at 4 V due to Mn redox. The dQ/dV peaks at 4.7 V are separated by 48 mV, which is closer to the value of 60 mV usually obtained for disordered LMNO. This suggests that the smaller lattice parameter of the EOL LMNO is due to small amounts of Co or Al doping as the redox activity at ~ 4 V indicates that some Mn^{3+} is present. The sample has an initial specific discharge capacity of 118.8 mAhg^{-1}. Unlike, pristine LMNO (Figure 4-9), the capacity remains at 118.8 mAhg^{-1} after 10 cycles. This shows that the EOL LMNO has an improved capacity retention compared to pristine LMNO. This could

be due to small amounts of Co or Al doping helping to improve the stability and prevent capacity fade.
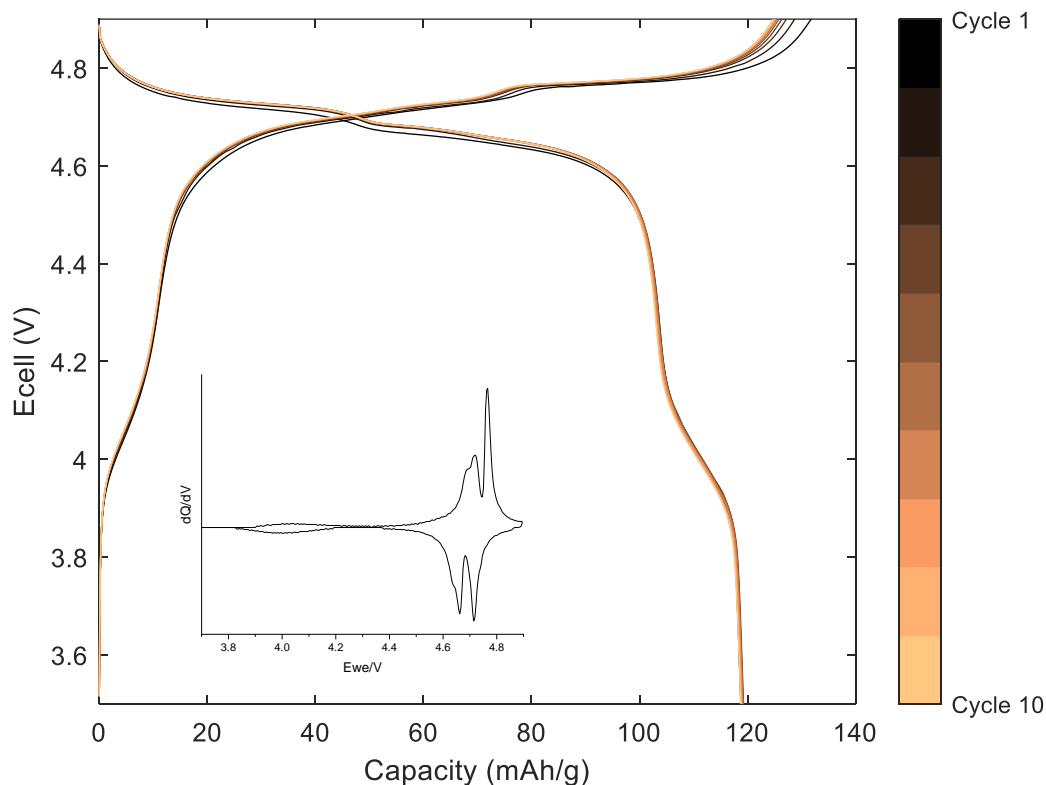
Figure 4-13: Galvanostatic charge-discharge profile and dQ/dV (inset) of EOL LMNO cycled at 10 mAg^{-1} between 3.5-4.9 V

These results show that LMNO can be synthesised using materials recycled from EOL cathodes. However, the EOL LMNO has different ordering and electrochemical properties to pristine LMNO synthesised using the same conditions. When heated at 700 °C, pristine LMNO forms the ordered phase while EOL LMNO forms the disordered phase. This is interesting as it suggests that the synthesis of the upcycled LMNO proceeds in a different way resulting in a product with different ordering. Furthermore, the EOL LMNO has superior capacity retention compared to the pristine LMNO.

4.4.2. Alternative synthesis procedures

In this section, the synthesis conditions were altered to investigate their impact upon the EOL LMNO structure, purity, and electrochemical performance. The conditions being investigated will be stated and any other synthesis conditions will be the same as mentioned in section 4.4.1..

4.4.2.1. Ni content

Firstly, $LiMn_{2-x}Ni_xO_4$ (x = 0.2, 0.4, 0.5 and 0.6 nominally, based upon amounts of reagents) was prepared by introducing different levels of Ni precursor into the leaching solution following the method in Section 4.4.1.. This was done to investigate whether the Ni content has an impact upon the structure ordering or electrochemical performance.

Figure 14-4 shows the XRD patterns of the products formed. In all cases, the desired LMNO structure is formed. The samples with higher Ni contents all contain a small amount of the $Li_xNi_{1-x}O$ impurity phase (Table 4-1). Only the sample with a low Ni content of x = 0.2 has no impurity present. Figure 4-14 shows that as the Ni content increases, the peaks are shifted toward higher angles, which corresponds to a smaller lattice parameter at higher Ni contents (Table 4-1). This is consistent with the literature, where decreasing the Ni^{2+} content increases the Mn^{3+}/Mn^{4+} ratio, leading to a small expansion in the lattice.[19]
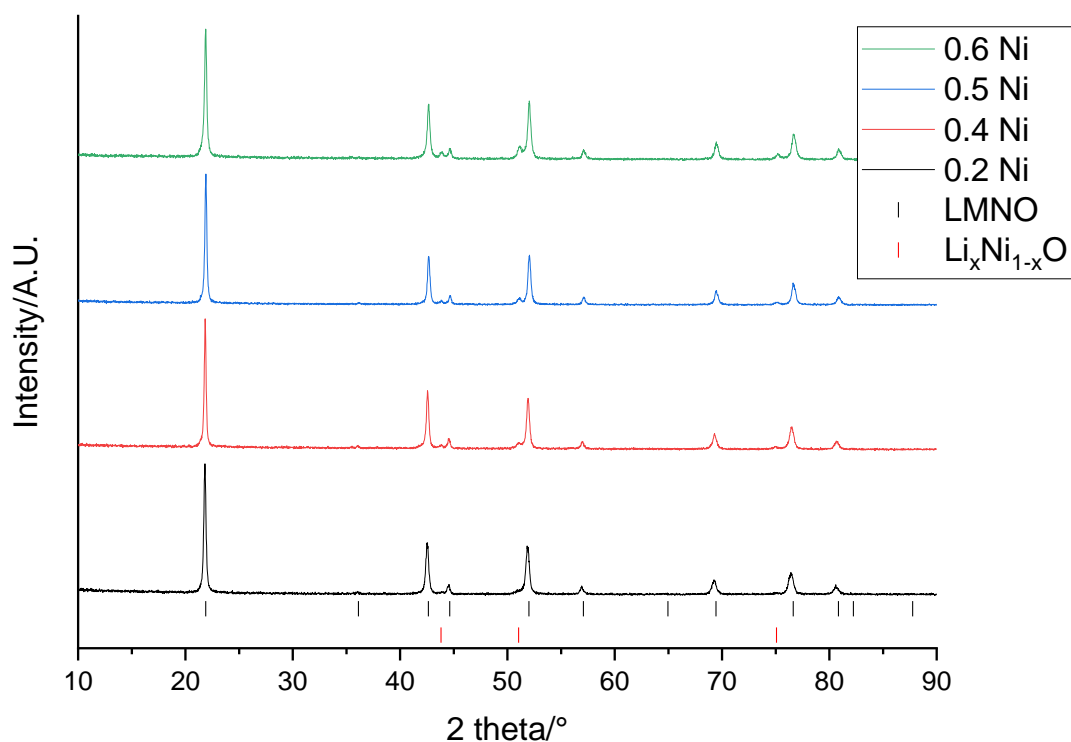
Figure 4-14: XRD pattern of EOL LiMn$_{2-x}$Ni$_x$O$_4$ where x = 0.2 (black), 0.4 (red), 0.5 (blue) and 0.6 (green) (λ = 1.79 Å). Tick marks correspond to LMNO (black) and Li$_x$Ni$_{1-x}$O (red).

Table 4-1: Lattice parameters of EOL LiMn$_{2-x}$Ni$_x$O$_4$ where x = 0.2, 0.4, 0.5 and 0.6 and wt% of Li$_x$Ni$_{1-x}$O

Cathode	a/Å	Li$_x$Ni$_{1-x}$O wt/%
0.2	8.1817(4)	0
0.4	8.1771(3)	5.4(1)
0.5	8.1611(3)	6.1(1)
0.6	8.1586(4)	11.2(1)

Figure 4-15 shows the Raman spectra for the different samples. For all the samples, the spectra look similar and show peaks with similar intensities in similar positions. The spectra all match to the disordered phase (Figure 4-8) suggesting that changing the Ni content does not have an impact upon the sample ordering.
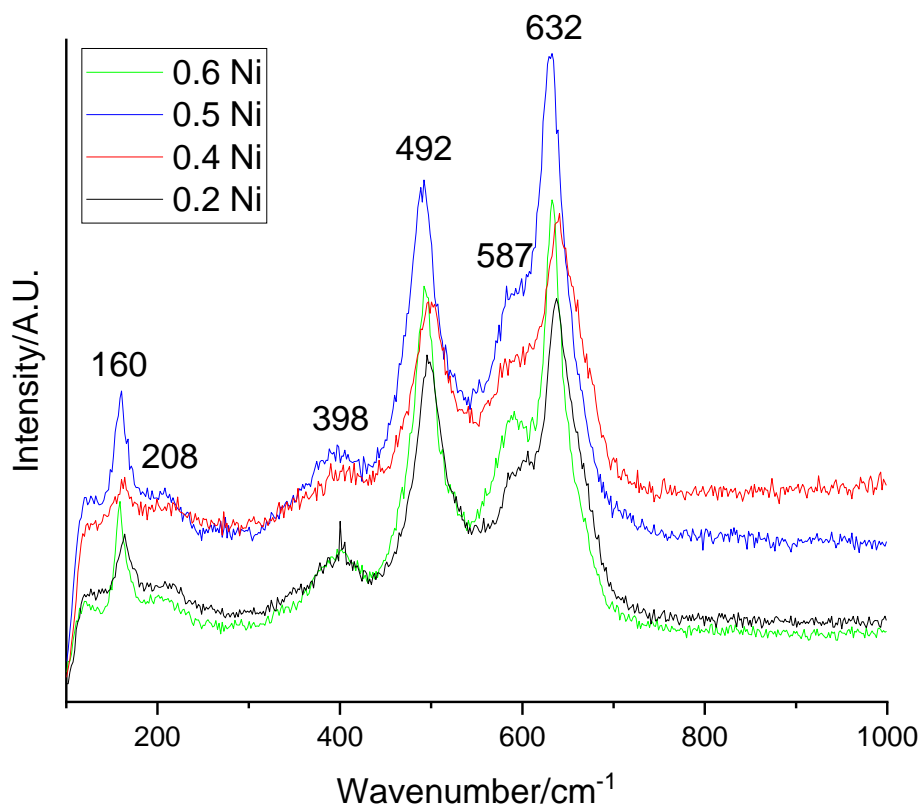
Figure 4-15: Raman spectra of EOL $LiMn_{2-x}Ni_xO_4$ where x = 0.2 (black), 0.4 (red), 0.5 (blue) and 0.6 (green).

Figure 4-16 shows the electrochemical performance of the different samples. The performance differs in two mains ways: the shape of the voltage profile and the charge/discharge capacity. Firstly, looking at the voltage profiles, the plateau at ~ 4 V decreases in size as the Ni content increases. This corresponds to a decrease in intensity of the 4 V peak in the dQ/dV plots. For x = 0.6, the plateau at 4 V is no longer present. This plateau is due to Mn^{3+} redox activity and therefore shows that Mn^{3+} is

present in the x = 0.2, 0.4 and 0.5 samples. As the Ni content increases, the Mn oxidation state should increase however, the presence of the $Li_xNi_{1-x}O$ impurity in the x = 0.4, 0.5 and 0.6 samples reduces the Ni content in the LMNO phase which could be causing the Mn oxidation state to be lower than expected based upon the stoichiometry alone. The Raman spectra show that all the samples are disordered (Figure 4-15) which suggests that any differences in the electrochemical performance are due to the Ni content rather than the structure ordering.
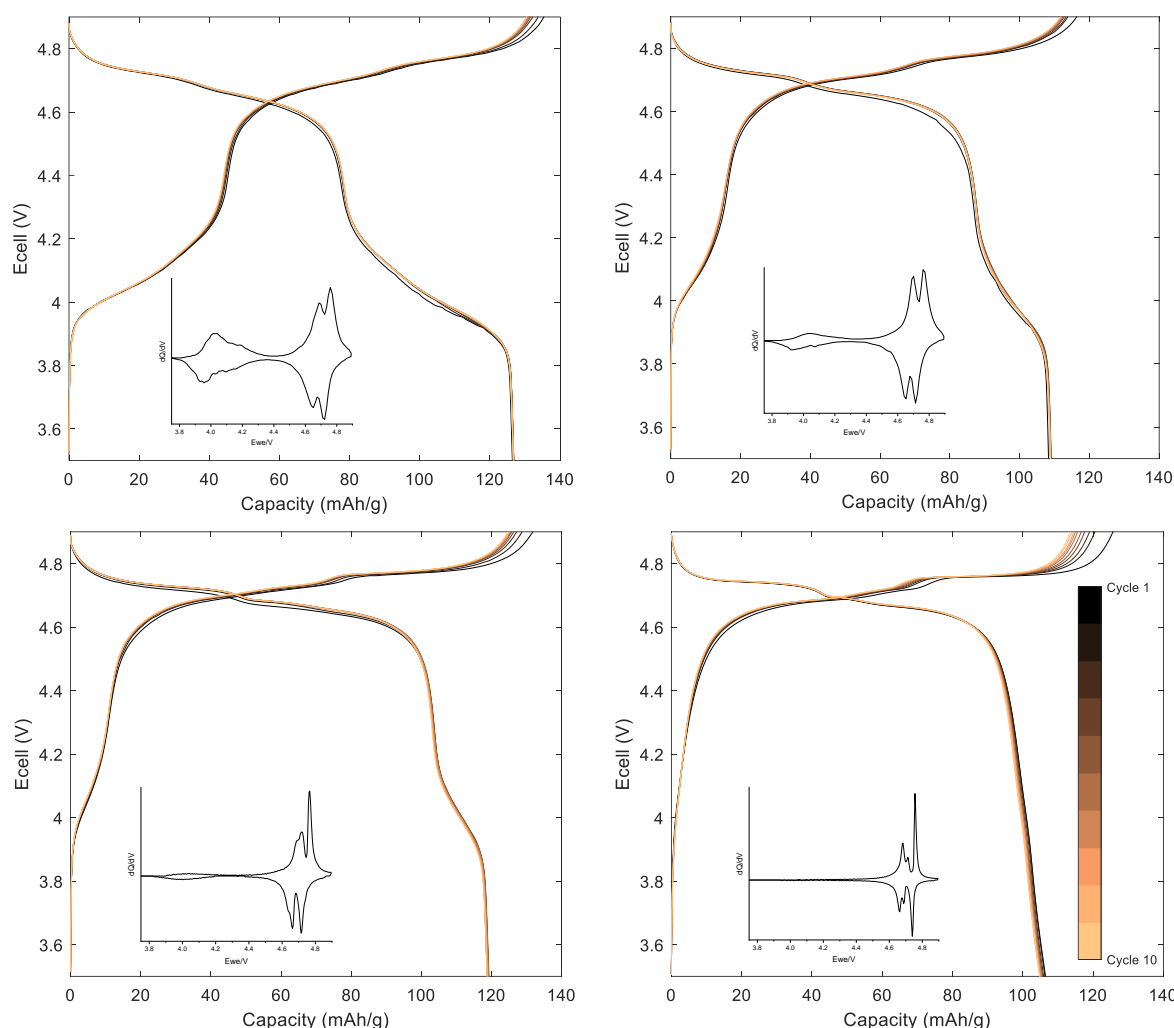
Figure 4-16: Galvanostatic charge-discharge profile and dQ/dV (inset) of EOL $LiMn_{2-x}Ni_xO_4$ where x = 0.2 (top left), 0.4 (top right), 0.5 (bottom left) and 0.6 (bottom right) cycled at 10 mAg^{-1} between 3.5-4.9 V

Table 4-2 shows the first cycle total charge/discharge capacity of each sample along with the discharge capacity contribution from the 4.7 V region. It shows that there is no trend between the total charge/discharge capacity and Ni content. However, it does show that the charge capacity is around 10 $mAhg^{-1}$ higher than the discharge capacity which suggests that some of the Li that is removed during charging is not inserted back into the structure upon discharging, perhaps related to potential electrolyte decomposition. For x = 0.6, the discrepancy between the charge and discharge

capacity is even higher (19 mAhg^{-1}) suggesting that the problem is exacerbated in this sample. Table 4-2 also shows that as the Ni content increases, the discharge capacity contribution from the 4.7 V region increases indicating an increased capacity contribution from Ni^{2+} redox activity. Figure 4-16 also shows that the samples all have a good capacity retention over 10 cycles. Again, this shows that EOL LMNO samples have improved capacity retention compared to pristine LMNO (Figure 4-9).

Table 4-2: First cycle total charge/discharge capacities of EOL LiMn$_{2-x}$Ni$_x$O$_4$ where x = 0.2, 0.4, 0.5 and 0.6

x	Charge capacity/mAhg^{-1}	Discharge capacity/mAhg^{-1}	Discharge capacity provided by 4.7 V plateau/%
0.2	135.4	126.4	61.6
0.4	116.4	108.3	80.4
0.5	131.8	118.8	86.4
0.6	125.7	106.5	100.0

In conclusion, this shows that changing the Ni content of LMNO changes the electrochemical performance. These changes to the electrochemistry are due to changes in the Mn oxidation state due to changing the Ni content, rather than changes to the structure ordering.

4.4.2.2. Furnace temperatures and cooling rates

Next, the synthesis was repeated using different temperatures (650, 700 and 900 °C) and cooling rates (50 and 300 °C hr^{-1}). In the literature, a lower temperature in combination with a slow cooling rate favours formation of the ordered phase.[4]

Figure 4-17 shows the XRD patterns of the products made using the different synthesis conditions: 650 °C (50 °C/hr), 700 °C (50 °C/hr), 700 °C (300 °C/hr) and 900 °C (300 °C/hr). The samples all formed the desired LMNO structure along with the $Li_xNi_{1-x}O$ impurity phase. Table 4-3 shows that there are small differences between the lattice parameters of the different samples. Faster cooling rates resulted in larger lattice parameters which could indicate that there is less Mn^{3+} present in these samples. The impurity phase is present in all the samples however, there are lower amounts present in the sample synthesised at 900 °C. This does not fit to behaviour seen in the literature for pristine LMNO where impurity formation is favoured at higher temperatures.[16] It therefore suggests that there may be differences between the pristine and EOL LMNO which influence impurity formation.
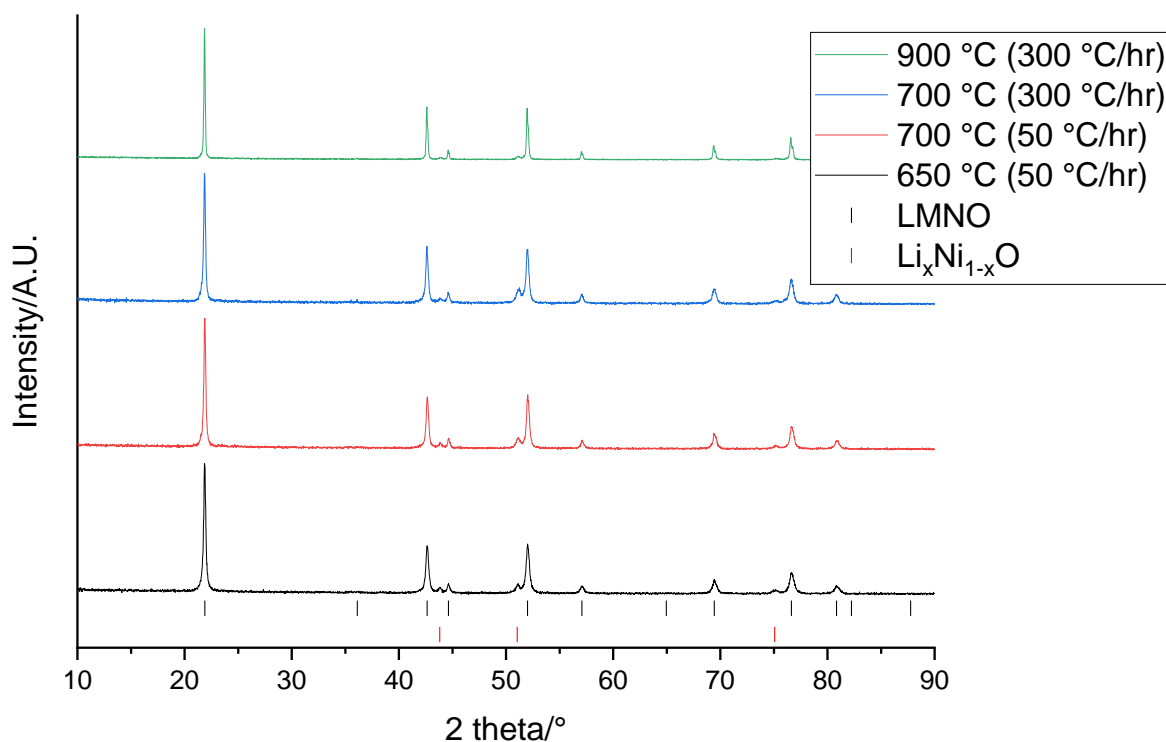
Figure 4-17: XRD pattern of EOL LMNO synthesised at 650 °C [50 °C/hr] (black), 700 °C [50 °C/hr] (red), 700 °C [300 °C/hr] (blue) and 900 °C [300 °C/hr] (red) (λ = 1.79 Å). Tick marks correspond to LMNO (black) and $Li_xNi_{1-x}O$ (red).

Table 4-3: Lattice parameters and wt% of $Li_xNi_{1-x}O$ impurity phase of EOL LMNO synthesised with different temperatures and cooling rates

Temperature/°C	Cooling rate/°C hr^{-1}	a/Å	$Li_xNi_{1-x}O$ wt/%
650	50	8.1595(3)	8.1(1)
700	50	8.1593(3)	9.5(1)
700	300	8.1646(3)	11.1(1)
900	300	8.1639(1)	3.8(1)

Figure 4-18 shows the Raman spectra of the EOL LMNO made using different synthesis temperature and cooling rates. The spectra look largely similar although for both the slow cooled samples (50 °C/hr), the band at 160 cm^{-1} appears to be more intense. This may indicate that there are increased levels of order within the slow cooled samples, as this peak is significantly more intense for ordered LMNO (Figure 4-3). However, the spectra still more closely resemble that of disordered LMNO therefore suggesting that although the slower cooling rate helps to promote order it has not fully transitioned the EOL LMNO to forming the ordered structure.
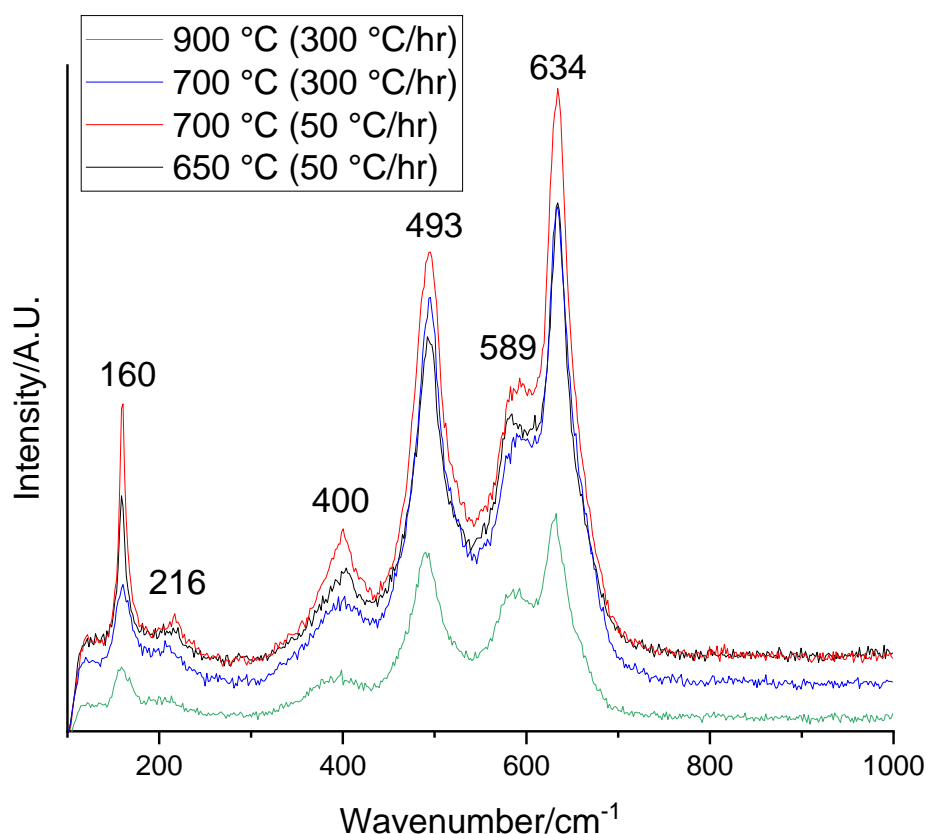
Figure 4-18: Raman spectra of EOL LMNO synthesised at 650 °C [50 °C/hr] (black), 700 °C [50 °C/hr] (red), 700 °C [300 °C/hr] (blue) and 900 °C [300 °C/hr] (red).

The electrochemical performances of the 650 °C (50 °C/hr) and 900 °C (300 °C/hr) samples were tested, and the charge-discharge profiles are shown in Figure 4-19. The performance of the 700 °C (300 °C/hr) sample was shown previously in Figure 4-13.

The voltage profiles are all similar and display a plateau at 4 V that is characteristic of disordered LMNO. Although the Raman spectra suggested that the slow cooled samples may have increased ordering, this is not reflected in the electrochemical performance. The dQ/dV plots look as expected for LMNO, with activity in $Ni^{2+/3+/4+}$ and $Mn^{3+/4+}$ regions. These results show that the synthesis temperature and cooling rate do not alter the voltage profile of EOL LMNO.
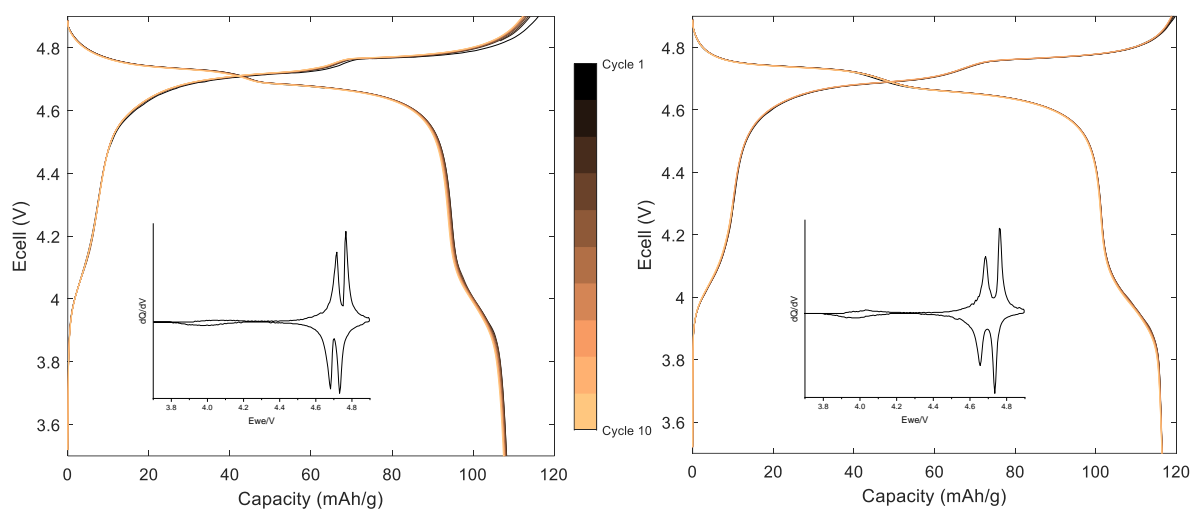
Figure 4-19: Galvanostatic charge-discharge profile and dQ/dV (inset) of EOL LMNO synthesised at 650 °C [50 °C/hr] (left) and 900 °C [300 °C/hr] (right) cycled at 10 mAg^{-1} between 3.5-4.9 V

Table 4-4 shows that the samples synthesised at 700 and 900 °C have similar discharge capacities while the discharge capacity of the 650 °C sample is slightly lower. The difference between the charge and discharge capacities is 7.8 and 13.0 mAhg^{-1} for the 650 and 700 °C samples but only 3.3 mAhg^{-1} for the 900 °C sample. This suggests that the higher temperature synthesis results in a more stable structure where Li can be removed/inserted without disruption. The percentage of redox activity provided by Ni redox from the 4.7 V region is consistent across the samples. In turn

this means that the redox activity provided by Mn^{3+} from the 4 V region is consistent across all the samples which suggests that they contain similar amounts of Mn^{3+}.

Table 4-4: First cycle total charge/discharge capacities of EOL LMNO synthesised with different temperatures and cooling rates

Temperature/°C	Cooling rate/°C hr^{-1}	Charge capacity/mAhg^{-1}	Discharge capacity/mAhg^{-1}	Discharge capacity provided by 4.7 V plateau/%
650	50	116.1	108.3	87.0
700	300	131.8	118.8	86.4
900	300	119.7	116.4	86.7

In conclusion, this shows that changing the synthesis temperature and cooling rate does not significantly change the voltage profile of EOL LMNO. The results show that neither of these parameters can be used to tune the amount of Mn^{3+} present in LMNO. This is in direct contrast to pristine LMNO where the synthesis temperatures can be used to tune the level of disorder and the electrochemical performance of LMNO.

4.4.2.3.   Furnace atmosphere

Next, the synthesis was repeated using different synthesis atmospheres (air and O_2). The LMNO was first heated in air at 700 °C for 12 hrs before then heating under O_2 in

a tube furnace (with a flow rate of 1 bubble per second) at 700 °C for 0, 1, 6 and 12 hrs.

Figure 4-20 shows the XRD patterns of the products synthesised with the different air/O_2 heat treatments. The samples all formed the LMNO structure along with a small amount of $Li_xNi_{1-x}O$ impurity. The peaks positions are consistent across the different samples and Table 4-5 shows that the samples have similar lattice parameters. Table 4-5 also shows that the amount of $Li_xNi_{1-x}O$ is smaller when the samples are heated for longer, which suggests that longer heating times helps to incorporate $Li_xNi_{1-x}O$ into the LMNO structure.
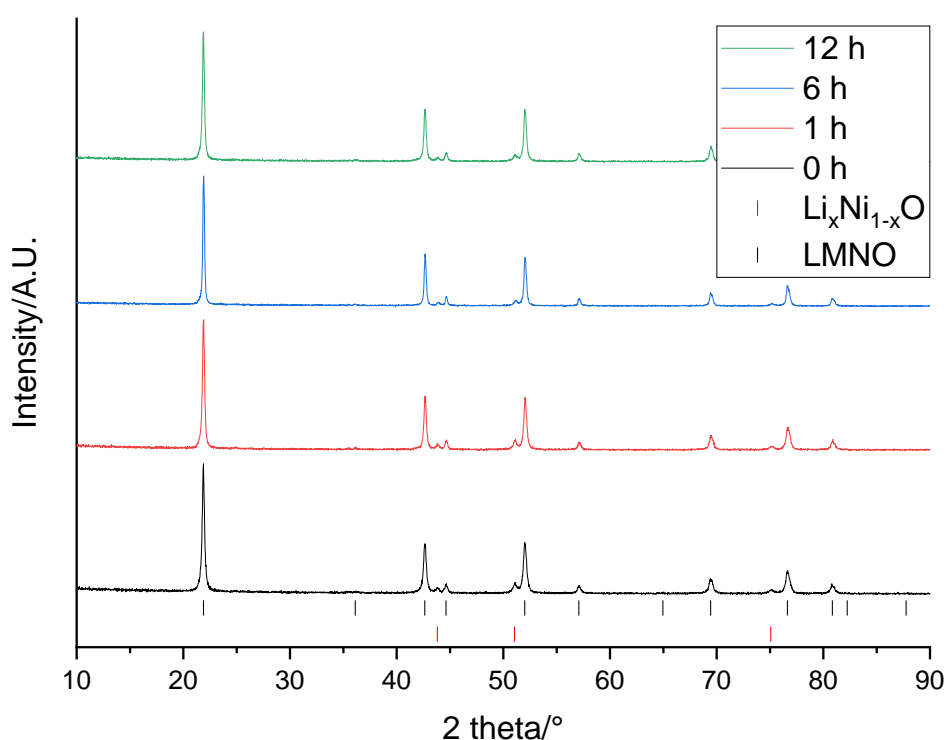
Figure 4-20: XRD pattern of EOL LMNO synthesised in air at 700 °C for 12 hrs before heating under O_2 at 700 °C for 0 (black), 1 (red), 6 (blue) and 12 (green) hrs (λ = 1.79 Å). Tick marks correspond to LMNO (black) and $Li_xNi_{1-x}O$ (red).

Table 4-5: Lattice parameters and wt% of $Li_xNi_{1-x}O$ impurity phase of EOL LMNO synthesised in air at 700 °C for 12 hrs before heating under O_2 at 700 °C

Time heated under O_2/h	a/Å	$Li_xNi_{1-x}O$ wt/%
0	8.1601(4)	8.0(2)
1	8.1576(3)	8.0(2)
6	8.1603(2)	6.1(2)
12	8.1587(3)	6.0(2)

Figure 4-21 shows the Raman spectra for the different samples. The spectra all look similar and have peaks in the same positions with similar intensities. The spectra all match to the disordered phase (Figure 4-8).
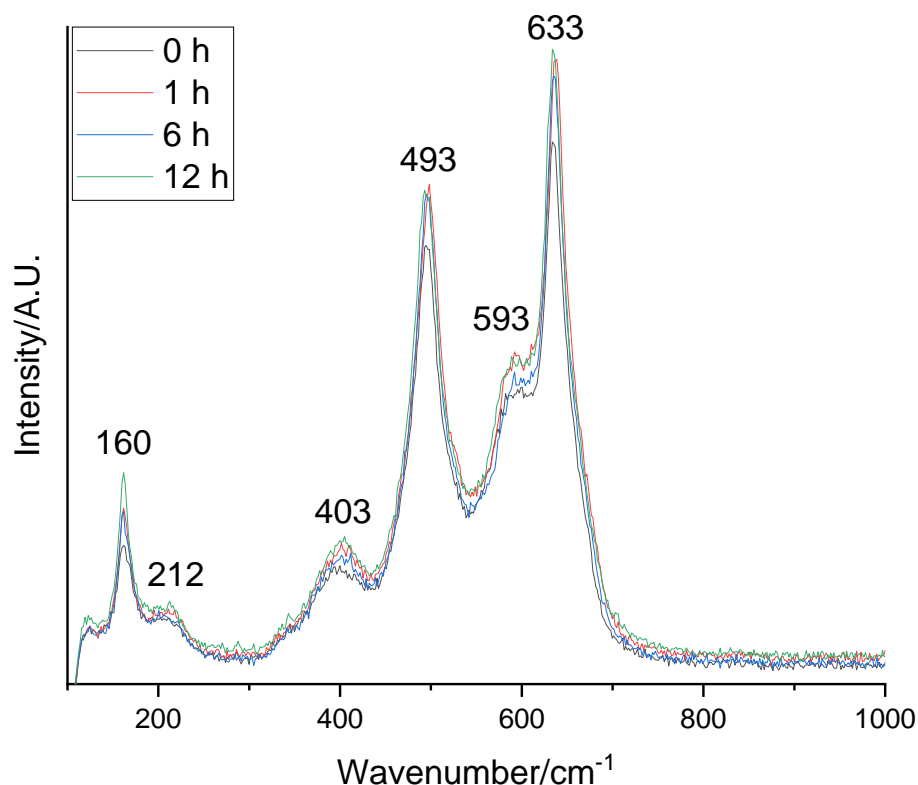
Figure 4-21: Raman spectra of EOL LMNO synthesised in air at 700 °C for 12 hrs before heating under O_2 at 700 °C for 0 (black), 1 (red), 6 (blue) and 12 (green) hrs.

The electrochemical performances of the different samples are shown in Figure 4-22. The discharge voltage profiles differ significantly between the different samples. As the heating time under O_2 is increased, the plateau at 4 V decreases in size. Once the sample has been heated for 12 h, there is no plateau remaining. The dQ/dV plots show these changes more clearly, with the presence of a small broad peak in the 4 V region. This suggests that longer O_2 heat treatments reduce the amount of Mn^{3+} present in the LMNO. Interestingly, the 4 V plateau is no longer present in the charge voltage profile after 1 h of O_2 treatment. This suggests that although Mn^{3+} is not present on charge, it is forming upon discharge of the LMNO.
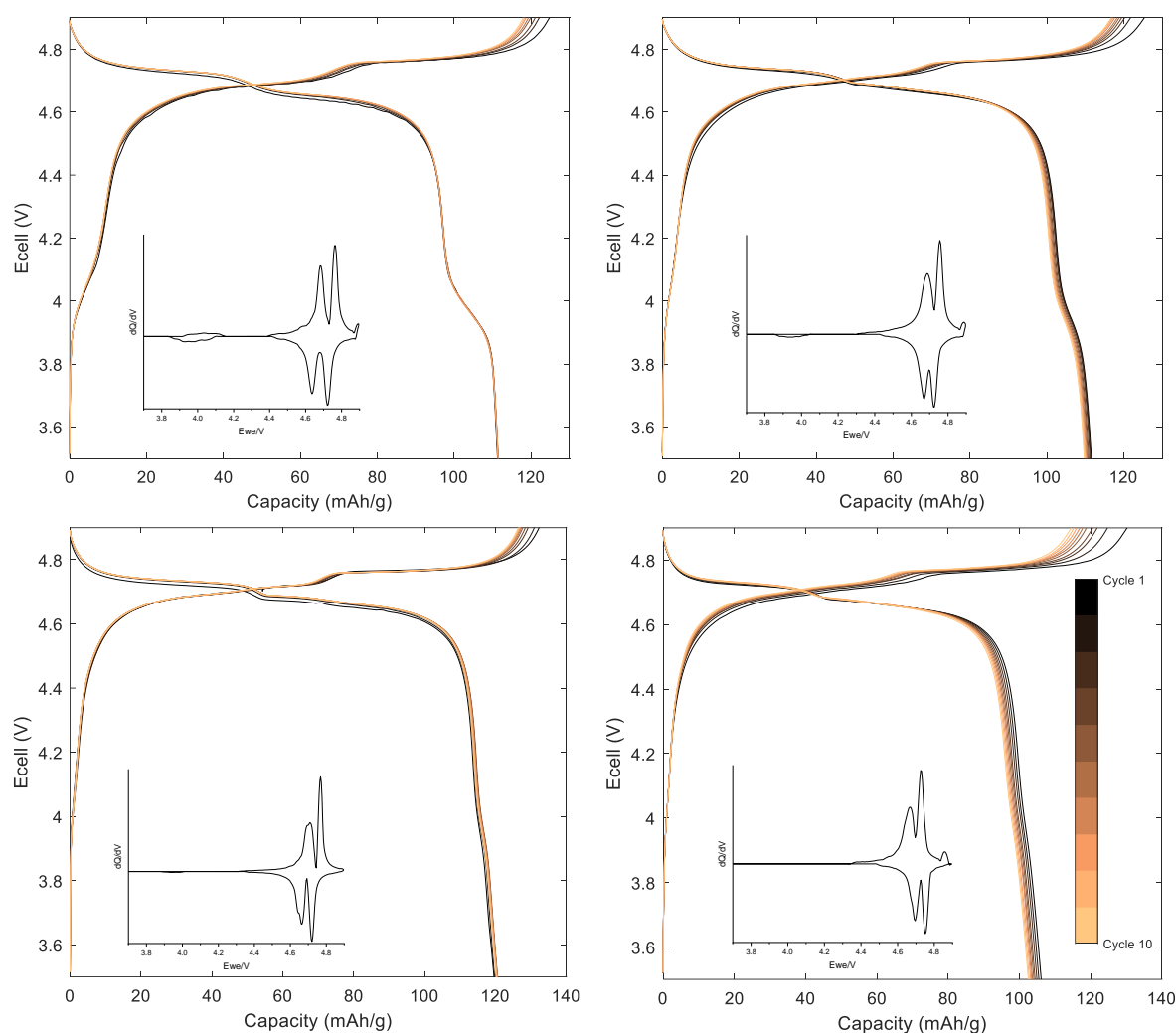
Figure 4-22: Galvanostatic charge-discharge profile and dQ/dV (inset) of EOL LMNO synthesised in air at 700 °C for 12 hrs before heating under O_2 at 700 °C for 0 (top left), 1 (top right), 6 (bottom left) and 12 (bottom right) hrs cycled at 10 mAg^{-1} between 3.5-4.9 V

Figure 4-22 also shows the capacity retention of the different samples. While the 0, 1 and 6 h samples all have an excellent capacity retention after 10 cycles, the 12 h sample shows increased capacity loss. This suggests that the presence of a small amount of Mn^{3+} in the structure is beneficial to the long-term capacity retention. In the literature, the improved capacity retention of disordered LMNO has been linked to the presence of Mn^{3+} which leads to better crystallinity and increased conductivity compared to Mn^{4+}.[15]

Table 4-6 shows that the 0 and 1 h samples have similar discharge capacities, the 6 h sample has a higher discharge capacity and the 12 h sample has a lower discharge capacity. The discharge capacity of the 6 h sample is comparable to pristine LMNO (Figure 4-9). The difference between the charge and discharge capacities is 13.5, 13.7, 12.7 and 24.1 mAhg^{-1} for the 0, 1, 6 and 12 h samples respectively. The lower discharge capacity of the 12 h sample is probably linked to the discrepancy between charge and discharge capacities. It suggests that Li is struggling to insert back into the structure upon charging. Table 4-6 also shows that the discharge capacity provided by the 4.7 V region increases with increased O_2 heating time.

Table 4-6: First cycle total charge/discharge capacities of EOL LMNO synthesised in air at 700 °C for 12 hrs before then heating under O_2 at 700 °C

Time heated under O_2/h	Charge capacity/mAhg^{-1}	Discharge capacity/mAhg^{-1}	Discharge capacity provided by 4.7 V plateau/%
0	124.8	111.3	86.4
1	125.3	111.6	91.4
6	132.3	119.6	94.2
12	130.2	106.1	100.0

Section 4.4.2.3. is interesting as it indicates that the furnace atmosphere can be used to control the electrochemical performance of EOL LMNO. An initial heat treatment in air followed by a heat treatment in O_2 is required to tune the amount of Mn^{3+} present in the LMNO and therefore tune the electrochemical performance. The O_2 treatment only changes the amount of Mn^{3+} present when the LMNO is first heated in air. In section, 4.4.1. the LMNO is synthesised directly in O_2 for 12 hours (without the air treatment) and there are high levels of Mn^{3+} indicated from the electrochemical performance which suggests that the air treatment step is critical to the process.

Initially it was proposed that the air treatment might be necessary to burn off any F impurities that are present in the EOL leached sample. It is not possible to detect F using the common analytical techniques used in solid state synthesis, such as ICP-OES or XRD, therefore alternative methods were used to identify whether it was present. Both F NMR and EDX imaging (Appendix G) indicated that there was no F present in the O_2 treated EOL LMNO material, although it is possible that F is present in levels too low to be detected by either of these techniques. Further work could utilise a F ion selective electrode to confirm the absence of F.

The longer the O_2 heating time the less Mn^{3+} is present in the LMNO which could be due to the O_2 atmosphere being oxidising and therefore long heat treatments allow the Mn to move to a higher oxidation state of Mn^{4+}. Alternatively, the O_2 atmosphere may help to prevent O deficiencies and inhibit formation of the $Li_xNi_{1-x}O$ impurity.[20] This encourages the Ni to be present in the LMNO phase and forces the Mn into a higher oxidation state. Table 4-5 indicates that a longer heat treatment in O_2 results in a decreased amount of $Li_xNi_{1-x}O$ impurity, although you might expect the amount of

$Li_xNi_{1-x}O$ to decrease in a linear fashion with increased heating time if this was the cause of the behaviour.

The results in this section also indicate that the presence of Mn^{3+} is not exclusively linked to the structure ordering. The Raman analysis in Figure 4-21 suggests that the samples are all disordered while the electrochemical analysis in Figure 4-22 shows that the samples contain different Mn oxidation states. However, Raman spectroscopy is not the best technique to analyse structure ordering and therefore additional analysis would be needed to explore this in more detail.

To further investigate the oxidation state, X-ray absorption near edge structure (XANES) spectroscopy was performed on the air and O_2 heat treated EOL LMNO samples along with the pristine LMNO samples. XANES spectroscopy can provide information about the oxidation state, site symmetry, surrounding ligands and nature of the bonding of a specific element present in the structure. Appendix F contains the Mn and Ni K-edge spectra. The samples all contain Ni^{2+} as expected. The Mn K-edge spectra for all the LMNO samples appear very similar in the XANES region and closely follow the position of the MnO_2 standard, which contains Mn^{4+}. However, they do show an extra feature at 6550 eV, which could indicate the presence of some Mn^{3+}. Alternatively, this feature could be due to differences in the structure/bonding of LMNO compared to the MnO_2 standard. This contrasts with the electrochemical results (Figure 4-22) which suggest that the Mn oxidation state is altered by adjusting the O_2 heating time. Further work is needed to analyse the XANES results in more detail.

In conclusion, the electrochemical results suggest that air/O_2 heat treatments can be used to control the amount of Mn^{3+} present in EOL LMNO samples. In turn this allows

the control of certain aspects such as the voltage profile and the capacity retention. Further work is needed to analyse the XANES results in more detail.

4.4.3. Comparison of pristine and EOL LiMn$_{1.5}$Ni$_{0.5}$O$_4$

In this section, additional experiments were used to investigate the differences between the pristine and EOL LMNO.

Figure 4-23 shows the long-term electrochemical performance of several of the LMNO samples. The pristine LMNO synthesised at 700 °C forms the ordered phase and displays no plateau at 4 V indicating that it contains no Mn^{3+} (Figure 4-5). Although it has a high initial capacity it has extremely poor capacity retention, falling to 84.3% by 50 cycles. In contrast, pristine LMNO synthesised at 900 °C forms the disordered phase which does contain some Mn^{3+} (Figure 4-9). The disordered phase has an improved capacity retention of 91.7% after 50 cycles which is attributed to the presence of Mn^{3+}. All the EOL LMNO samples were synthesised at 700 °C. The EOL LMNO synthesised with O$_2$ 12h (Figure 4-13) and air + O$_2$ 6h (Figure 4-22) both have a voltage plateau at 4 V and contain some Mn^{3+}. These two samples have high initial discharge capacities that are comparable to pristine LMNO. They also have a good capacity retention (98% after 40 cycles) which is significantly improved compared to pristine LMNO. The EOL LMNO synthesised with air + O$_2$ 12h (Figure 4-22) does not have a plateau at 4 V and contains no Mn^{3+}. Although it has a lower discharge capacity compared to pristine LMNO, Figure 4-23 shows that it has an improved capacity retention compared to pristine LMNO synthesised at 700 °C, which also contains no Mn^{3+}. These results show that the EOL LMNO has an improved capacity retention compared to pristine LMNO, regardless of whether the EOL LMNO contains any Mn^{3+}.

This could be related to disorder improving the capacity retention, as all the EOL samples are disordered. Alternatively, it could be related to the presence of impurity elements (Co/Al) in the EOL samples, which could act to stabilise the structure.
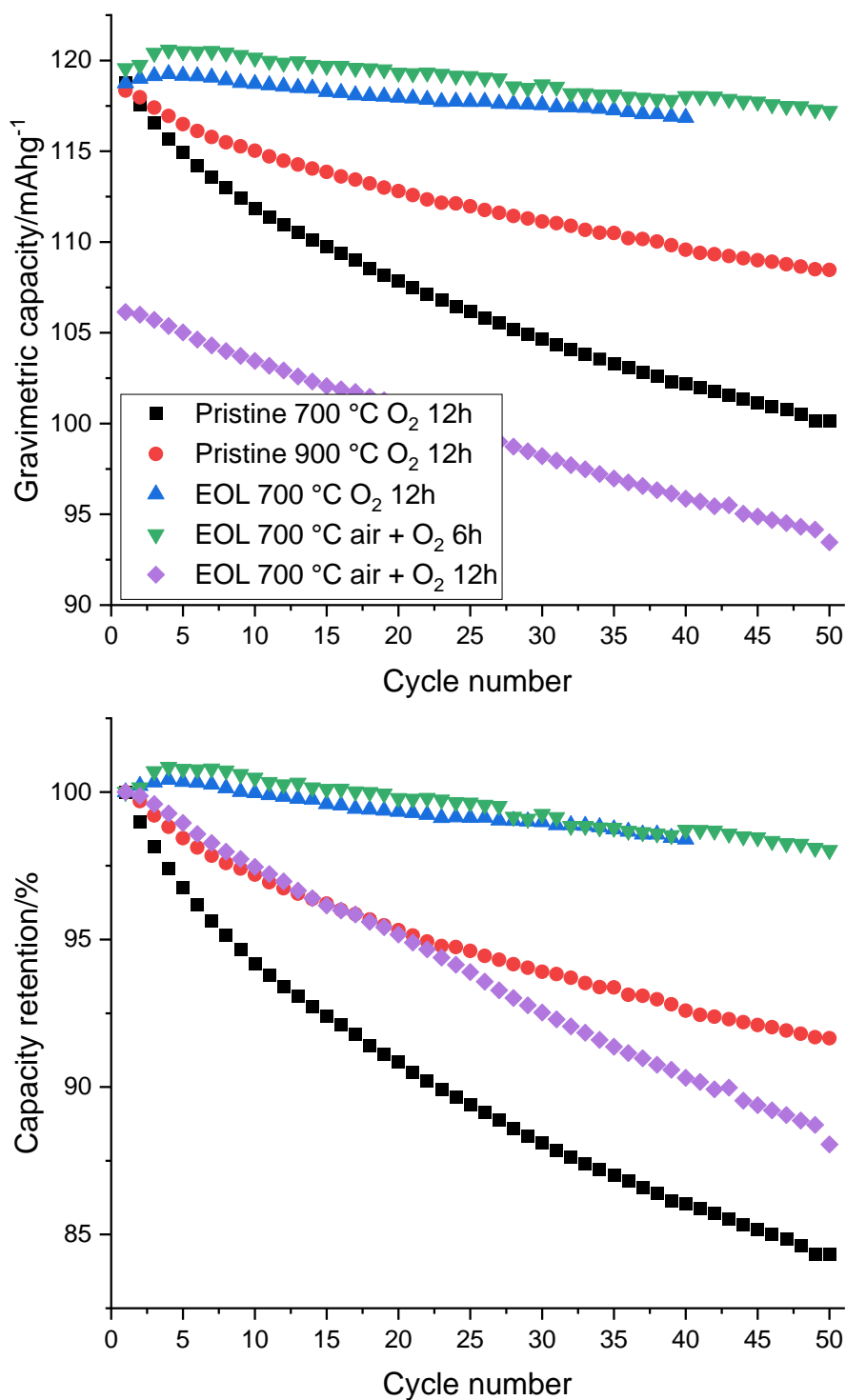
Figure 4-23: Discharge capacity (above) and capacity retention (below) of pristine 700 °C (black), pristine 900 °C (red), EOL O₂ 12h (blue), EOL air + O₂ 6h (green) and EOL air + O₂ 12h (purple) LMNO cycled at 10 mAg⁻¹ between 3.5-4.9 V

To examine whether the differences between the EOL and pristine LMNO are related to the impurity elements (Co and Al), a replica sample of EOL LMNO with the same amounts of impurity elements was made using pristine LMO and adding Co and Al dopants. The Co/Al doped LMNO was made using the same conditions needed to produce ordered pristine LMNO (700 °C 12 hrs under O_2 atmosphere).

Figure 4-24 shows the XRD pattern of the Co/Al doped LMNO. The LMNO structure is formed along with a small amount of $Li_xNi_{1-x}O$ impurity (3.7 wt%). There are no other phases present indicating that the Co and Al have incorporated into the LMNO structure. The LMNO has a lattice parameter of a = 8.1581(4) Å. The lattice parameter is smaller than pristine LMNO (a = 8.17 Å) which confirms that the Co and Al have doped into the LMNO structure. There is a small amount of $Li_xNi_{1-x}O$ impurity formed which does not form when synthesising pristine LMNO using these conditions. This suggests that the presence of Co/Al is encouraging formation of the impurity phase, which would explain why the impurity is present in all the EOL LMNO samples. These results are in contrast to the literature where other dopants (such as Cr, Cu and Zn) have been found to prevent formation of $Li_xNi_{1-x}O$.[21,22]
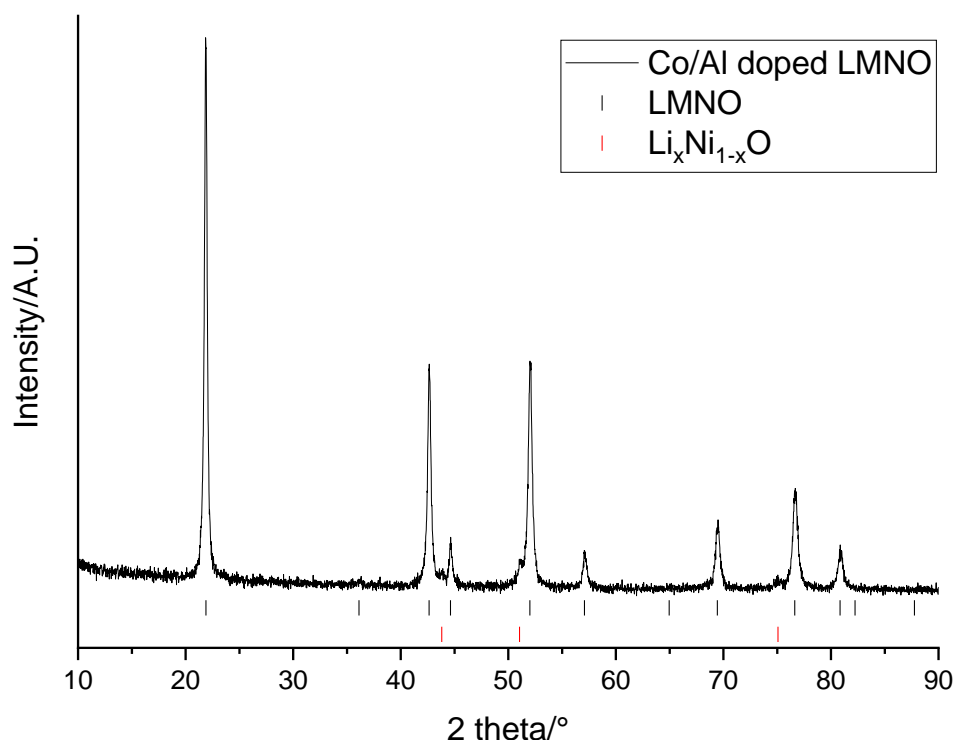
Figure 4-24: XRD pattern of Co/Al doped LMNO (λ = 1.79 Å). Tick marks correspond to LMNO (black) and $Li_xNi_{1-x}O$ (red).

Figure 4-25 shows the Raman spectrum of Co/Al doped LMNO. The spectrum has features from both the ordered and disordered spectra (Figures 4-3 and 4-8). The peaks are sharper than seen for disordered LMNO however, the peak at 160 cm^{-1} is less intense than seen for ordered LMNO. This suggests that the presence of Co and Al is inhibiting the ordering and causing a more disordered structure to be formed. However, the structure is not as disordered as seen for the EOL samples which suggests that there is another factor causing the higher levels of disorder seen in the EOL samples.
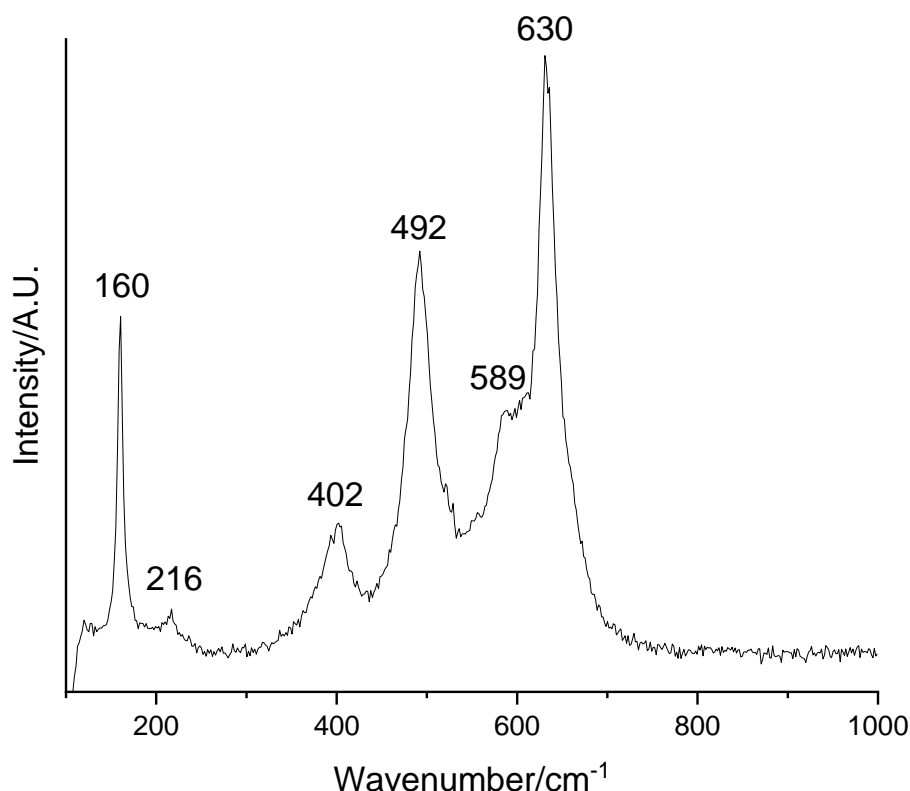
Figure 4-25: Raman spectrum of Co/Al doped LMNO

Figure 4-26 shows the electrochemical data for Co/Al doped LMNO. The voltage profile looks like ordered LMNO with no voltage plateau at 4 V. This suggests that the Co and Al impurities are not influencing the ordering or presence of Mn^{3+} in the EOL samples. The sample has a specific discharge capacity of 108.8 mAhg^{-1} which falls to 104.2 mAhg^{-1} after 10 cycles, which corresponds to a 95.8% capacity retention. The capacity fade is similar to the pristine samples and worse than the EOL samples (Figure 4-23). This suggests that the improved capacity retention of the EOL samples is not due to the Co and Al impurities.
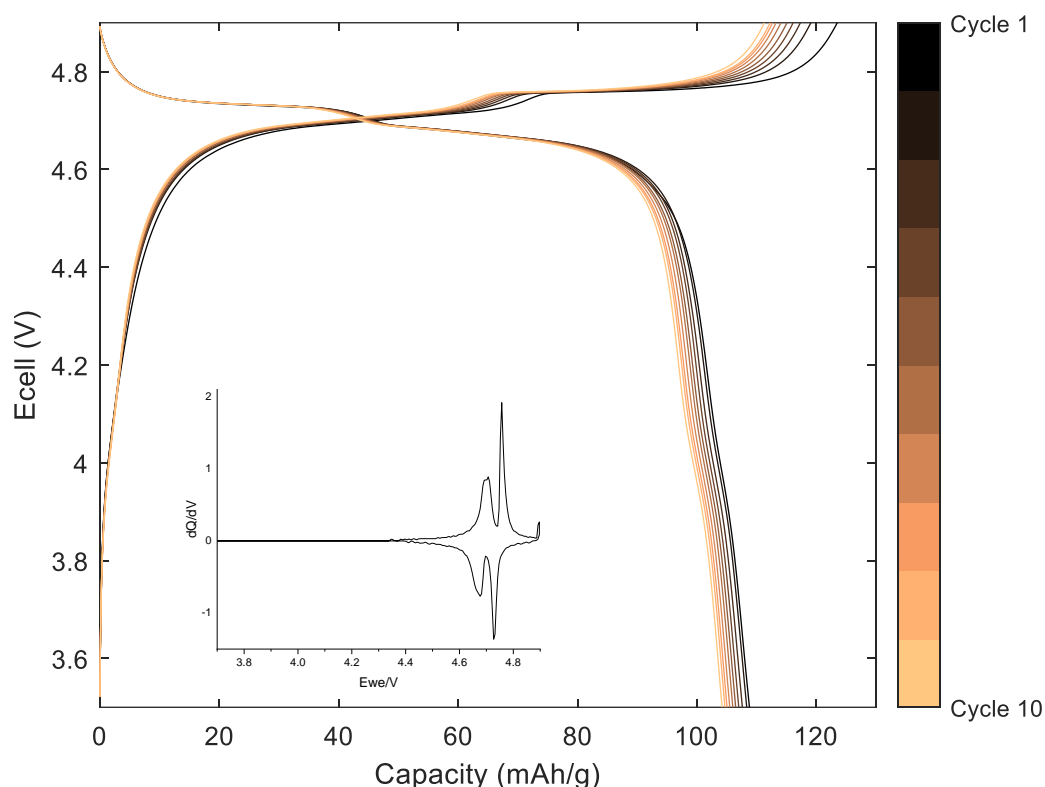
Figure 4-26: Galvanostatic charge-discharge profile and dQ/dV (inset) of Co/Al doped LMNO when cycled at 10 mAg⁻¹ between 3.5-4.9 V

To analyse any differences that are occurring during the heating procedure, a VT-XRD study was performed on the sample prepared from the solution containing the EOL LMNO (Figure 4-27). This is analogous to Figure 4-10 performed using pristine reagents. As mentioned previously, it is worth noting that the VT-XRD was performed under air rather than O_2. Similarly to the pristine LMNO, the peaks match to the LMNO phase throughout and the sample becomes more crystalline upon heating. The XRD patterns also show that the $Li_xNi_{1-x}O$ impurity is present at lower temperatures and that a temperature of 900 °C is required to incorporate it into the LMNO structure, as for pristine LMNO. The VT-XRD results for EOL LMNO do not indicate any differences compared to pristine LMNO.
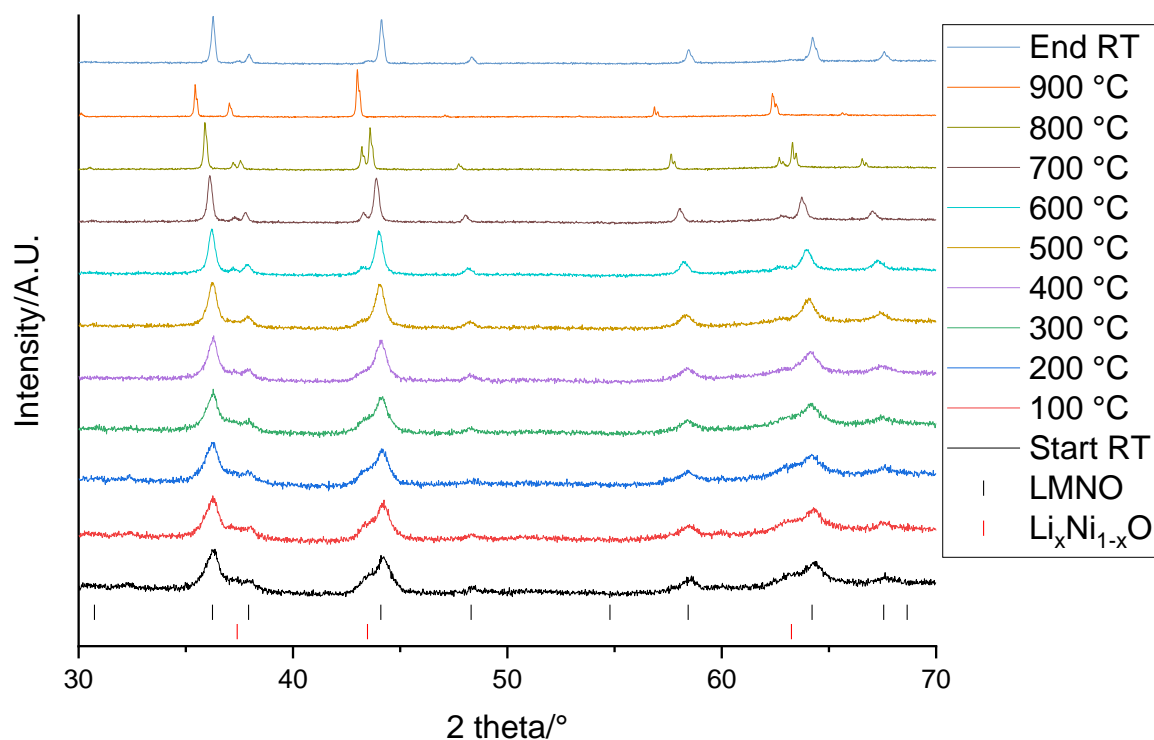
Figure 4-27: VT-XRD patterns of EOL LMNO heated from 100 to 900 °C at 100 °C intervals (λ = 1.54 Å). Tick marks correspond to LMNO (black) and $Li_xNi_{1-x}O$ (red).

In conclusion the EOL LMNO has a significantly improved capacity retention compared to pristine LMNO. This is the case regardless of whether the EOL LMNO contains Mn^{3+}. The results suggest that the presence of Co and Al impurities may be encouraging the EOL LMNO to form disordered structures although they do not appear to be the cause of the improved capacity retention. Further studies are needed to identify differences between the EOL and pristine LMNO and therefore propose reasons for the differences in capacity retention.

4.5. Synthesis of upcycled LiMn$_{1.5}$Ni$_{0.5}$O$_4$ from QC material

In this section, upcycled LMNO was synthesised using materials recovered from the QC cathode. The QC cathode was leached using the process detailed in Chapter 3.

4.5.1. Initial synthesis

The synthesis method from section 4.3. was used as a starting point. A furnace temperature of 700 °C was used to see if this would form the ordered structure with the QC material.

Figure 4-28 shows the XRD pattern of upcycled LMNO synthesised using material recycled from the QC cathode (QC LMNO). The desired spinel phase is formed without any impurity elements. Pristine LMNO was also pure when formed using these synthesis conditions while EOL LMNO contained Li$_x$Ni$_{1-x}$O impurities. This suggests that there is a feature of the EOL LMNO that is not present in pristine or QC LMNO that encourages impurity formation. The QC LMNO has a lattice parameter of 8.1617(5) Å. Similarly to EOL LMNO, the lattice parameter is smaller than pristine LMNO which could be due to Al impurities causing a lattice parameter decrease.[18]
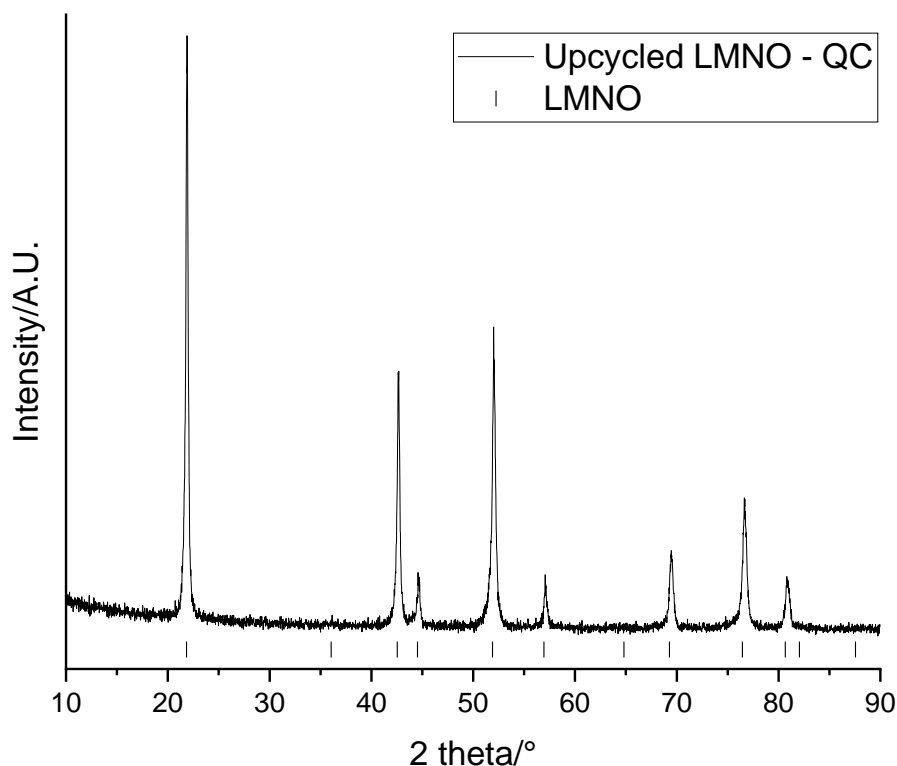
Figure 4-28: XRD pattern of QC LMNO (λ = 1.79 Å). Tick marks correspond to LMNO (black).

Figure 4-29 shows the Raman spectrum of QC LMNO. The spectrum is very similar to the spectrum obtained for replica EOL LMNO (Figure 4-25) with features from both the ordered and disordered structures. The spectrum matches to the ordered phase as there is a more intense peak at 160 cm^{-1}. However, the peaks are not as distinct as the ordered phase indicating that the sample may contain a level of disorder. These results suggest that there is a difference between the QC, pristine and EOL LMNO as they all form structures with different levels of ordering.
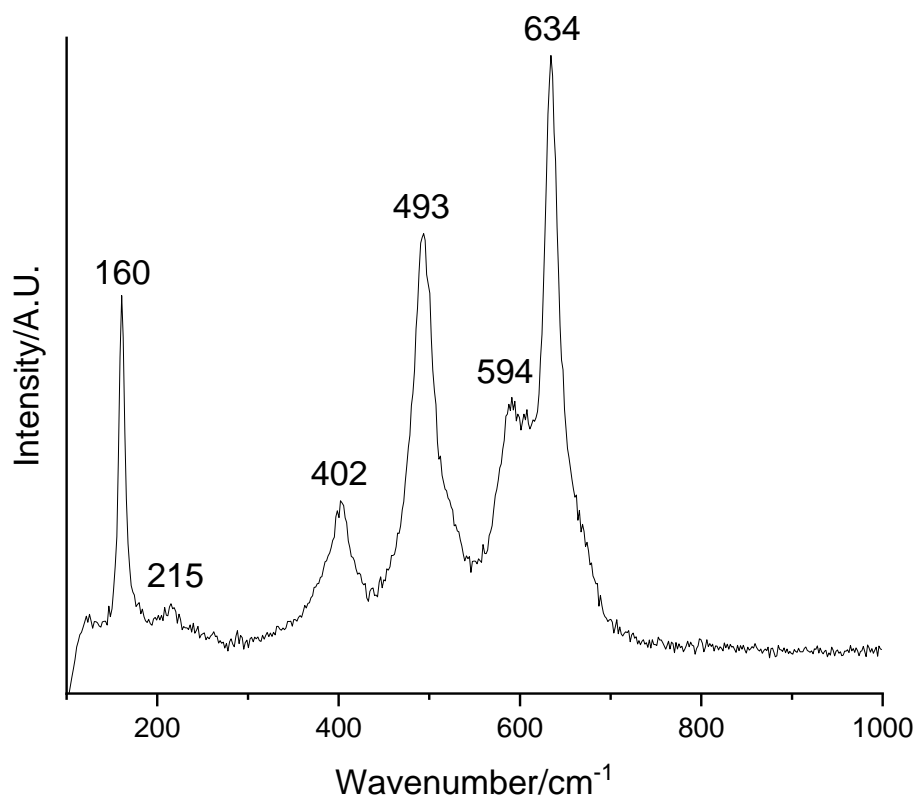
Figure 4-29: Raman spectrum of QC LMNO

Figure 4-30 shows the electrochemical data for QC LMNO. The voltage profile looks like ordered LMNO with no voltage plateau at 4 V. The dQ/dV plot shows the two peaks at 4.7 V due to Ni redox but no presence of redox activity at 4 V which suggests that all the Mn is present as Mn^{4+}. The voltage plateau at 4.7 V is split into 2 regions and this is another indication that there is some disorder within the structure. The dQ/dV peaks at 4.7 V are also separated by 50 mV, which is close to the value of 60 mV obtained for disordered LMNO. This suggests that although there is no voltage plateau at 4 V, the structure does contain some disorder. This differs to the pristine LMNO where an ordered structure was formed and the EOL LMNO where a disordered structure with the present of Mn^{3+} was formed under these conditions.
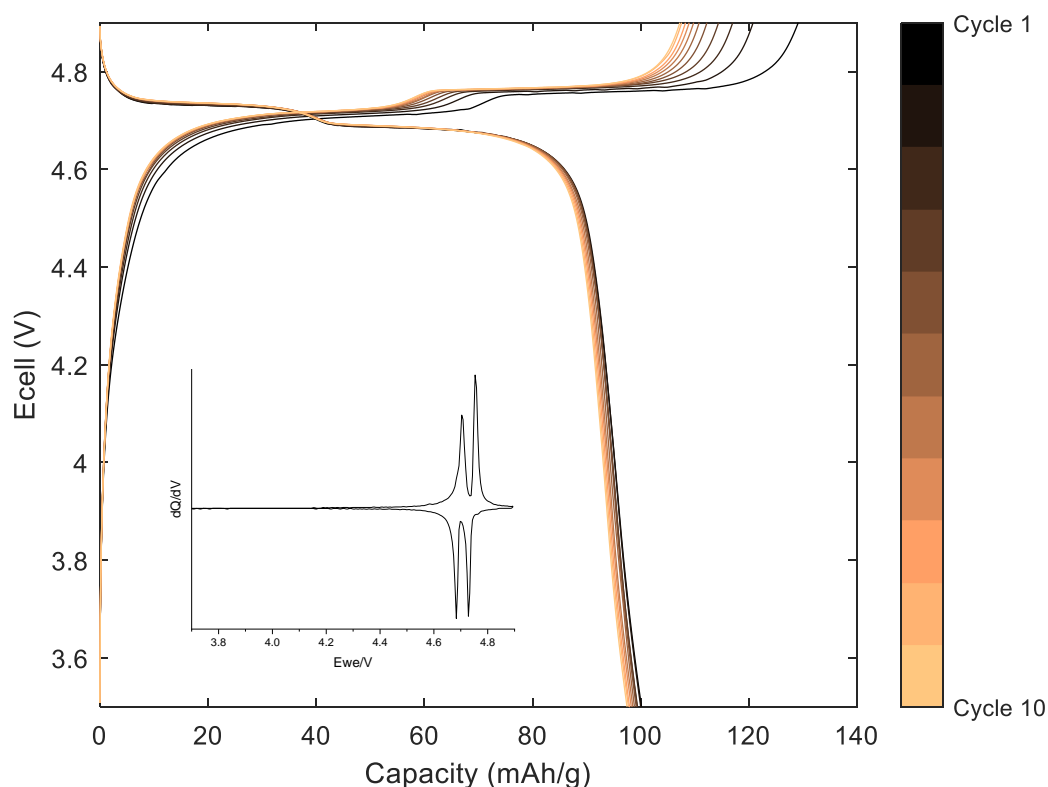
Figure 4-30: Galvanostatic charge-discharge profile and dQ/dV (inset) of QC LMNO cycled at 10 mAg^{-1} between 3.5-4.9 V

Figure 4-30 also shows that QC LMNO gives an initial charge capacity of 129.1 mAhg^{-1} and an initial specific discharge capacity of 100.1 mAhg^{-1}. There is a large difference between the charge and discharge capacities. The charge capacity is similar to pristine LMNO (130.1 mAhg^{-1}) while the discharge capacity is significantly lower than pristine LMNO (118.7 mAhg^{-1}). This suggests that Li can be removed from the structure during charging however, some of the Li cannot be inserted back into the structure upon discharging. The discharge capacity falls to 97.5 mAhg^{-1} after 10 cycles which corresponds to a capacity retention of 97.4%. This is an improved capacity retention compared to pristine LMNO (94.6%) but worse than EOL LMNO (100.0%). The retention is not as good as EOL LMNO which could be due to no Mn^{3+} being present.

Further electrochemical cycling was then performed to investigate the capacity retention after extended cycling (Figure 4-31). The QC LMNO had a specific discharge capcacity of 91.0 mAhg^{-1} after 40 cycles which corresponds to a capacity retention of 90.9%. Comparing these results to Figure 4-23, the capacity retention is similar to the EOL LMNO air + O$_2$ 12h sample but higher than the pristine LMNO. This provides further evidence to show that the capacity retention of the upcycled LMNO is improved compared to pristine LMNO.
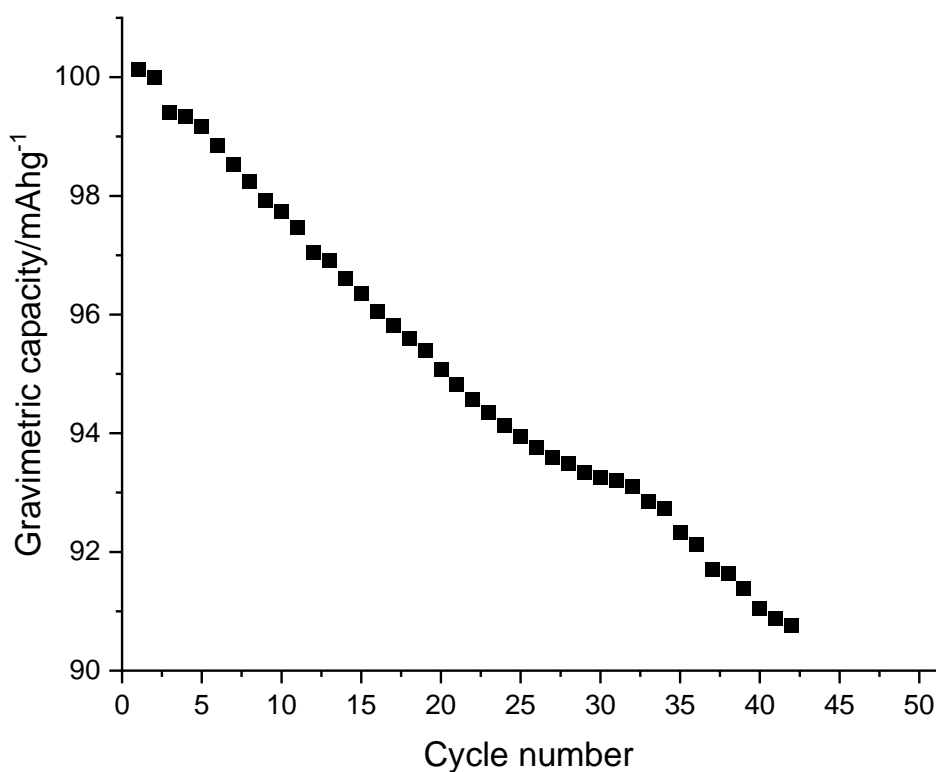
Figure 4-31: Discharge capacity of QC LMNO

These results show that LMNO can be synthesised using materials recycled from QC cathodes. The results suggest that the QC and EOL LMNO behave differently with different electrochemical properties shown when the same synthesis conditions were

used. The QC LMNO has a lower discharge capacity compared to pristine LMNO however, it has an improved capacity retention.

4.5.2. Alternative synthesis procedures

In this section, the synthesis conditions were altered to try and optimise the electrochemical performance of QC LMNO. The conditions being investigated will be stated and any other synthesis conditions will be the same as mentioned in section 4.5.1..

4.5.2.1. Excess Li

Firstly, the synthesis was performed using different amounts of excess Li to see if this would increase the discharge capacity of the QC LMNO. 10, 20 and 30 wt% excess Li were used while in section 4.5.1. 0 wt% excess Li was used. The excess Li was added into solution along with the other precursors.

Figure 4-32 shows the XRD patterns of QC LMNO synthesised with different amounts of excess Li. In all cases, the desired spinel phase is formed along with a small amount of $Li_xNi_{1-x}O$ impurity. When 0 wt% excess Li was used, LMNO was formed without any impurity phase (Figure 4-28). This suggests that the additional Li present is encouraging the formation of the impurity phase. Table 4-7 shows that the lattice parameters are all similar although they are smaller than obtained for 0 wt% excess Li (8.1617(5) Å). This fits to the literature where LMNO with increased Li content has smaller lattice parameters.[4] It also suggests that when the amount of excess Li is increased beyond 10 wt%, it is either being lost during synthesis or forming the impurity

phase as the lattice parameter does not decrease further when the excess is increased
to 20 and 30 wt%.
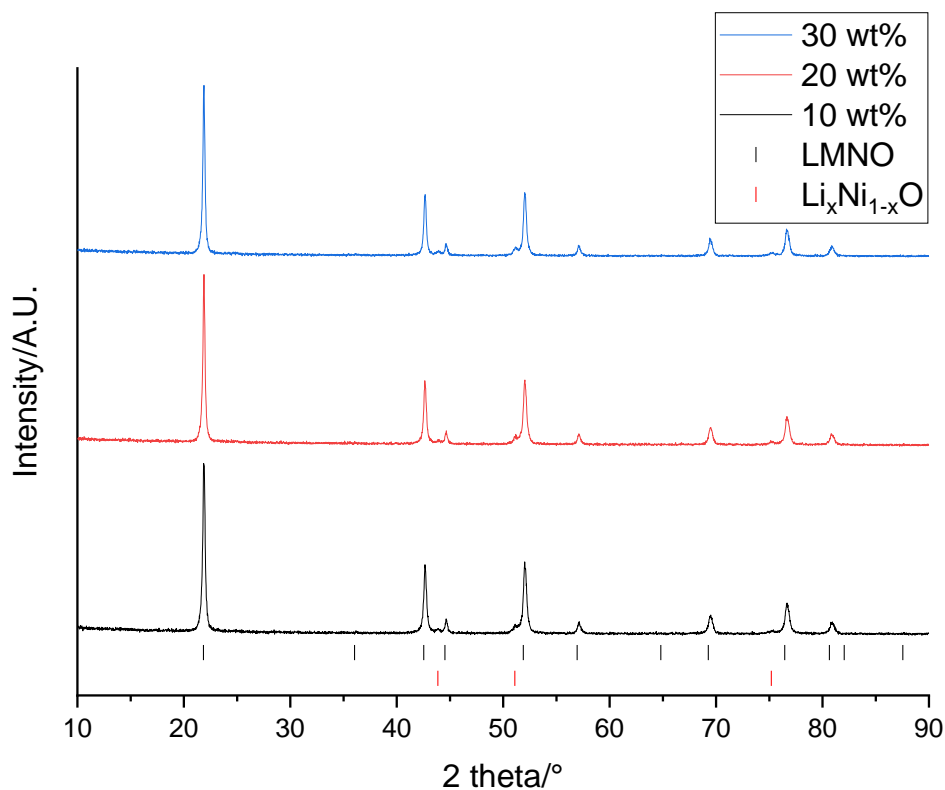
Figure 4-32: XRD pattern of QC LMNO synthesised with 10 (black), 20 (red) and 30 (blue) wt% excess Li (λ = 1.79 Å). Tick marks correspond to LMNO (black) and $Li_xNi_{1-x}O$ (red).

Table 4-7: Lattice parameters and wt% of $Li_xNi_{1-x}O$ impurity phase of QC LMNO synthesised with different wt% excess Li

Excess Li/wt%	a/Å	$Li_xNi_{1-x}O$ wt/%
10	8.1576(4)	4.9
20	8.1585(4)	5.0
30	8.1579(3)	6.0

Figure 4-33 shows the Raman spectra of the different samples. The spectra are very similar to that of QC LMNO with 0 wt% excess Li (Figure 4-29) which suggests that the addition of excess Li does not change the ordering of the QC LMNO.
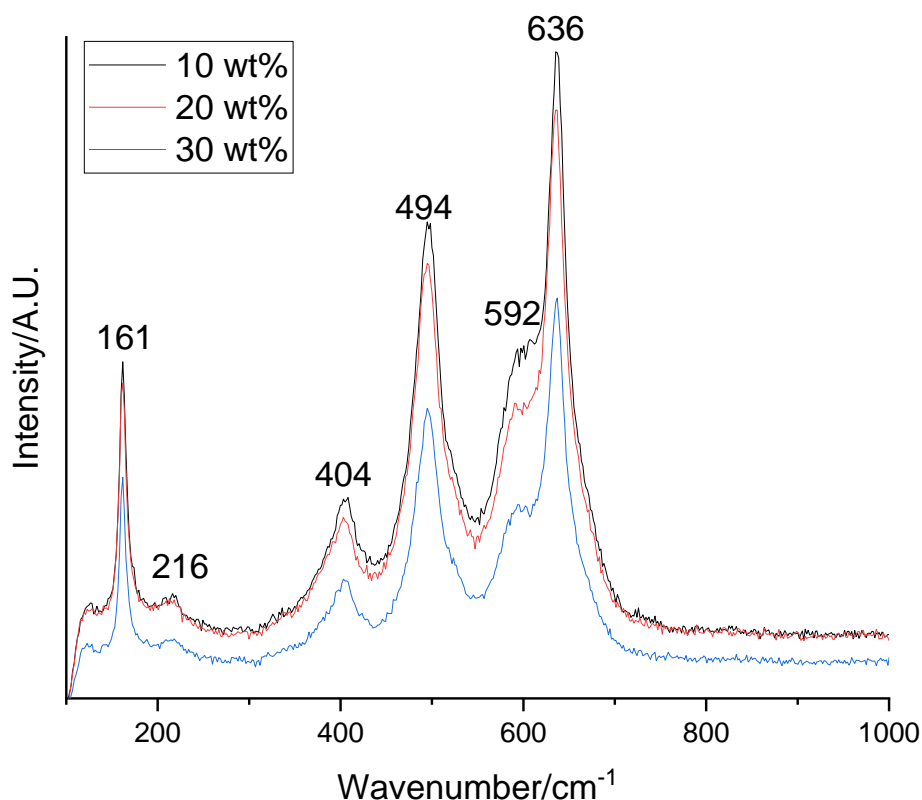
Figure 4-33: Raman spectra of QC LMNO synthesised with 10 (black), 20 (red) and 30 (blue) wt% excess Li.

Figure 4-34 shows the electrochemical data for the different samples. The voltage profile for the 10 and 20 wt% excess Li samples is the same with all the redox activity in the 4. 7 V region. In comparison, the 30 wt% excess Li sample has a small amount of redox activity at 4 V indicating that it contains some Mn^{3+}. Table 4-8 shows that the discharge capacity is slightly higher when the synthesis was performed using excess Li. This suggests that the addition of a small amount of excess Li can be used to slightly improve the discharge capacity however, moving to higher excesses does not improve

the capacity further. Furthermore, the capacity is still significantly lower than pristine LMNO (118.7 mAhg^{-1}). This suggests that the QC LMNO is not Li deficient and instead the lower capacity is related to problems inserting Li back into the LMNO structure during discharging.
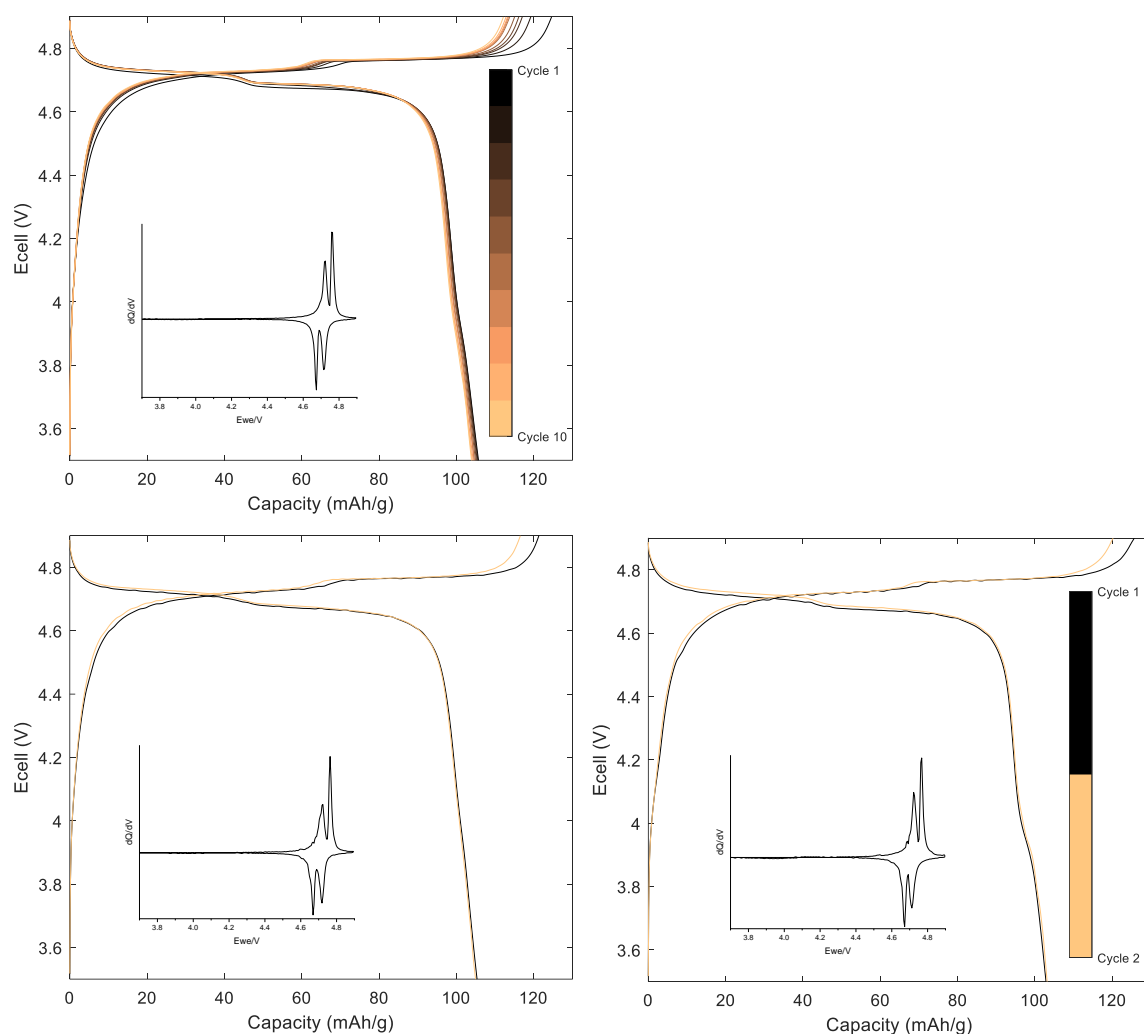
Figure 4-34: Galvanostatic charge-discharge profile and dQ/dV (inset) of QC LMNO synthesised with 10 (top), 20 (bottom left) and 30 (bottom right) wt% excess Li cycled at 10 mAg^{-1} between 3.5-4.9 V

Table 4-8: First cycle total charge/discharge capacities of QC LMNO synthesised with different wt% excess Li

Excess Li/wt%	Charge capacity/mAhg^{-1}	Discharge capacity/mAhg^{-1}
0	129.1	100.1
10	124.6	105.7
20	121.3	105.3
30	125.7	102.9

These results show that the addition of a small amount of excess Li (10 wt%) during the synthesis of QC LMNO results in a slightly improved discharge capacity. However, increasing the amount of excess Li to 30 wt% results in changes to the voltage profile and no additional capacity increases.

4.5.2.2. Furnace atmosphere

Next, the synthesis was performed by heating in an air atmosphere rather than an O_2 atmosphere. This was done to see whether changing the synthesis atmosphere would change the electrochemical behaviour of QC LMNO.

Figure 4-35 shows the XRD pattern of the QC LMNO synthesised under air. The spinel phase is formed with a lattice parameter of 8.1600(4) Å and 5.4 wt% $Li_xNi_{1-x}O$ impurity phase. This matches to the pristine LMNO which also formed impurities when

synthesised under air but not when synthesised under O_2. The lattice parameter is similar to QC LMNO synthesised under O_2 and remains smaller than pristine LMNO.
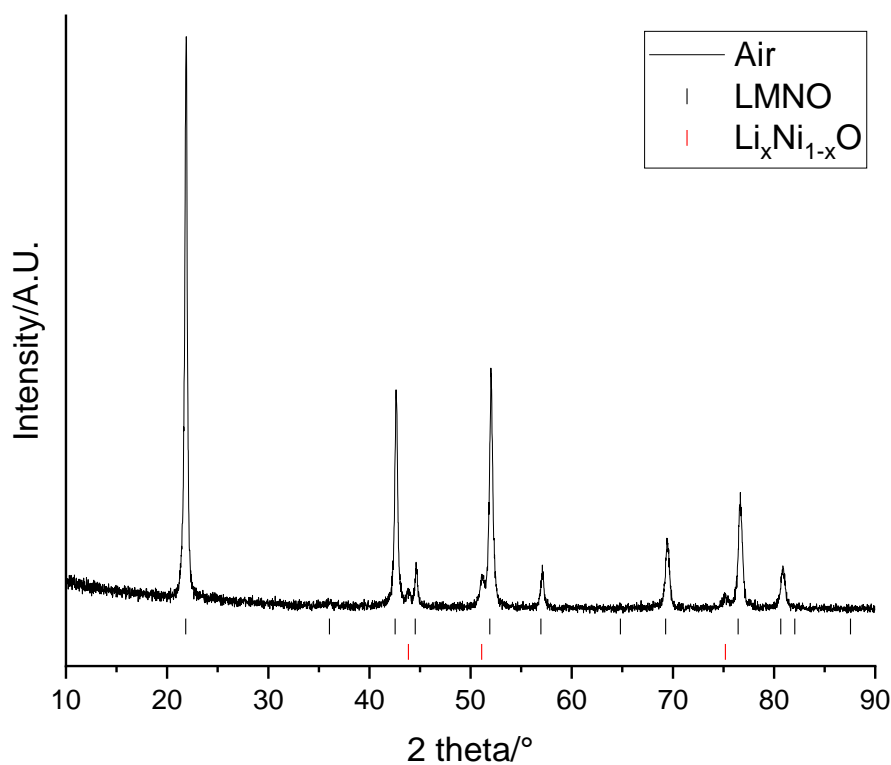
Figure 4-35: XRD pattern of QC LMNO synthesised in air at 700 °C for 12 hrs (λ = 1.79 Å). Tick marks correspond to LMNO (black) and $Li_xNi_{1-x}O$ (red).

Figure 4-36 shows the Raman spectrum of QC LMNO synthesised under air. The spectrum matches to the spectra obtained previously for QC LMNO (Figures 4-29 and 4-33) with the peaks indicating a structure intermediate between ordered and disordered. This suggests that the synthesis conditions do not affect the ordering of the QC LMNO structure.
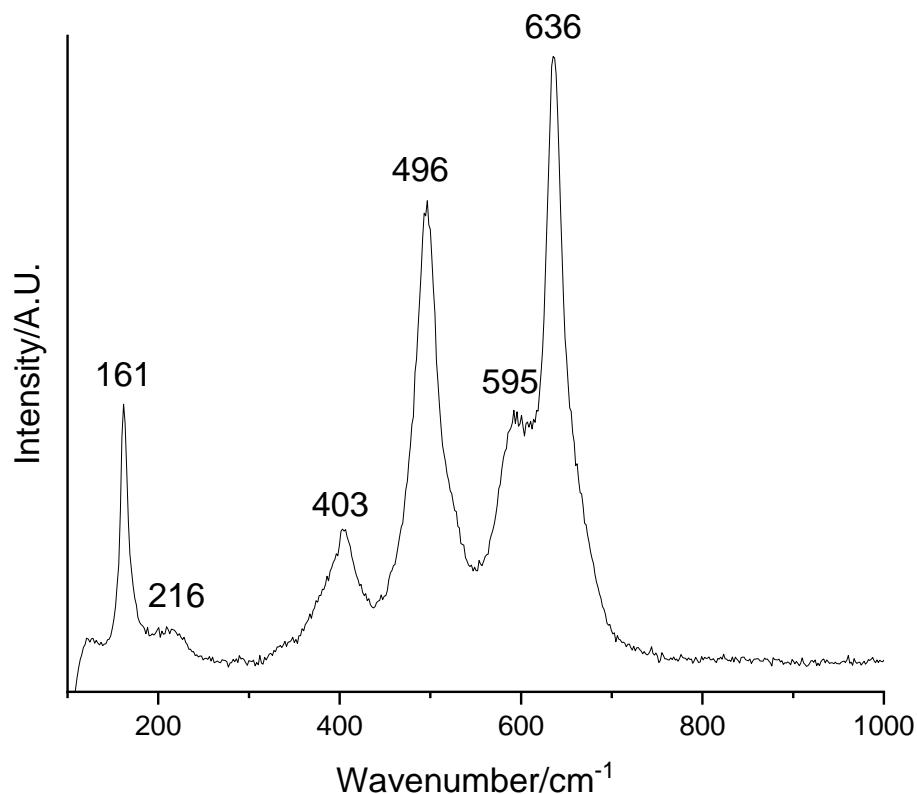
Figure 4-36: Raman spectra of QC LMNO synthesised in air at 700 °C for 12 hrs.

Figure 4-37 shows the electrochemical data for the QC LMNO synthesised under air. Comparing the voltage profile to that of QC LMNO synthesised under O_2 (Figure 4-30) there are some differences. The voltage plateau at 4.7 V is flatter, which is also shown by the peaks in the dQ/dV plot being less separate. Furthermore, the discharge voltage profile may suggest that there is a tiny amount of redox activity at 4 V. However, this is not clearly indicated in the dQ/dV plot and therefore further work would be needed to investigate this further. Figure 4-37 also shows that there is an initial specific charge capacity of 123.7 mAhg^{-1} and an initial discharge capacity of 104.0 mAhg^{-1}. The discharge capacity decreases to 99.8 mAhg^{-1} after 10 cycles which corresponds to a capacity retention of 96.0%. The charge/discharge capacity and capacity retention are

similar to QC LMNO synthesised under O_2 showing that the synthesis atmosphere does not have an impact upon the capacities obtained.
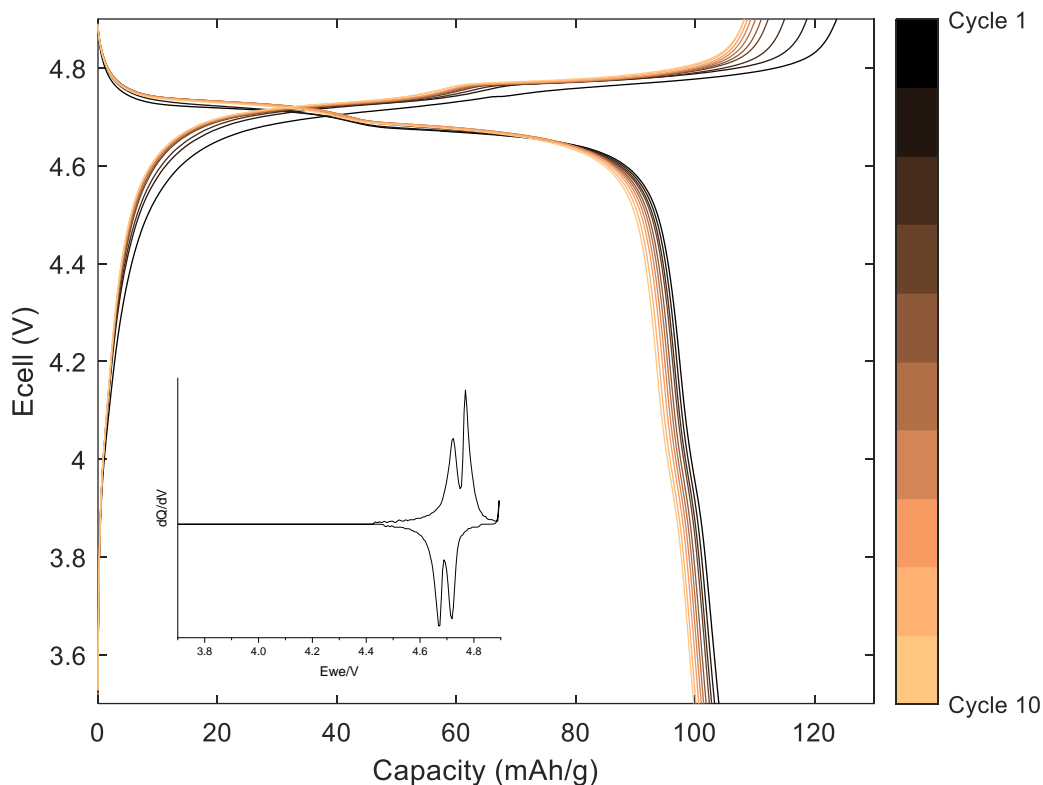
Figure 4-37: Galvanostatic charge-discharge profile and dQ/dV (inset) of QC LMNO synthesised in air at 700 °C for 12 hrs cycled at 10 mAg^{-1} between 3.5-4.9 V

These results suggest that different furnace atmospheres have little impact on the synthesis of QC LMNO as the QC LMNO has a similar electrochemical performance regardless of the furnace atmosphere used. The main difference was $Li_xNi_{1-x}O$ impurities, which were only present when the synthesis was performed under air. This is similar behaviour to the pristine LMNO which also had impurities under these conditions. This differs significantly from the EOL LMNO which shows different electrochemical behaviour under different synthesis atmospheres. Further work, comparable to section 4.4.2.3., would be required to investigate whether subsequent

O_2 heat treatments after an air treatment would allow the voltage profile of QC LMNO to be tuned.

4.5.3. Discussion on QC $LiMn_{1.5}Ni_{0.5}O_4$

This section will discuss the results found in section 4.5. which looks at the synthesis and performance of QC LMNO. With all the conditions investigated, QC LMNO was formed with a spinel structure. Changing the synthesis conditions resulted in formation of $Li_xNi_{1-x}O$ impurities and a pure LMNO sample was only obtained when the synthesis was performed under O_2 without any excess Li. A similar Raman spectrum was obtained in every case with characteristics that suggest that QC LMNO has ordering intermediate between ordered and disordered.

The voltage profile was also similar for most of the QC LMNO samples with all the redox activity in the 4.7 V region and no activity at 4 V due to Mn^{3+}. The exception being 30 wt% excess Li which did have some Mn^{3+} present. This is interesting as usually the presence of disorder or $Li_xNi_{1-x}O$ impurity results in the presence of Mn^{3+}. The addition of a small amount of excess Li (10 wt%) was found to increase the discharge capacity of the QC LMNO although the discharge capacity was still lower than pristine LMNO. This could be related to Al impurities as discussed in section 4.4.3.. Alternatively, it could be due to disorder resulting in some immobile Li which cannot contribute to the capacity. Further work would be required to investigate this more fully.

4.6. Conclusions

Pristine LMNO has been shown to form both ordered and disordered phases. The furnace temperature can be used to favour formation of each phase with the ordered phase forming at 700 °C and the disordered phase forming at 900 °C. While these phases are hard to distinguish using XRD analysis, both Raman analysis and electrochemical data can be used to show their differences. The ordered phase has a voltage plateau at 4.7 V while the disordered phase also has a voltage plateau at 4 V due to the presence of Mn^{3+}. The Raman spectra of the ordered phase has more intense peaks with increased definition compared to the disordered phase. The presence of Mn^{3+} results in improvements to the capacity retention.

The leaching solution containing Li/Mn from Chapter 3 has been shown to work as a precursor in the synthesis of LMNO therefore allowing LMO to be upcycled into LMNO with a higher voltage. This method works with both the EOL and QC cathodes.

EOL $LiMn_{2-x}Ni_xO_4$ with x = 0.2, 0.4, 0.5 and 0.6 was synthesised and it was shown that changing the amount of Ni present in the LMNO also changed the electrochemical performance with increased Ni resulting in decreased Mn^{3+}. In contrast to pristine LMNO, the furnace temperature was not found to have an impact upon the structure ordering with EOL LMNO. The same electrochemical performance was obtained at 650, 700 and 900 °C even when different ramping rates were used (50 and 300 °C/hr). In contrast, the furnace atmosphere was found to have an impact upon the electrochemical performance. A heat treatment in air followed by a heat treatment in O_2 was found to allow control of the amount of Mn^{3+} in the EOL LMNO. Increasing the time of the O_2 heat treatment decreased the amount of Mn^{3+} present in the LMNO

structure. Further work is required to understand XANES results in more detail. Another significant difference between the EOL and pristine LMNO was the capacity retention. The EOL LMNO displayed an improved capacity retention compared to pristine LMNO with all the synthesis conditions tested. It is suggested that the improved retention is due to small levels of disorder within the EOL LMNO. Further work is required to investigate the capacity retention differences in more detail.

QC LMNO synthesised at 700 °C under O_2 did not contain any Mn^{3+} and had no voltage profile at 4 V however it had a lower discharge capacity than pristine LMNO. The addition of 10 wt% excess Li was found to slightly increase the discharge capacity however it was still lower than pristine LMNO. The addition of 30 wt% excess Li resulted in the formation of Mn^{3+} and a change to the voltage profile. Synthesis of the QC LMNO in air rather than O_2 was not found to have a significant impact upon the electrochemical performance. The Raman spectra of QC LMNO suggested that the structure was intermediate between the ordered and disordered phases. Therefore, it is proposed that disorder is forming 'trapped' Li within the structure which cannot contribute to the discharge capacity. The capacity retention of QC LMNO also appears to be higher than pristine LMNO which again could be related to the presence of small levels of disorder within the QC LMNO.

Overall, this chapter shows that different synthesis conditions are needed to control the electrochemical performance of pristine, EOL and QC LMNO. Table 4-9 provides a summary of the electrochemical data for the numerous samples discussed in Chapter 4. Table 4-9 shows that although similar discharge capacities are obtained for pristine and EOL LMNO, further work is required to improve the discharge capacity of

QC LMNO. Table 4-9 also shows that both EOL and QC LMNO have an improved

capacity retention compared to pristine LMNO.

Table 4-9: Summary of electrochemical results for Chapter 4. Unless stated otherwise ramp rates are 300 °C/hr, an O_2 atmosphere was employed, and no excess Li was used

Precursor	Synthesis conditions	Initial charge capacity/mAhg⁻¹	Initial discharge capacity/mAhg⁻¹	Percentage from 4.7 V region/%	Capacity retention after 10 cycles/%
Pristine	700 °C 12h	130.1	118.7	100.0	94.6
	900 °C 12h	123.8	118.3	90.0	97.2
	700 °C 12h	131.8	118.8	86.4	100.0
	700 °C 12h (0.2 Ni)	135.4	126.4	61.6	100.2
EOL cathode	700 °C 12h (0.4 Ni)	116.4	108.3	80.4	100.5
	700 °C 12h (0.5 Ni)	131.8	118.8	86.4	100.0
	700 °C 12h (0.6 Ni)	125.7	106.5	100.0	98.4

Precursor	Synthesis conditions	Initial charge capacity/mAhg^{-1}	Initial discharge capacity/mAhg^{-1}	Percentage from 4.7 V region/%	Capacity retention after 10 cycles/%
	650 °C 12h 50 °C/hr	116.1	108.3	87.0	99.2
	900 °C 12h	119.7	116.4	86.7	99.9
	Air 700 °C 12h	124.8	111.3	86.4	100.0
EOL cathode cont.	Air 700 °C 12h + O$_2$ 700 °C 1h	125.3	111.6	91.4	98.3
	Air 700 °C 12h + O$_2$ 700 °C 6h	132.3	119.6	94.2	100.4
	Air 700 °C 12h + O$_2$ 700 °C 12h	130.2	106.1	100.0	96.6

Precursor	Synthesis conditions	Initial charge capacity/mAhg^{-1}	Initial discharge capacity/mAhg^{-1}	Percentage from 4.7 V region/%	Capacity retention after 10 cycles/%
	700 °C 12h	129.1	100.1	100.0	97.4
	700 °C 12h (10 wt% ex Li)	124.6	105.7	100.0	98.3
QC cathode	700 °C 12h (20 wt% ex Li)	121.3	105.3	100.0	/
	700 °C 12h (30 wt% ex Li)	125.7	102.9	91.2	/
	Air 700 °C 12h	123.7	104.0	100.0	96.0

4.7. References

1   S. Ahmed, P. A. Nelson, K. G. Gallagher, N. Susarla and D. W. Dees, *J. Power Sources*, 2017, **342**, 733–740.

2   R. Amin, N. Muralidharan, R. K. Petla, H. Ben Yahia, S. A. Jassim Al-Hail, R. Essehli, C. Daniel, M. A. Khaleel and I. Belharouak, *J. Power Sources*, 2020, **467**, 228318.

3   J. Kim, A. Huq, M. Chi, N. P. W. Pieczonka, E. Lee, C. A. Bridges, M. M. Tessema, A. Manthiram, K. A. Persson and B. R. Powell, *Chem. Mater.*, 2014, **26**, 4377–4386.

4   M. Kunduraci and G. G. Amatucci, *J. Electrochem. Soc.*, 2006, **153**, A1345.

5   A. Manthiram, K. Chemelewski and E. S. Lee, *Energy Environ. Sci.*, 2014, **7**, 1339–1350.

6   J. Song, D. W. Shin, Y. Lu, C. D. Amos, A. Manthiram and J. B. Goodenough, *Chem. Mater.*, 2012, **24**, 3101–3109.

7   D. Pasero, N. Reeves, V. Pralong and A. R. West, *J. Electrochem. Soc.*, 2008, **155**, A282.

8   W. Zhu, D. Liu, J. Trottier, C. Gagnon, J. Howe, A. Mauger, C. M. Julien and K. Zaghib, *J. Power Sources*, 2015, **298**, 341–348.

9   N. Amdouni, K. Zaghib, F. Gendron, A. Mauger and C. M. Julien, *Ionics (Kiel).*, 2006, **12**, 117–126.

10   H. Duncan, B. Hai, M. Leskes, C. P. Grey and G. Chen, *Chem. Mater.*, 2014, **26**, 5374–5382.

11   Y. Sun, Y. Yang, H. Zhan, H. Shao and Y. Zhou, *J. Power Sources*, 2010, **195**, 4322–4326.

12   L. Yang, B. Ravdel and B. L. Lucht, *Electrochem. Solid-State Lett.*, 2010, **13**, 6–9.

13   J.-H. Kim, S.-T. Myung, C. S. Yoon, S. G. Kang and Y.-K. Sun, *Chem. Mater.*, 2004, **16**, 906–914.

14   P. Stüble, H. Geßwein, S. Indris, M. Müller and J. R. Binder, *J. Mater. Chem. A*, 2022, **10**, 9010–9024.

15   C. J. Jafta, M. K. Mathe, N. Manyala, W. D. Roos and K. I. Ozoemena, *ACS Appl Mater Interfaces*, 2013, **5**, 7592–7598.

16   N. Emery, A. Bhatia, Y. Ghaleb, A. O. Mitrushchenkov, C. Léonard, J. P. Pereira-Ramos, R. Baddour-Hadjean and R. I. Smith, *Chem. Mater.*, 2022, **34**, 3152–3167.

17   G. Garhi, M. Aklalouch, C. Favotto, M. Mansori and I. Saadoune, *J. Electroanal. Chem.*, 2020, **873**, 114413.

18   A. Chen, L. Kong, Y. Shu, W. Yan, W. Wu, Y. Xu, H. Gao and Y. Jin, *RSC Adv.*, 2019, **9**, 12656–12666.

19   Y. Wei, K. Kim and G. Chen, *Electrochim. Acta*, 2006, **51**, 3365–3373.

20   Y. Idemoto, H. Narai and N. Koura, *J. Power Sources*, 2003, **119**–**121**, 125–129.

21   K. Chemelewski and A. Manthiram, *J. Phys. Chem. C*, 2013, **117**, 12465−12471.

22   T. A. Arunkumar and A. Manthiram, *Electrochim. Acta*, 2005, **50**, 5568–5572.

Chapter 5: Upcycling of LiMn$_2$O$_4$ into cation disordered rocksalt materials

5.1. Introduction

In this chapter the focus will be on cation disordered rocksalt (DRS) materials. The properties of pristine DRS materials will be investigated, and different methods will be used to improve these materials. An optimised electrochemical testing method will also be developed to accommodate for the air sensitivity of DRS systems. This chapter will then build on from Chapter 4 by demonstrating an alternative route for upcycling LMO into DRS materials. As discussed in section 1.3.2., DRS are a class of materials that can act as cathode materials. They can have an extremely high capacity (> 250 mAhg^{-1}) and can utilise low cost and naturally abundant elements, such as Fe, Mn and Ti.[1] DRS usually contain Li, O and/or F, and a range of TM. DRS have a CCP arrangement of O with a random arrangement of TM/Li in the octahedral sites. When DRS contain excess Li they have excellent 3D networks for Li to diffuse via, allowing them to function as a cathode.[2]

However, DRS do have several problems. They utilise O redox to achieve high capacities, however, this leads to poor capacity retention.[3,4] In the literature, methods such as F doping and surface coatings have been used to counteract this.[5–8] They also have a sloping voltage profile and experience voltage fading upon extended cycling.[5] DRS are commonly synthesised in two ways; solid state synthesis at high temperatures following by milling to reduce particle size or mechanochemical synthesis. Unfortunately, both these methods are unsuitable synthetic pathways for

commercialisation. Furthermore, prolonged air exposure of DRS can lead to the formation of surface species, such as Li_2CO_3, which can degrade the electrolyte and cause capacity fading.[9]

The focus of this chapter was to use recycled LMO as a starting material to synthesise upcycled DRS. Initially, pristine DRS were investigated to look at their performance and explore methods to improve them, such as coatings and doping. The differences between DRS made from pristine and end-of-life (EOL) cathodes were then compared.

5.2. Experimental

5.2.1. Synthesis of pristine DRS

The pristine DRS were synthesised by weighing out stoichiometric amounts of reagents using an analytical balance (± 0.1 mg) in an Ar-filled glovebox. The reagents used for each sample are detailed in Table 5-1. Stoichiometric amounts of these reagents were then ground together using a Pulverisette 7 planetary ball-mill with silicon nitride milling balls and a 45 mL silicon nitride pot. The dry synthesis was either performed at 700 rpm for 18 hours using 10 mm diameter balls or at 900 rpm for 8 hours using 5 mm diameter balls. These conditions were chosen to investigate the differences between synthesis at different speeds. The synthesis was performed using the 5 mm balls unless stated otherwise. The total milling time was broken up into 10-minute intervals followed by a 5-minute rest period to ensure that there was no excessive heating of the samples.

Table 5-1: Reagents used for the synthesis of the different DRS compositions

DRS composition	Reagents
$Li_4Mn_2O_5$	$LiMn_2O_4$, MnO, Li_2O
$Li_2MnO_{2.25}F$	$LiMn_2O_4$, MnO, LiF
$Li_2MnO_{2.5}F_{0.5}$	$LiMn_2O_4$, LiF, Li_2O
$Li_2MnO_{1.625}F_{1.5}$, $Li_2MnO_{1.75}F_{1.25}$, Li_2MnO_2F	$LiMn_2O_4$, MnO, LiF, Li_2O
$Li_4Mn_{1.67}Ni_{0.33}O_5$	LMO, MnO, NiO, Li_2O
$Li_4Mn_{1.67}Zn_{0.33}O_5$	LMO, MnO, ZnO, Li_2O
$Li_{1.9}Na_{0.1}MnO_2F$, $Li_{1.8}Na_{0.2}MnO_2F$, $Li_{1.7}Na_{0.3}MnO_2F$, $Li_{1.6}Na_{0.4}MnO_2F$	LiF, NaF, Mn_2O_3, Li_2O

5.2.2. Synthesis of DRS from QC and EOL cathode materials

The cathode materials and leaching procedure from Chapter 3 (section 3.2.) were used to obtain the recycled LMO. The recycled LMO was then used as a starting material in the synthesis of the DRS instead of pristine LMO. The rest of the synthesis was performed as detailed in section 5.2.1.

5.2.3. Pawley refinements

Pawley refinements were carried out using the XRD data. In each case, the primary phase was fitted with the space group $Fm\bar{3}m$. Lattice parameters, sample displacement, strain and crystallite size were refined for all samples. The Pawley refinement plots for this chapter are shown in Appendix H.

5.3. Pristine $Li_4Mn_2O_5$

Firstly, this work investigated synthesising $Li_4Mn_2O_5$ as it is a DRS that contains only Li, Mn and O and has a high capacity. The structure contains Mn^{3+}. In the literature it is synthesised by ball milling Li_2O and $LiMnO_2$ for 20 hours at 700 rpm.[10] In this work, $Li_4Mn_2O_5$ was synthesised using LMO as a reagent. For the pristine $Li_4Mn_2O_5$, pristine LMO was used as a reagent.

5.3.1. Synthesis of $Li_4Mn_2O_5$

Different synthesis conditions were employed to see how this would impact the reaction process. The synthesis was performed at 700 rpm using large milling balls (10 mm) and at 900 rpm using small milling balls (5 mm). Samples were taken at various time intervals to interrogate the progress of the synthesis.

Figure 5-1 shows the XRD patterns of the $Li_4Mn_2O_5$ synthesised using large milling balls. Samples were taken at 6, 12 and 18 hours. After 18 hours of milling $Li_4Mn_2O_5$ was formed with the desired rocksalt structure and all the peaks can be indexed based upon the F$m\overline{3}m$ space group. Pawley refinements gave a lattice parameter of 4.163(5) Å. The lattice parameter is similar to lattice parameters reported in the literature for $Li_4Mn_2O_5$.[10] There are no other peaks present indicating that there are no other phases present. In contrast, after only 6 hours of milling there are peaks corresponding to both Li_2O and MnO. These are likely to be due to unreacted reagents remaining. After 12 hours of milling there still appears to be some Li_2O remaining. This shows that 18 hours of milling is required to form a pure $Li_4Mn_2O_5$ product under these conditions. Nevertheless the synthesis has been achieved in a shorter milling time than detailed

in the literature.[10] The XRD peaks are extremely broad due to the high intensity ball

milling used in the synthesis which results in a small particle size.
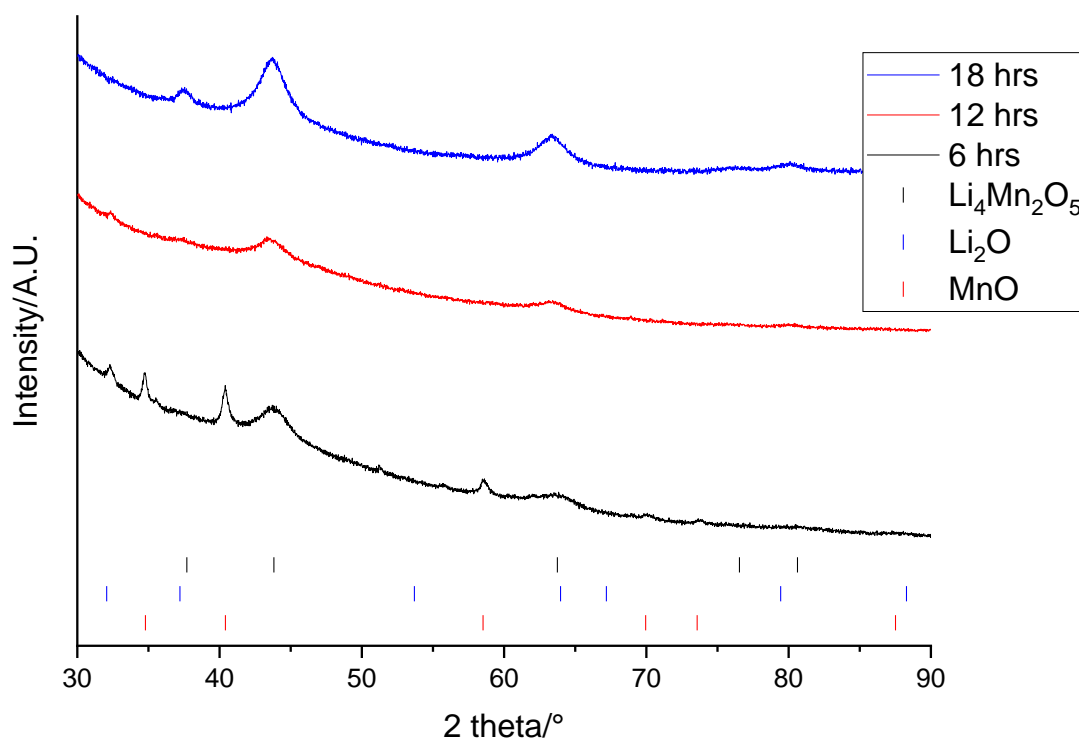
Figure 5-1: XRD patterns of Li$_4$Mn$_2$O$_5$ after 6 (black), 12 (red) and 18 (blue) hrs milling using large milling balls (λ = 1.54 Å). Tick marks correspond to Li$_4$Mn$_2$O$_5$ (black), Li$_2$O (blue) and MnO (red).

Figure 5-2 shows the XRD patterns of Li$_4$Mn$_2$O$_5$ synthesised using small milling balls.

Samples were taken at 4 and 8 hours. After 8 hours of milling Li$_4$Mn$_2$O$_5$ was formed

with the desired rocksalt structure and a lattice parameter of 4.17(1) Å. This is a

considerably shorter milling time than required when using the larger milling balls which

can be attributed to the faster milling speed. After 4 hours of milling there are peaks

corresponding to unreacted Li$_2$O. This shows that 8 hours of milling is required to form

a pure Li$_4$Mn$_2$O$_5$ product under these conditions.
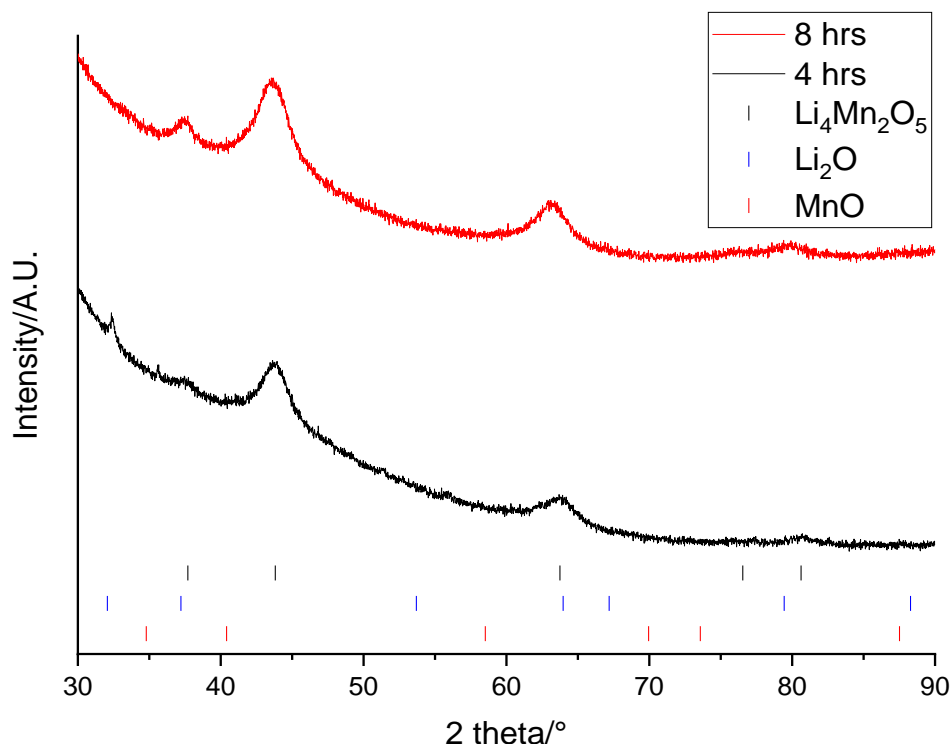
Figure 5-2: XRD patterns of Li₄Mn₂O₅ after 4 (black) and 8 (red) hrs milling using small milling balls (λ = 1.54 Å). Tick marks correspond to Li₄Mn₂O₅ (black), Li₂O (blue) and MnO (red).

Li₄Mn₂O₅ was also synthesised using MnO and Li₂O as regents rather than LMO. The same Li₄Mn₂O₅ phase was formed (Appendix I).

5.3.2. Analysis of Li₄Mn₂O₅

In this section, further analysis was performed on pristine Li₄Mn₂O₅ to investigate its structure and electrochemical properties. All analysis in this section was performed on Li₄Mn₂O₅ made using the small milling balls.

Figure 5-3 shows the VT-XRD patterns of Li₄Mn₂O₅ heated under air with the top figure showing the patterns when Li₄Mn₂O₅ was heated from 100 to 800 °C. Initially, the peaks match to Li₄Mn₂O₅ and as the sample is heated it becomes more crystalline and

the peak intensity increases. However, at 700 °C there is a structural transition, and the peaks no longer match to a rocksalt phase. Instead, a layered structure is formed, and all the peaks can be indexed based upon the C$\bar{2}$m space group. The new phase matches to Li_2MnO_3. This shows that the rocksalt structure is unstable and decomposes to a more stable layered structure upon heating. The final product had the brick red colour commonly associated with Li_2MnO_3 indicating Mn oxidation to 4+.[11] Additional VT-XRD patterns were taken of $Li_4Mn_2O_5$ over a targeted temperature range to investigate the transition further (Figure 5-3 below). It shows that Li_2MnO_3 is formed at 625 °C; shown by a peak at 37° appearing and the peak at 64.7° splitting into two peaks. There are no other phases present suggesting that there is a direct transition from a rocksalt to a layered structure.
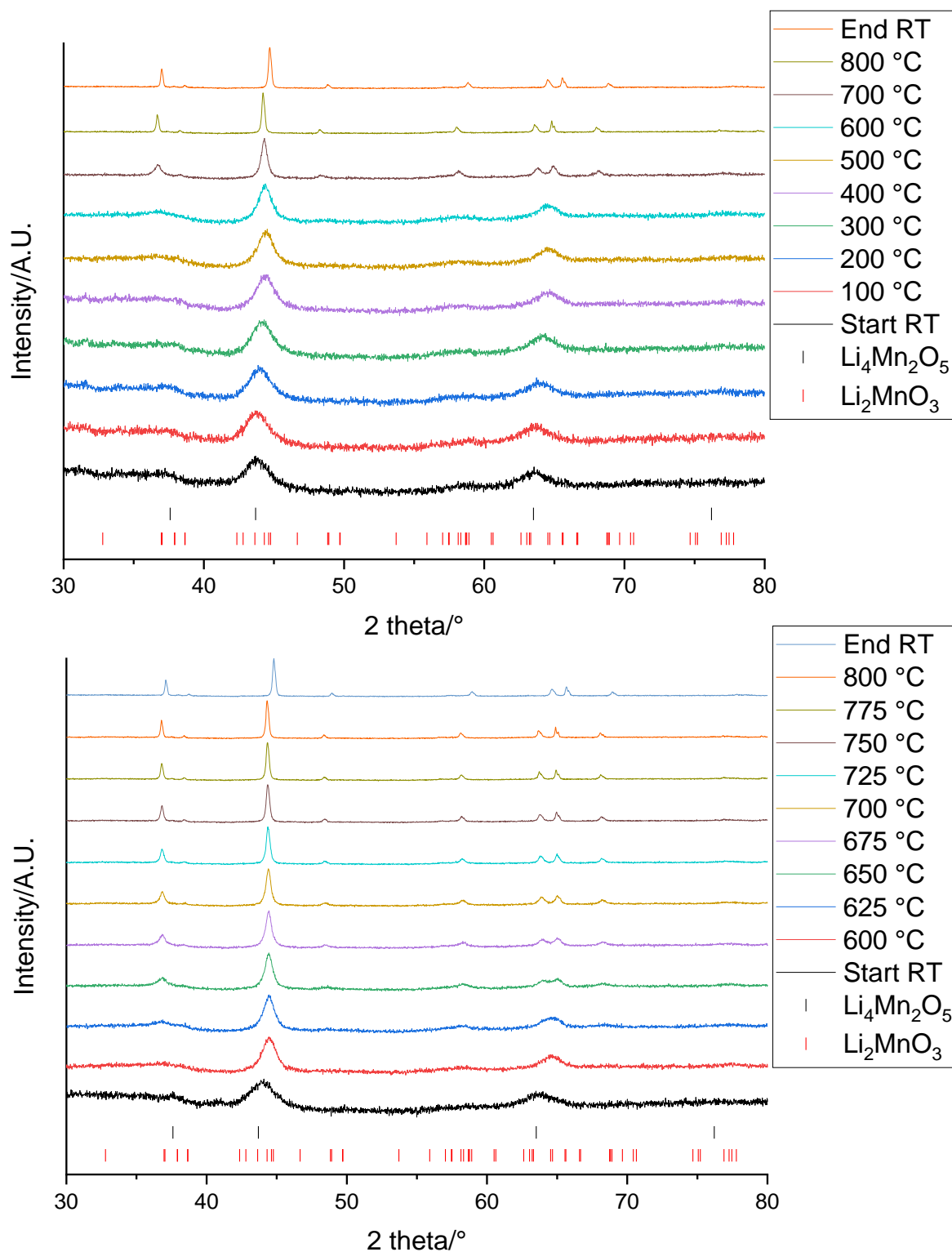
Figure 5-3: VT-XRD patterns of pristine Li₄Mn₂O₅ heated from 100 to 800 °C at 100 °C intervals (above) and 600 to 800 °C at 25°C intervals (below) (λ = 1.54 Å). Tick marks correspond to Li₄Mn₂O₅ (black) and Li₂MnO₃ (red).

Figure 5-4 shows the Raman spectrum for pristine $Li_4Mn_2O_5$ made using small balls. There are peaks at 480, 595, 1088 and 1204 cm^{-1}. The Raman spectrum is similar to spectra shown in the literature for other DRS compounds.[12,13] The peak at 480 cm^{-1} is due to a F_{2g} mode of the MnO_6 framework while the peak at 595 cm^{-1} is attributed to an A_{1g} symmetric stretching mode of the MnO_6 framework.[14] The peaks above 1000 cm^{-1} are second-order bands.[13] The fact that $Li_4Mn_2O_5$ exhibits Raman bands suggests that the structure is not fully disordered and must contain some short-range order.[15]
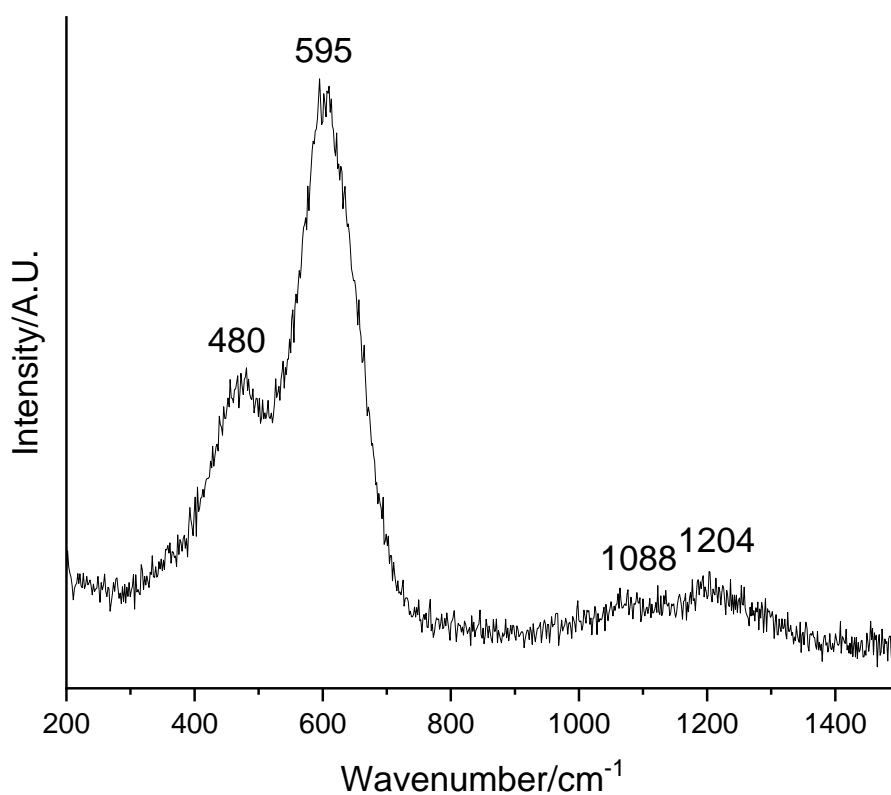
Figure 5-4: Raman spectrum of pristine $Li_4Mn_2O_5$

Figure 5-5 shows SEM and EDX images of pristine $Li_4Mn_2O_5$. The SEM image shows that the powder consists of large particles (~ 700 μm) which are made up of agglomerations of much smaller particles shown in the bottom image. The EDX image shows that Mn is evenly distributed over the surface of the powder.
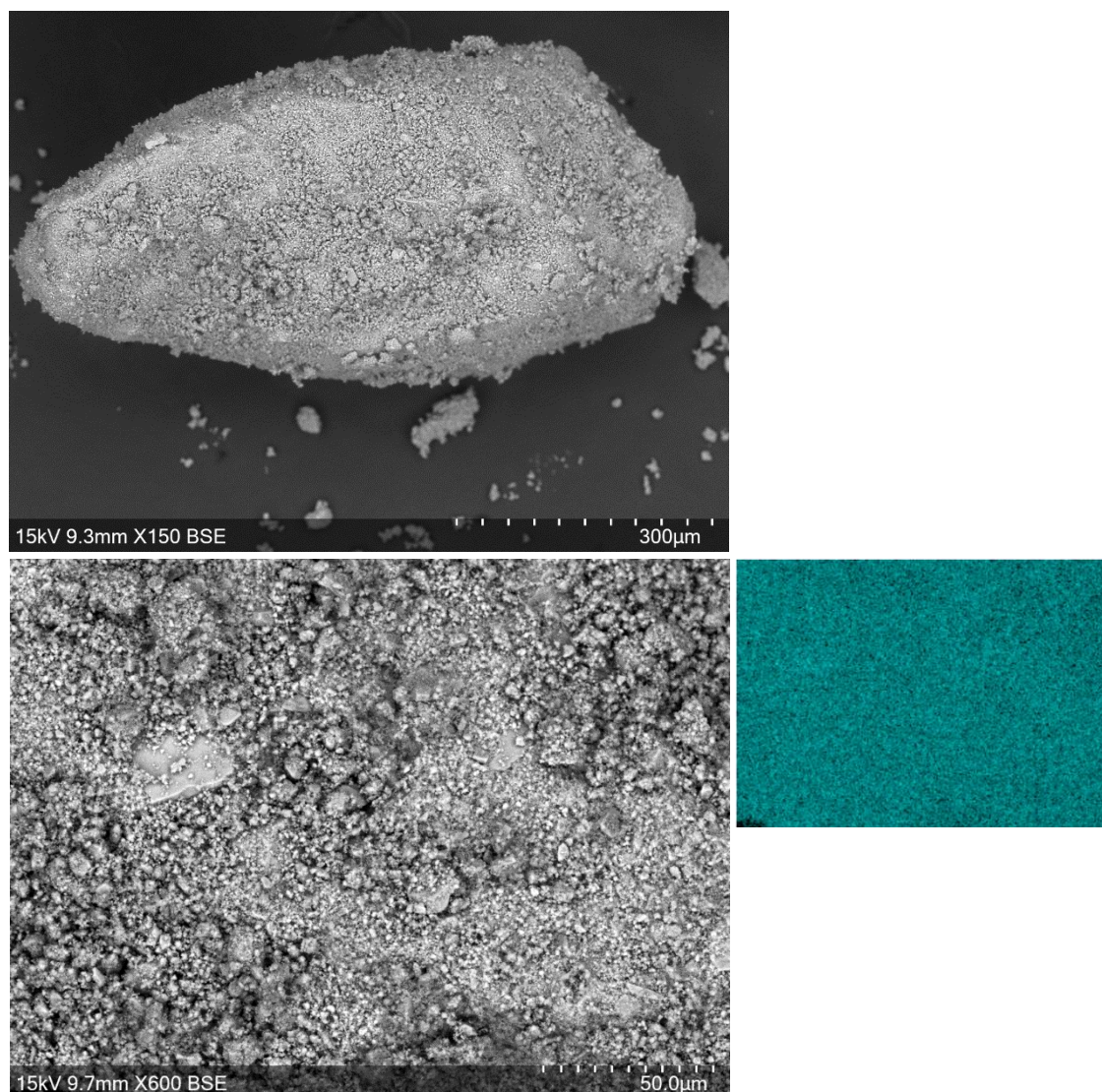
Figure 5-5: SEM (left) and EDX (right) images of pristine Li$_4$Mn$_2$O$_5$. EDX image shows Mn (teal).

Figure 5-6 shows the XRD patterns of Li$_4$Mn$_2$O$_5$ after exposure to air. Prior to this, Li$_4$Mn$_2$O$_5$ was kept in a glovebox and XRD patterns were taken while the sample was in an airtight holder. The patterns show that after 8 hrs of air exposure, peaks due to Li$_2$CO$_3$ are present. This could suggest that when exposed to air the sample degrades to Li$_2$O which then reacts with CO$_2$ to form Li$_2$CO$_3$.[16] Alternatively, the sample could have Li$_2$O remaining on the surface which is reacting. After an additional 40 hrs, the peaks due to Li$_2$CO$_3$ are more intense indicating that more Li$_2$CO$_3$ has been formed.

This work shows that $Li_4Mn_2O_5$ must be kept under inert atmosphere to prevent the formation of Li_2CO_3; as Li_2CO_3 is known to have a detrimental impact upon the cycling performance of cathode materials.[17–19]
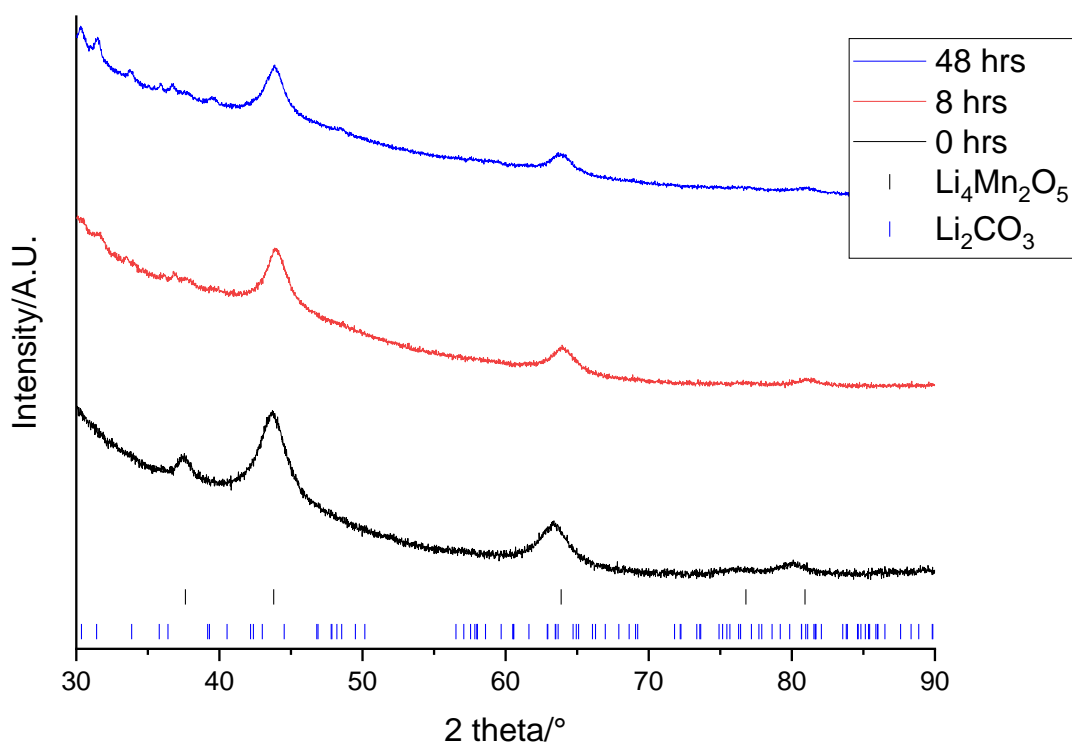
Figure 5-6: XRD patterns of $Li_4Mn_2O_5$ after exposure to air for 0 (black), 8 (red) and 48 (blue) hrs (λ = 1.54 Å). Tick marks correspond to $Li_4Mn_2O_5$ (black) and Li_2CO_3 (blue).

Figure 5-7 shows the Raman spectrum of $Li_4Mn_2O_5$ after air exposure for 48 hrs. The spectrum looks the same as Figure 5-4 indicating that exposure to air has no impact upon the Raman spectrum of $Li_4Mn_2O_5$. There are no additional bands present to indicate the presence of Li_2CO_3 (1090 cm^{-1})[20] or Li_2O (529 cm^{-1})[21] on the surface of the sample. Although, a peak due to Li_2O might be present and not visible due to the peaks at 475/605 cm^{-1}. The surface of the $Li_4Mn_2O_5$ particles is exposed to air so you would expect formation of Li_2CO_3/Li_2O to occur on the surface rather than the bulk of the particles and therefore you would expect it to be detected by Raman spectroscopy, as

it is a surface sensitive technique. This suggests that Li_2CO_3 is not present on the surface but instead is present in the bulk of the particles. Alternatively, the Raman peaks due to Li_2CO_3 may be hidden under the broad peaks at 1093/1219 cm^{-1}.
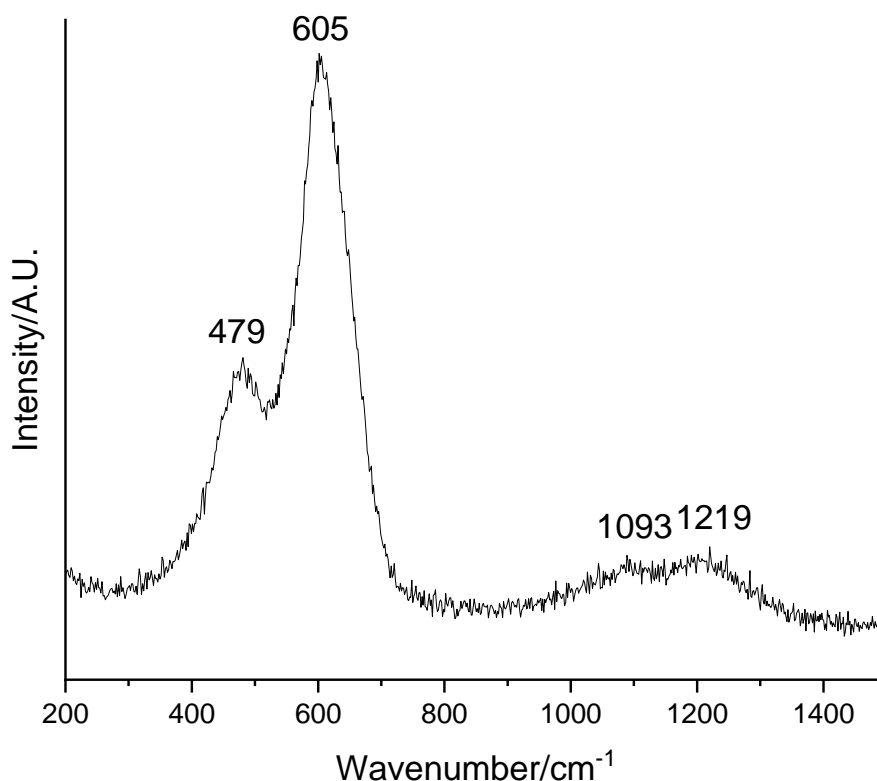
Figure 5-7: Raman spectrum of pristine Li$_4$Mn$_2$O$_5$ after air exposure for 48 hrs

The next step taken was to look at the electrochemical performance of $Li_4Mn_2O_5$. Initially, the same method as the previous chapters was used to prepare the cathodes. Active material ($Li_4Mn_2O_5$) was mixed with PVDF and carbon black before coating onto an Al current collector. However, this method did not work when using $Li_4Mn_2O_5$ as there were problems with both the mixing and coating steps. During mixing, after addition of $Li_4Mn_2O_5$ the slurry formed a gel. According to the literature, this is likely due to Li_2CO_3 present on the surface which absorbs H_2O and increases the alkalinity of the slurry. This then triggers defluorination of the PVDF binder and causes

gelation.[22,23] During coating, the mixture appeared to contain large particles which resulted in an uneven coating. These larger particles are assumed to be the agglomerations seen in the SEM image in Figure 5. Cells were made from this coating however, the problems encountered are likely to result in poor electrochemical data.

Figure 5-8 shows the electrochemical data for $Li_4Mn_2O_5$ when coated in air. The voltage profile looks as expected with a sloping voltage throughout. However, the discharge capacities are significantly lower than seen in the literature (120 mAhg^{-1} compared to 355 mAhg^{-1}). This is probably related to the issues experienced during coating leading to a lower active material loading than expected. Furthermore, the formation of Li_2CO_3 may have resulted in a decreased Li content in the $Li_4Mn_2O_5$ structure.
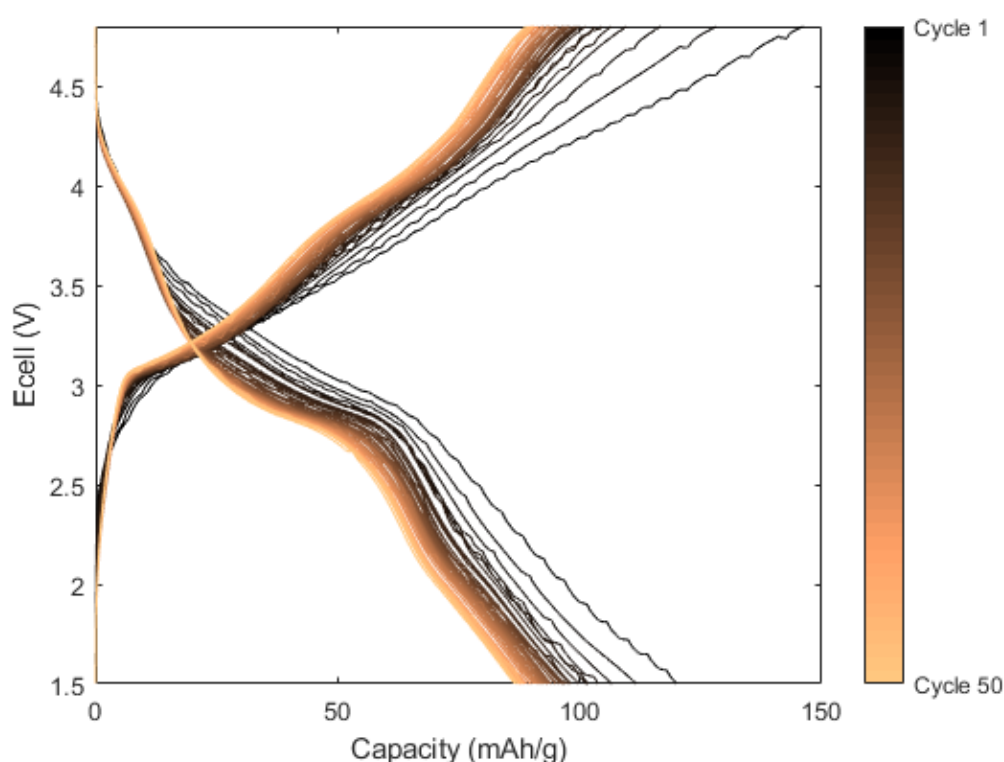
Figure 5-8: Galvanostatic charge-discharge profile of pristine $Li_4Mn_2O_5$ when cycled at 10 mAg^{-1} between 1.5-4.8 V

Overall, these results show that pristine $Li_4Mn_2O_5$ has been formed with the desired rocksalt structure and appropriate lattice parameter. The synthesis can be performed faster when smaller milling balls are used at a faster milling speed. When $Li_4Mn_2O_5$ is heated to above 625 °C, it transforms to a layered Li_2MnO_3 structure. This indicates the instability of the rocksalt structure upon heating. SEM images show that the $Li_4Mn_2O_5$ consists of small particles which agglomerate into larger particles. Upon exposure to air, $Li_4Mn_2O_5$ degrades, and this results in formation of Li_2CO_3. Initial, electrochemical testing in air provided low capacities, much below those in the literature, suggesting that alternative electrochemical testing methods are required.

5.3.3. Improvements to $Li_4Mn_2O_5$

In this section, different methods were used to try to improve the stability in air and electrochemical performance of $Li_4Mn_2O_5$. These methods will be taken forward when testing other materials in this chapter.

Firstly, $Li_4Mn_2O_5$ was milled with 10, 20 and 30 wt% PVDF powder at slow speeds (500 rpm for 2 hrs) to see whether a protective coating could be formed around the particles to prevent degradation in air. Figure 5-9 shows the XRD patterns of the PVDF coated $Li_4Mn_2O_5$ taken after 48 hrs exposure to air. All the patterns show peaks corresponding to the rocksalt phase. Both the 20 and 30 wt% PVDF coated samples show peaks due to Li_2CO_3 while the 10 wt% sample does not. This suggests that a small amount (10 wt%) of PVDF is required to provide a protective coating. This is unexpected as you would assume that a larger amount of PVDF would create a thicker coating. However, large amounts of PVDF may clump together and therefore prevent the $Li_4Mn_2O_5$ particles from being coated effectively. It is worth noting that the 20 and 30 wt%

samples do have less intense Li_2CO_3 peaks than seen for uncoated $Li_4Mn_2O_5$ (Figure 5-6).
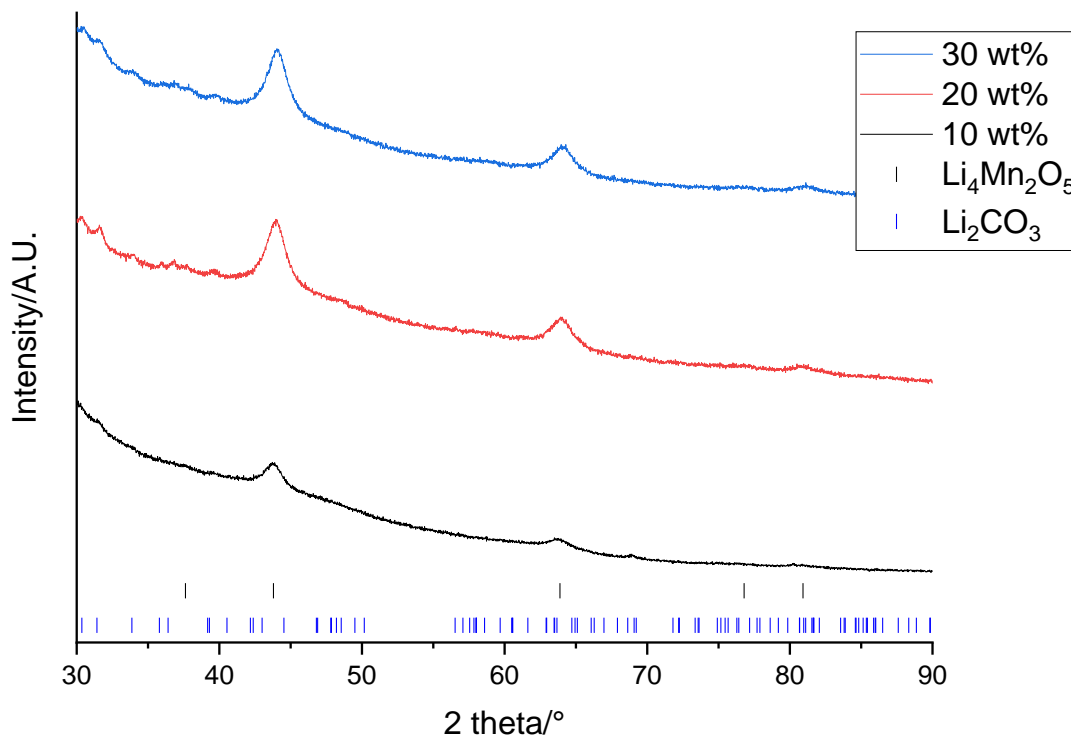
Figure 5-9: XRD patterns of $Li_4Mn_2O_5$ coated in 10 (black), 20 (red) and 30 (blue) wt% PVDF after exposure to air for 48 hrs ($\lambda = 1.54$ Å). Tick marks correspond to $Li_4Mn_2O_5$ (black) and Li_2CO_3 (blue).

Although coating $Li_4Mn_2O_5$ with 10 wt% PVDF was found to prevent Li_2CO_3 formation, the coated $Li_4Mn_2O_5$ still encountered the same problems when mixing/coating to prepare cathodes. This could suggest that there is still a small amount of Li_2CO_3 present on the surface which is not detected using XRD analysis.

An alternative method of electrochemical testing was therefore investigated. Swagelok cells were made under an Ar atmosphere with the cathode consisting of a mixture of $Li_4Mn_2O_5$ and carbon black. For more detail on the Swagelok set-up see Chapter 2 (section 2.2.5.2.). This therefore allowed the entire cell making procedure to be performed under Ar and therefore avoided exposing $Li_4Mn_2O_5$ to air.

Figure 5-10 shows the electrochemical data of a $Li_4Mn_2O_5$ powder cell. Although the voltage profile matches to Figure 5-8, the charge/discharge capacities are significantly higher and show that this method of making cells is superior for this material. The first charge and discharge have sloping voltage profiles with a significant voltage hysteresis. The first charge/discharge profile differs from subsequent cycles and appears to be irreversible. This is similar to the literature where it has been suggested that the material may undergo an activation during the first charge/discharge process.[24] Upon subsequent cycling, the voltage profile changes and plateaus begin to appear at 3.1 and 4.0 V on charge and 2.8 and 4.0 V on discharge.
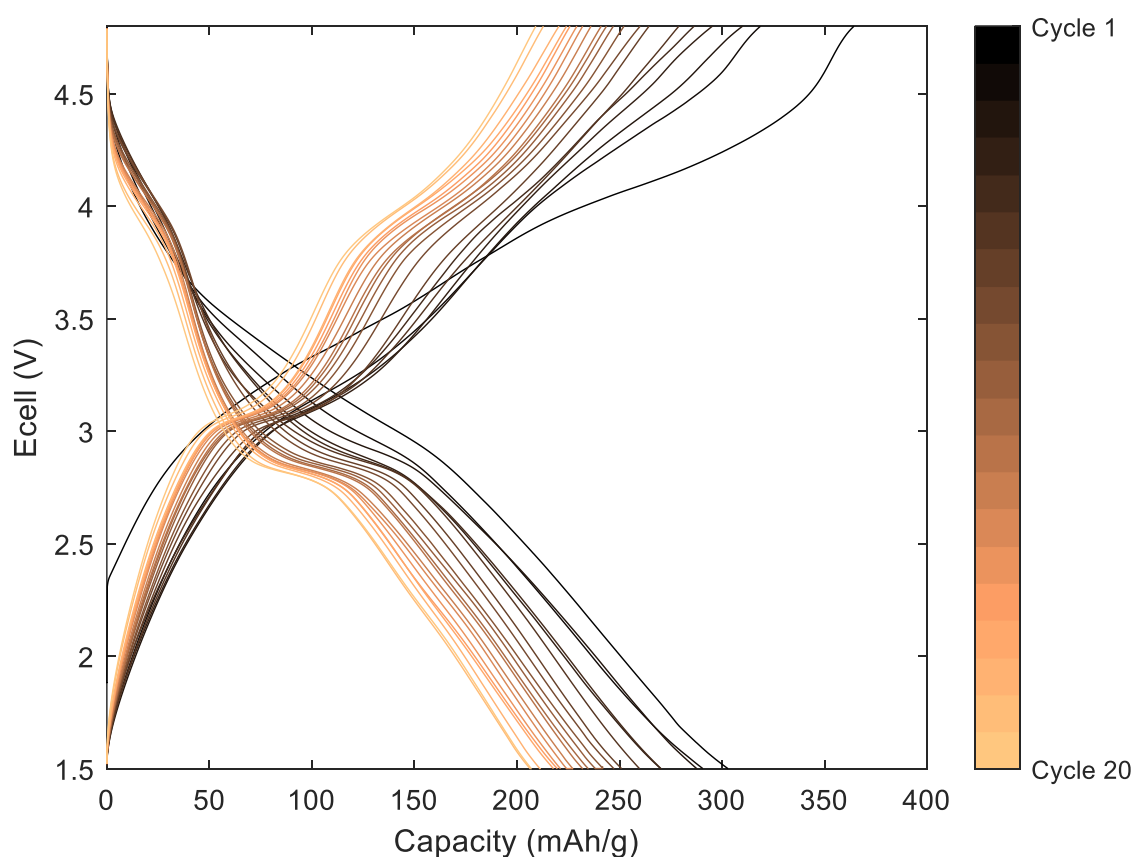
Figure 5-10: Galvanostatic charge-discharge profile of a pristine $Li_4Mn_2O_5$ powder cell cycled at 10 mAg^{-1} between 1.5-4.8 V

Figure 5-11 shows the dQ/dV plot of the $Li_4Mn_2O_5$ powder cell. Note that only selected cycles are shown. On the first cycle, redox processes are observed during charging at ~ 3.4 and 4.1 V and discharging at ~ 3.0 V. The peaks differ significantly upon further cycling, again indicating that the initial charging/discharging process is irreversible. During the second charge, there is a peak at 3.1 V due to $Mn^{3+/4+}$ redox and a broader peak at ~ 4.3 V due to O related redox couples (either $O^{2-/-}$ or O^-/O_2).[25] During the second discharge, there is a peak at 2.9 V due to the reduction of Mn^{4+} however there is no peak at 4.0 V indicating that any O redox upon charging is irreversible. By 20 cycles there are peaks at 3.1/2.8 and 4.0/3.9 V on charging/discharging which are due to Mn and O redox respectively. This shows that O redox becomes reversible on subsequent cycles.
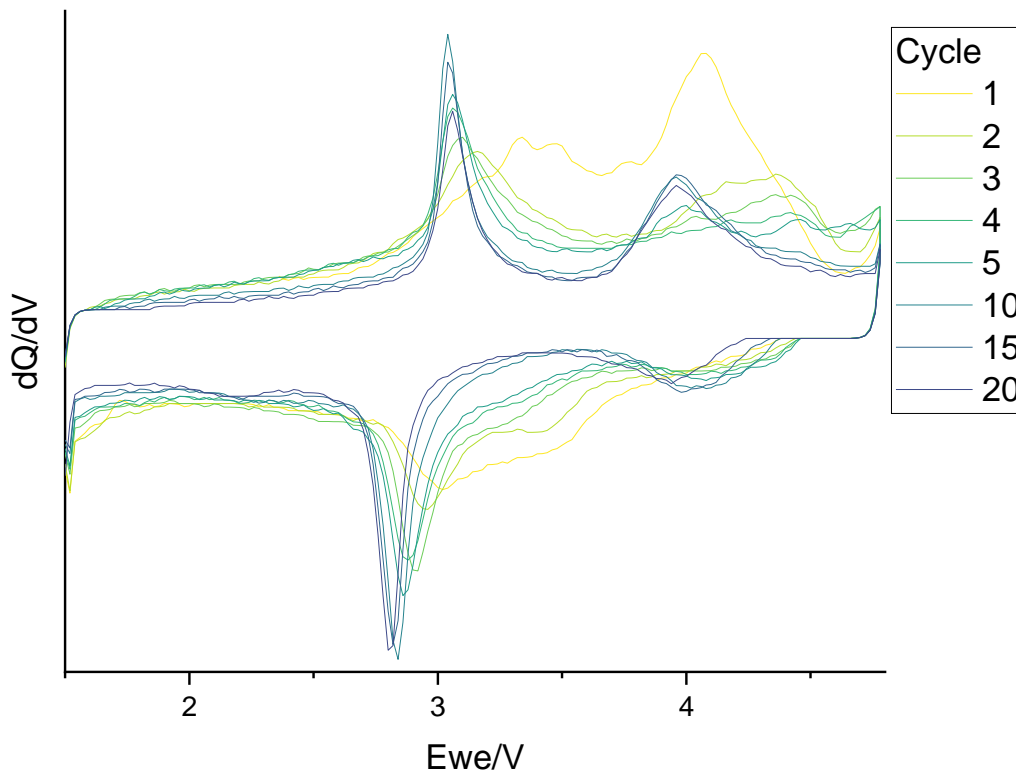
Figure 5-11: dQ/dV plot of a pristine $Li_4Mn_2O_5$ powder cell

Figure 5-12 shows the charge and discharge capacities for the $Li_4Mn_2O_5$ powder cell. The first cycle specific charge and discharge capacities are 364.3 and 302.9 mAhg^{-1} respectively which are comparable to capacities obtained in the literature for $Li_4Mn_2O_5$.[10] The capacities obtained suggest that in the first cycle 3.0 Li are extracted during charging and 2.5 Li are inserted back into the structure upon discharging. There is a 61.4 mAhg^{-1} difference between the charge and discharge capacities and this corresponds to 0.5 Li being "lost" during the cycling process. This difference between the charge and discharge capacities decreases upon further cycling and by 20 cycles there is only 2.2 mAhg^{-1} difference. The charge and discharge capacity both decrease upon cycling however, even after 20 cycles, the capacity is still relatively high.
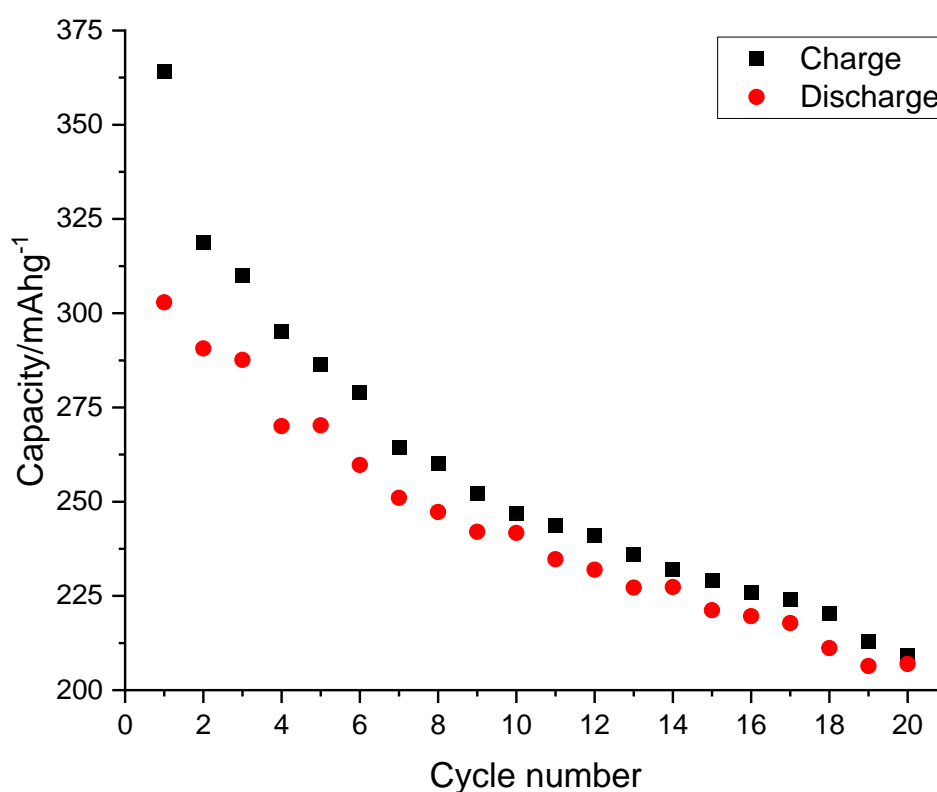
Figure 5-12: Charge (black) and discharge (red) capacities of a pristine $Li_4Mn_2O_5$ powder cell

Figure 5-13 shows the capacity retention for the $Li_4Mn_2O_5$ powder cell. The capacity

retention is 79.8% after 10 cycles and 68.3% after 20 cycles. In the literature, Freire

reported a 70.4% capacity retention after 8 cycles.[10] The capacity fade is worse during

the initial cycles which indicates that the problems related to capacity fade are most

prominent at the beginning of cycling. The capacity fade of DRS materials has been

linked to the activation of O redox so methods to mitigate this are required to improve

the capacity retention of these materials.[3,4]
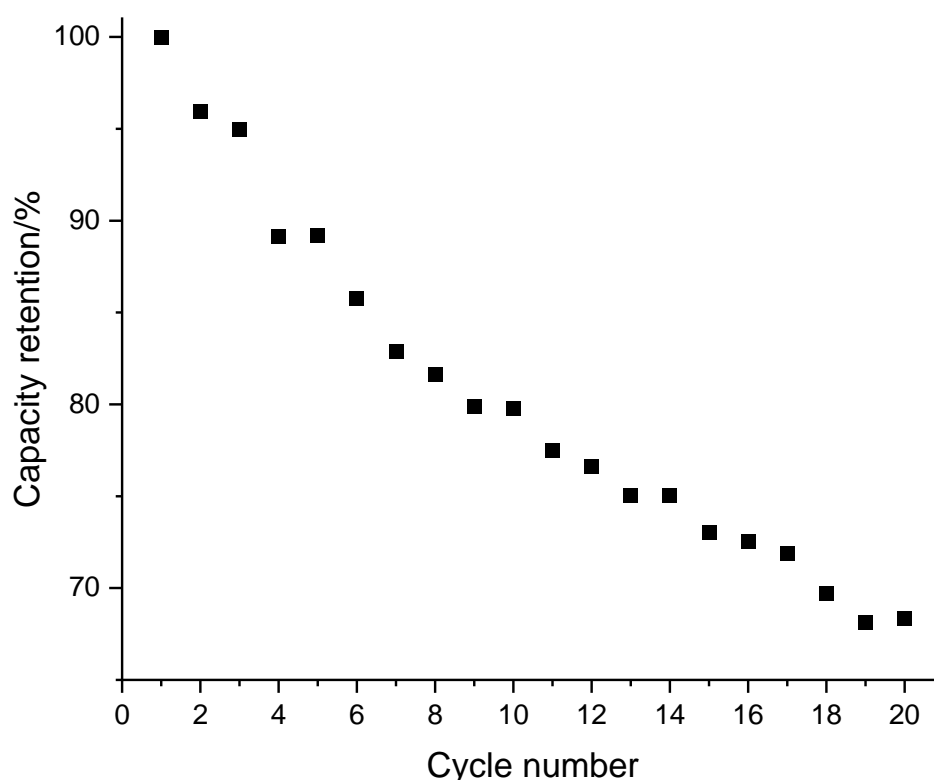
Figure 5-13: Capacity retention of a pristine $Li_4Mn_2O_5$ powder cell

Figure 5-14 shows the average discharge capacity of $Li_4Mn_2O_5$ powder cells run in

triplicate. The initial specific discharge capacity is 298.1 mAhg^{-1} which falls to 243.4

mAhg^{-1} after 6 cycles. The initial discharge capacity has a small error although the

error increases as the cells are cycled more. This shows that the repeatability

decreases upon cycling. It could suggest that there are different levels of degradation in different cells. This could be due to the small amounts of cathode used in powder cells not being representative of the entire sample.
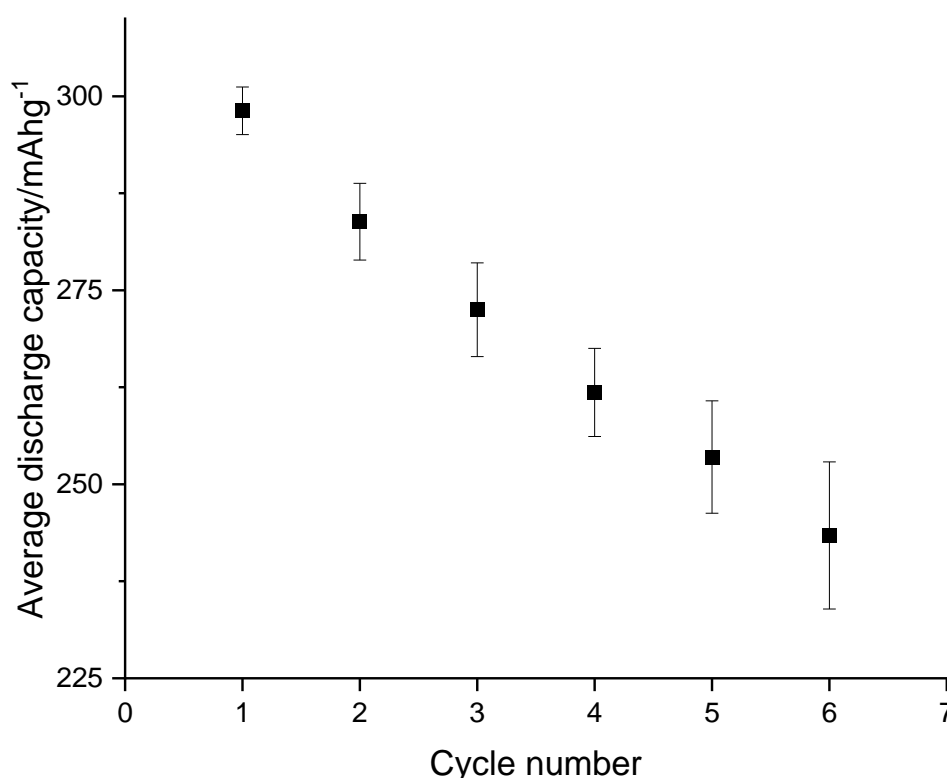
Figure 5-14: Average discharge capacity of pristine Li₄Mn₂O₅ powder cells. Error bars show relative standard deviation across 3 cells.

The next step taken was to use pellet cathodes instead of powder cathodes. Pellets were chosen as they could be made in a glovebox, therefore avoiding air exposure, and because it is easier to control their mass and surface area. Figure 5-15 shows the average discharge capacity of Li₄Mn₂O₅ pellet cells run in triplicate. Interestingly, the discharge capacity is higher than obtained for powder cells (373.7 compared to 298.1 mAhg⁻¹). This could be due to the PVDF in the pellets providing improved contact between the cathode particles which enables higher capacities to be achieved. The

pellet cells have significantly reduced error compared to the powder cells showing that pellet cells have an improved repeatability. However, the pellet cells all failed after 8-10 cycles. The cells were dismantled which showed that the pellets had cracked and therefore cell failure was attributed to this.
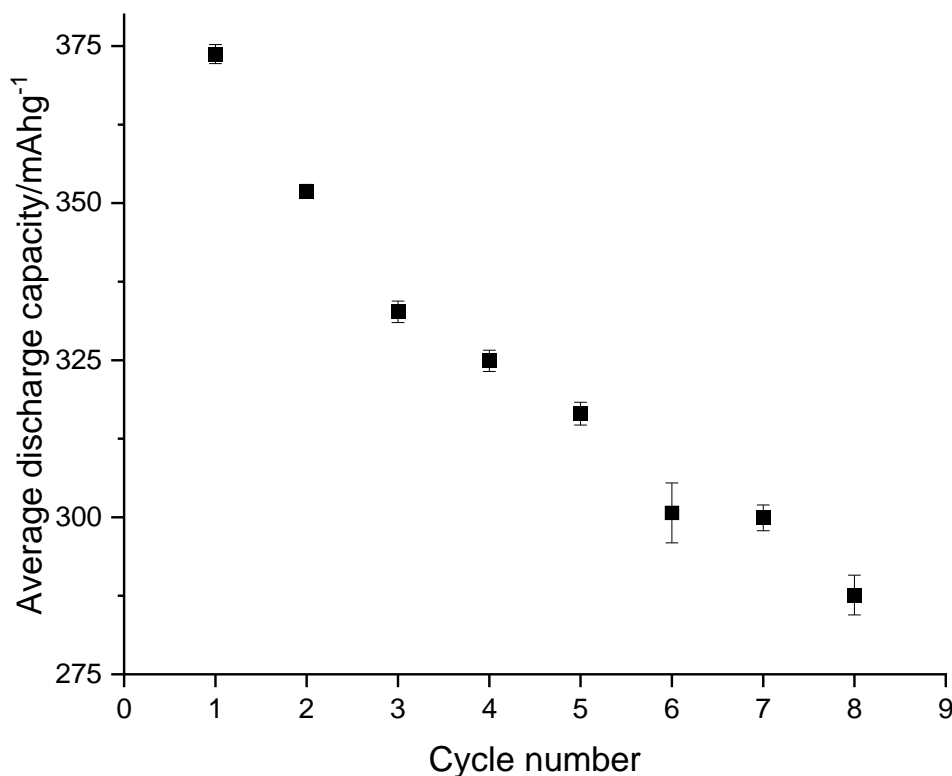
Figure 5-15: Average discharge capacity of pristine Li$_4$Mn$_2$O$_5$ pellet cells. Error bars show relative standard deviation across 3 cells.

In conclusion, it has been shown that 10 wt% PVDF can be used as a protective coating to prevent degradation of Li$_4$Mn$_2$O$_5$ upon exposure to air. Li$_4$Mn$_2$O$_5$ that is tested using powder Swageloks instead of coatings in air has been shown to have an improved electrochemical performance. Further improvements have been made by using pellet Swageloks. These have been shown to give an improved repeatability compared to powder cells and a higher discharge capacity. However, they experience

cell failure upon numerous cycles. Therefore, all the subsequent electrochemical testing performed in this chapter will be performed using powder cells. This is to allow 10 cycles to be reliably obtained. Pellet Swagelok cells will then be made of the most promising samples.

5.3.4. Electrochemical testing of $Li_4Mn_2O_5$

In this section, different electrochemical testing conditions were used to further analyse the electrochemical performance of $Li_4Mn_2O_5$. Smaller voltage ranges and faster cycling rates were investigated.

Figure 5-16 shows the electrochemical performance of $Li_4Mn_2O_5$ when it is cycled between a voltage range of 2-4.3 and 2.5-4.3 V. This contrasts with Figure 5-10 where a larger voltage range of 1.5-4.8 V was used. Under all these conditions, the first charge and discharge have sloping voltage profiles. In subsequent cycles, the voltage profile changes and plateaus appear at 3.1 and 4.0 V on charge and 2.8 V on discharge. This is also shown by peaks in the dQ/dV plots. The redox activity at 2.8/3.1 V is due to Mn redox while the activity at 4.0 V is due to O redox. In contrast to Figure 5-11, there is no peak at 4.0 V upon discharging which suggests that O redox is irreversible.
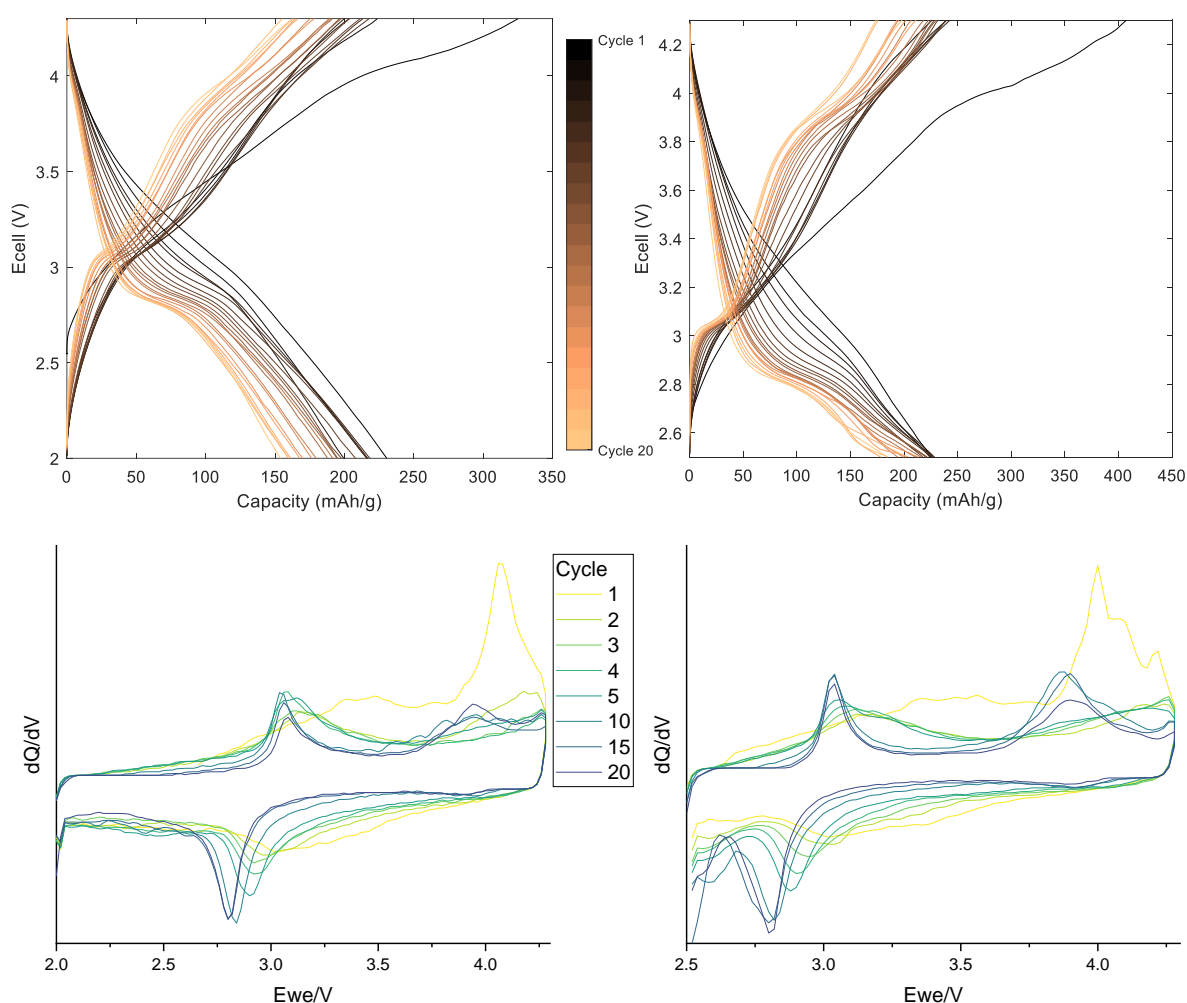
Figure 5-16: Galvanostatic charge-discharge profiles (above) and dQ/dV plots (below) of pristine Li$_4$Mn$_2$O$_5$ powder cells cycled at 10 mAg^{-1} between 2-4.3 (left) and 2.5-4.3 (right) V

Figure 5-17 shows the discharge capacities for Li$_4$Mn$_2$O$_5$ cycled between different voltage limits. As the voltage limits are decreased the initial specific discharge capacity decreases from 302.9 to 230.5 and 211.7 mAhg^{-1} for 1.5-4.8, 2-4.3 and 2.5-4.3 V respectively. Lower discharge capacities are expected as smaller voltage ranges limit the amount of Li that can be removed/inserted into the structure. Figure 5-17 also shows that the 2.5-4.3 V cell has a decreased capacity fade. 1.5-4.8 V has a 68.3% capacity retention after 20 cycles, 2-4.3 V has 66.8% and 2.5-4.3 V has 81.8%. This shows that decreasing the voltage range to 2-4.3 V does not have a significant impact

upon the capacity retention however a further decrease in the voltage range to 2.5-4.3 V results in a better capacity retention. This suggests that the lower voltage limit is important which is interesting as you would assume that the higher voltage limit which controls the amount of O redox/electrolyte decomposition would play a larger role.
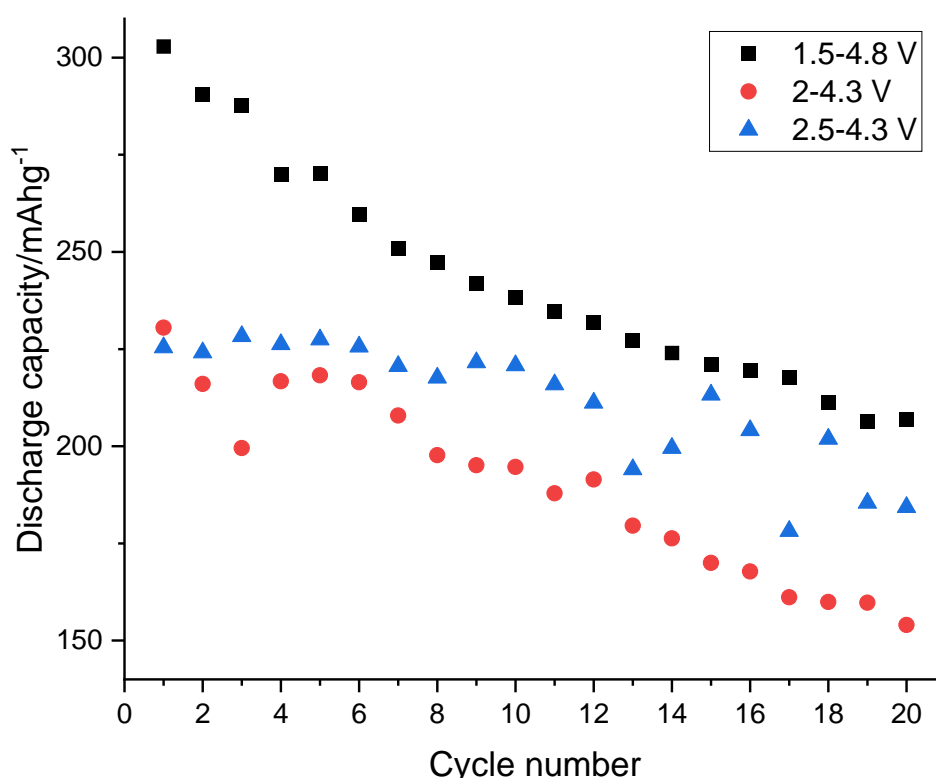
Figure 5-17: Discharge capacity of pristine Li$_4$Mn$_2$O$_5$ powder cells cycled between 1.5-4.8 (black), 2-4.3 (red) and 2.5-4.3 (blue) V

Figure 5-18 shows the electrochemical performance of Li$_4$Mn$_2$O$_5$ when it is cycled at a faster cycling rate of 100 mAhg^{-1}. The voltage profile is different to cycling at 10 mAg^{-1} (Figure 5-10) as it is more sloping and shows less distinct voltage plateaus. The initial specific discharge capacity is 238.9 mAhg^{-1} which is considerably lower than when cycling at 10 mAg^{-1} (302.9 mAhg^{-1}). This is probably because of Li diffusion limitations in the shorter charging time. Figure 5-18 (right) shows that the capacity retention is

similar at both cycling rates for the first 10 cycles: 78.6 and 74.6% for 10 and 100 mAg^{-1} respectively. However, after 20 cycles the capacity retention of the 100 mAg^{-1} cell drops significantly to 59.9% compared to 74.6% for 10 mAg^{-1}. This suggests that although the initial degradation is similar at both cycling rates, faster cycling rates result in additional degradation upon further cycling.
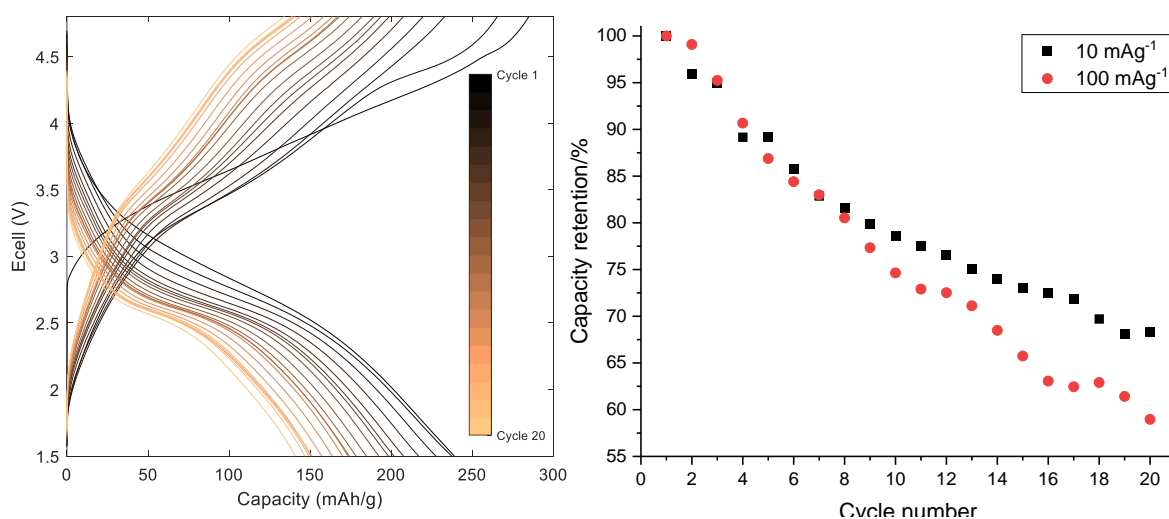
Figure 5-18: Galvanostatic charge-discharge profile (left) and capacity retention (right) of a pristine Li$_4$Mn$_2$O$_5$ powder cell cycled at 100 mAg^{-1} (red) between 1.5-4.8 V (10 mAg^{-1} shown for reference in black)

This section shows that the use of a smaller voltage range of 2.5-4.3 V can be used to improve the capacity retention of Li$_4$Mn$_2$O$_5$ however it does result in a lower discharge capacity. The use of an intermediate voltage range of 2-4.3 V results in a lower discharge capacity without any appreciable improvements to the capacity retention. A faster cycling rate of 100 mAg^{-1} causes a decrease in the discharge capacity and significantly worse capacity retention over multiple cycles. Further work is needed to understand these behaviours more comprehensively.

5.4. Doped rocksalts

Next, a range of rocksalts containing Li, Mn and O along with other dopants, such as F, Ni, Zn and Na, were synthesised to investigate whether this would lead to improvements in the electrochemical performance.

5.4.1. F-doping

5.4.1.1.   Pristine $Li_2MnO_{2.25}F$

Firstly $Li_2MnO_{2.25}F$ was synthesised. $Li_2MnO_{2.25}F$ contains $Mn^{3.5+}$ and has an anion excess. LMO was again used as a reagent in the synthesis. Figure 5-19 shows the XRD pattern of pristine $Li_2MnO_{2.25}F$. The desired rocksalt structure has been formed and all the peaks can be indexed based upon the $Fm\bar{3}m$ space group. There are no other peaks present indicating that there are no other phases present. Pawley refinements gave a lattice parameter of 4.112(2) Å. The lattice parameter is smaller than $Li_4Mn_2O_5$ (4.17(1) Å). The Mn oxidation state is higher for $Li_2MnO_{2.25}F$ ($Mn^{3.5+}$ compared to Mn^{3+}) therefore the average Mn ionic radius is smaller in $Li_2MnO_{2.25}F$ leading to a smaller lattice parameter. It is worth noting that the (111) peak at 38.2° is not present for $Li_2MnO_{2.25}F$, which could be due to F-doping changing the long-range order in the structure.[26,27]
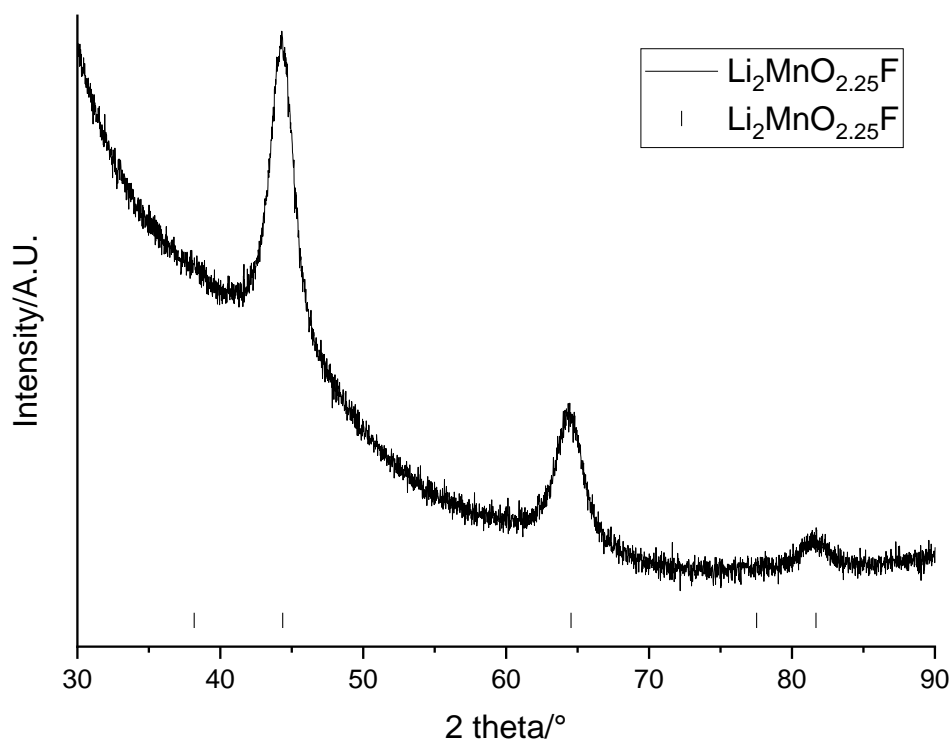
Figure 5-19: XRD patterns of pristine Li₂MnO₂.₂₅F (λ = 1.54 Å). Tick marks correspond to Li₂MnO₂.₂₅F (black)

Figure 5-20 shows the Raman spectrum for $Li_2MnO_{2.25}F$. There are peaks at 484, 618 and 1166 cm^{-1}. The Raman spectrum is similar to the spectra obtained for $Li_4Mn_2O_5$ (Figure 5-4) although the peak at 1166 cm^{-1} is not distinguishable as two peaks. There are no additional bands present due to the introduction of F.
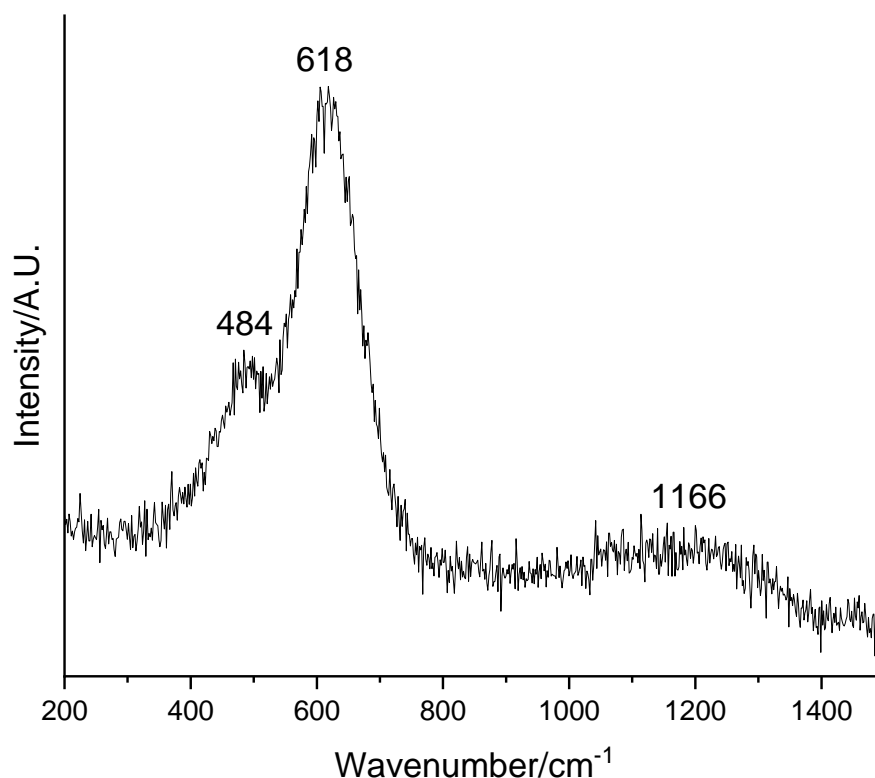
Figure 5-20: Raman spectrum of pristine Li$_2$MnO$_{2.25}$F

Figure 5-21 shows the XRD patterns of Li$_2$MnO$_{2.25}$F after exposure to air. After 8 hrs

of air exposure, there are peaks present at 51 and 75° (marked with *). These peaks

could not be matched and therefore it is unknown what they are due to. They do not

match to another rocksalt phase or to LiF. The unknown phase was not present in the

air exposed patterns of Li$_4$Mn$_2$O$_5$ (Figure 5-6) which suggests that it is linked to the

presence of F. There are also small peaks which indicate that Li$_2$CO$_3$ is beginning to

form. After 48 hrs of air exposure, the unknown phase is still present and the peaks

due to Li$_2$CO$_3$ have increased in intensity indicating that more Li$_2$CO$_3$ is present. These

results show that Li$_2$MnO$_{2.25}$F must also be kept under inert atmosphere to prevent the

formation of Li$_2$CO$_3$.
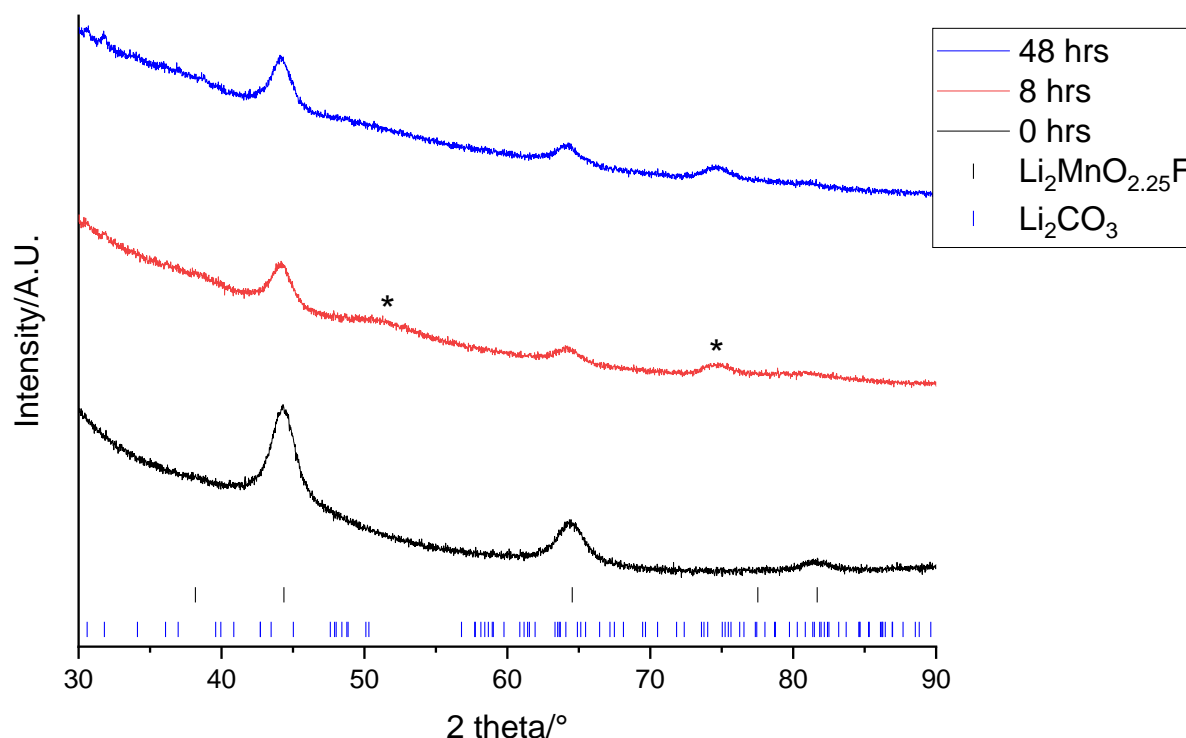
*Figure 5-21: XRD patterns of Li$_2$MnO$_{2.25}$F after exposure to air for 0 (black), 8 (red) and 48 (blue) hrs (λ = 1.54 Å). Tick marks correspond to Li$_2$MnO$_{2.25}$F (black), Li$_2$CO$_3$ (blue) and * mark unknown phase.*

Li$_2$MnO$_{2.25}$F was coated with 10 wt% PVDF as explored in section 5.3.3. for Li$_4$Mn$_2$O$_5$. Figure 5-22 shows the XRD patterns of the PVDF coated Li$_2$MnO$_{2.25}$F after exposure to air. After 8 hrs of air exposure, the rocksalt phase is present along with peaks due to the unknown impurity seen in Figure 5-21. However, there are no peaks due to Li$_2$CO$_3$. The pattern taken after 48 hrs of exposure shows the same phases present. This suggests that the PVDF coating helps to prevent formation of Li$_2$CO$_3$ however it does not prevent formation of the unknown phase.
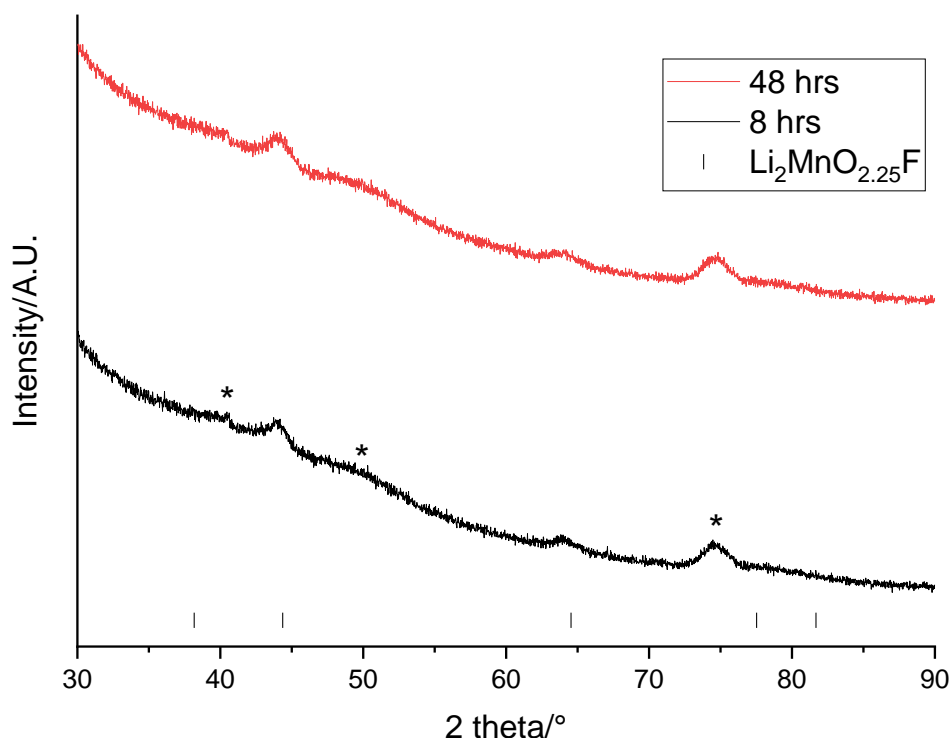
*Figure 5-22: XRD patterns of $Li_2MnO_{2.25}F$ coated in 10 wt% PVDF after exposure to air for 8 (black) and 48 (red) hrs ($\lambda = 1.54$ Å). Tick marks correspond to $Li_2MnO_{2.25}F$ (black) and * mark unknown phase.*

Figure 5-23 shows the VT-XRD patterns of $Li_2MnO_{2.25}F$ when heated under air from 100 to 800 °C. Initially, the peaks match to the rocksalt phase however at 600 °C there are additional peaks present which can be matched to $LiMn_2O_4$. At 700 °C the rocksalt phase is no longer present and instead the peaks match to both $LiMn_2O_4$ and Li_2MnO_3. At 800 °C the $LiMn_2O_4$ phase is no longer present, and the peaks can all be assigned to Li_2MnO_3. In the final XRD pattern taken at room temperature, the peaks again match to only Li_2MnO_3. This shows that $Li_2MnO_{2.25}F$ changes structure when heated and transitions from a rocksalt structure to a layered Li_2MnO_3 structure via a $LiMn_2O_4$ intermediate.
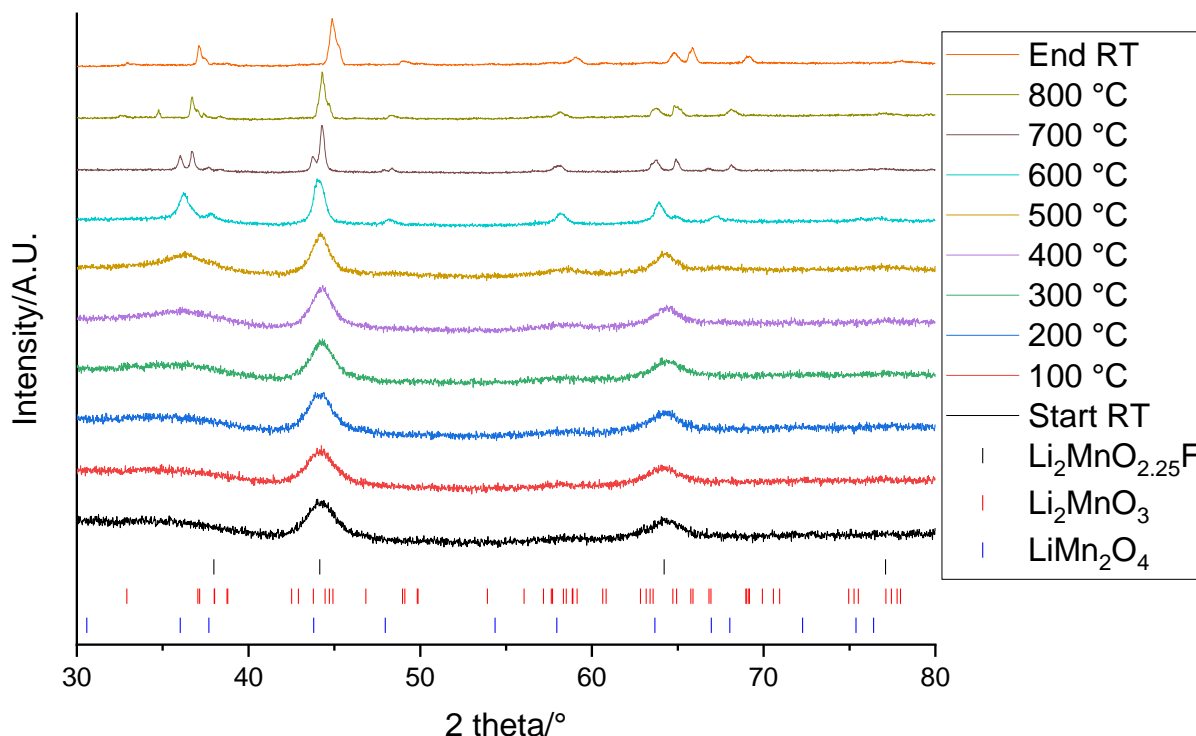
Figure 5-23: VT-XRD patterns of pristine Li₂MnO₂.₂₅F heated from 100 to 800 °C at 100 °C intervals (λ = 1.54 Å). Tick marks correspond to Li₂MnO₂.₂₅F (black), Li₂MnO₃ (red) and LiMn₂O₄ (blue).

Figure 5-24 shows the electrochemical data of a $Li_2MnO_{2.25}F$ powder cell. The first charge and discharge voltage profiles are different to subsequent cycles. The first discharge has a voltage plateau at ~ 3.5 V. As the sample undergoes further cycles the voltage profile becomes increasingly sloping and by 10 cycles there is no plateau present. As with $Li_4Mn_2O_5$, this may suggest that there is an activation process occurring upon the first cycle that results in a different appearance to the initial voltage profile. Figure 5-24 below shows the corresponding dQ/dV plot. On the first cycle, peaks are observed during charging at 4.3-4.8 V. These correspond to O redox and suggests that the addition of F has not prevented the activation of O redox. The first discharge shows a peak at 3.4 V which is likely to be due to Mn redox. The presence

of F causes the voltage of the $Mn^{3+/4+}$ redox couple to increase compared to $Li_4Mn_2O_5$.[28] Upon further cycling there are peaks at 3.3 and 4.5 V upon charging which are likely to be due to Mn and O redox respectively. Upon discharge there is only one peak at 3.4 V due to Mn redox and no peak corresponding to O redox. This suggests that any O redox activity is irreversible. The peaks due to O redox are more intense than seen for $Li_4Mn_2O_5$ (Figure 5-11) which suggests that more O redox is occurring.
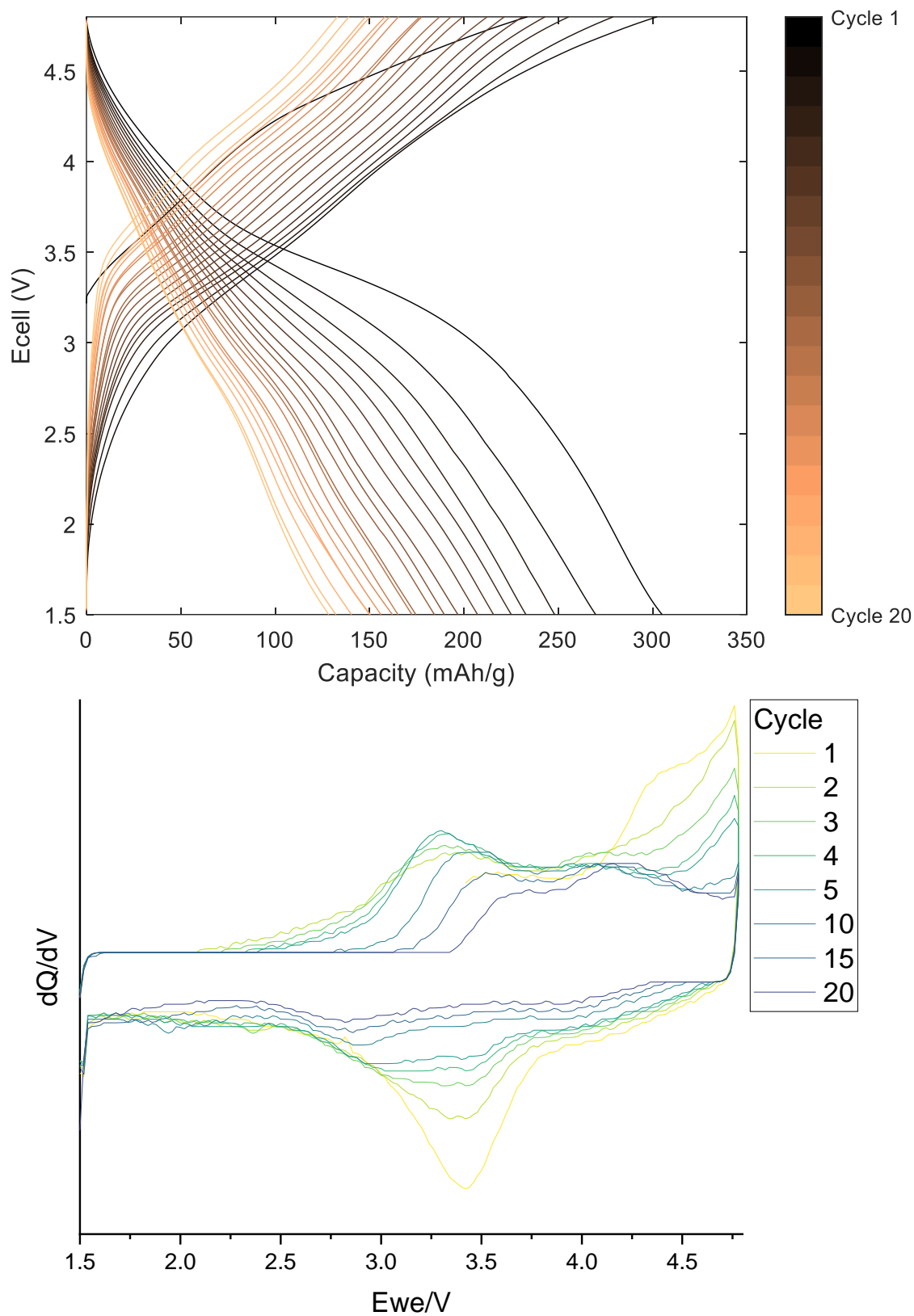
Figure 5-24: Galvanostatic charge-discharge profile (above) and dQ/dV plot (below) of a pristine Li₂MnO₂.₂₅F powder cell cycled at 10 mAg⁻¹ between 1.5-4.8 V

Figure 5-25 shows the charge and discharge capacities for the $Li_2MnO_{2.25}F$ powder cell. The first cycle specific charge and discharge capacities are 233.5 and 305.0 $mAhg^{-1}$ respectively. The discharge capacity is comparable to $Li_4Mn_2O_5$ above. The charge capacity is much lower (71.4 $mAhg^{-1}$) than the discharge capacity which suggests some of the capacity during discharge must be provided by the Li metal anode. In the second cycle the charge capacity is 32.5 $mAhg^{-1}$ higher than the discharge capacity however by 20 cycles the charge capacity is only 4.6 $mAhg^{-1}$ higher than the discharge. This suggests that in the initial cycles some Li is lost during the charge/discharge process and upon further cycles the Li is cycled more reversibly.
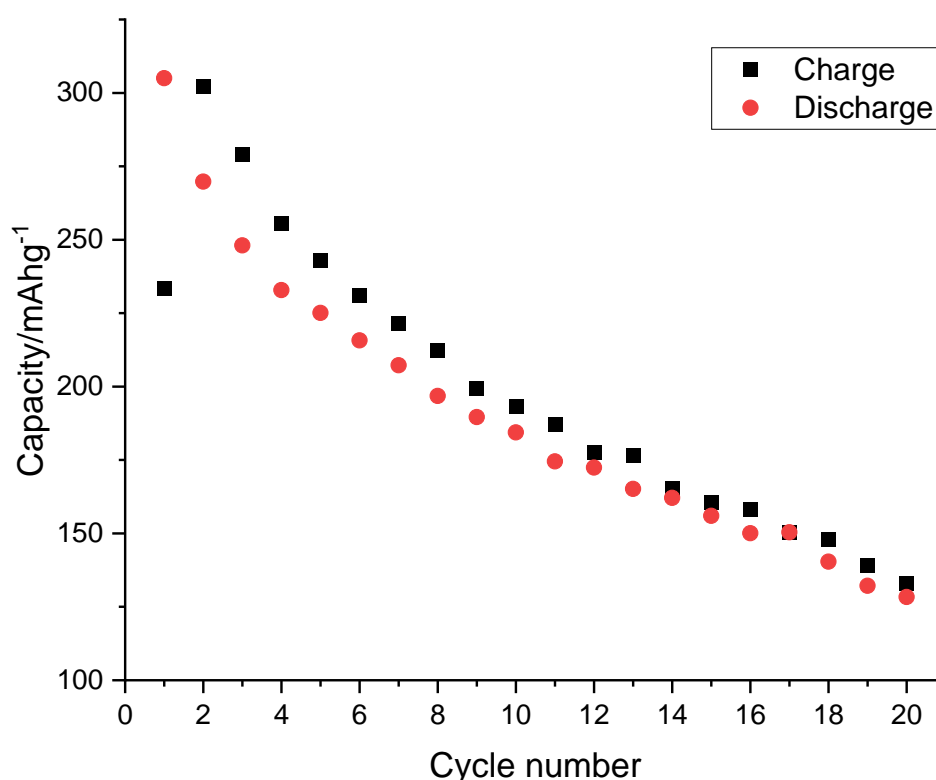
Figure 5-25: Charge (black) and discharge (red) capacities of a pristine $Li_2MnO_{2.25}F$ powder cell

Figure 5-26 shows the capacity retention of the $Li_2MnO_{2.25}F$ powder cell. The capacity retention is 60.4% after 10 cycles and 42.1% after 20 cycles. The capacity retention is worse than $Li_4Mn_2O_5$ (Figure 5-13). The dQ/dV plot (Figure 5-24) suggests that $Li_2MnO_{2.25}F$ has more O redox occurring than $Li_4Mn_2O_5$ and this might be causing the poorer capacity retention. This suggests that different F-doped rocksalt compositions should be investigated to see if they can avoid the activation of O redox and improve the capacity retention. Similarly to $Li_4Mn_2O_5$, the capacity fade is worse during the initial cycles indicating that the problems related to capacity fade are most prominent at the beginning of cycling.
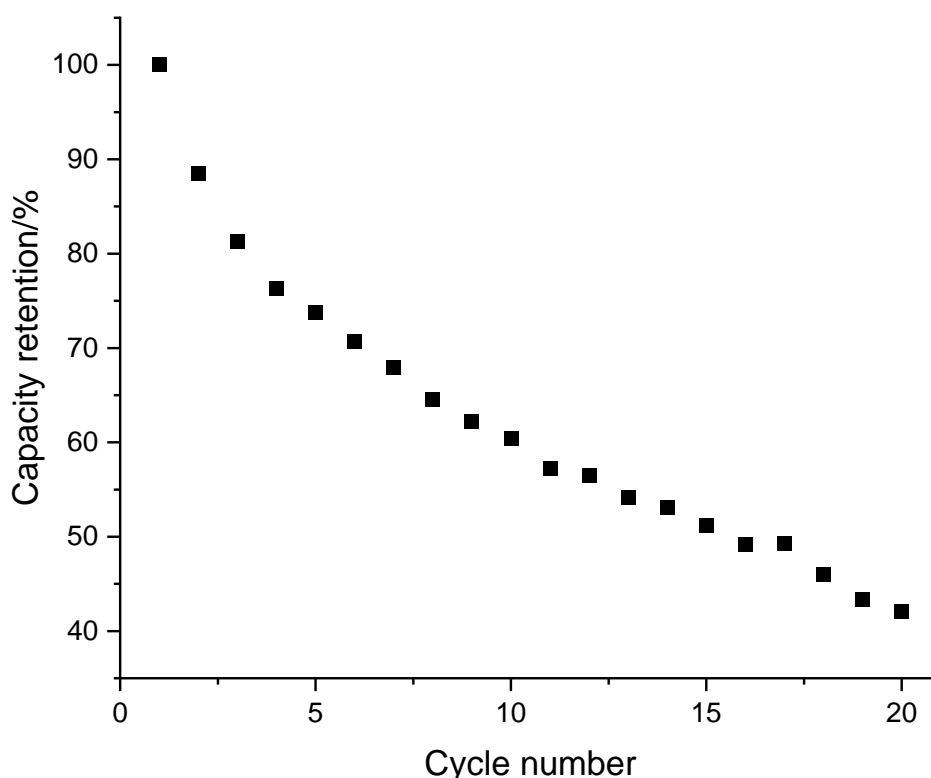
Figure 5-26: Capacity retention of a pristine $Li_2MnO_{2.25}F$ powder cell

Figure 5-27 shows the average discharge capacity of $Li_2MnO_{2.25}F$ powder cells run in triplicate. The initial specific discharge capacity is 326.3 mAhg^{-1} which falls to 185.3

mAhg^{-1} after 10 cycles. As seen for Li$_4$Mn$_2$O$_5$, the error increases as the cells are cycled, showing that the repeatability decreases upon cycling.
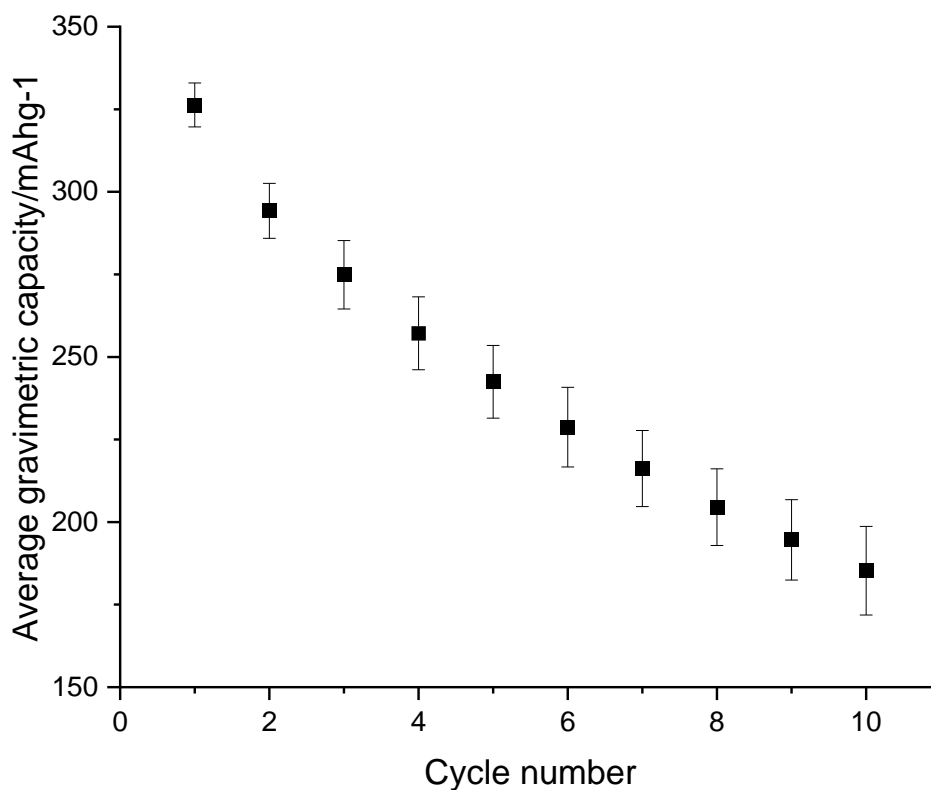
Figure 5-27: Average discharge capacity of pristine Li$_2$MnO$_{2.25}$F powder cells. Error bars show relative standard deviation across 3 cells.

Figure 5-28 shows the electrochemical performance of Li$_2$MnO$_{2.25}$F when it is cycled between a voltage range of 2-4.3 and 2.5-4.3 V. The voltage figures look extremely different to Figure 5-24 where a larger voltage range of 1.5-4.8 V was used. As the 2-4.3 V cell (left) is cycled, voltage plateaus appear at 3.9 V on charging and 2.6 and 2.7 V on discharging. There are corresponding peaks in the dQ/dV plot. The splitting of the peak at ~2.7 V is interesting as this suggests that there may be different Mn environments which results in redox activity at different voltages. The peak at 3.9 V is likely to be due to O redox so this suggests that O redox is still activated when using

these voltage ranges. The 2.5-4.3 V cell (right) shows similar characteristics with evolution of a voltage plateau at 3.9 V on charging and a flattening of the voltage at 2.6 V on discharging. Although these cells do appear to have O redox occurring, the intensity of the peaks is smaller compared to the 1.5-4.8 V cell which suggests that less O redox is occurring.
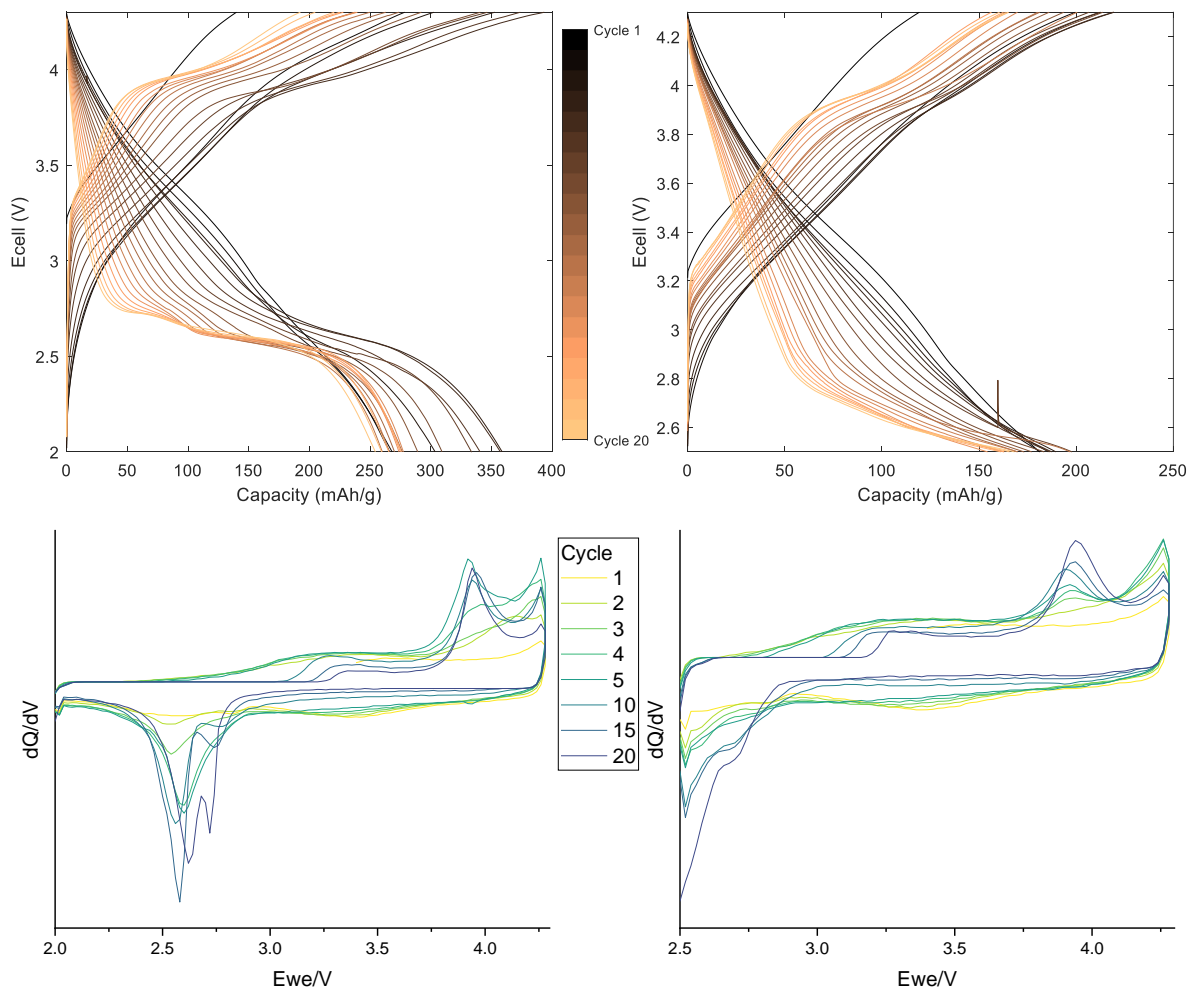
Figure 5-28: Galvanostatic charge-discharge profiles (above) and dQ/dV plots (below) of pristine Li$_2$MnO$_{2.25}$F powder cells cycled at 10 mAg^{-1} between 2-4.3 (left) and 2.5-4.3 (right) V

Figure 5-29 shows the discharge capacities for Li$_2$MnO$_{2.25}$F cycled between different voltage limits. The 1.5-4.8 V has a higher initial specific discharge capacity (305.0 mAhg^{-1}) than 2-4.3 or 2.5-4.3 V (266.1 and 181.1 mAhg^{-1}). However, on subsequent cycles the smaller voltage ranges show different behaviour. The 2-4.3 V cell has an

initial increase in specific discharge capacity to 358.7 mAhg^{-1} after 4 cycles. Then the

capacity decreases upon further cycling to give a 95.6% capacity retention after 20

cycles. In contrast, the capacity of the 2.5-4.3 V cell remains more constant, and it has

a capacity retention of 92.9% after 20 cycles. Both contrast with the 1.5-4.8 V cell,

which has a much poorer capacity retention of 42.1% after 20 cycles. These results

are interesting as they show that by changing the voltage range, Li$_2$MnO$_{2.25}$F can

achieve a significantly improved capacity retention. This is likely to be due to less O

redox being activated which in turn means that less degradation occurs.
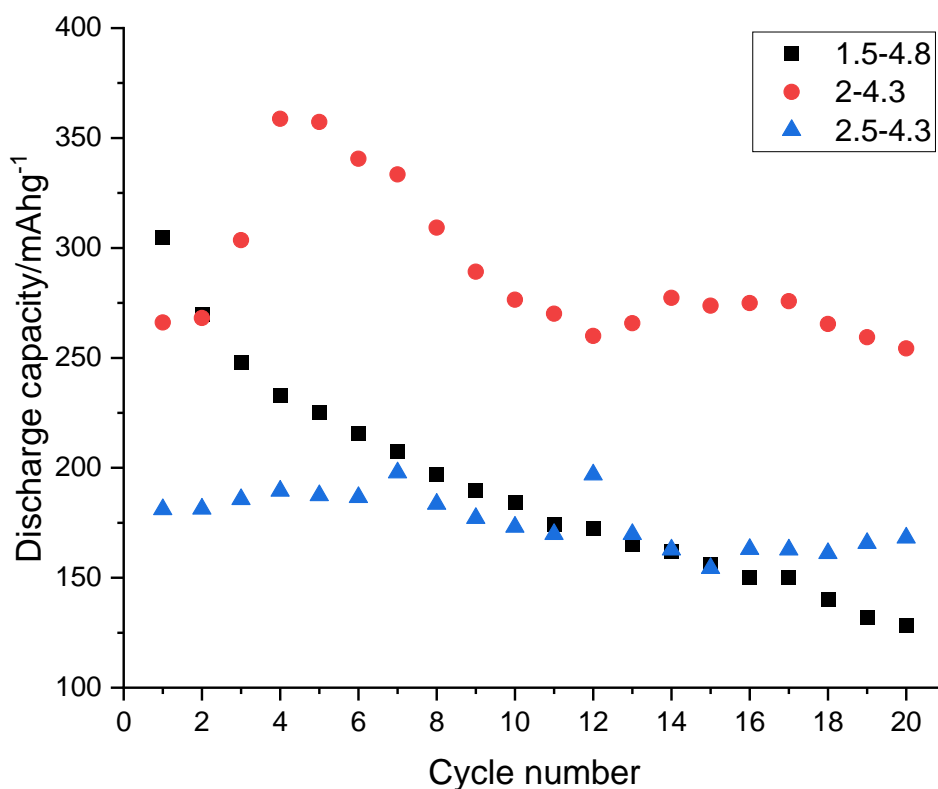
Figure 5-29: Discharge capacity of pristine Li$_2$MnO$_{2.25}$F powder cells cycled between 1.5-4.8 (black), 2-4.3 (red) and 2.5-4.3 (blue) V

In conclusion, this section shows that Li$_2$MnO$_{2.25}$F can be synthesised with the desired

rocksalt structure. Upon exposure to air, Li$_2$MnO$_{2.25}$F degrades, and this results in

formation of Li_2CO_3 along with an unknown phase. Electrochemical testing of $Li_2MnO_{2.25}F$ provided a high discharge capacity although there was extremely poor capacity retention which is attributed to activation of O redox. Improvements to the capacity retention have been achieved by cycling with reduced voltage ranges.

5.4.1.2. Alternative F-doped compositions

In this section a range of F containing compositions were made to investigate whether this would have an impact upon the electrochemical performance. Compounds with a range of Mn oxidation states and F contents were synthesised.

Table 5-2 shows the range of F-doped samples that were synthesised. The Mn oxidation state of the samples varies from 2.75 to 3.5+. As the Mn oxidation state increases, there is a corresponding decrease in the amount of F present. It is worth noting that $Li_2MnO_{1.625}F_{1.5}$ and $Li_2MnO_{2.25}F$ both contain an anion excess suggesting that there will be cation vacancies in these samples if they are successfully prepared. Figure 5-30 shows that all the samples have the desired rocksalt structure without any other impurity phases present. The peaks in the XRD pattern shift to lower 2 theta values as the Mn oxidation state decreases (going from bottom to top pattern). This is reflected by the lower Mn oxidation state samples having a larger lattice parameter (Table 5-2) and can be explained by the fact that as the Mn oxidation state decreases, the average Mn ionic radius increases.

Table 5-2: F-doped rocksalt samples with Mn oxidation state and lattice parameter

Sample	Mn oxidation state	a/Å
$Li_2MnO_{1.625}F_{1.5}$	2.75+	4.180(2)
$Li_2MnO_{1.75}F_{1.25}$	2.75+	4.173(1)
Li_2MnO_2F	3+	4.154(1)
$Li_2MnO_{2.25}F$	3.5+	4.112(2)
$Li_2MnO_{2.5}F_{0.5}$	3.5+	4.113(1)
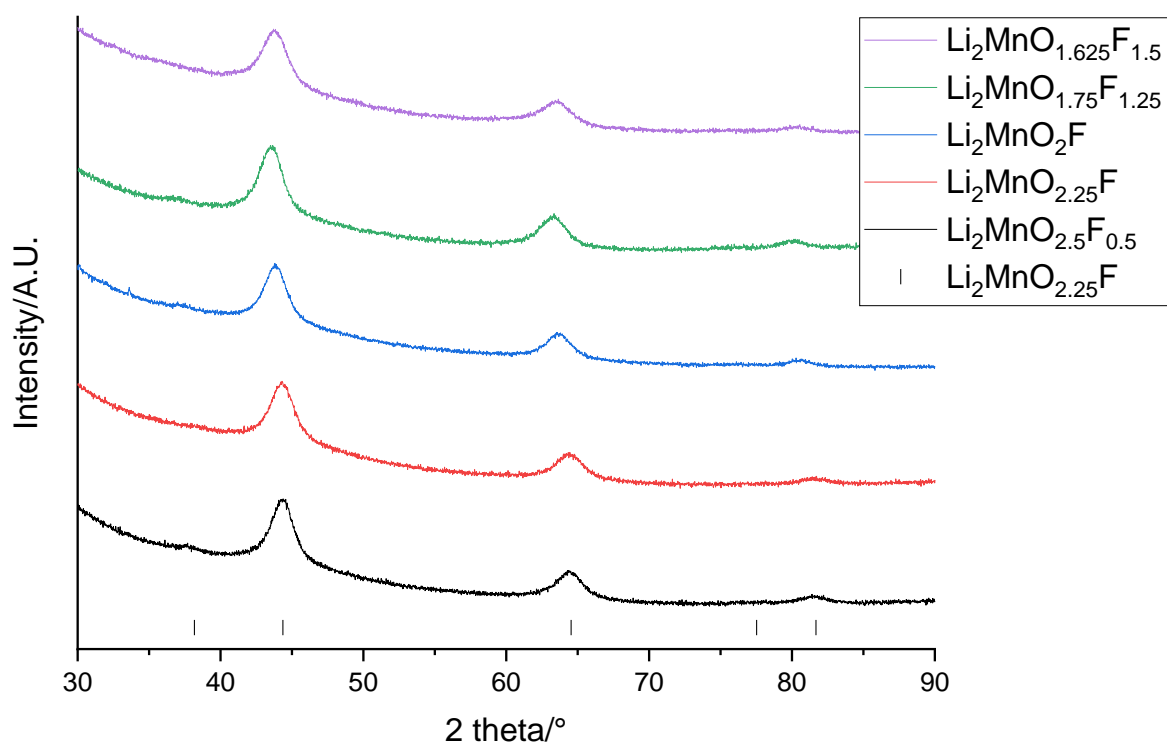
Figure 5-30: XRD patterns of $Li_2MnO_{2.5}F_{0.5}$ (black), $Li_2MnO_{2.25}F$ (red), Li_2MnO_2F (blue), $Li_2MnO_{1.75}F_{1.25}$ (green) and $Li_2MnO_{1.625}F_{1.5}$ (purple) (λ = 1.54 Å). Tick marks correspond to $Li_2MnO_{2.25}F$ (black).

Figure 5-31 shows the electrochemical performance of Li_2MnO_2F and $Li_2MnO_{1.625}F_{1.5}$. The electrochemical data for $Li_2MnO_{2.25}F$ are shown in Figure 5-24 while the electrochemical data for $Li_2MnO_{1.75}F_{1.25}$ and $Li_2MnO_{2.5}F_{0.5}$ is shown in Appendix J. The voltage profile for Li_2MnO_2F (left) contains several regions with different gradients; these regions cause corresponding peaks in the dQ/dV plot. On charging there are peaks at 3.2 and 4.1 V while on discharging there is a peak at 2.5 V. The peaks at 3.2/2.5 V are likely to be due to Mn redox while the peak at 4.1 V is likely to be due to O redox. In contrast, $Li_2MnO_{1.625}F_{1.5}$ has a voltage profile with a constant sloping gradient. This is suggestive of the delithiation having a solid solution mechanism and in turn corresponds to broad peaks over a wide voltage range in the dQ/dV plot. The peaks in the dQ/dV plot for the first cycle are the same as subsequent cycles, suggesting that $Li_2MnO_{1.625}F_{1.5}$ does not undergo an activation process on the first cycle. There are significant changes between these voltage profiles and the voltage profile for $Li_2MnO_{2.25}F$ which shows that changes to the chemical composition of the rocksalt can have an impact upon the electrochemical performance, although, it is worth noting that all the F-doped samples display some level of O redox activity.
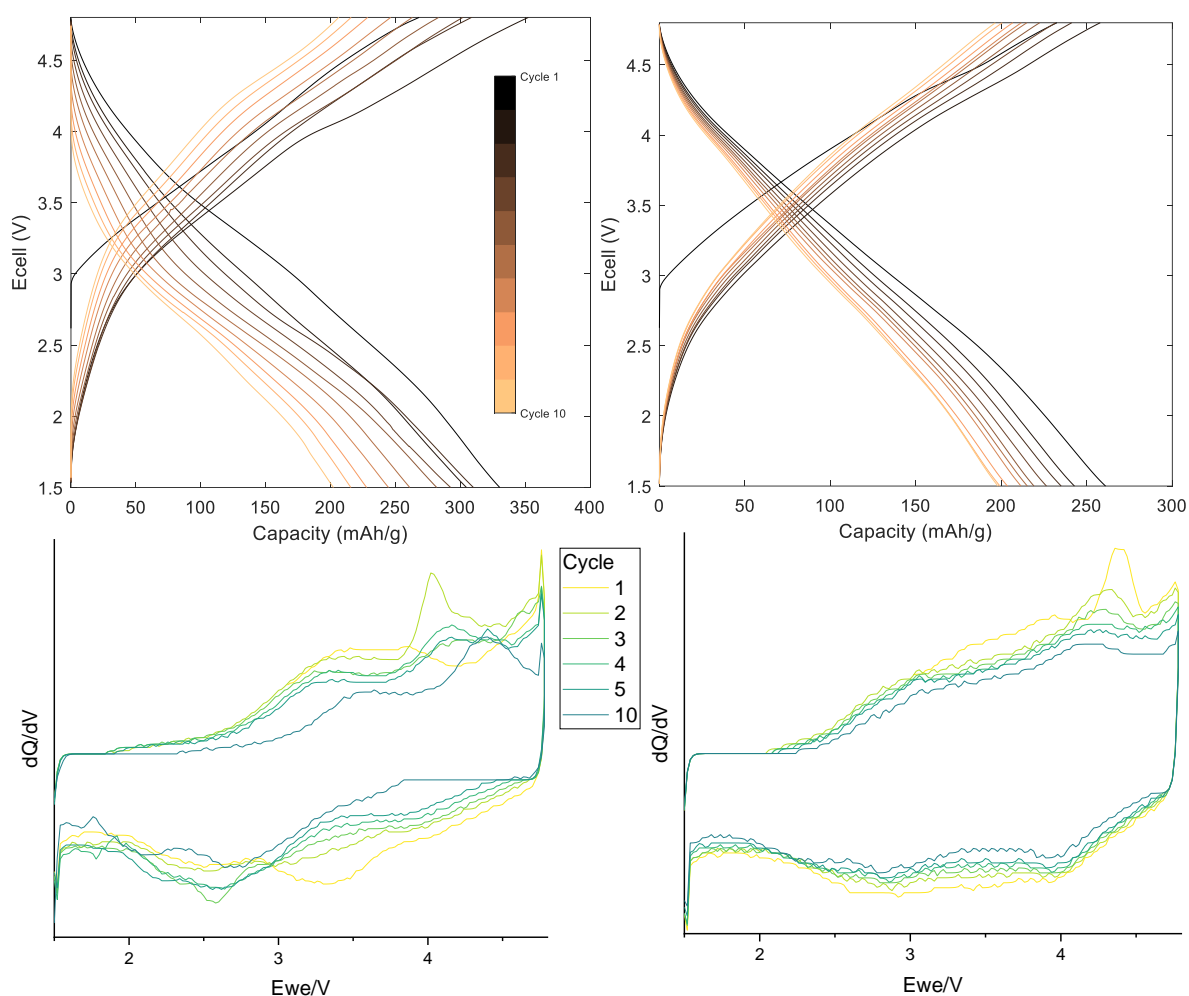
Figure 5-31: Galvanostatic charge-discharge profiles (above) and dQ/dV plots (below) of Li$_2$MnO$_2$F (left) and Li$_2$MnO$_{1.625}$F$_{1.5}$ (right) powder cells cycled at 10 mAg^{-1} between 1.5-4.8 V

Figure 5-32 shows the average discharge capacities for Li$_2$MnO$_2$F and Li$_2$MnO$_{1.625}$F$_{1.5}$. Li$_2$MnO$_2$F has an initial specific discharge capacity of 320.7 mAhg^{-1} which decreases to 192.9 mAhg^{-1} after 10 cycles. Li$_2$MnO$_{1.625}$F$_{1.5}$ has an initial specific discharge capacity of 253.0 mAhg^{-1} which decreases to 193.4 mAhg^{-1} after 10 cycles. Li$_2$MnO$_2$F gives a very high initial discharge capacity however the capacity retention is poor and falls to 60.2% after 10 cycles. This is similar to the capacity retention of Li$_2$MnO$_{2.25}$F (60.4%), whereas Li$_2$MnO$_{1.625}$F$_{1.5}$ has a lower initial discharge capacity however an improved capacity retention of 76.4%. The improved capacity retention of

$Li_2MnO_{1.625}F_{1.5}$ could be due to the delithiation having a different mechanism to the other F containing compositions or alternatively it could be due to $Li_2MnO_{1.625}F_{1.5}$ containing a higher proportion of F, which acts to stabilise the structure at higher voltages.
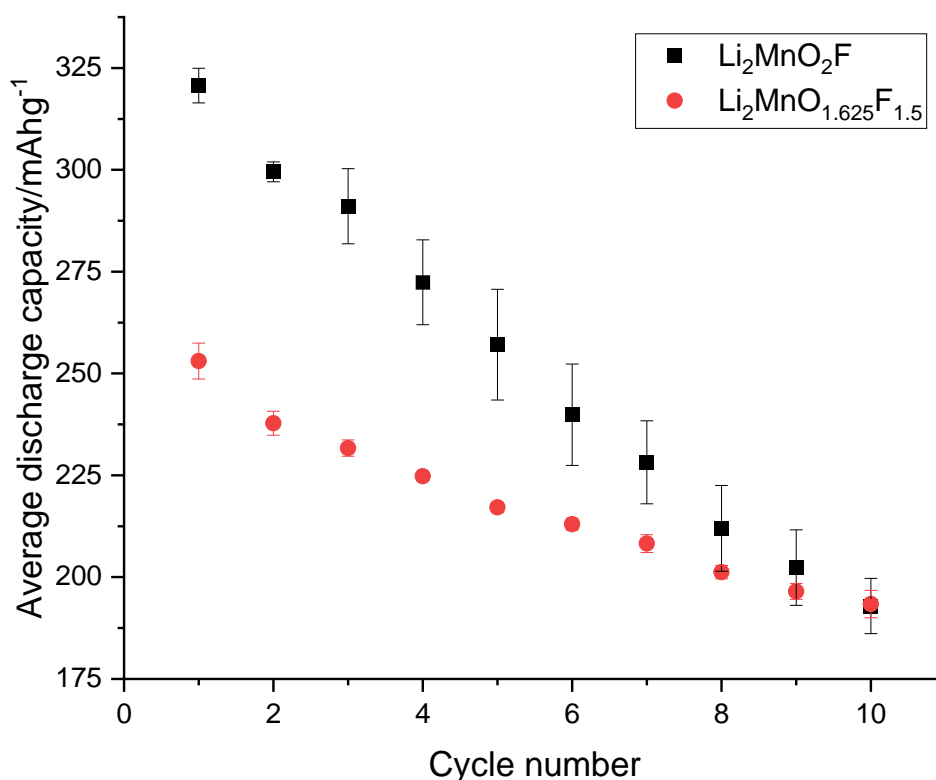
Figure 5-32: Average discharge capacity of Li_2MnO_2F (black) and $Li_2MnO_{1.625}F_{1.5}$ (red) powder cells. Error bars show relative standard deviation across 3 cells.

This section shows that a range of rocksalt compositions can be made with varying amounts of F and differing Mn oxidation states. The different compositions have differing electrochemical performances. The F-doping did not appear to cause an improvement to the capacity retention compared to $Li_4Mn_2O_5$ although this is likely to be due to O redox still being active.

5.4.2. Ni/Zn doping

In this section, Ni and Zn were doped into the rocksalt structure to investigate the impact upon the structure and the electrochemical properties. $Li_4Mn_{1.67}Ni_{0.33}O_5$ and $Li_4Mn_{1.67}Zn_{0.33}O_5$ were synthesised as they have a similar composition to $Li_4Mn_2O_5$ but with substitution of a third of the Mn for Ni/Zn. Assuming that the Ni and Zn in the structures is 2+, they both contain $Mn^{3.2+}$.

Figure 5-33 shows the XRD patterns of $Li_4Mn_{1.67}Ni_{0.33}O_5$ and $Li_4Mn_{1.67}Zn_{0.33}O_5$. Both samples form the rocksalt structure without the presence of any impurity phases. Pawley refinements gave a lattice parameter of 4.147(2) and 4.155(2) Å for $Li_4Mn_{1.67}Ni_{0.33}O_5$ and $Li_4Mn_{1.67}Zn_{0.33}O_5$ respectively. $Li_4Mn_{1.67}Zn_{0.33}O_5$ has a larger lattice parameter than $Li_4Mn_{1.67}Ni_{0.33}O_5$ which is likely to be due to Zn^{2+} having a larger ionic radius than Ni^{2+}. However, the lattice parameters are smaller than $Li_4Mn_2O_5$ (4.17 Å). Ni^{2+} and Zn^{2+} have larger ionic radii than Mn^{3+} therefore you would expect the lattice parameter to increase upon Ni/Zn-doping. The lattice parameter however decreases which could either suggest that doping is unsuccessful or that the decrease is due to the presence of a small amount of Mn^{4+}.
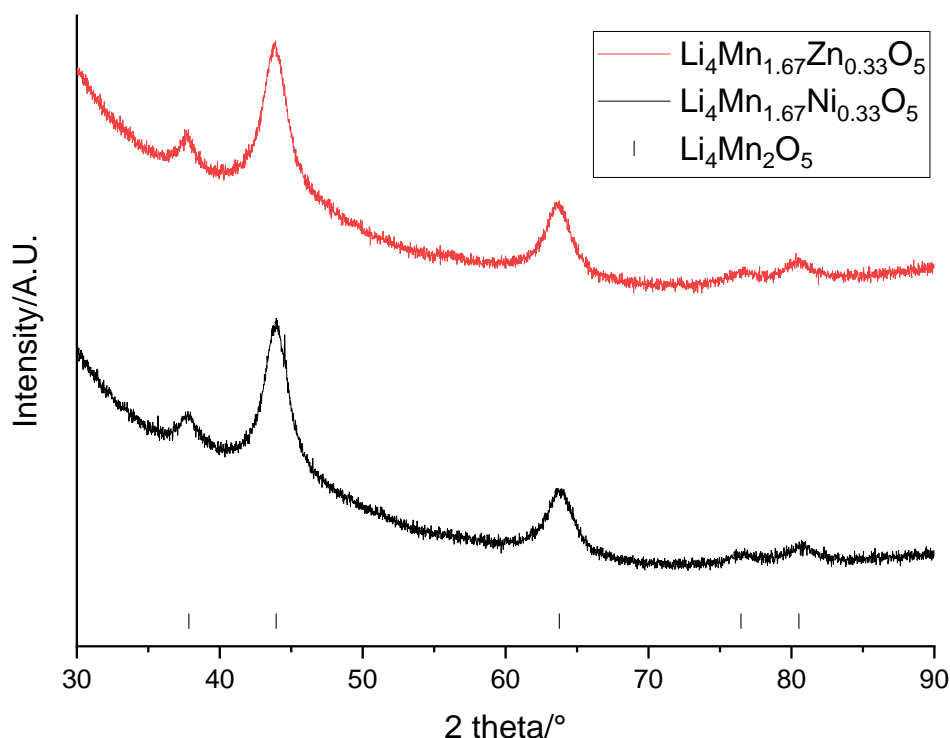
Figure 5-33: XRD patterns of $Li_4Mn_{1.67}Ni_{0.33}O_5$ (black) and $Li_4Mn_{1.67}Zn_{0.33}O_5$ (red) (λ = 1.54 Å). Tick marks correspond to $Li_4Mn_2O_5$ (black).

Figure 5-34 shows the electrochemical performance of $Li_4Mn_{1.67}Ni_{0.33}O_5$ and $Li_4Mn_{1.67}Zn_{0.33}O_5$. The voltage profiles of both samples have a similar appearance which shares some features with the voltage profile of $Li_4Mn_2O_5$ (Figure 5-10). They have a voltage plateau at 2.8 V on discharging but do not show the other voltage plateaus that are present for $Li_4Mn_2O_5$. This suggests that doping the structure with Ni and Zn has resulted in changes to the redox activity. The dQ/dV plots are similar and both show a peak at 3.2 V on charging and 2.6 V on discharge which can be attributed to Mn redox. On the initial cycles there are peaks at ~ 4.1 V on charging which can be attributed to O redox occurring. However, there is no O redox occurring on discharge showing that the process is irreversible. There are no significant differences in the

voltage profile of the Ni and Zn doped samples which suggests that Ni redox is not being activated.
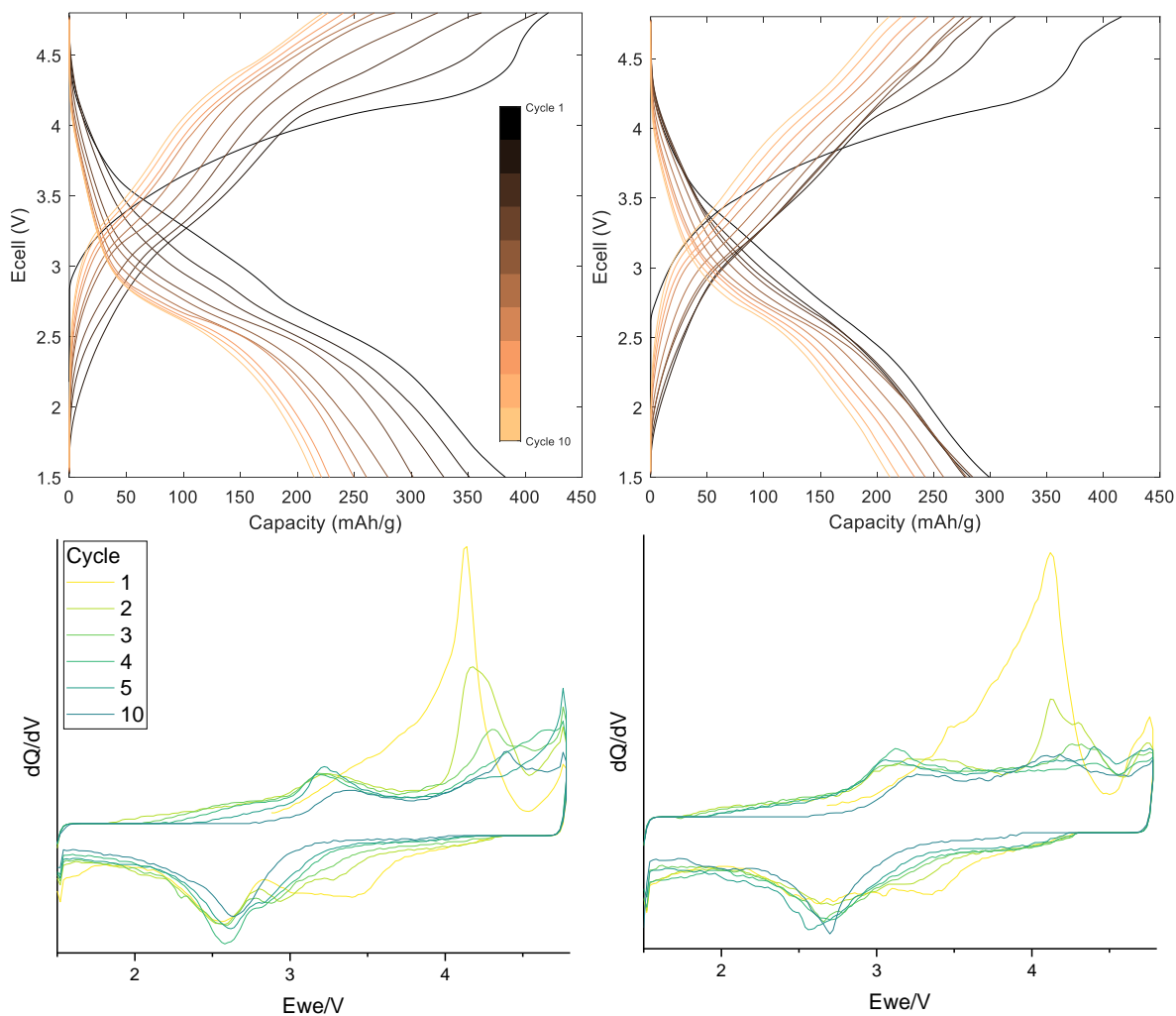
Figure 5-34: Galvanostatic charge-discharge profiles (above) and dQ/dV plots (below) of Li$_4$Mn$_{1.67}$Ni$_{0.33}$O$_5$ (left) and Li$_4$Mn$_{1.67}$Zn$_{0.33}$O$_5$ (right) powder cells cycled at 10 mAg^{-1} between 1.5-4.8 V

Figure 5-35 shows the average discharge capacities for Li$_4$Mn$_2$O$_5$, Li$_4$Mn$_{1.67}$Ni$_{0.33}$O$_5$ and Li$_4$Mn$_{1.67}$Zn$_{0.33}$O$_5$. Li$_4$Mn$_{1.67}$Ni$_{0.33}$O$_5$ gives a very high initial specific discharge capacity of 382.8 mAhg^{-1} which decreases to 214.9 mAhg^{-1} after 10 cycles. Li$_4$Mn$_{1.67}$Zn$_{0.33}$O$_5$ gives a lower initial specific discharge capacity of 299.1 mAhg^{-1} which decreases to 211.4 mAhg^{-1} after 10 cycles. Li$_4$Mn$_{1.67}$Zn$_{0.33}$O$_5$ has a similar initial

discharge capacity to $Li_4Mn_2O_5$ whereas $Li_4Mn_{1.67}Ni_{0.33}O_5$ has a significantly higher capacity. However, the capacity retention of $Li_4Mn_{1.67}Ni_{0.33}O_5$ is extremely poor and the capacity falls to 56.1% after 10 cycles. This suggests that although Ni-doping allows a higher discharge capacity to be accessed, it does not help to improve the capacity retention. $Li_4Mn_{1.67}Zn_{0.33}O_5$ has a lower initial capacity with an improved capacity retention of 70.7% after 10 cycles. However, this is still not as good as the capacity retention of the undoped $Li_4Mn_2O_5$ (79.8%).
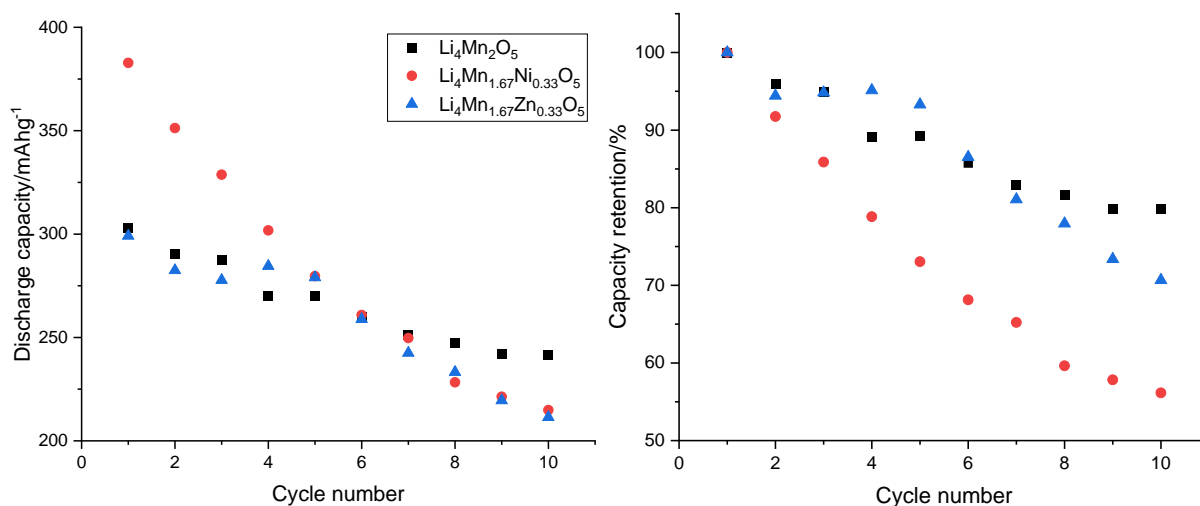
Figure 5-35: Discharge capacity (left) and capacity retention (right) of $Li_4Mn_2O_5$ (black), $Li_4Mn_{1.67}Ni_{0.33}O_5$ (red) and $Li_4Mn_{1.67}Zn_{0.33}O_5$ (blue) powder cells

The work in this section has therefore shown that both Ni and Zn can be doped into the $Li_4Mn_2O_5$ structure. Ni-doping of $Li_4Mn_2O_5$ increases the initial discharge capacity however it results in a significantly poorer capacity retention. In contrast, Zn-doping results in a similar capacity however a slightly poorer capacity retention than $Li_4Mn_2O_5$.

5.4.3. Na doping

In this section, Na was doped into the rocksalt structure, although, in this case Na was substituted for Li as opposed to Mn. Different levels of Na-doping were investigated. Note that LMO was not used as a starting material in the synthesis of these materials (starting materials are detailed in Table 5-1) and that all the samples contain Mn^{3+}.

Figure 5-36 shows the XRD patterns of $Li_{1.8}Na_{0.2}MnO_2F$ after milling for 8 and 12 hrs using the small milling balls. After 8 hrs of milling there are peaks corresponding to the rocksalt phase but there are also peaks corresponding to unreacted Mn_2O_3. After milling for 12 hrs, the peaks due to Mn_2O_3 are no longer present and a pure rocksalt phase is formed. This shows that when Na is doped into the rocksalt structure, a longer synthesis time is required than for the other dopants.
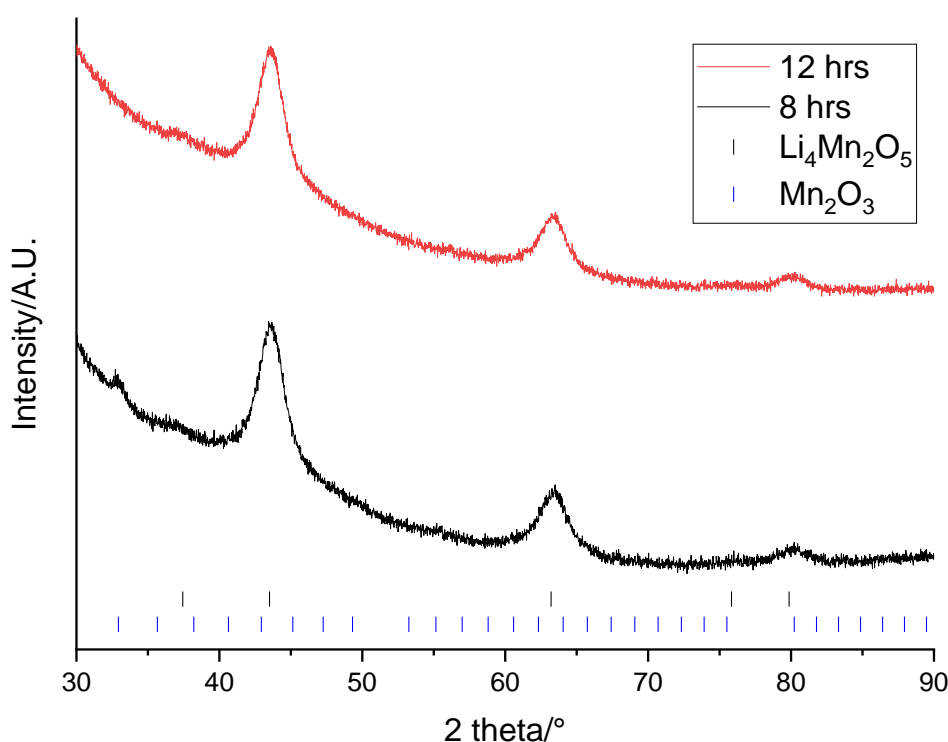
Figure 5-36: XRD patterns of $Li_{1.8}Na_{0.2}MnO_2F$ after 8 (black) and 12 (red) hrs milling using small milling balls ($\lambda = 1.54$ Å). Tick marks correspond to $Li_4Mn_2O_5$ (black) and Mn_2O_3 (blue).

Table 5-3 shows the range of Na-doped samples that were synthesised. Figure 5-37 shows that the samples have all formed the desired rocksalt structure. The $Li_{1.7}Na_{0.3}MnO_2F$ and $Li_{1.6}Na_{0.4}MnO_2F$ samples both contain additional small peaks at 38.7 and 56.0°. These peaks are due to NaF and this is probably due to some unreacted reagent remaining. Milling for longer times may help to incorporate the remaining NaF into the structure or alternatively, a limit may have been reached for the level of Na that can be doped into the structure. Further testing would be needed to investigate this. As the amount of Na present in the samples increases, the diffraction peaks shift to lower 2 theta values. This is reflected by the lattice parameter increasing with increased Na content. Na^+ has a larger ionic radius than Li^+ therefore this fits the expected trend.

Table 5-3: Na-doped rocksalt samples with lattice parameter

Sample	a/Å
$Li_{1.9}Na_{0.1}MnO_2F$	4.150(1)
$Li_{1.8}Na_{0.2}MnO_2F$	4.157(9)
$Li_{1.7}Na_{0.3}MnO_2F$	4.159(2)
$Li_{1.6}Na_{0.4}MnO_2F$	4.178(2)
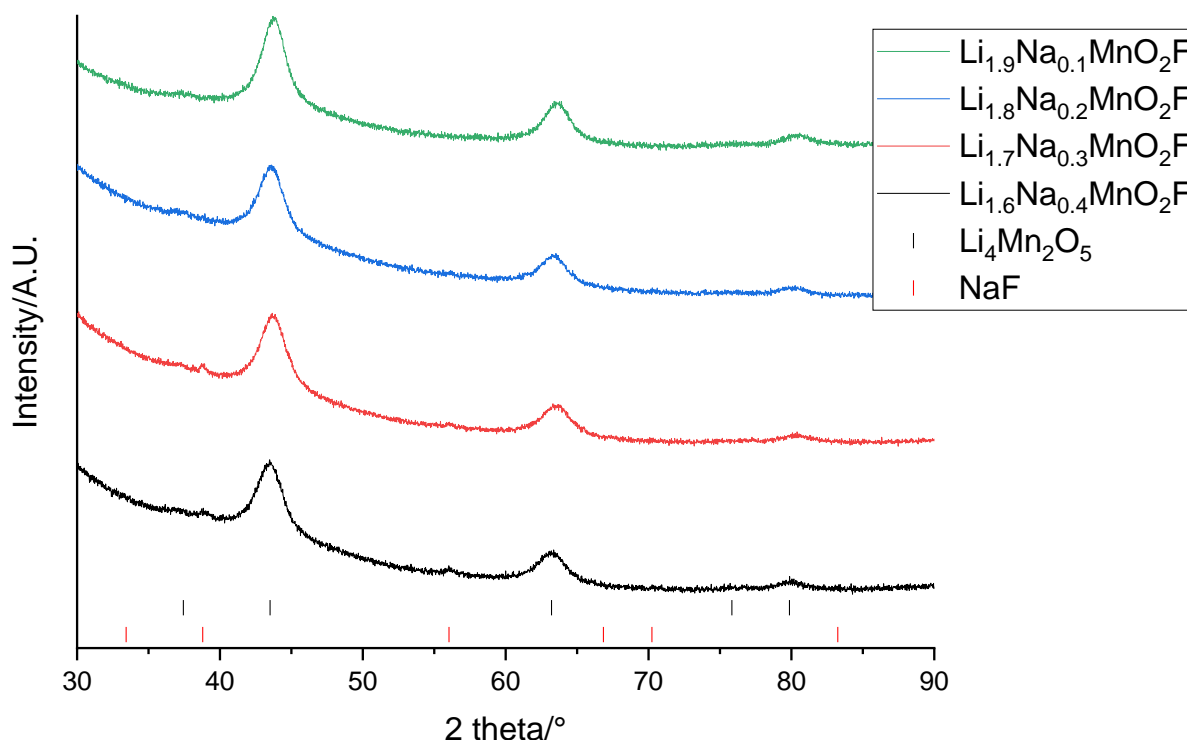
Figure 5-37: XRD patterns of Li$_{1.9}$Na$_{0.1}$MnO$_2$F (black), Li$_{1.8}$Na$_{0.2}$MnO$_2$F (red), Li$_{1.7}$Na$_{0.3}$MnO$_2$F (blue) and Li$_{1.6}$Na$_{0.4}$MnO$_2$F (green) (λ = 1.54 Å). Tick marks correspond to Li$_4$Mn$_2$O$_5$ (black) and NaF (red).

Li$_{1.8}$Na$_{0.2}$MnO$_2$F was selected as the sample to perform further electrochemical studies. Figure 5-38 shows the electrochemical performance of a Li$_{1.8}$Na$_{0.2}$MnO$_2$F powder cell. The charging profile consists of two regions with different gradients; the profile is steeper from 1.5 to 3 V and then has a shallower gradient from 3 to 4.8 V. The same pattern is reflected in the discharge profile. Figure 5-38 shows the corresponding dQ/dV plot. On the first cycle there are peaks at ~ 3.5 V on charge and discharge which are likely to be due to Mn redox. There is a relatively small voltage difference between the position of this peak on charge and discharge which may suggest that less anionic redox is occurring for this material compared to those previously tested in this chapter.[29] There is also a peak at 4.7 V on charging which is

likely to be due to O redox. On further cycling the peak at 4.7 V decreases in intensity, indicating that less O redox is being activated. After 5 cycles a peak at 4.1 V appears on charging and after 10 cycles peaks at 2.3 and 3.8 V appear on discharging. This suggests that the structure is changing during cycling and therefore redox activity is occurring at different voltages. Further work is needed to examine this in more detail. For example, the cathodes would have to be analysed after cycling to investigate changes to the structure.
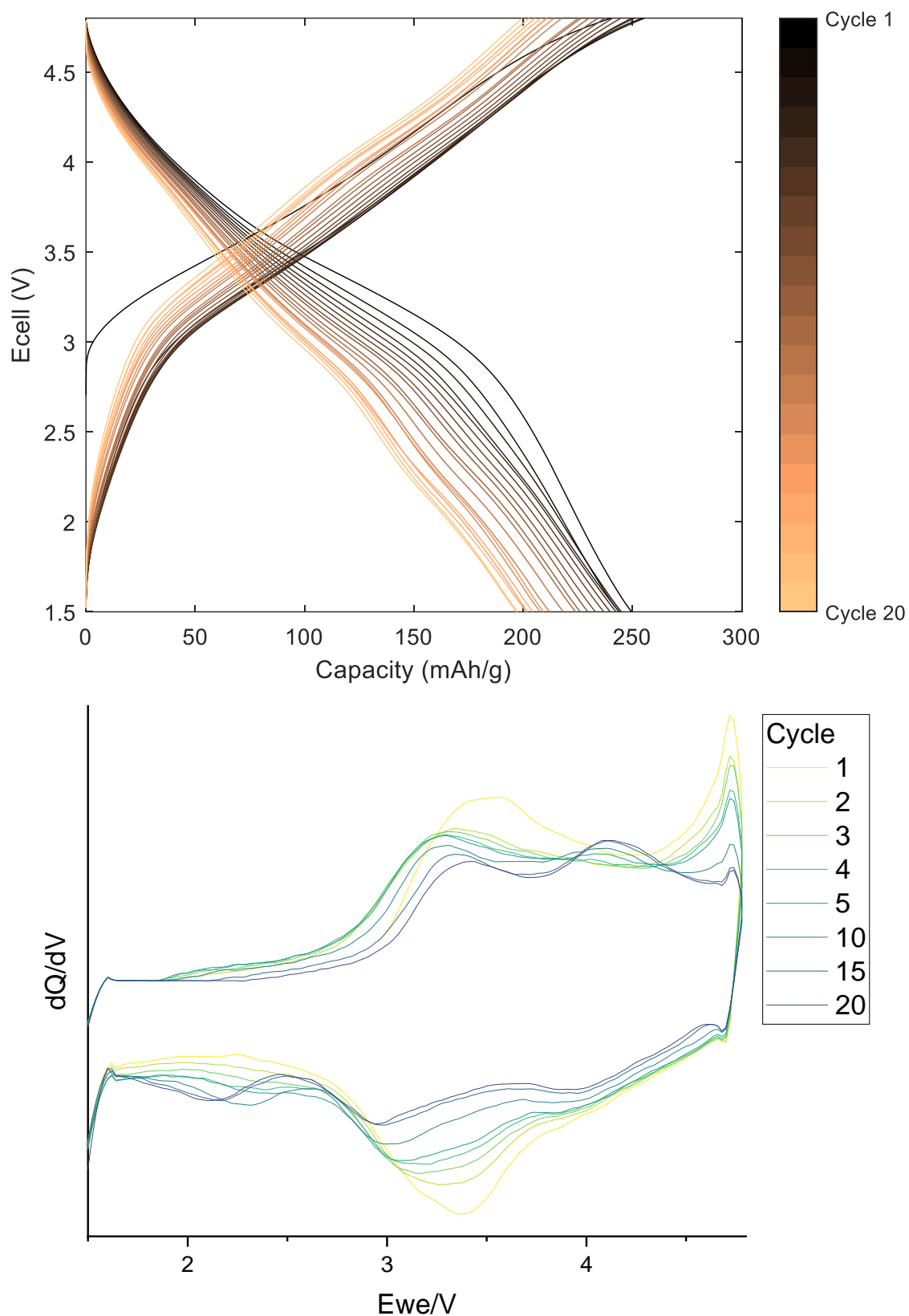
Figure 5-38: Galvanostatic charge-discharge profile (above) and dQ/dV plot (below) of a pristine $Li_{1.8}Na_{0.2}MnO_2F$ powder cell cycled at 10 mAg^{-1} between 1.5-4.8 V

Figure 5-39 shows the charge and discharge capacities for $Li_{1.8}Na_{0.2}MnO_2F$. $Li_{1.8}Na_{0.2}MnO_2F$ gives an initial specific charge capacity of 240.1 mAhg^{-1} and an initial specific discharge capacity of 249.5 mAhg^{-1}. Initially there is a 9 mAhg^{-1} difference between the charge and discharge capacities and by 20 cycles the difference is only 3 mAhg^{-1}. The initial difference is considerably smaller than seen for other cathodes tested in this chapter suggesting that lithiation/delithiation of $Li_{1.8}Na_{0.2}MnO_2F$ is occurring reversibly throughout the cycling life. While the capacities are lower than other materials tested in this chapter, the capacity retention is significantly better. $Li_{1.8}Na_{0.2}MnO_2F$ has a capacity retention of 90.5% after 10 cycles and 78.9% after 20 cycles. This is considerable improvement, especially the short-term retention after 10 cycles. This suggests that Na may be stabilising the structure and allowing Li to be removed/inserted in a more reversible manner. This could be due to the larger size of Na allowing for improved Li pathways through the structure. Pellet cells were also made check the repeatability. Appendix J (Figure J3) shows that similar discharge capacities were obtained for $Li_{1.8}Na_{0.2}MnO_2F$ pellet cells with limited error.
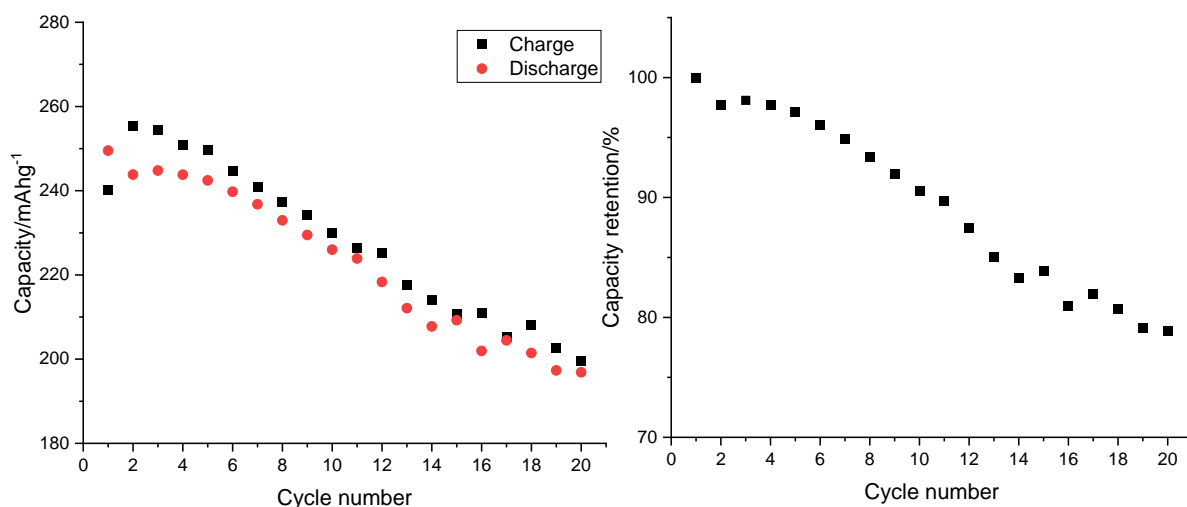
Figure 5-39: Charge/discharge capacity (left) and capacity retention (right) of a $Li_{1.8}Na_{0.2}MnO_2F$ powder cell

Figure 5-40 shows the electrochemical performance of $Li_{1.8}Na_{0.2}MnO_2F$ when it is cycled between smaller voltage limits 2-4.3 V and at a faster cycling rate of 100 mAhg⁻¹. The voltage profile remains the same even when the cycling conditions are changed, this contrasts with some of the materials tested previously in this chapter which experienced changes to the voltage profile upon changing the cycling conditions. This could be due to the bulk of the redox activity occurring between 3-4.3 V (see Figure 5-38 below) and therefore this is uninterrupted when a voltage range of 2-4.3 V is used instead. There is a dip in the voltage between ~ 150 and 200 mAhg⁻¹, the cause of this dip could be related to the Swagelok testing set up used however, the definitive cause is unknown.
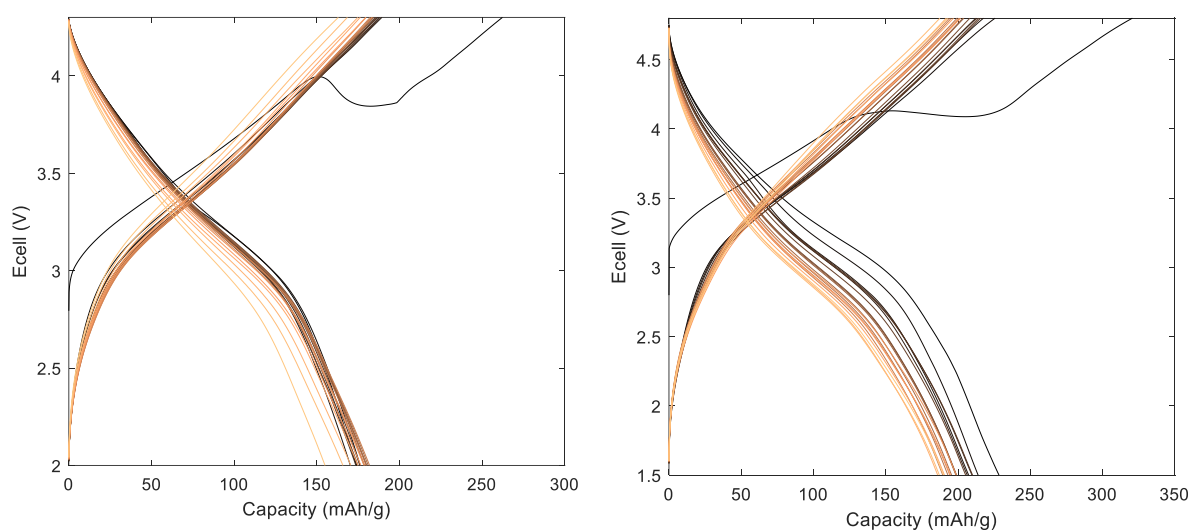
Figure 5-40: Galvanostatic charge-discharge profile of a $Li_{1.8}Na_{0.2}MnO_2F$ powder cell cycled at 10 mAg^{-1} between 2-4.3 V (left) and at 100 mAg^{-1} between 1.5-4.8 V (right)

Figure 5-41 shows the specific discharge capacities of $Li_{1.8}Na_{0.2}MnO_2F$ under the different cycling conditions. As expected, a move to faster cycling rates or to smaller voltage ranges results in a decrease in the discharge capacity (228.4 and 174.0 mAhg^{-1} respectively). Cycling at 100 mAg^{-1} has a more significant capacity fade in the first 3 cycles than cycling at 10 mAg^{-1}. However, after 20 cycles, the 100 mAg^{-1} sample gives a capacity retention of 83.2% which is marginally higher than cycling at a slower rate (78.9% for 10 mAg^{-1}). This may be due to the larger Na encouraging fast Li transfer through the material. In contrast, the smaller voltage range of 2-4.3 V shows an initial increase in the discharge capacity with a significant capacity decrease only occurring after 18 cycles. The capacity retention after 20 cycles is 89.0% which is significant improvement. This improvement could be linked to O redox no longer being activated at 4.7 V.
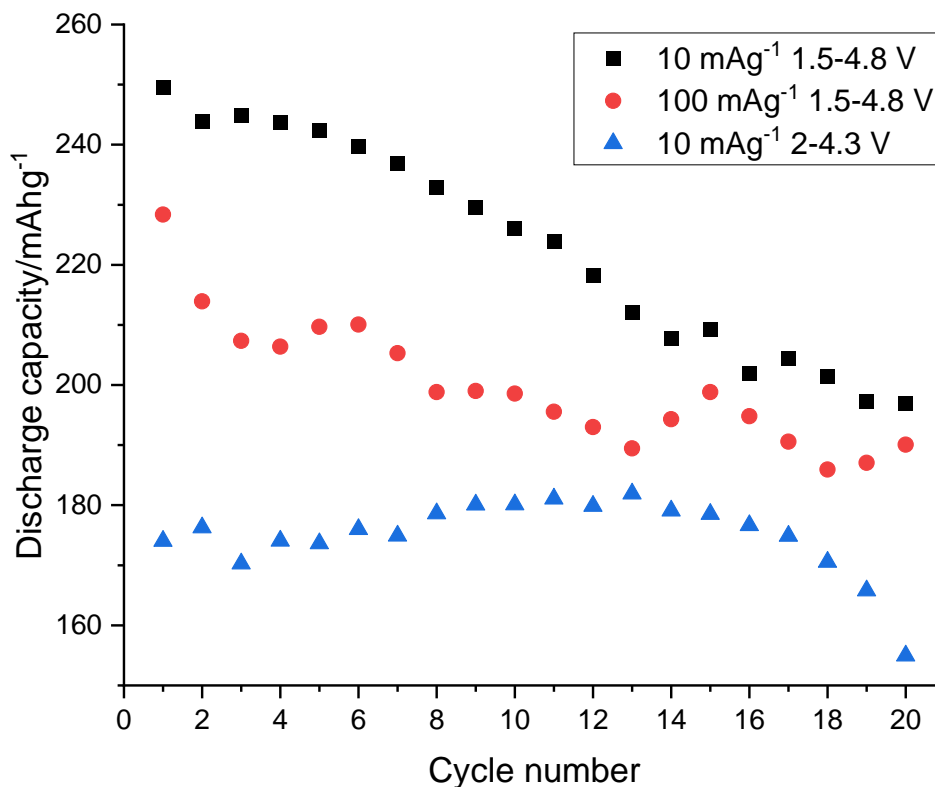
Figure 5-41: Discharge capacity of $Li_{1.8}Na_{0.2}MnO_2F$ when cycled at 10 mAg^{-1} between 1.5-4.8 V (black), 100 mAg^{-1} between 1.5-4.8 V (red) and 10 mAg^{-1} between 2-4.3 V (blue)

This section shows that Na can be doped into the rocksalt structure, although higher levels of doping (>0.3 Na) have NaF remaining which could suggest that there is a limit on the amount of Na that can be doped into the structure. Electrochemical testing of $Li_{1.8}Na_{0.2}MnO_2F$ shows that it performs with a good capacity retention albeit with a lower discharge capacity than other DRS materials tested. Significant improvements to the capacity retention have been achieved by reducing the voltage range that is used. Further work is needed to investigate the electrochemical properties of these materials in more detail.

5.5. Synthesis of upcycled DRS from EOL material

In this section, DRS were synthesised using LMO recovered from the EOL cathode. The LMO was recovered using the process outlined in Chapter 3 and then used as a reagent in the synthesis. $Li_4Mn_2O_5$ and $Li_2MnO_{2.25}F$ were selected as the target compounds. The upcycled DRS were then compared to the pristine rocksalts discussed previously in the chapter.

Figure 5-42 shows the XRD patterns of the upcycled $Li_4Mn_2O_5$ and $Li_2MnO_{2.25}F$. The samples form the desired rocksalt structure without the presence of impurity phases. Pawley refinements gave lattice parameters of 4.16(1) and 4.108(1), respectively. These are comparable to the pristine materials discussed previously (Section 5.3.1. and 5.4.1.1.). These results show that recovered LMO can be used as a reagent with negligible changes to the resulting rocksalt structure. $Li_4Mn_2O_5$ and $Li_2MnO_{2.25}F$ were also synthesised using LMO recovered from the QC cathode. The XRD patterns and corresponding lattice parameters are in Appendix K. They show that the QC cathode also works in this process and DRS phases with similar lattice parameters were produced.
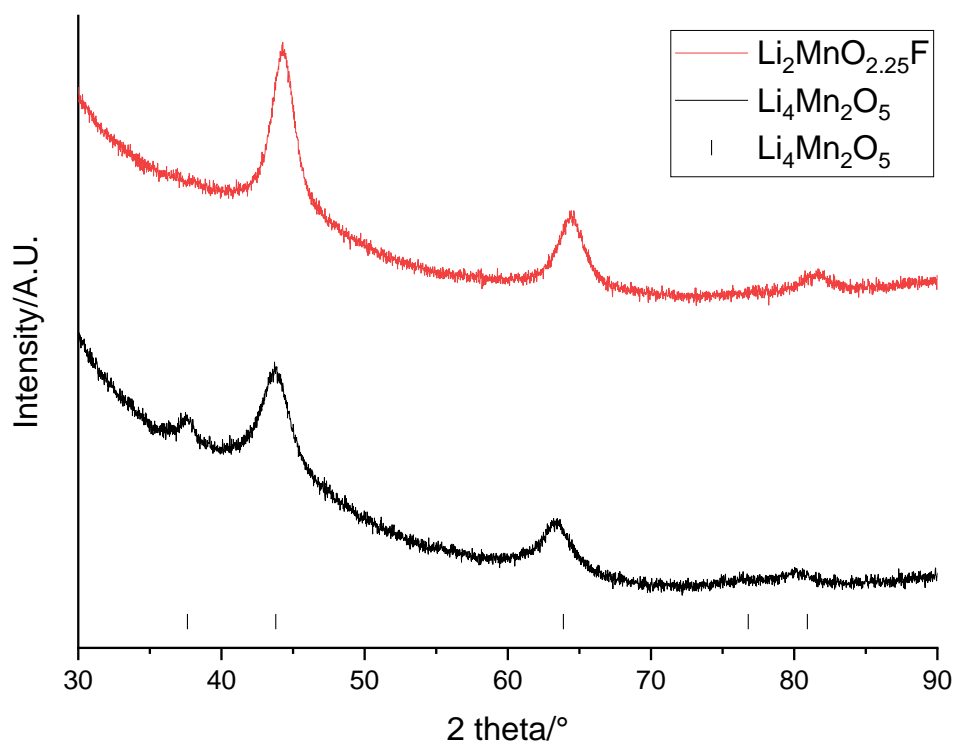
Figure 5-42: XRD patterns of Li₄Mn₂O₅ (black) and Li₂MnO₂.₂₅F (red) made from recovered LMO from the EOL cathode (λ = 1.54 Å). Tick marks correspond to Li₄Mn₂O₅.

Figure 5-43 shows the Raman spectra of the upcycled $Li_4Mn_2O_5$ and $Li_2MnO_{2.25}F$. There are peaks at 485, 603 and 1219 cm^{-1}. The Raman specta are similar to the spectra obtained for the pristine materials (Figures 5-4 and 5-20).
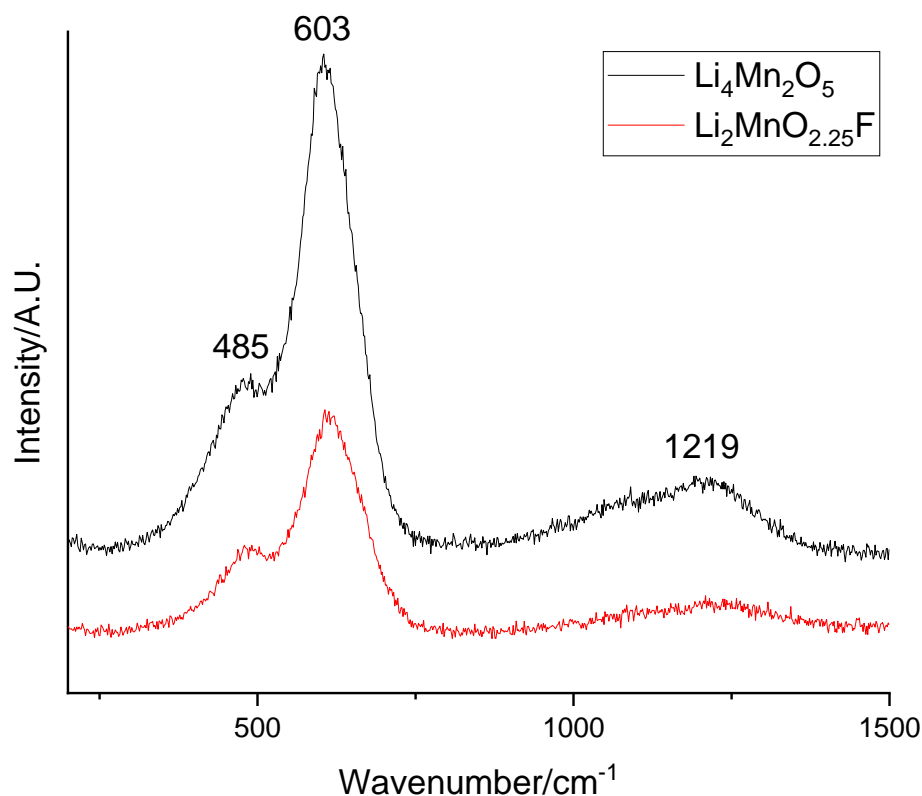
Figure 5-43: Raman spectrum of Li$_4$Mn$_2$O$_5$ (black) and Li$_2$MnO$_{2.25}$F (red) made from recovered LMO from the EOL cathode

Figure 5-44 shows the electrochemical performance of upcycled Li$_4$Mn$_2$O$_5$ and Li$_2$MnO$_{2.25}$F. The voltage profiles look the same as the pristine materials (Figures 5-10 and 5-24). They contain the same sloping profile alongside voltage plateaus at the same points. Upcycled Li$_4$Mn$_2$O$_5$ gives an initial specific discharge capacity of 292.6 mAhg^{-1} which falls to 214.8 mAhg^{-1} after 10 cycles. This corresponds to a capacity retention of 73.4%. Upcycled Li$_2$MnO$_{2.25}$F gives an initial specific discharge capacity of 279.1 mAhg^{-1} which falls to 168.0 mAhg^{-1} after 10 cycles. This corresponds to a capacity retention of 60.2%. The capacity retention of upcycled Li$_2$MnO$_{2.25}$F is comparable with pristine Li$_2$MnO$_{2.25}$F (60.4% after 10 cycles) whereas the capacity retention of upcycled Li$_4$Mn$_2$O$_5$ is lower than pristine Li$_4$Mn$_2$O$_5$ (79.8% after 10 cycles).

Further work is required to investigate the cause of the lower capacity retention in more detail. Overall, the electrochemistry of the upcycled materials is similar to that of the pristine materials which shows that EOL material can be used as a reagent without a significant detrimental impact to the electrochemical performance.
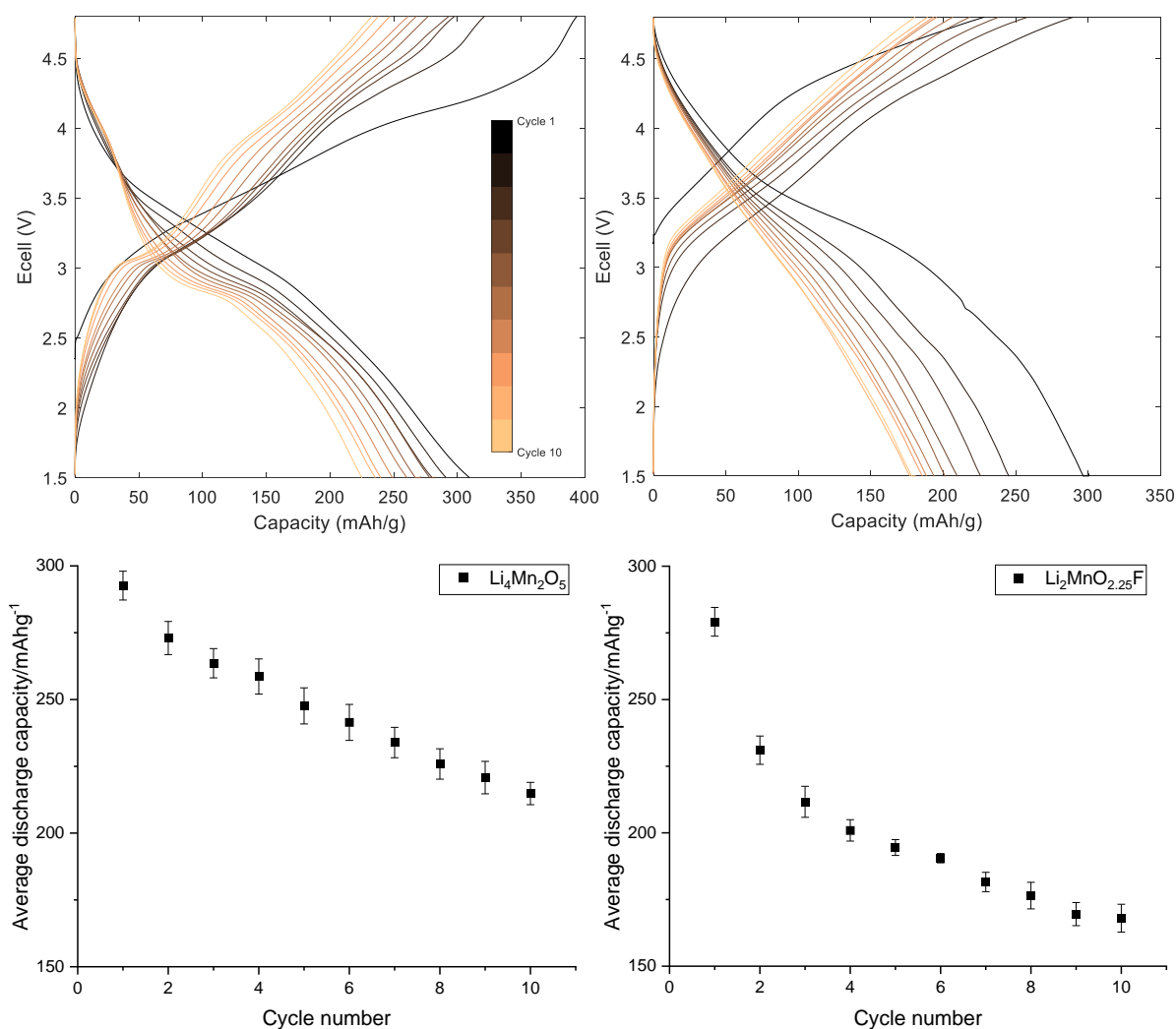
Figure 5-44: Galvanostatic charge-discharge profile (above) and average discharge capacity (below) of upcycled Li$_4$Mn$_2$O$_5$ (left) and Li$_2$MnO$_{2.25}$F (right) powder cells cycled at 10 mAg^{-1} between 1.5-4.8 V. Error bars show relative standard deviation across 3 cells.

This section shows that recovered LMO can be used as a reagent to synthesise rocksalts. These upcycled rocksalts form the desired phase without the presence of any impurities. The upcycled rocksalts also have comparable electrochemical

performance to pristine rocksalts showing that this is a viable method to produce cathode materials using recycled material.

5.6. Conclusions

Pristine $Li_4Mn_2O_5$ has been synthesised using two different milling speeds and times. The use of small milling balls and synthesis at high speeds of 900 rpm formed the desired rocksalt structure after 8 hrs. XRD patterns showed that $Li_4Mn_2O_5$ degrades upon exposure to air to form Li_2CO_3, which can have a detrimental impact upon the electrochemical performance. Different methods were then investigated to try to prevent degradation and improve the electrochemical performance of $Li_4Mn_2O_5$. A coating of 10 wt% PVDF was found to prevent formation of Li_2CO_3 even after 48 hrs of air exposure. The electrochemical performance was improved using Swagelok cells with powder and pellet cathodes. Future work would be to make coatings in a glovebox as these would be likely to give more accurate and repeatable results. $Li_4Mn_2O_5$ gives an excellent initial specific discharge capacity of 302.9 $mAhg^{-1}$ with a 68.3% capacity retention after 20 cycles. Electrochemical testing of $Li_4Mn_2O_5$ showed that smaller voltage ranges can be used to improve the capacity retention (2.5-4.3 V gives 81.8% capacity retention after 20 cycles) and that faster cycling rates (100 mAg^{-1}) can be employed without a detrimental impact upon the performance.

F, Ni and Zn doped rocksalt structures were also successfully synthesised and their electrochemical properties were tested (Table 5-5). $Li_2MnO_{2.25}F$ was shown to have a capacity retention of 42.1% after 20 cycles, which is poorer than $Li_4Mn_2O_5$ and is attributed to O redox being active. Again, improvements to the capacity retention were achieved by cycling using smaller voltage ranges. A range of F-doped DRS were synthesised and shown to have varying electrochemical performances. $Li_4Mn_{1.67}Ni_{0.33}O_5$ and $Li_4Mn_{1.67}Zn_{0.33}O_5$ were synthesised and gave initial specific

discharge capacities of 382.8 and 299.1 mAhg^{-1}, respectively. However, they gave a poorer capacity retention than $Li_4Mn_2O_5$ suggesting that they are not ideal candidates for further doping strategies.

A range of Na containing DRS were also synthesised. Unlike the other dopants, they required an additional 4 hrs of milling to form the desired rocksalt phase. $Li_{1.8}Na_{0.2}MnO_2F$ gave an initial specific discharge capacity of 249.5 mAhg^{-1} and a capacity retention of 78.9% after 20 cycles. This is significantly improved capacity retention compared to $Li_4Mn_2O_5$ and suggests that further work should investigate Na doping in the future. The improved capacity retention is attributed to Na stabilising the structure and allowing for easy Li diffusion through the material.

DRS materials, $Li_4Mn_2O_5$ and $Li_2MnO_{2.25}F$, were also synthesised using material recovered from the EOL and QC cathodes. These upcycled rocksalts formed the desired structure with comparable lattice parameters to the pristine samples. They also had a comparable electrochemical performance. This shows that recovered reagents can be used in the synthesis of DRS and that this is a viable method for using recycled materials in the future. Further work could investigate the use of other recovered materials as reagents.

Table 5-5: Summary of electrochemical results for Chapter 5. Unless stated otherwise electrochemical data for powder cells cycled at 10 mAhg^{-1} between 1.5-4.8V

Precursor	Stoichiometry	Lattice parameter/Å	Initial charge capacity/mAhg^{-1}	Initial discharge capacity/mAhg^{-1}	Capacity retention after 10 cycles/%
	$Li_4Mn_2O_5$	4.17(1)	364.3	302.9	79.8
	$Li_2MnO_{2.25}F$	4.112(2)	233.5	305.0	60.4
	Li_2MnO_2F	4.154(1)	268.1	320.7	60.2
Pristine	$Li_2MnO_{1.625}F_{1.5}$	4.180(2)	232.5	253.0	76.4
	$Li_2MnO_{2.5}F_{0.5}$	4.113(1)	308.3	384.4	29.5
	$Li_2MnO_{1.75}F_{1.25}$	4.173(1)	263.3	364.4	27.0
	$Li_4Mn_{1.67}Ni_{0.33}O_5$	4.147(2)	420.3	382.8	56.1

Precursor	Stoichiometry	Lattice parameter/Å	Initial charge capacity/mAhg^{-1}	Initial discharge capacity/mAhg^{-1}	Capacity retention after 10 cycles/%
Pristine	$Li_4Mn_{1.67}Zn_{0.33}O_5$	4.155(2)	415.8	299.1	70.7
	$Li_{1.8}Na_{0.2}MnO_2F$	4.157(9)	240.1	249.5	90.5
EOL cathode	$Li_4Mn_2O_5$	4.16(1)	393.6	292.6	73.4
	$Li_2MnO_{2.25}F$	4.108(1)	228.3	279.1	60.2

5.7. References

1   H. Li, R. Fong, M. Woo, H. Ahmed, D. H. Seo, R. Malik and J. Lee, *Joule*, 2022, **6**, 53–91.

2   J. Lee, A. Urban, X. Li, D. Su, G. Hautier and G. Ceder, *Science (80-.).*, 2014, **343**, 519–522.

3   E. Zhao, L. He, B. Wang, X. Li, J. Zhang, Y. Wu, J. Chen, S. Zhang, T. Liang, Y. Chen, X. Yu, H. Li, L. Chen, X. Huang, H. Chen and F. Wang, *Energy Storage Mater.*, 2019, **16**, 354–363.

4   D. Chen, W. H. Kan and G. Chen, *Adv. Energy Mater.*, 2019, **9**, 1–15.

5   R. A. House, L. Jin, U. Maitra, K. Tsuruta, J. W. Somerville, D. P. Förstermann, F. Massel, L. Duda, M. R. Roberts and P. G. Bruce, *Energy Environ. Sci.*, 2018, **11**, 926–932.

6   J. Lee, D. A. Kitchaev, D. H. Kwon, C. W. Lee, J. K. Papp, Y. S. Liu, Z. Lun, R. J. Clément, T. Shi, B. D. McCloskey, J. Guo, M. Balasubramanian and G. Ceder, *Nature*, 2018, **556**, 185–190.

7   B. Huang, M. Wang, X. Yang, G. Xu and Y. Gu, *J. Alloys Compd.*, 2019, **808**, 151683.

8   K. Zhou, S. Zheng, H. Liu, C. Zhang, H. Gao, M. Luo, N. Xu, Y. Xiang, X. Liu, G. Zhong and Y. Yang, *ACS Appl. Mater. Interfaces*, 2019, **11**, 45674–45682.

9   H. Chung, Z. Lebens-Higgins, B. Sayahpour, C. Mejia, A. Grenier, G. E. Kamm,

Y. Li, R. Huang, L. F. J. Piper, K. W. Chapman, J. M. Doux and Y. S. Meng, *J. Mater. Chem. A*, 2021, **9**, 1720–1732.

10   M. Freire, N. V. Kosova, C. Jordy, D. Chateigner, O. I. Lebedev, A. Maignan and V. Pralong, *Nat. Mater.*, 2016, **15**, 173–177.

11   S. Tamilarasan, S. Laha, S. Natarajan and J. Gopalakrishnan, *J. Mater. Chem. C*, 2015, **3**, 4794–4800.

12   J. Ahn, Y. Ha, R. Satish, R. Giovine, L. Li, J. Liu, C. Wang, R. J. Clement, R. Kostecki, W. Yang and G. Chen, *Adv. Energy Mater.*, 2022, **12**, 1–12.

13   Y. Wang, S. Huang, B. Raji-Adefila, A. Outka, J. H. Wang and D. Chen, *J. Am. Chem. Soc.*, 2022, **144**, 19838–19848.

14   Y. Shirazi Moghadam, S. Dinda, A. El Kharbachi, G. Melinte, C. Kübel and M. Fichtner, *Chem. Mater.*, 2022, **34**, 2268–2281.

15   W. Tang, A. Li, G. Zhou, Z. Chen, Z. Yang, J. Su and W. Zhang, *ACS Appl. Mater. Interfaces*, 2022, **14**, 38865–38874.

16   S. Hy, F. Felix, J. Rick, W. N. Su and B. J. Hwang, *J. Am. Chem. Soc.*, 2014, **136**, 999–1007.

17   L. A. Kaufman and B. D. McCloskey, *Chem. Mater.*, 2021, **33**, 4170–4176.

18   O. Haik, N. Leifer, Z. Samuk-Fromovich, E. Zinigrad, B. Markovsky, L. Larush, Y. Goffer, G. Goobes and D. Aurbach, *J. Electrochem. Soc.*, 2010, **157**, A1099.

19   H. Liu, Y. Yang and J. Zhang, *J. Power Sources*, 2006, **162**, 644–650.

20   P. Pasierb, S. Komornicki, M. Rokita and M. Rękas, *J. Mol. Struct.*, 2001, **596**, 151–156.

21   F. S. Gittleson, K. P. C. Yao, D. G. Kwabi, S. Y. Sayed, W. H. Ryu, Y. Shao-Horn and A. D. Taylor, *ChemElectroChem*, 2015, **2**, 1446–1457.

22   S. Roberts, L. Chen, B. Kishore, C. E. J. Dancer, M. J. H. Simmons and E. Kendrick, *J. Colloid Interface Sci.*, 2022, **627**, 427–437.

23   Y. Su, L. Li, G. Chen, L. Chen, N. Li, Y. Lu, L. Bao, S. Chen and F. Wu, *Chinese J. Chem.*, 2021, **39**, 189–198.

24   M. Freire, M. Diaz-Lopez, P. Bordet, C. V. Colin, O. I. Lebedev, N. V. Kosova, C. Jordy, D. Chateigner, A. L. Chuvilin, A. Maignan and V. Pralong, *J. Mater. Chem. A*, 2018, **6**, 5156–5165.

25   J. Qian, Y. Ha, K. P. Koirala, D. Huang, Z. Huang, V. S. Battaglia, C. Wang, W. Yang and W. Tong, *Adv. Funct. Mater.*, 2023, **33**, 1–9.

26   B. Ouyang, N. Artrith, Z. Lun, Z. Jadidi, D. A. Kitchaev, H. Ji, A. Urban and G. Ceder, *Adv. Energy Mater.*, 2020, **1903240**, 1–11.

27   R. J. Clément, D. Kitchaev, J. Lee and Gerbrand Ceder, *Chem. Mater.*, 2018, **30**, 6945–6956.

28   R. Sharpe, R. A. House, M. J. Clarke, D. Förstermann, J. J. Marie, G. Cibin, K. J. Zhou, H. Y. Playford, P. G. Bruce and M. S. Islam, *J. Am. Chem. Soc.*, 2020, **142**, 21799–21809.

29   Y. Yue, N. Li, L. Li, E. E. Foley, Y. Fu, V. S. Battaglia, R. J. Clément, C. Wang
and W. Tong, *Chem. Mater.*, 2020, **32**, 4490–4498.

Chapter 6: Conclusions

The main aim of this thesis was to develop a method to allow the separation of mixed cathode materials containing a layered oxide and LMO, and to then upcycle the LMO component into current and next generation cathode materials.

6.1. Summary

Chapter 3 developed a method that uses citric acid to selectively leach LMO from blended cathode material (LMO/LO) and subsequently regenerates the LMO and LO phases. Cathodes taken from both QC and EOL cells were characterized and shown to contain LMO alongside a LO phase. The major differences between the two cathodes is the presence of Cu in the QC cathode due to over discharging and an extreme Li deficiency in the EOL cathode. Citric acid was shown to work as a selective leaching agent for LMO, leaving the LO phase remaining in the cathode. Optimisation of the leaching process was achieved through changes to the acid concentration, acid temperature, and S:L ratio. The selectivity of the leaching process is related to the pH of the solution, with Mn citrate having a higher stability constant than Ni citrate under the reaction conditions. Once separated, the LMO was then recovered out of the solution and was used to remake a LMO cathode. The remanufactured LMO had a poorer capacity than pristine LMO which could be due to impurity elements or crystallite size issues. The LO phase was also recovered, and thermal and hydrothermal treatments were investigated as methods to remove the remaining PVDF binder.

Chapter 4 investigated the impact of synthesis conditions to prepare pristine LMNO and explored upcycling QC and EOL cathodes into LMNO. The synthesis temperature

was found to alter the ordering and subsequent electrochemical performance of pristine LMNO. Higher temperatures favoured formation of the disordered phase which displays an additional lower voltage plateau due to the presence of Mn^{3+}. EOL and QC LMO were successfully upcycled into LMNO by the addition of a stoichiometric amount of Ni reagent. EOL LMNO was found to display different properties to pristine LMNO synthesised under the same conditions. Changes to the Ni content, synthesis temperature and synthesis atmosphere were investigated as methods to control the ordering of EOL LMNO. An O_2 synthesis atmosphere was found to provide the best control over the amount of Mn^{3+} and subsequent electrochemical performance of EOL LMNO. EOL LMNO was found to display an improved capacity retention compared to pristine LMNO which has been attributed to low levels of disorder within the EOL LMNO. QC LMO was also upcycled into LMNO. QC LMNO displayed different properties to pristine and EOL LMNO synthesised under the same conditions, and it also had an improved capacity retention compared to pristine LMNO. The discharge capacity of QC LMNO was lower than the pristine/EOL LMNO, however the capacity was increased by the addition of 10 wt% excess Li during synthesis.

Chapter 5 focussed on Mn-based DRS; firstly, optimising their performance and secondly, aiming to synthesise them via upcycling of EOL/QC LMO. $Li_4Mn_2O_5$ was synthesised and different methods were used to try and prevent degradation and to improve its electrochemical performance. A PVDF surface coating was found to improve the structural stability in air. Different electrochemical testing methods and testing conditions were found to improve the electrochemical performance. Then this work investigated optimising the performance of Mn-based DRS by doping with elements such as F, Ni, Zn and Na. Na doping was found to give superior capacity

retention which is attributed to Na stabilising the structure and allowing for easy Li diffusion. EOL and QC LMO were upcycled into $Li_4Mn_2O_5$ and $Li_2MnO_{2.25}F$, with these initial results showing that the electrochemical performance of the upcycled DRS was comparable to pristine DRS.

6.2. Context

This thesis has a wider impact upon the recycling of LIBs and in particular, upcycling of LIB cathode materials. This section explores the broader context of the discoveries within this thesis.

Chapter 3 has developed a method which allows for separation of LMO/LO blended cathodes. This provides a new approach for LIB recycling as literature mostly focuses on recycling of single-phase cathodes. In addition to allowing separation of blended cathode materials, this work also has the potential to be used on mixtures of cathode materials, which are obtained from shredding different LIBs together and is what the recycling feedstock is likely to consist of. This method aims to directly resynthesize the cathode materials or to upcycle into other cathode materials, rather than the convoluted approach to separate into the individual metal precursors. This results in fewer steps compared to a traditional hydrometallurgical route and therefore would have lower cost and increased carbon savings. The selectivity of citric acid for LMO over the LO phase is interesting as traditional routes dissolve all the metals into solution and then achieve selectivity when precipitating them out. This work therefore changes the point at which the selectivity is occurring and may have benefits for reducing contamination and reducing the number of recycling steps.

Chapter 4 shows that LMO can be upcycled into LMNO and therefore proves that there is a potential to upcycle LMO into newer, more commercially relevant cathode materials. While previous literature has highlighted the impact of synthesis temperatures upon the ordering of pristine LMNO, this work has shown that synthesis temperatures have a different impact upon the ordering of LMNO prepared from

different feedstocks (EOL and QC cathodes). This demonstrates that synthesis using upcycled materials can result in differences to the final material properties and therefore this must be considered when creating upcycling processes. In addition, the upcycled LMNO has an improved capacity retention compared to pristine LMNO. This shows that there is the potential for upcycled materials to have a superior performance compared to pristine materials and this is something that could push recycling interests if superior products can be produced.

Chapter 5 shows that LMO recovered from LIBs can be upcycled into DRS phases and therefore indicates that there is a potential for low value Mn-based cathodes to retain value by upcycling them into next generation cathode materials such as these. This work also showed that the best capacity retention was obtained by Na doping. This contrasts with literature on DRS which often focuses on doping with TM. There is room for this doping strategy to be explored further and for investigation to understand why Na doping improves the performance.

Looking at the wider context, the EU's Critical Raw Minerals Act lists Mn as a strategic critical raw mineral and the UK's Critical Minerals Strategy has Mn on its watchlist.[1,2] This is mainly related to the fact that Mn is not currently recycled as it is considered too low value, which ironically contradicts its strategic importance. This work which directly looks at upcycling of LMO improves the recycling economics by creating a higher value product. While the EU has created legislation that requires LIBs to contain a minimum level of recycled content (12% Co, 4% Li and 4% Ni) by 2030[3] it is possible that, given the inclusion on the EU Critical Raw Minerals Act, legislation on Mn

recycling will be introduced in the future and so methods discussed in this thesis will

enable such targets to be easily achieved.

6.3. Further work

There is extensive further work that could be undertaken to understand some of observations from this thesis work in more detail, and then expand upon the work in this thesis to further improve the recycling process.

Further work could be undertaken on the hydrometallurgical portion of this thesis. The leaching study could be expanded in future to investigate whether selectivity can be achieved for mixtures of cathodes rather than blended cathodes. This could involve LMO present in mixtures of NMCs, NCAs, etc. Additional work could be done to explore alternative ways to recover the LMO out of solution rather than using thermal treatments which have a high energy intensity and carbon output. More work is needed to optimise the electrochemical performance of the recycled LMO and NCA. Commercially, shredding of LIBs and separating into a shredded cathode component (black mass) is favoured as a pre-processing method. Therefore, it would be interesting to test the leaching process on commercial black mass rather than separated cathode material. Also, it would be useful to investigate the scale up of this work. This would allow us to test the compatibility with commercially used processes/equipment while also to allowing a life-cycle assessment to identify whether energy and carbon savings are made when compared to a traditional hydrometallurgical method.

Further work could also be done on the upcycling portions of this thesis. More work is needed to understand the behaviours seen in some of the materials synthesised to explain, for example, why pristine/EOL/QC LMNO displayed different properties when synthesised under the same conditions. Additional characterisation could be employed

to investigate the presence of Mn^{3+} in the O_2 heat treated EOL LMNO and understand why the EOL/QC LMNO had an improved capacity retention compared to pristine LMNO. Further work is also needed to optimise the electrochemical performance of QC LMNO. The DRS samples should be tested using coatings to ensure that optimum performance is obtained. Additional work would be useful to understand the positive characteristics seen when Na-doping was used and to investigate whether further optimisation can be achieved. Further work could also be done to create a comprehensive picture of all the potential routes to upcycle LMO, for example, there is potential to upcycle LMO to make Mn-doped LFP (LMFP), which is seen as the next commercial step for LFP cathodes due to the higher operating voltage and hence higher energy density.

Overall, this thesis represents a significant first step towards the upcycling of Mn-based LIB cathodes, showing the potential to deliver value from Mn-based waste products and helping towards inspiring the battery community to consider the circularity of LIB recycling in more detail.

6.4. References

1   HM Government, *Resilience for the Future: The United Kingdom's Critical Minerals Strategy*, 2022.

2   European Commission, *Regulation of the European Parliament and of the council for establishing a framework for ensuring a secure and sustainable supply of critical raw materials*, 2023.

3   European Commission, *Regulation (EU) 2023/1542 of the European Parliament and of the Council concerning batteries and waste batteries*, 2023.

Appendix A: Rietveld refinements for Chapter 3
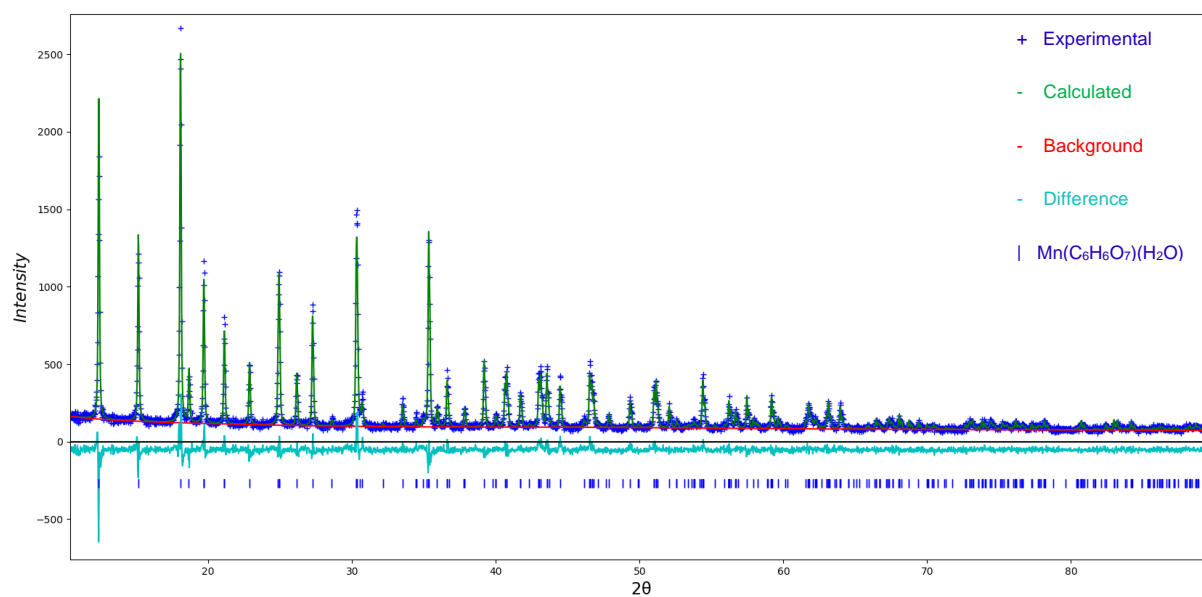
Figure A1: Rietveld refinement plot for the dried citric acid leaching solution (λ = 1.79 Å). R_{wp} = 10.81% and GOF = 1.29.
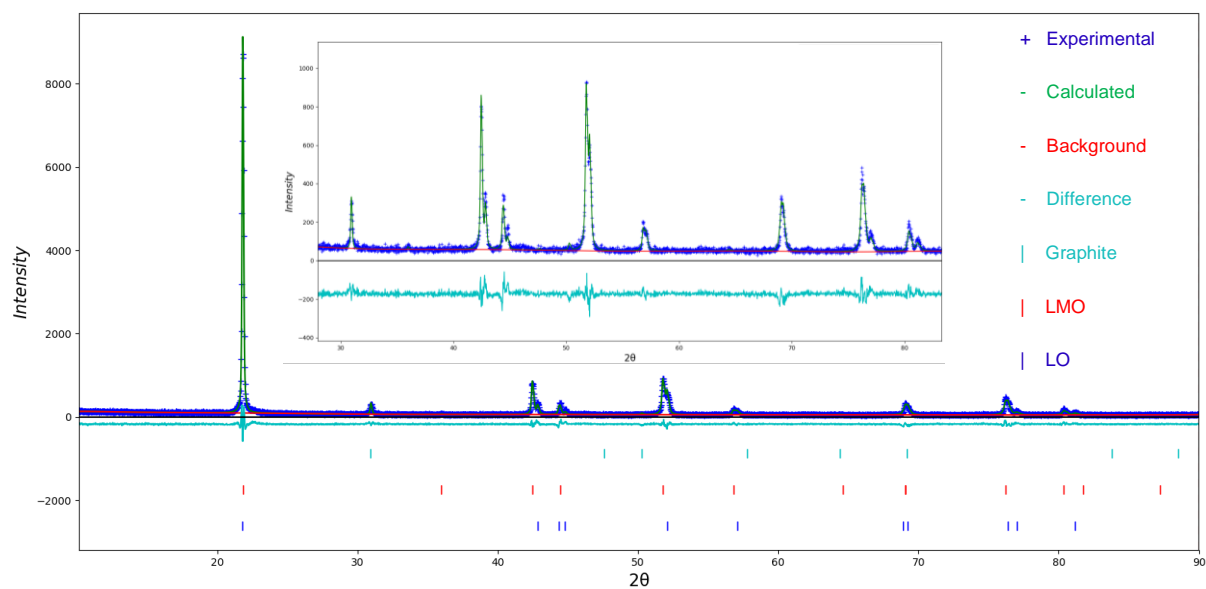
Figure A2: Rietveld refinement plot for the QC cathode (λ = 1.79 Å). R_{wp} = 12.86% and GOF = 1.30.
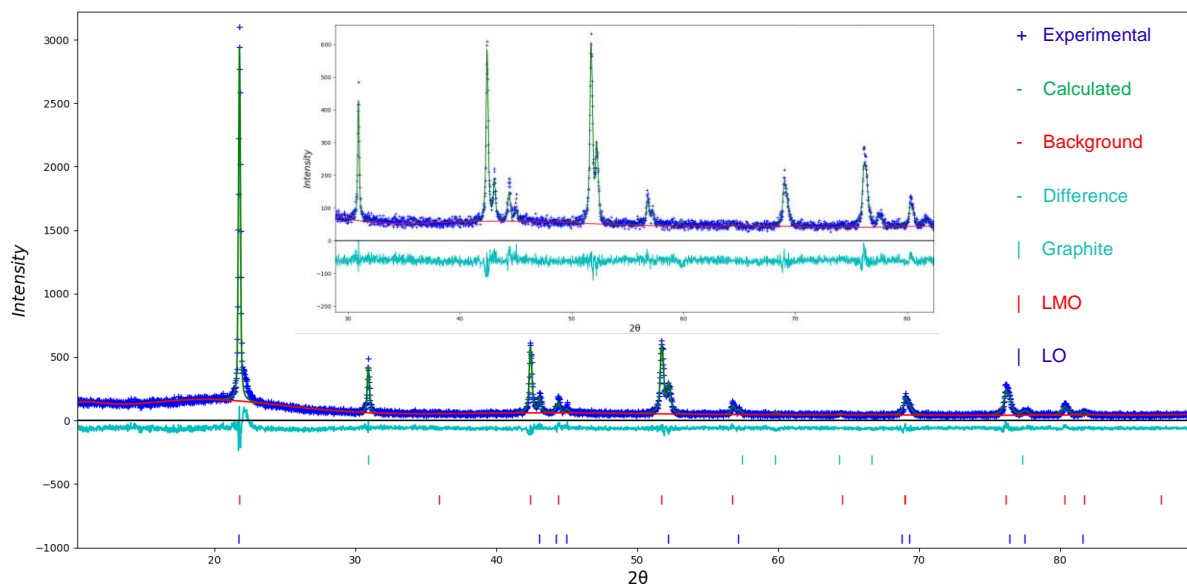
Figure A3: Rietveld refinement plot for the EOL cathode (λ = 1.79 Å). R$_{wp}$ = 12.82% and GOF = 1.23.
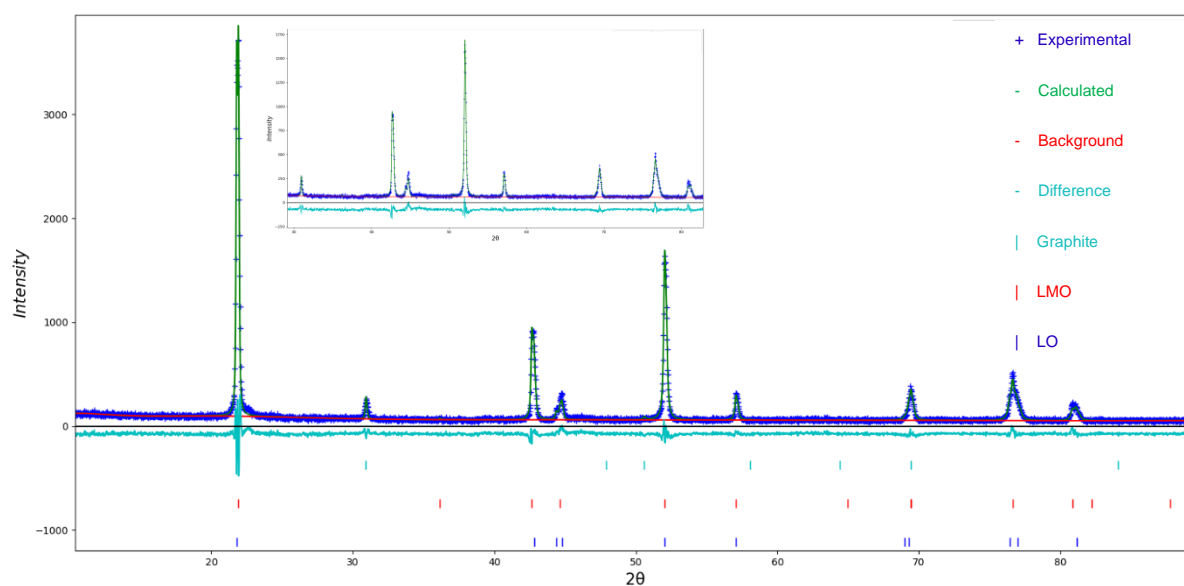
Figure A4: Rietveld refinement plot for 0.3 g of QC cathode after leaching for 5 minutes in 10 mL of 1 M citric acid (λ = 1.79 Å). R$_{wp}$ = 14.05% and GOF = 1.43.
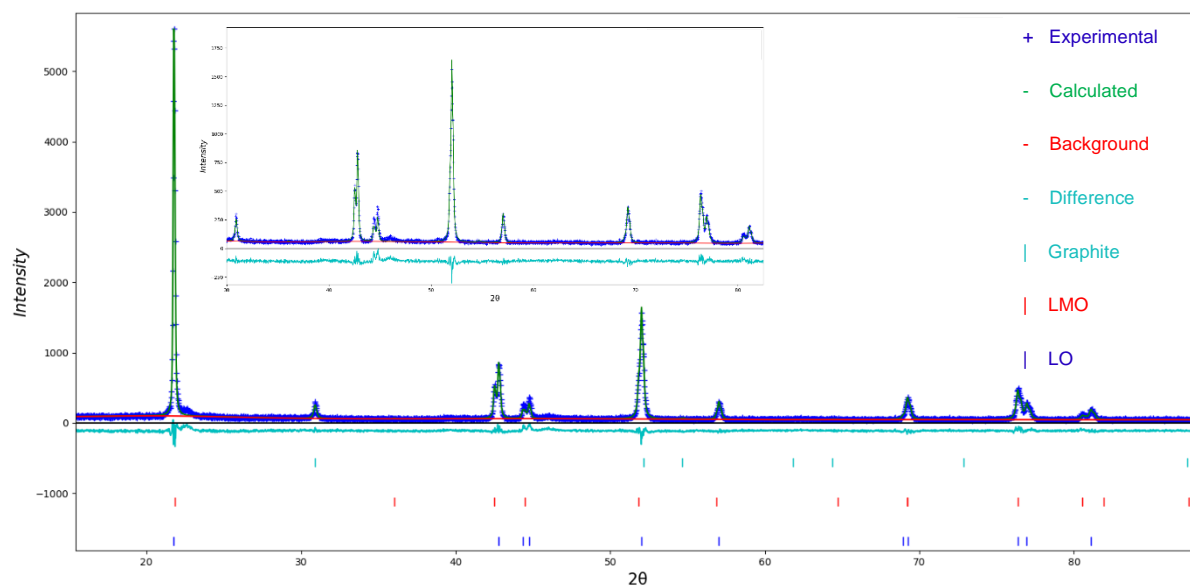
Figure A5: Rietveld refinement plot for 0.3 g of QC cathode after leaching for 10 minutes in 10 mL of 1 M citric acid (λ = 1.79 Å). R_{wp} = 14.21% and GOF = 1.41.
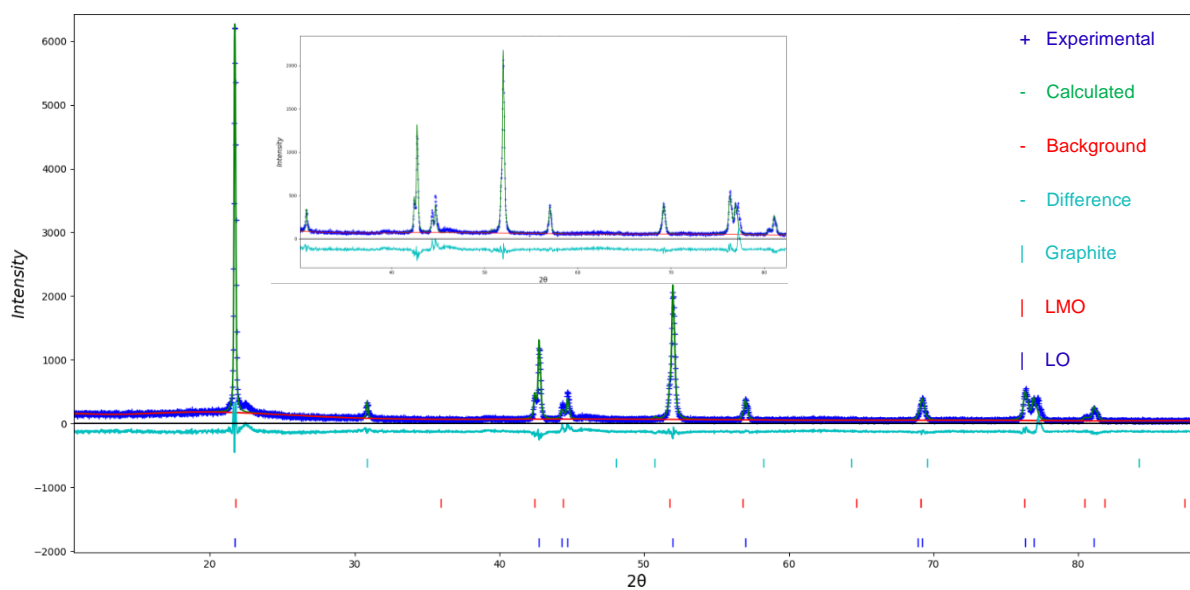
Figure A6: Rietveld refinement plot for 0.3 g of QC cathode after leaching for 15 minutes in 10 mL of 1 M citric acid (λ = 1.79 Å). R_{wp} = 14.32% and GOF = 1.60.
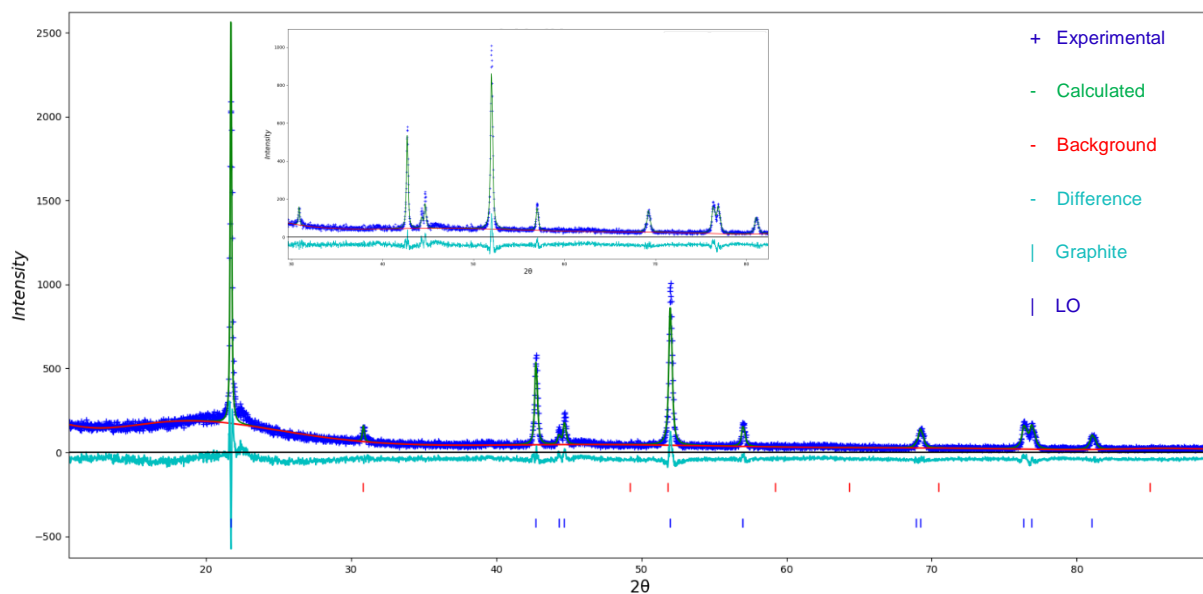
Figure A7: Rietveld refinement plot for 0.3 g of QC cathode after leaching for 20 minutes in 10 mL of 1 M citric acid (λ = 1.79 Å). R$_{wp}$ = 15.90% and GOF = 1.43.
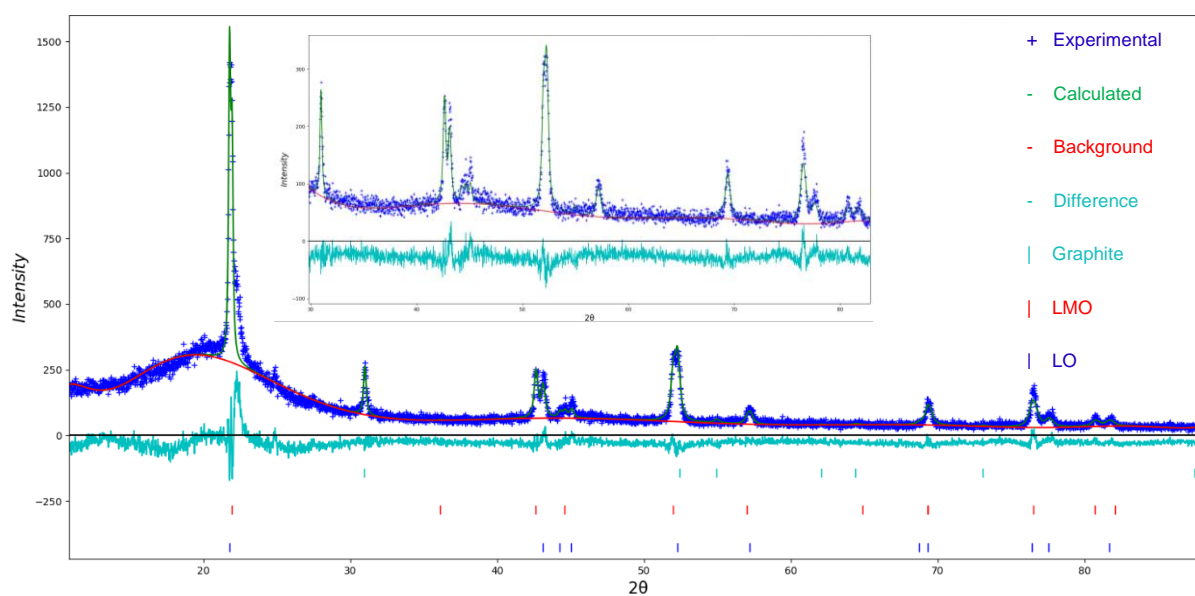
Figure A8: Rietveld refinement plot for 0.3 g of EOL cathode after leaching for 5 minutes in 10 mL of 1 M citric acid (λ = 1.79 Å). R$_{wp}$ = 14.67% and GOF = 1.52.
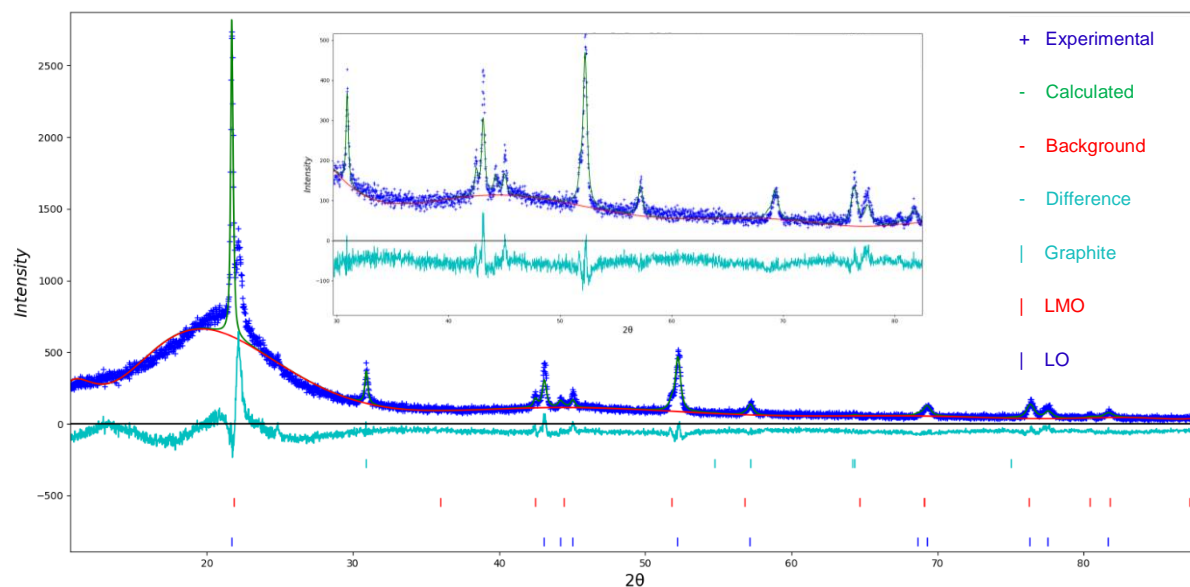
Figure A9: Rietveld refinement plot for 0.3 g of EOL cathode after leaching for 10 minutes in 10 mL of 1 M citric acid (λ = 1.79 Å). R_{wp} = 15.66% and GOF = 2.13.
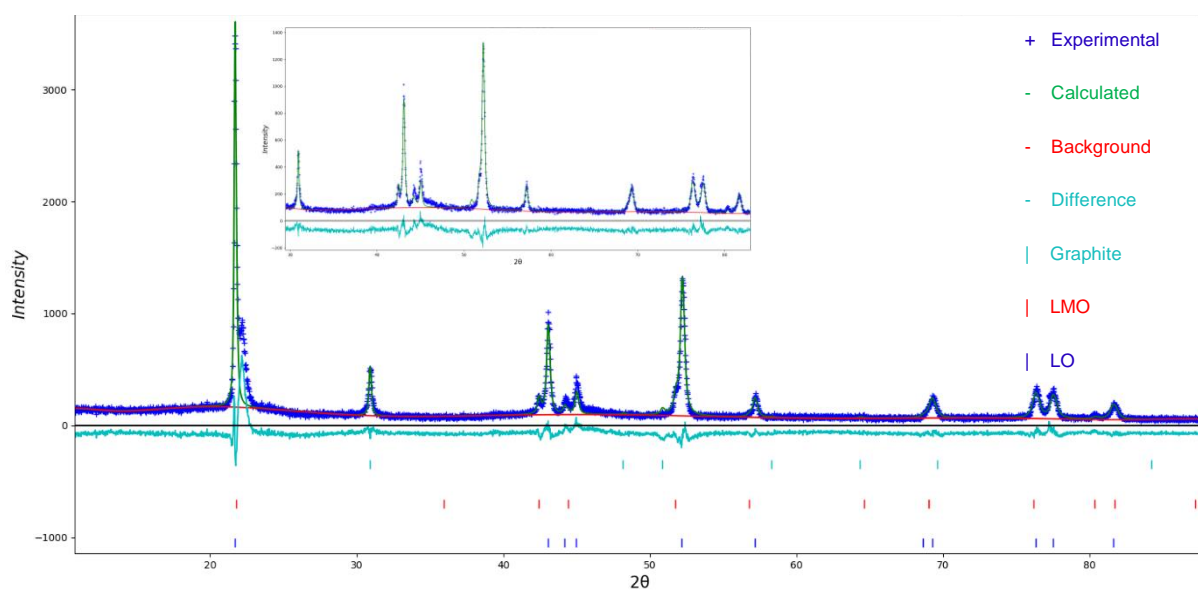
Figure A10: Rietveld refinement plot for 0.3 g of EOL cathode after leaching for 15 minutes in 10 mL of 1 M citric acid (λ = 1.79 Å). R_{wp} = 19.22% and GOF = 2.22.
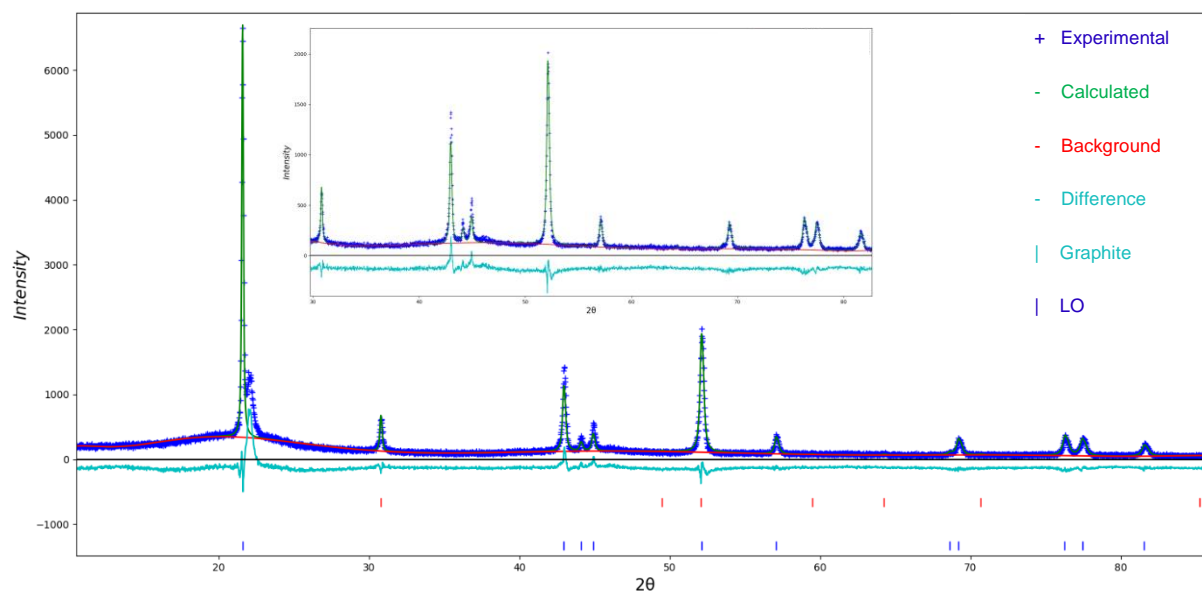
Figure A11: Rietveld refinement plot for 0.3 g of EOL cathode after leaching for 20 minutes in 10 mL of 1 M citric acid (λ = 1.79 Å). R_{wp} = 18.17% and GOF = 2.41.
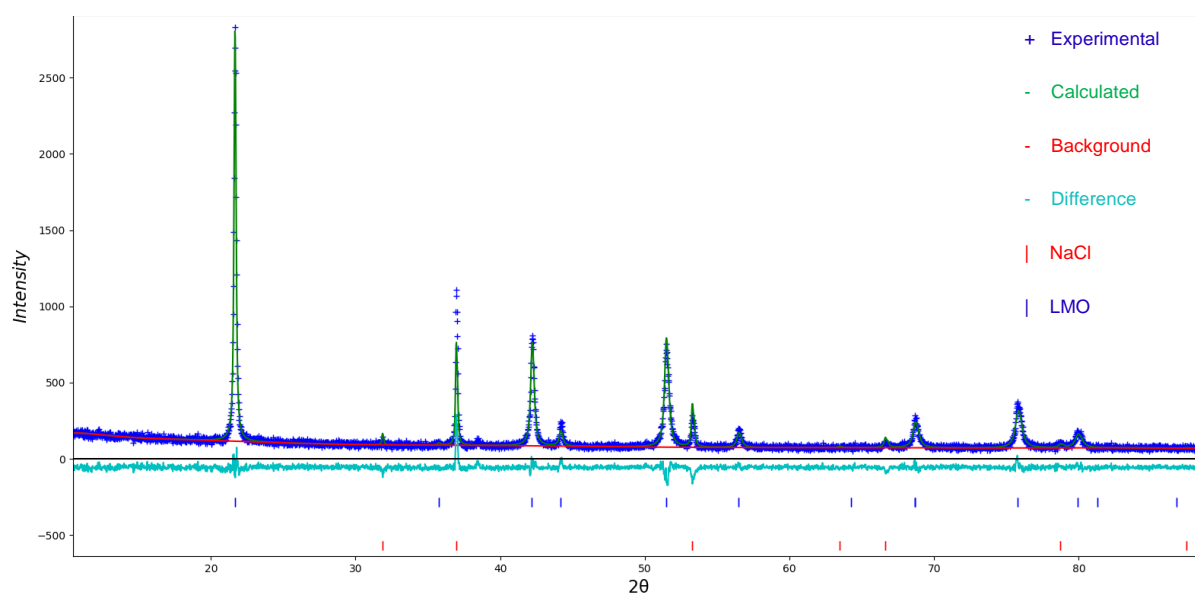
Figure A12: Rietveld refinement plot of 85 wt% recycled LMO mixed with 15 wt% NaCl (λ = 1.79 Å). R_{wp} = 11.20% and GOF = 1.22. Refinement results gave matching wt% values showing that there is no amorphous content present in the recycled LMO.

Appendix B: XRD patterns of the leaching optimisation study
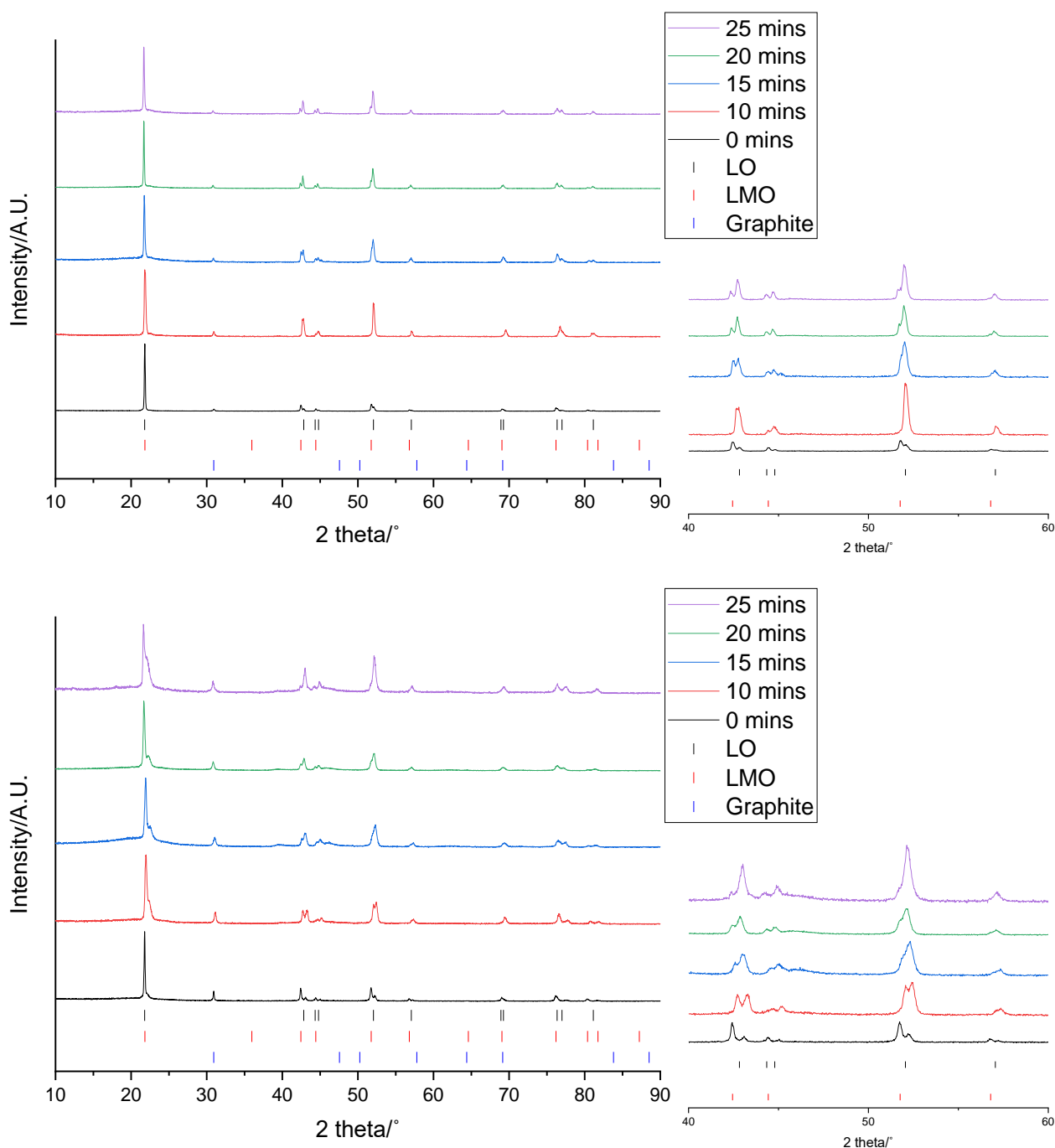
Figure B1: XRD patterns of 0.3 g QC (top) and EOL (bottom) cathodes after leaching in 10 mL of 0.5 M citric acid at 50 °C for 0 (black), 5 (red), 10 (blue), 15 (green) and 20 minutes (purple) (λ = 1.79 Å). Tick marks correspond to LO (black), LMO (red) and graphite (blue).
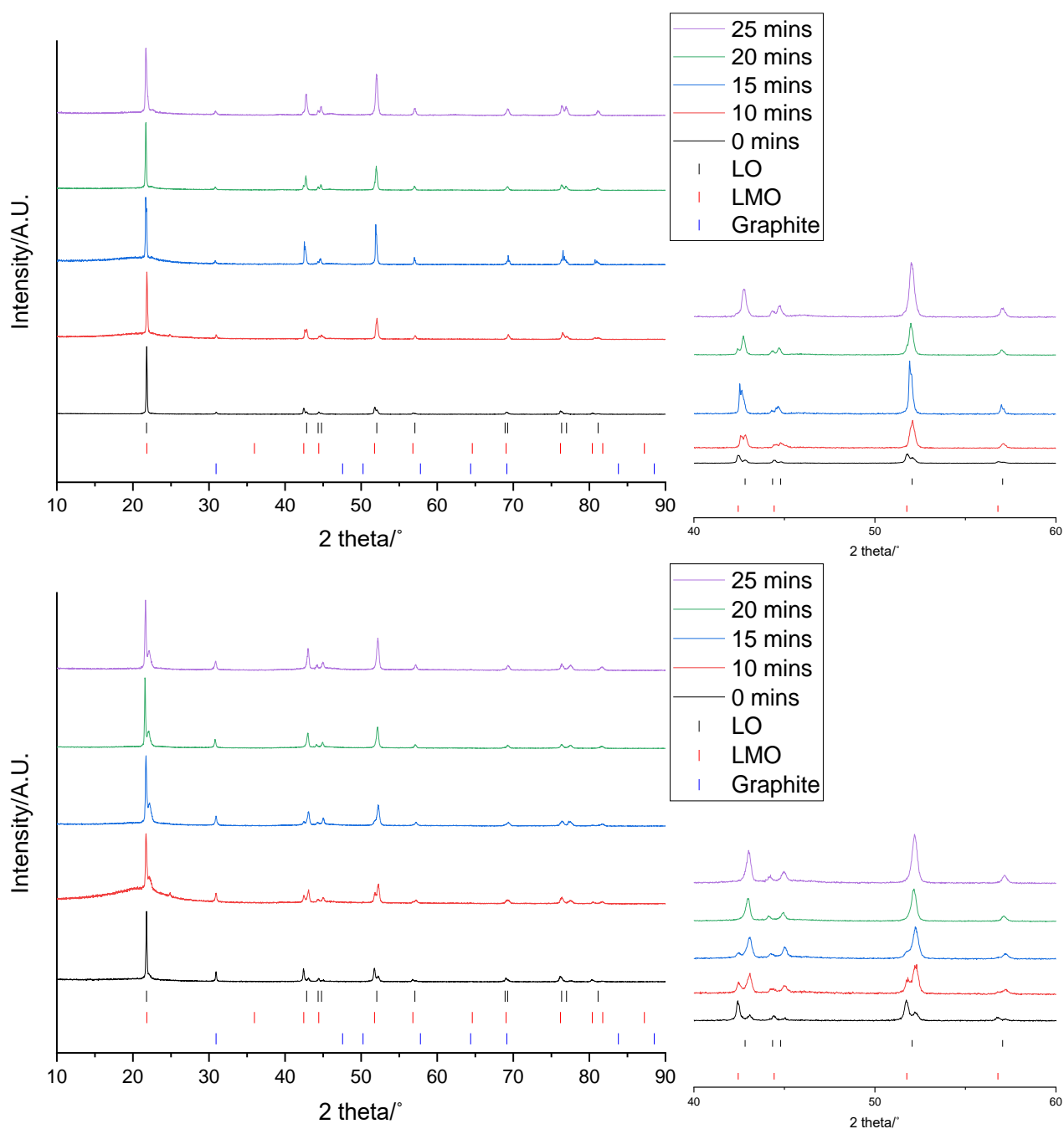
Figure B2: XRD patterns of 0.3 g QC (top) and EOL (bottom) cathodes after leaching in 10 mL of 0.75 M citric acid at 50 °C for 0 (black), 5 (red), 10 (blue), 15 (green) and 20 minutes (purple) (λ = 1.79 Å). Tick marks correspond to LO (black), LMO (red) and graphite (blue).
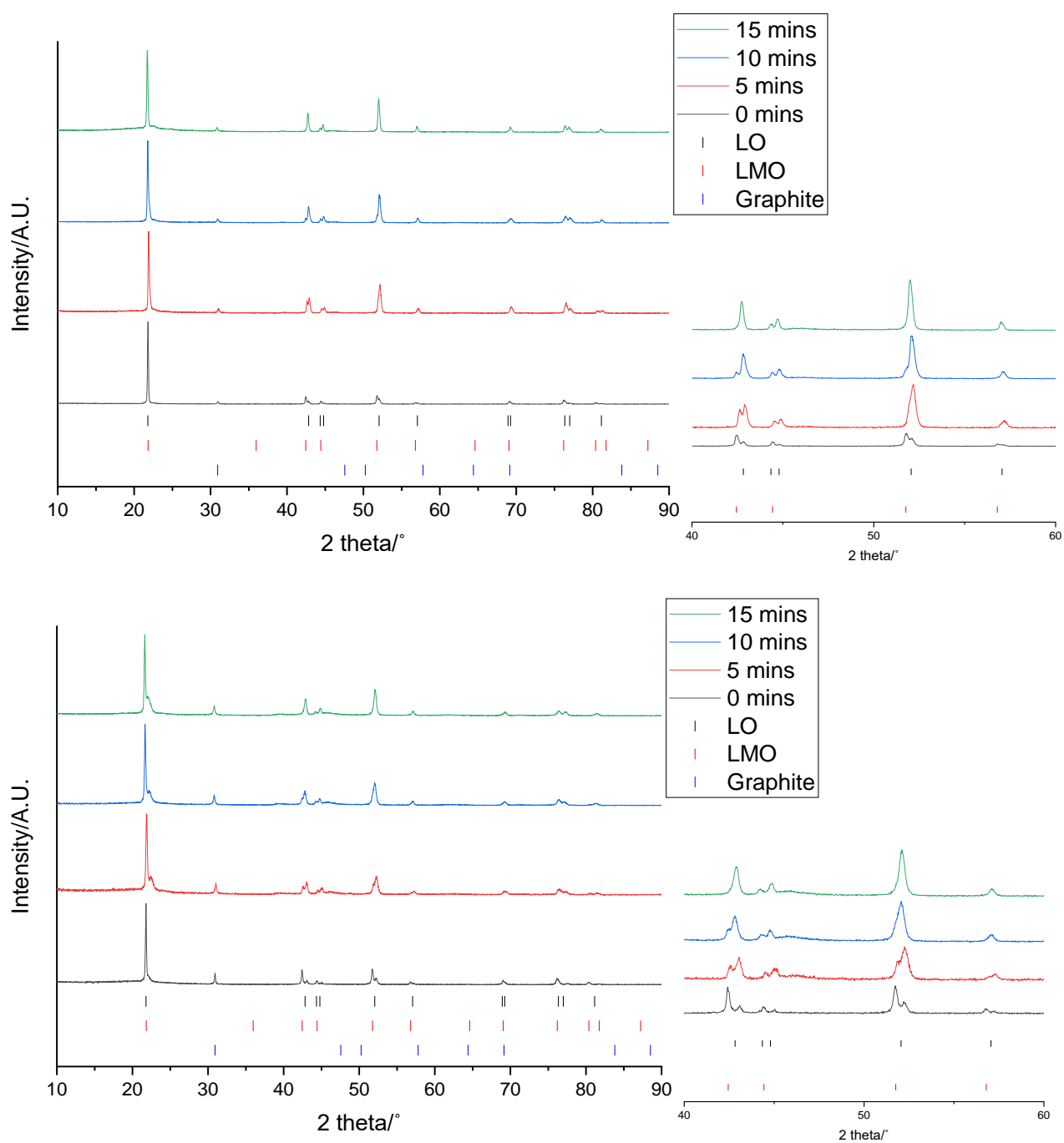
Figure B3: XRD patterns of 0.3 g QC (top) and EOL (bottom) cathodes after leaching in 10 mL of 1 M citric acid at 60 °C for 0 (black), 5 (red), 10 (blue), 15 (green) and 20 minutes (purple) (λ = 1.79 Å). Tick marks correspond to LO (black), LMO (red) and graphite (blue).
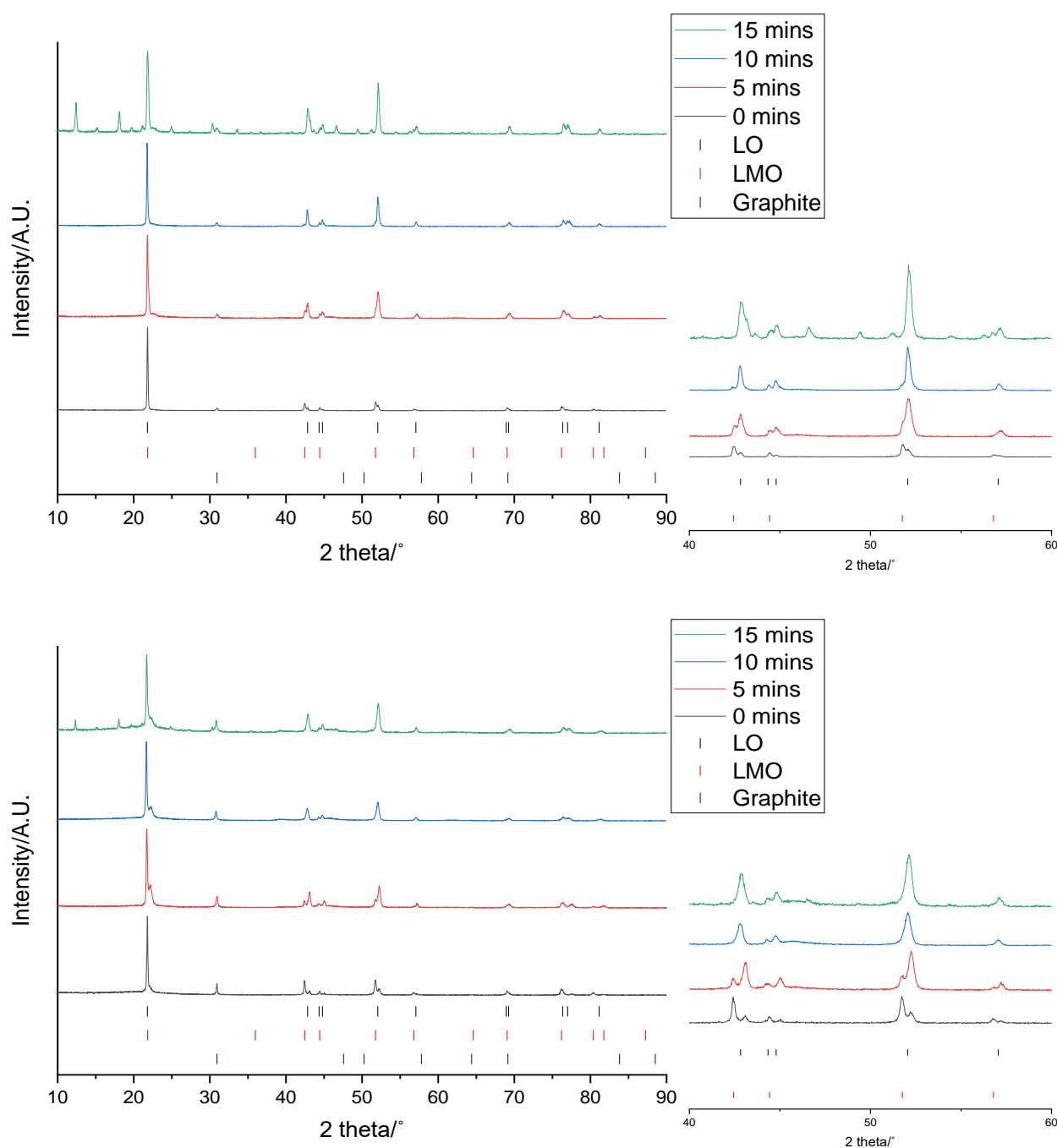
Figure B4: XRD patterns of 0.3 g QC (top) and EOL (bottom) cathodes after leaching in 10 mL of 1 M citric acid at 70 °C for 0 (black), 5 (red), 10 (blue), 15 (green) and 20 minutes (purple) (λ = 1.79 Å). Tick marks correspond to LO (black), LMO (red) and graphite (blue).
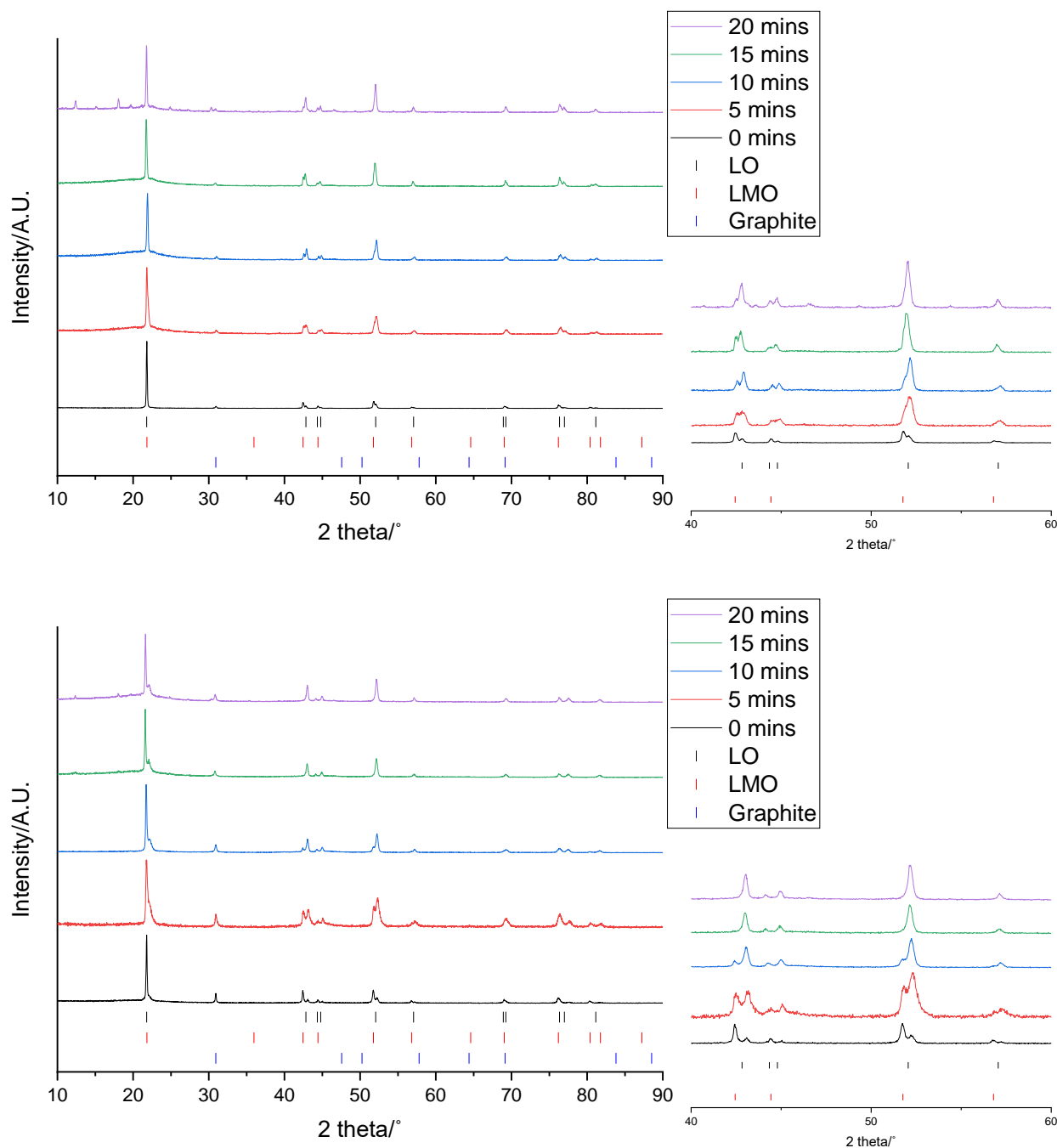
Figure B5: XRD patterns of 0.4 g QC (top) and EOL (bottom) cathodes after leaching in 10 mL of 1 M citric acid at 50 °C for 0 (black), 5 (red), 10 (blue), 15 (green) and 20 minutes (purple) (λ = 1.79 Å). Tick marks correspond to LO (black), LMO (red) and graphite (blue).

Appendix C: ICP-OES results of the leaching

optimisation study
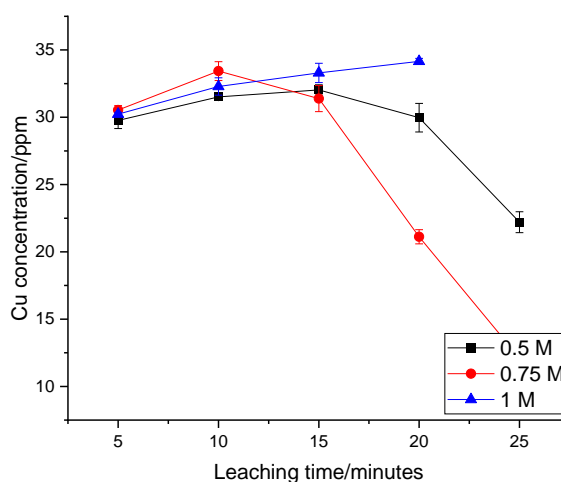
Figure C1: ICP-OES results showing the concentration of Cu in solution at different leaching times for the QC cathode with 0.5 M (square), 0.75 M (circle) and 1 M (triangle) acid concentration. Error bars show relative standard deviation across 3 repeats.
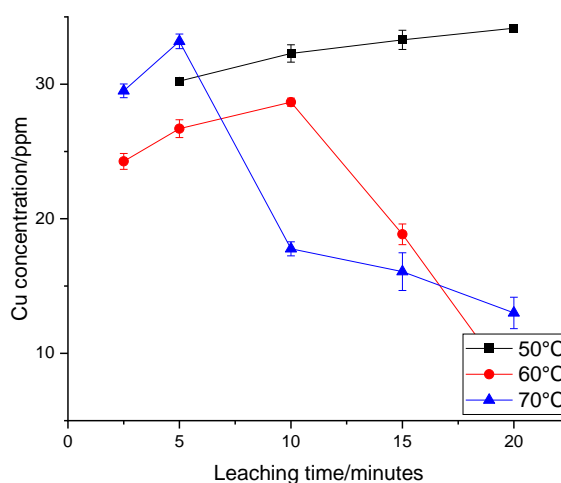
Figure C2: ICP-OES results showing the concentration of Cu in solution at different leaching times for the QC cathode with 50 °C (square), 60 °C (circle) and 70 °C (triangle) acid temperature. Error bars show relative standard deviation across 3 repeats.
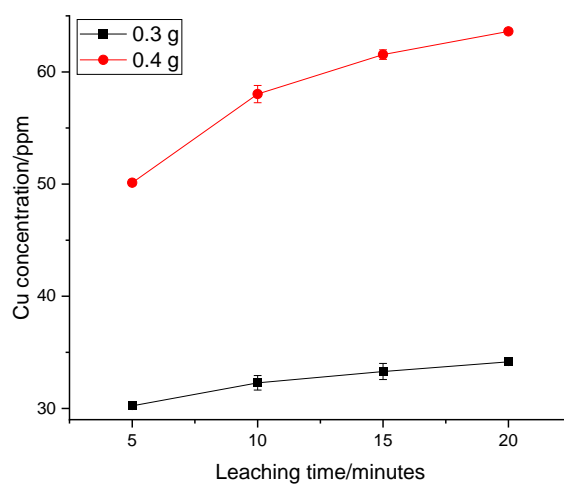
Figure C3: ICP-OES results showing the concentration of Cu in solution at different leaching times for the QC cathode with 0.3 g (square) and 0.4 g (circle) cathode in 10 mL acid solution. Error bars show relative standard deviation across 3 repeats.

Appendix D: Percentage of LMO present in the active material for the leaching optimisation study
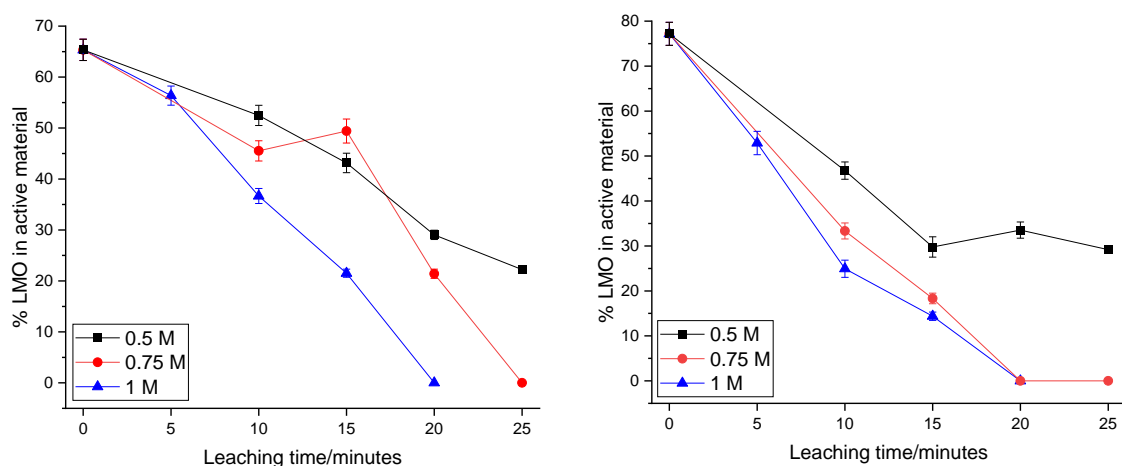
Figure D1: Percentage of LMO in the active material in the QC (left) and EOL (right) cathodes at different leaching times when using 0.5 M (square), 0.75 M (circle) and 1 M (triangle) acid concentration at 50 °C and 30 g/L S:L ratio. Error bars were calculated by combining the uncertainty from refinement results.
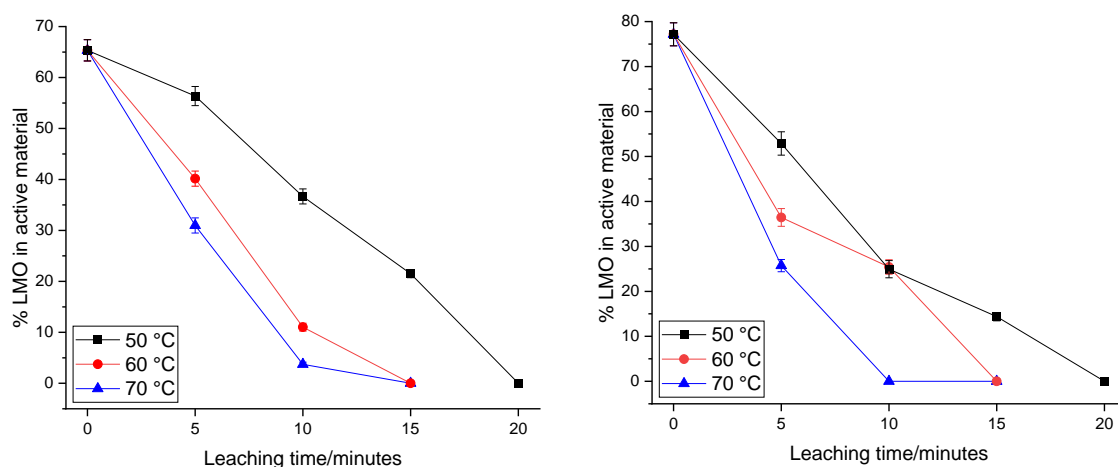
Figure D2: Percentage of LMO in the active material in the QC (left) and EOL (right) cathodes at different leaching times when using 50 °C (square), 60 °C (circle) and 70 °C (triangle) 1 M citric acid and 30 g/L S:L ratio. Error bars were calculated by combining the uncertainty from refinement results.
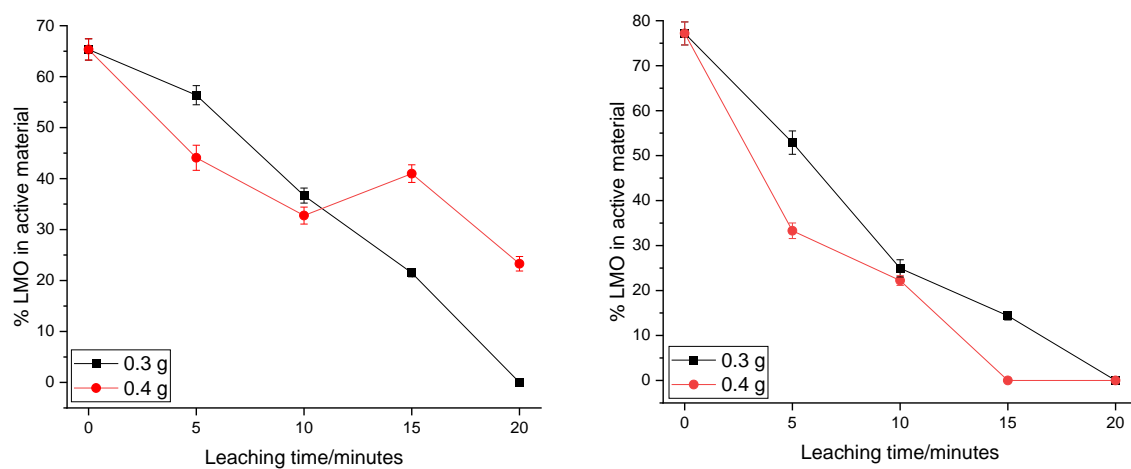
Figure D3: Percentage of LMO in the active material in the QC (left) and EOL (right) cathodes at different leaching times when using 0.3 g (square) and 0.4 g (circle) cathode material in 1 M citric acid at 50 °C. Error bars were calculated by combining the uncertainty from refinement results.

Appendix E: Recycled LMO made from the QC

cathode
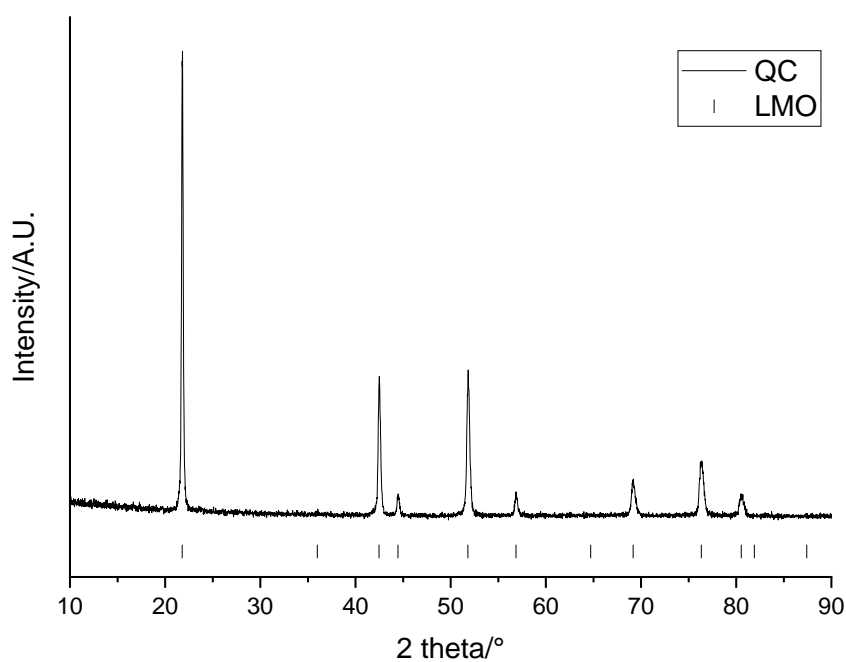
Figure E1: XRD pattern of recycled LiMn$_2$O$_4$ made from the QC cathode (a= 8.1869(3) Å) (λ = 1.79 Å). The synthesis was performed at 700 °C for 6h. Tick marks correspond to LiMn$_2$O$_4$.
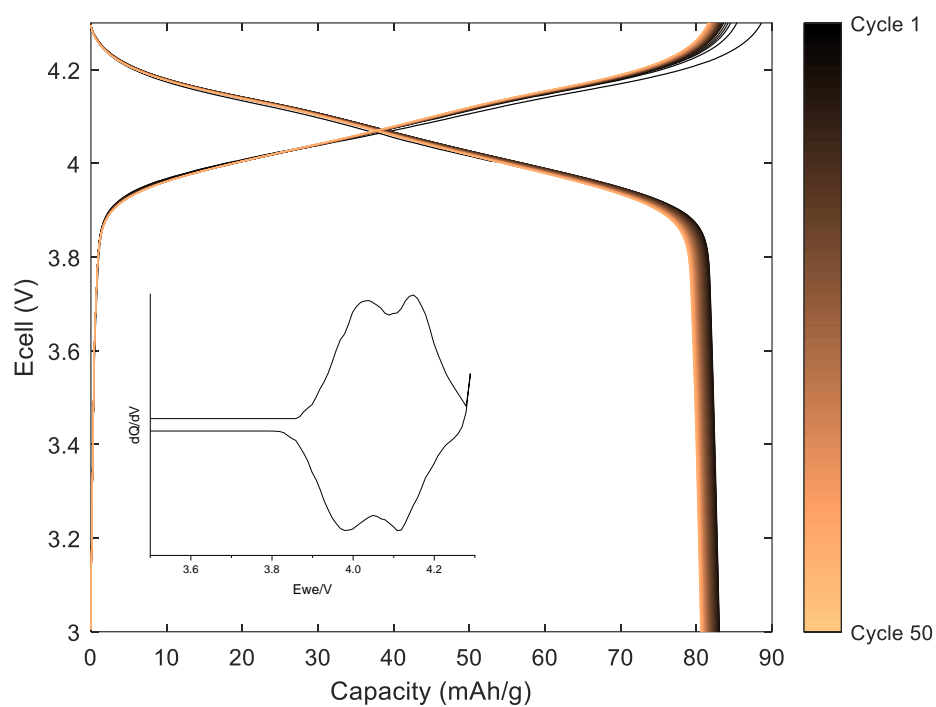
Figure E2: Galvanostatic charge-discharge profile and dQ/dV plot (inset) of recycled LiMn$_2$O$_4$ made from the QC cathode when cycled at 10 mAg^{-1} between 3-4.3 V

Appendix F: XANES results for LMNO samples
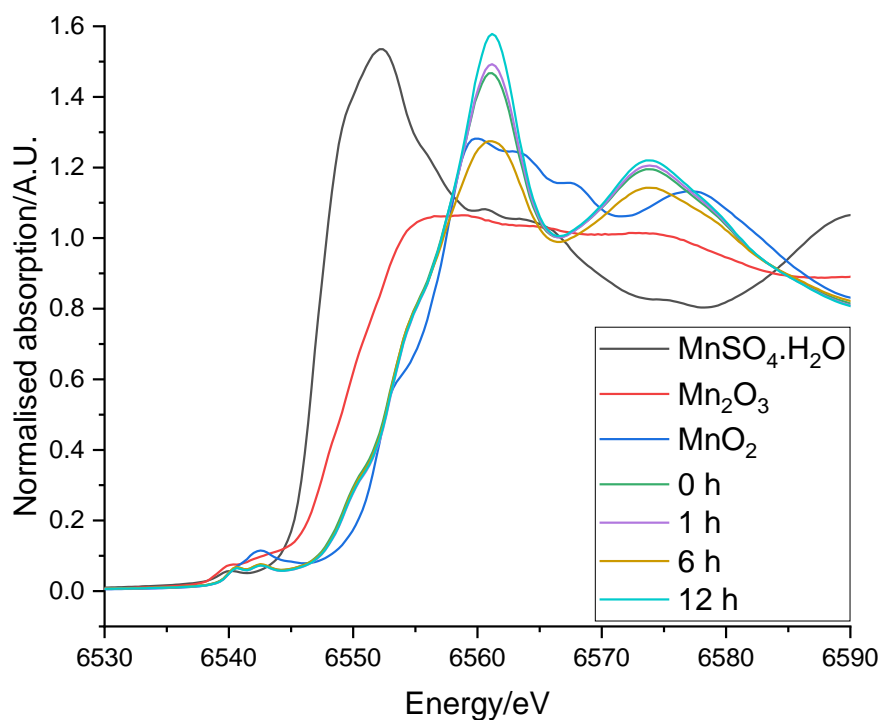
Figure F1: Mn K-edge XANES spectra for Mn references and EOL LMNO synthesised in air at 700 °C for 12 hrs before then heating under O_2 at 700 °C for 0-12 hrs
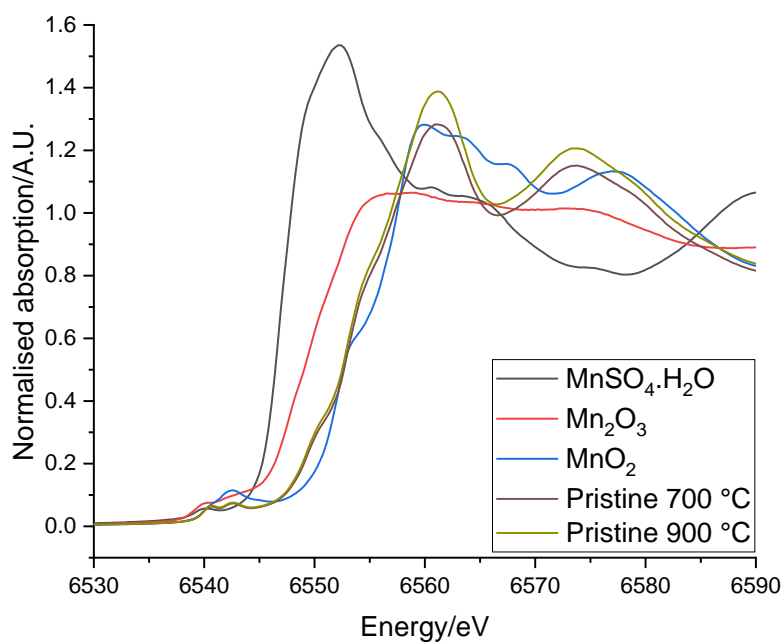
Figure F2: Mn K-edge XANES spectra for Mn references and pristine LMNO synthesised in O$_2$ at 700 and 900 °C
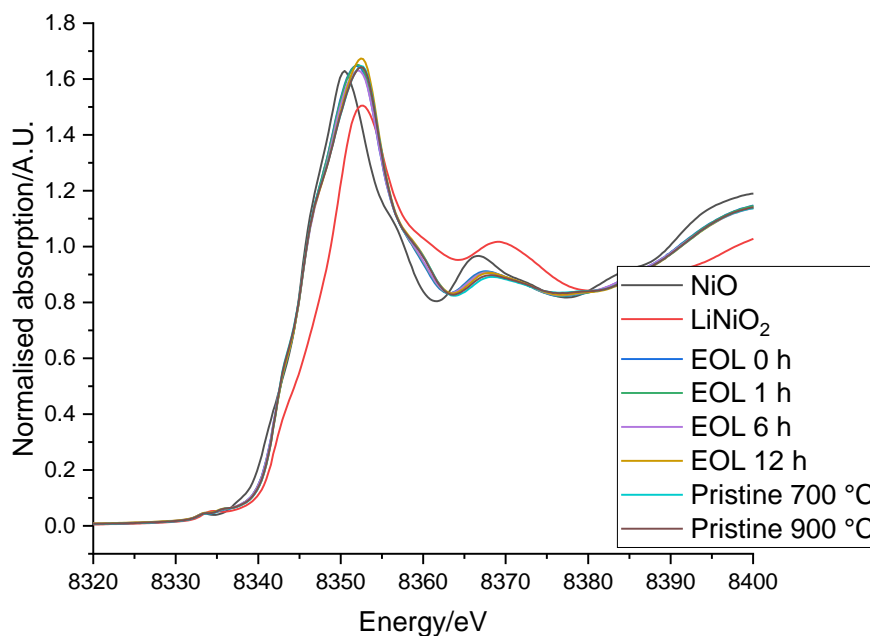
Figure F3: Ni K-edge XANES spectra for Ni references, EOL LMNO synthesised in air at 700 °C for 12 hrs before then heating under O$_2$ at 700 °C for 0-12 hrs and pristine LMNO synthesised in O$_2$ at 700 and 900 °C

Appendix G: SEM/EDX images of EOL LMNO
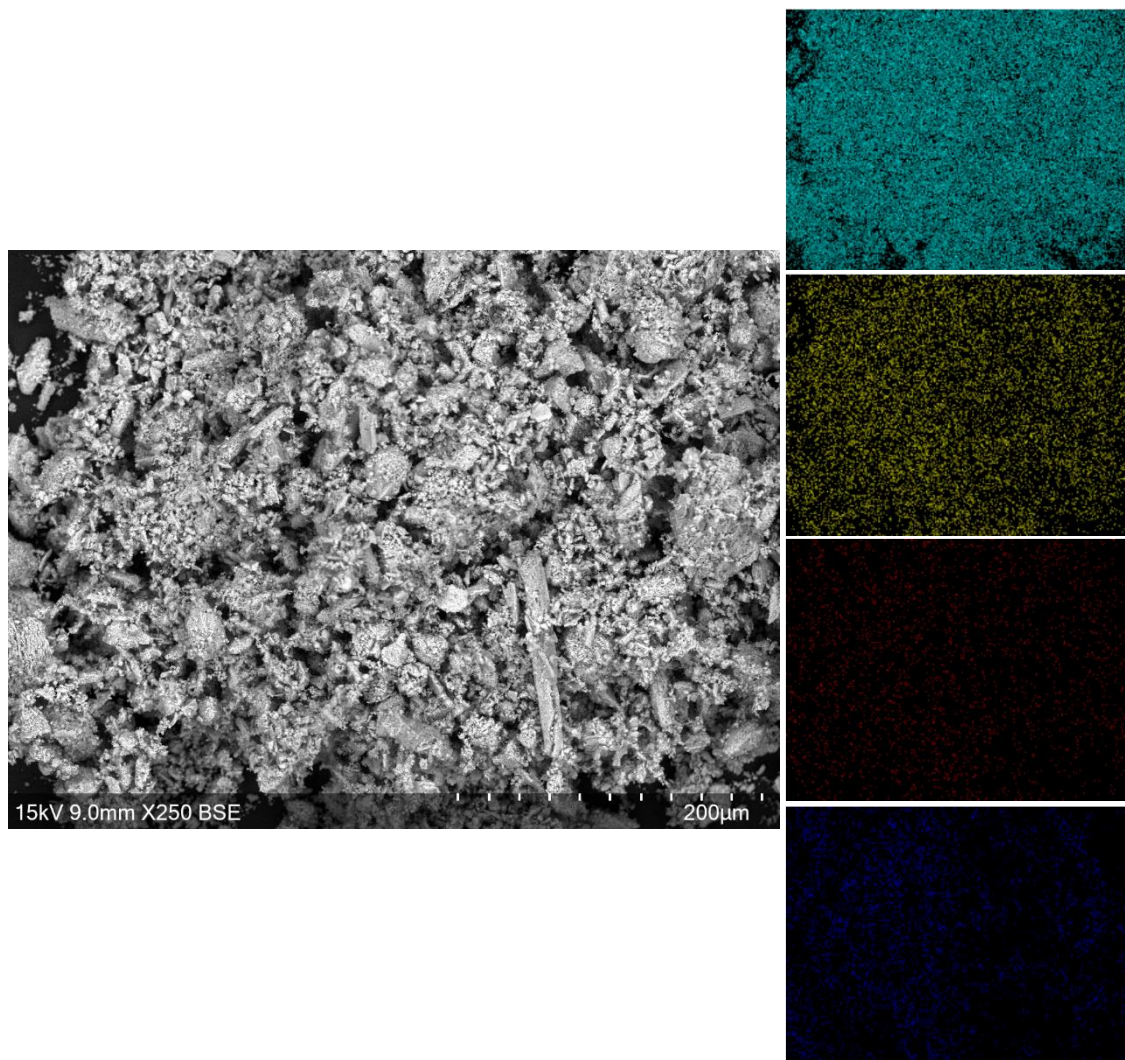
Figure G1: SEM (left) and EDX (right) images of EOL LMNO synthesised in O_2 at 700 °C for 12 hrs. EDX images shows Mn (teal), Ni (yellow), Co (red) and Al (blue) from top to bottom.

Appendix H: Pawley refinements for Chapter 5
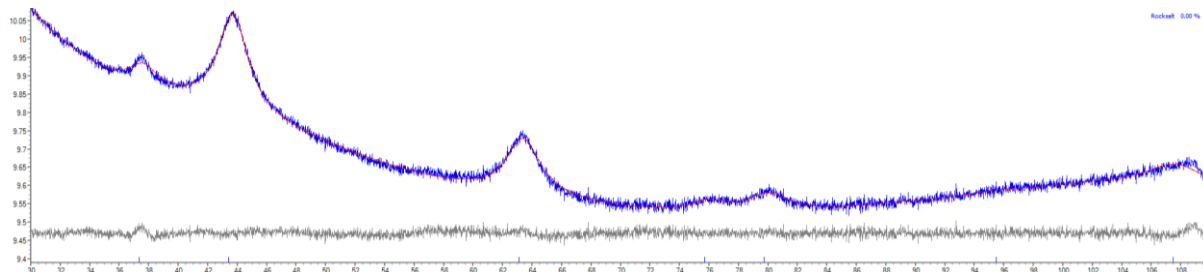
Figure H1: Pawley refinement plot of Li$_4$Mn$_2$O$_5$ synthesised using large milling balls (λ = 1.54 Å). R$_{wp}$ = 0.90%, R$_p$ = 0.71% and GOF = 1.14.
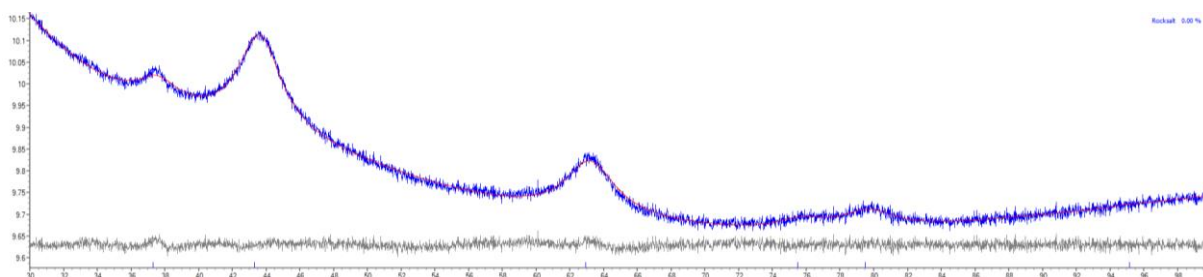
Figure H2: Pawley refinement plot of Li$_4$Mn$_2$O$_5$ synthesised using small milling balls (λ = 1.54 Å). R$_{wp}$ = 0.80%, R$_p$ = 0.64% and GOF = 1.08.
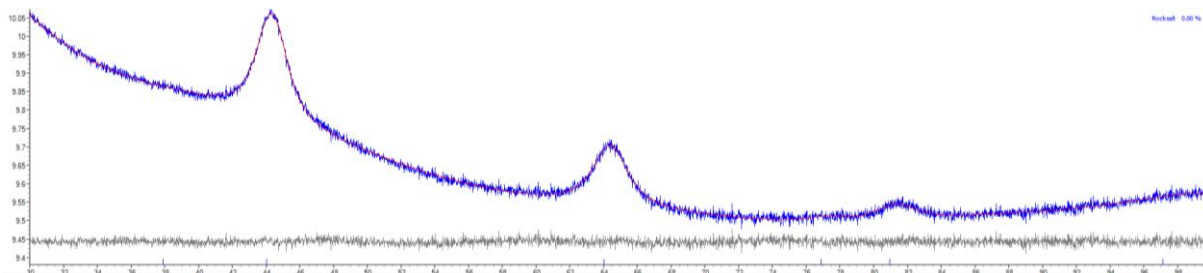
Figure H3: Pawley refinement plot of Li$_2$MnO$_{2.25}$F (λ = 1.54 Å). R$_{wp}$ = 0.83%, R$_p$ = 0.66% and GOF = 1.05.
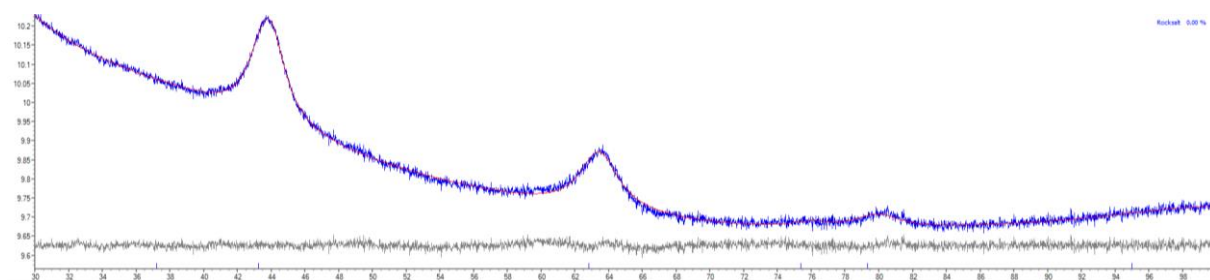
Figure H4: Pawley refinement plot of Li$_2$MnO$_{1.625}$F$_{1.5}$ (λ = 1.54 Å). R$_{wp}$ = 0.79%, R$_p$ = 0.63% and GOF = 1.08.
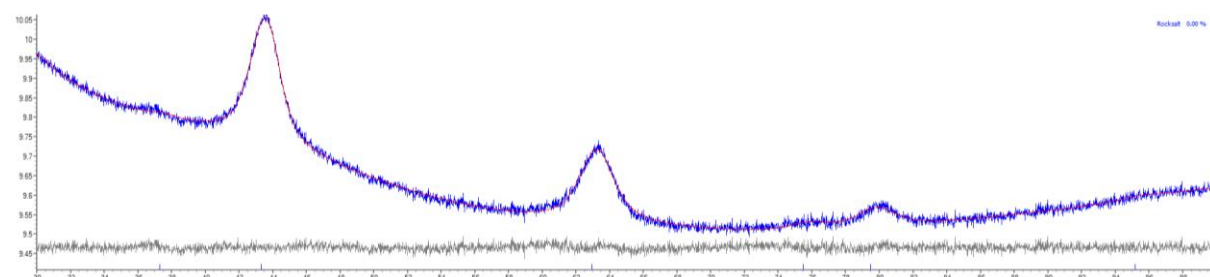
Figure H5: Pawley refinement plot of Li$_2$MnO$_{1.75}$F$_{1.25}$ (λ = 1.54 Å). R$_{wp}$ = 0.84%, R$_p$ = 0.67% and GOF = 1.05.
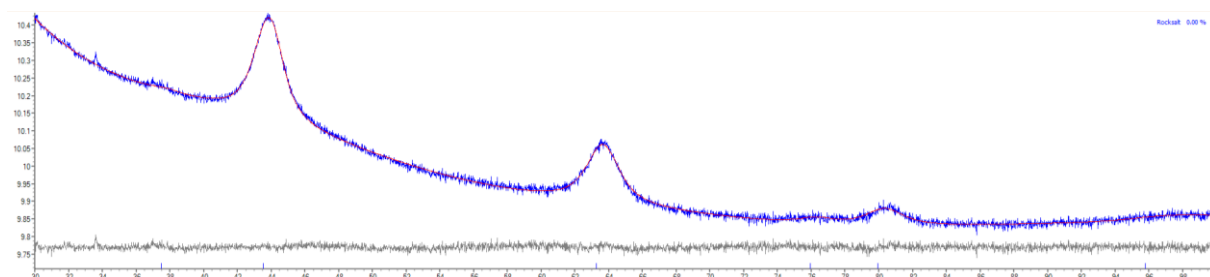
Figure H6: Pawley refinement plot of Li$_2$MnO$_2$F (λ = 1.54 Å). R$_{wp}$ = 0.74%, R$_p$ = 0.58% and GOF = 1.11.
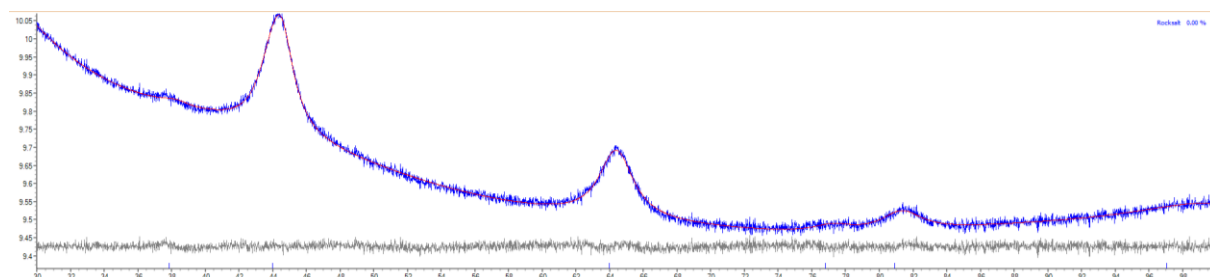
Figure H7: Pawley refinement plot of Li$_2$MnO$_{2.5}$F$_{0.5}$ (λ = 1.54 Å). R$_{wp}$ = 0.84%, R$_p$ = 0.67% and GOF = 1.05.
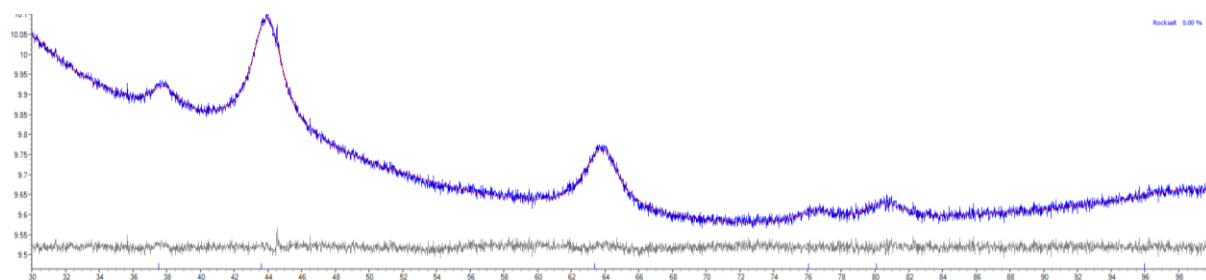
Figure H8: Pawley refinement plot of Li$_4$Mn$_{1.67}$Ni$_{0.33}$O$_5$ (λ = 1.54 Å). R$_{wp}$ = 0.81%, R$_p$ = 0.64% and GOF = 1.05.
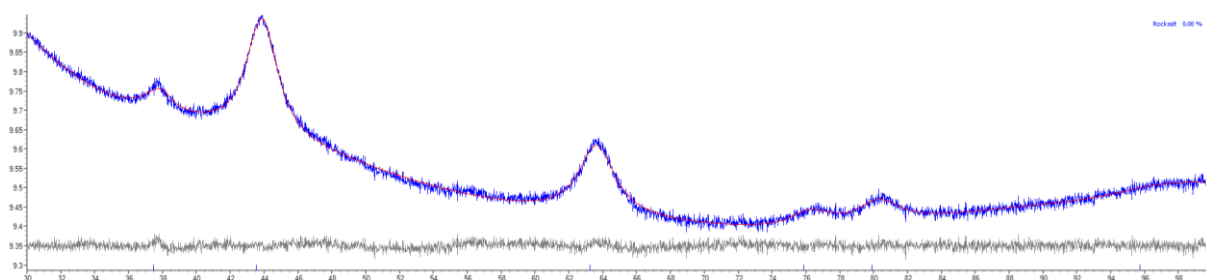
Figure H9: Pawley refinement plot of Li$_4$Mn$_{1.67}$Zn$_{0.33}$O$_5$ (λ = 1.54 Å). R$_{wp}$ = 0.91%, R$_p$ = 0.72% and GOF = 1.08.
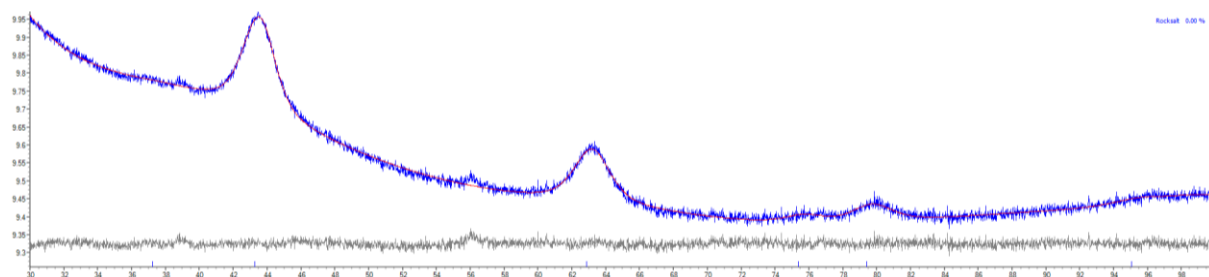
Figure H10: Pawley refinement plot of $Li_{1.6}Na_{0.4}MnO_2F$ (λ = 1.54 Å). R_{wp} = 0.92%, R_p = 0.73% and GOF = 1.10.
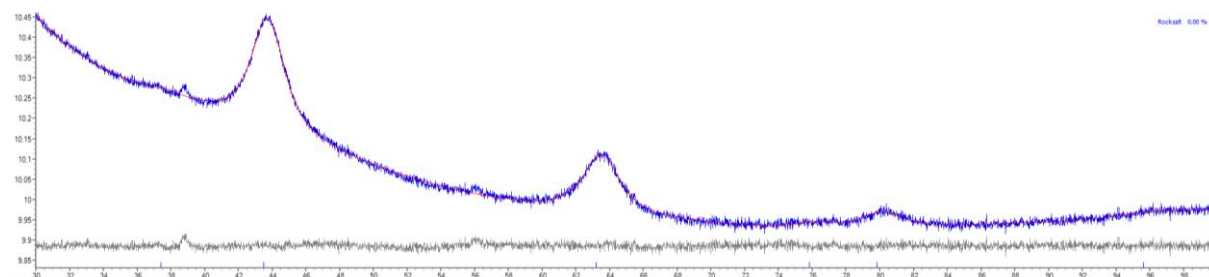
Figure H11: Pawley refinement plot of $Li_{1.7}Na_{0.3}MnO_2F$ (λ = 1.54 Å). R_{wp} = 0.70%, R_p = 0.55% and GOF = 1.08.
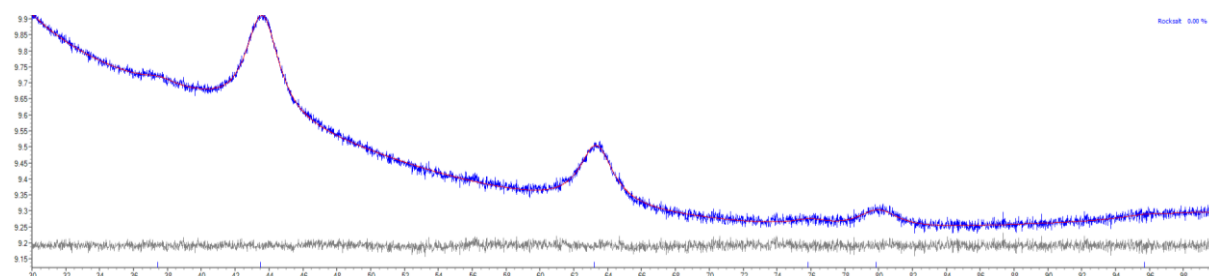
Figure H12: Pawley refinement plot of $Li_{1.8}Na_{0.2}MnO_2F$ (λ = 1.54 Å). R_{wp} = 0.91%, R_p = 0.73% and GOF = 1.04.
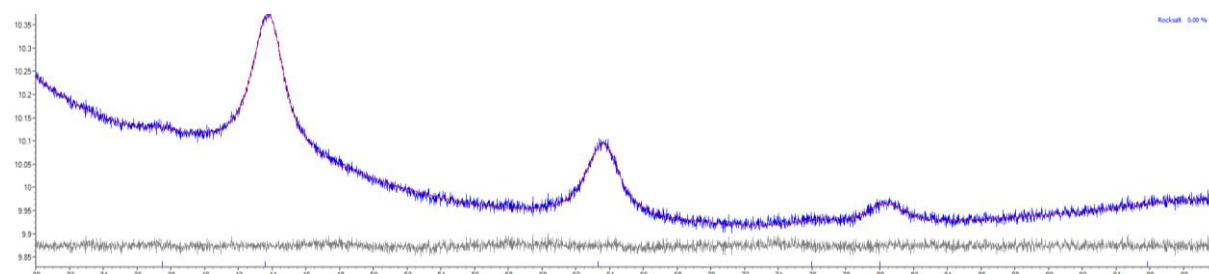
Figure H13: Pawley refinement plot of $Li_{1.9}Na_{0.1}MnO_2F$ (λ = 1.54 Å). R_{wp} = 0.70%, R_p = 0.55% and GOF = 1.04.
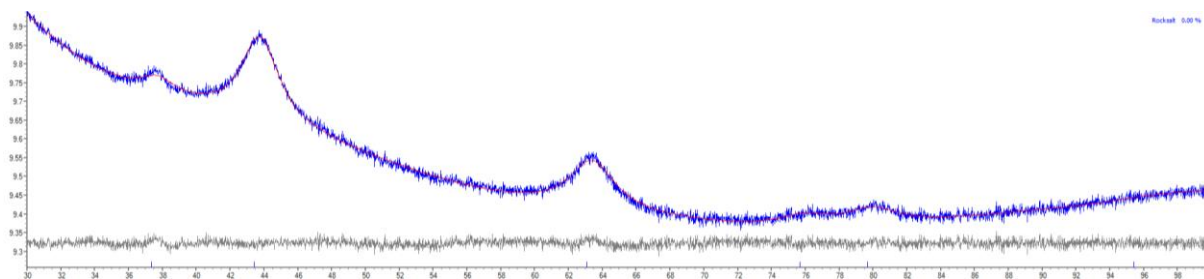
Figure H14: Pawley refinement plot of Li₄Mn₂O₅ synthesised using EOL cathode material (λ = 1.54 Å). R$_{wp}$ = 0.91%, R$_p$ = 0.72% and GOF = 1.08.
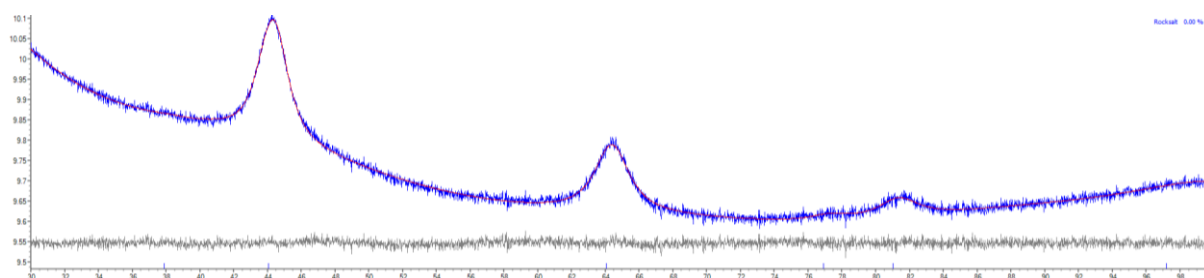
Figure H15: Pawley refinement plot of Li₂MnO₂.₂₅F synthesised using EOL cathode material (λ = 1.54 Å). R$_{wp}$ = 0.80%, R$_p$ = 0.64% and GOF = 1.04.
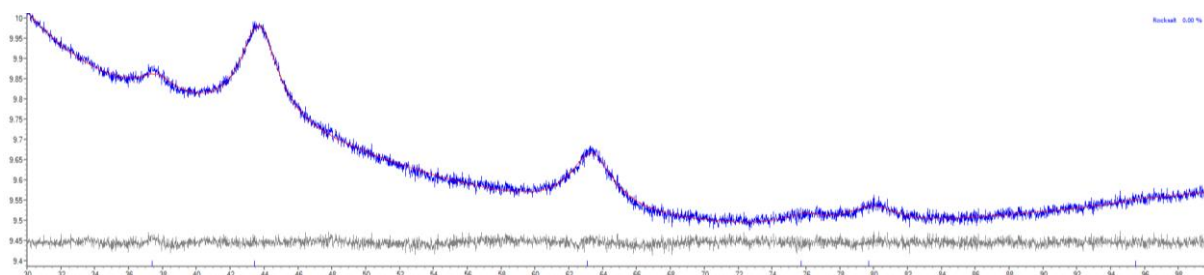
Figure H16: Pawley refinement plot of Li₄Mn₂O₅ synthesised using QC cathode material (λ = 1.54 Å). R$_{wp}$ = 0.84%, R$_p$ = 0.67% and GOF = 1.05.
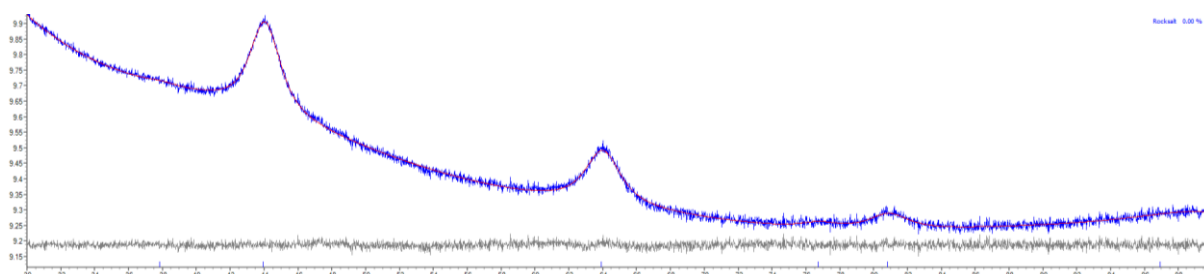
Figure H17: Pawley refinement plot of Li₂MnO₂.₂₅F synthesised using QC cathode material (λ = 1.54 Å). R$_{wp}$ = 0.91%, R$_p$ = 0.72% and GOF = 1.03.

Appendix I: XRD pattern of $Li_4Mn_2O_5$ made from MnO

and Li_2O
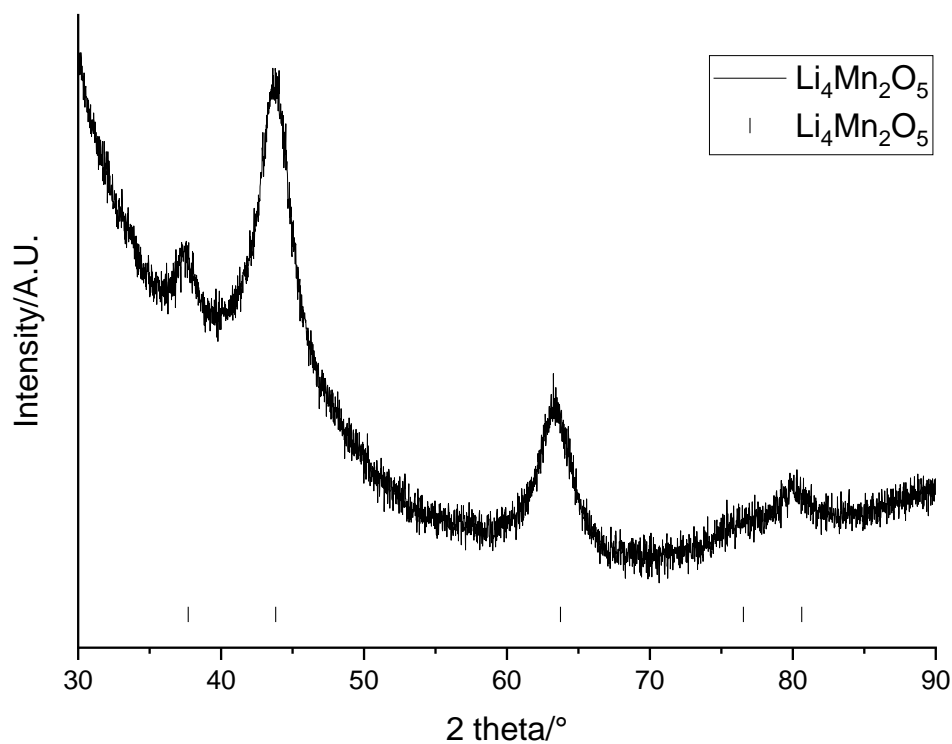
Figure I1: XRD pattern of $Li_4Mn_2O_5$ synthesised using Li_2O and MnO (λ = 1.54 Å)

Appendix J: Additional electrochemical data for

Chapter 5

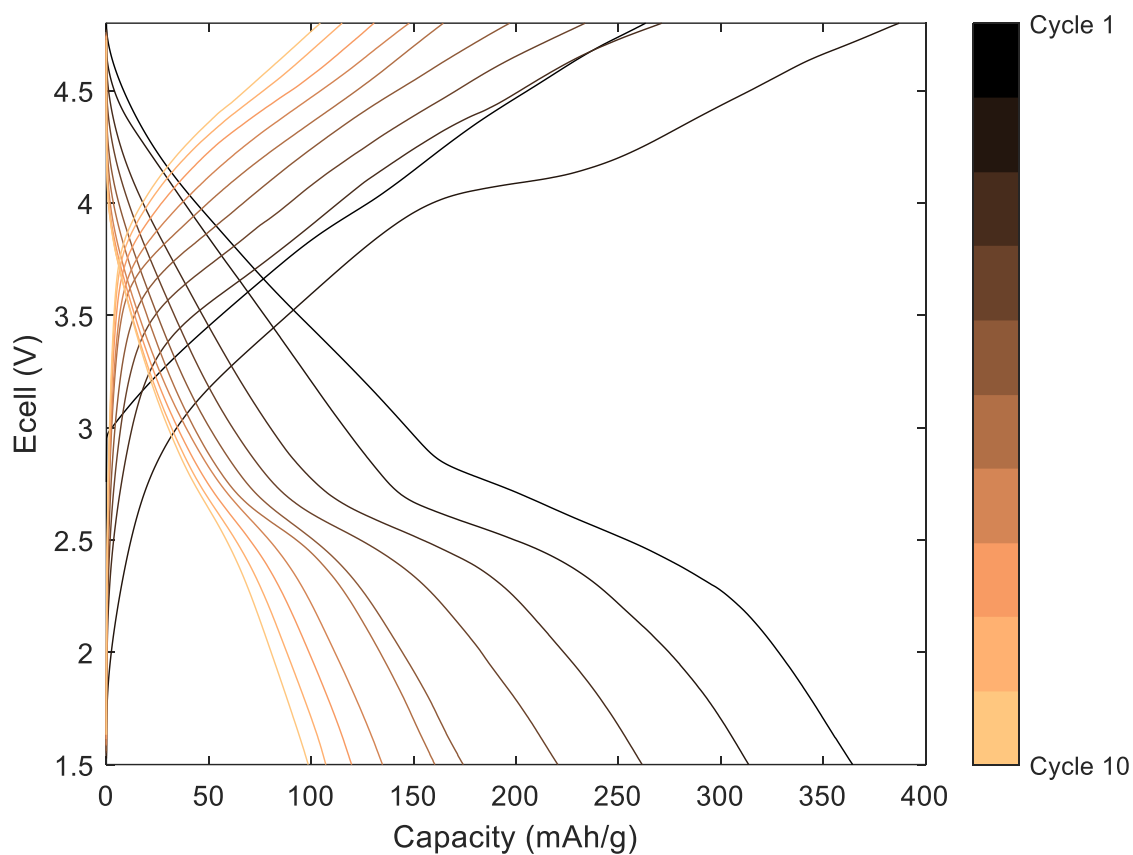*Figure J1: Galvanostatic charge-discharge profiles of a Li$_2$MnO$_{1.75}$F$_{1.25}$ powder cell cycled at 10 mAg^{-1} between 1.5-4.8 V*

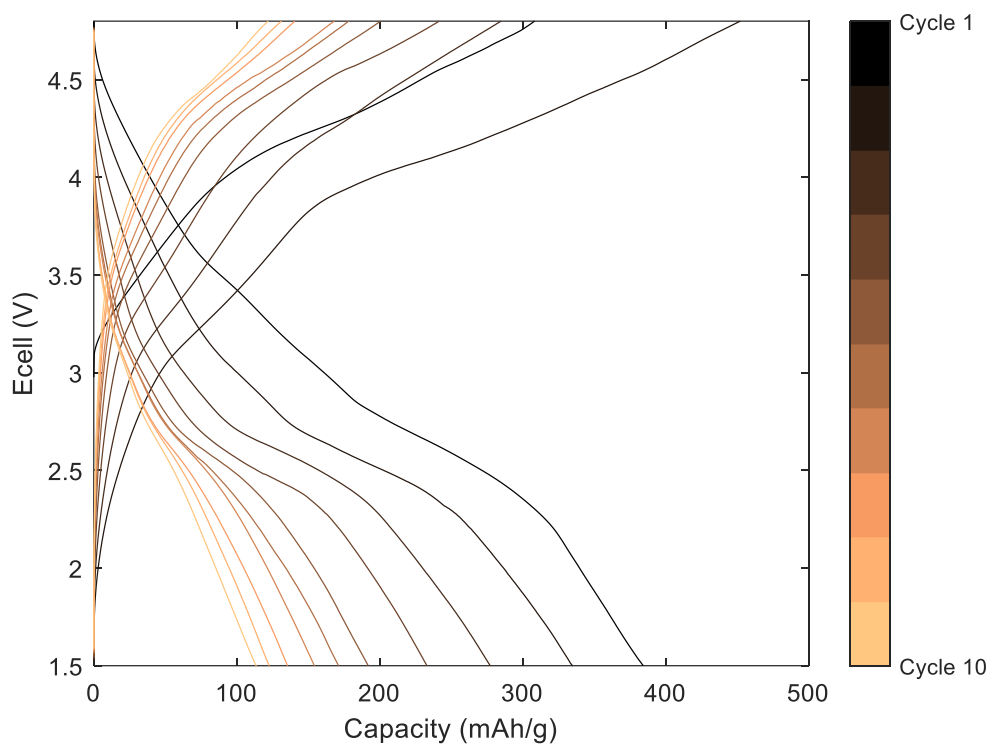*Figure J2: Galvanostatic charge-discharge profiles of a Li$_2$MnO$_{2.5}$F$_{0.5}$ powder cell cycled at 10 mAg^{-1} between 1.5-4.8 V*
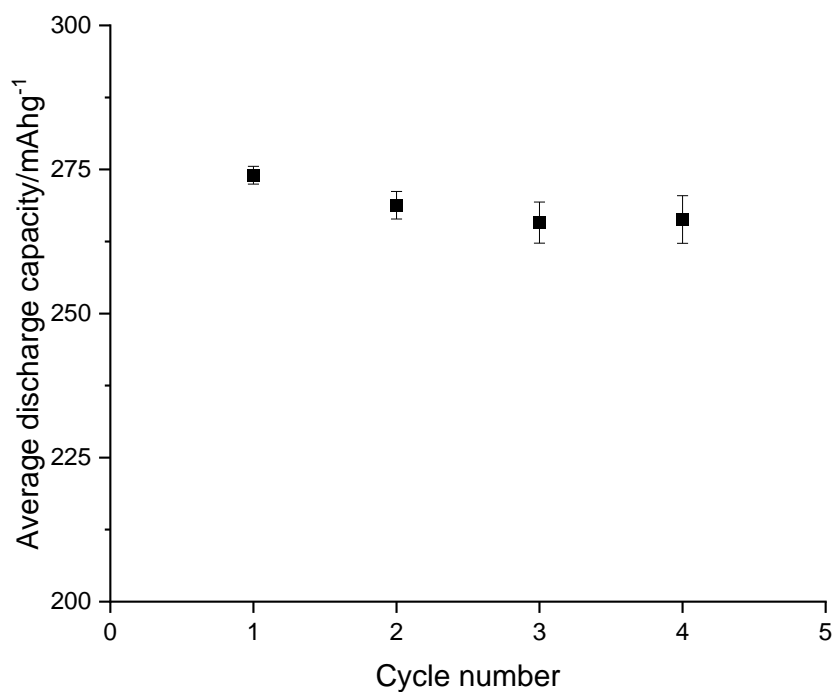

Figure J3: Average discharge capacity of pristine Li$_{1.8}$Na$_{0.2}$MnO$_2$F pellet cells. Error bars show relative standard deviation across 3 cells.
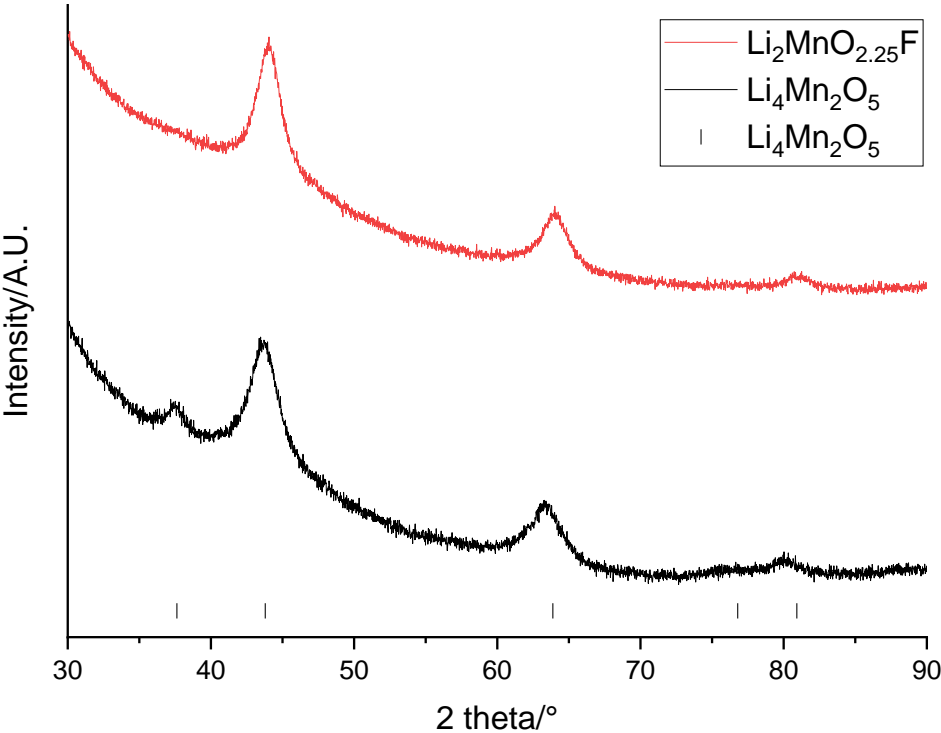
Appendix K: Synthesis of upcycled DRS from QC material

Figure K1: XRD patterns of Li₄Mn₂O₅ (black) and Li₂MnO₂.₂₅F (red) made from recovered LMO from the QC cathode (λ = 1.54 Å). Tick marks correspond to Li₄Mn₂O₅.

Table K1: Upcycled rocksalts made from LMO recovered from the QC cathode and corresponding lattice parameters

Sample	a/Å
$Li_4Mn_2O_5$	4.16(1)
$Li_2MnO_{2.25}F$	4.11(1)

Appendix L: Publications arising from this work

1. R. Madge, A. Jarvis, W. Lima da Silva, L. L. Driscoll, P. A. Anderson and P. R. Slater, *RSC Sustain.*, 2024, **2**, 1408-1417.

2. L. L. Driscoll, A. Jarvis, R. Madge, J. Price, R. Sommerville, F. S. Totini, M. Bahri, B. L. Mehdi, E. Kendrick, N. D. Browning, P. K. Allan, P. A. Anderson and P. R. Slater, Phase-selective recovery and regeneration of end-of-life electric vehicle blended cathodes via selective leaching and direct recycling, *ChemRxiv*, 2023, DOI:10.26434/chemrxiv-2023-56rkk. This content is a preprint and has not been peer-reviewed.